# Bending Vibrations of a Pipe Line Containing Flowing Fluid

By HOLT ASHLEY[1] and GEORGE HAVILAND,[2] CAMBRIDGE, MASS.

**Free vibrations and forced motions due to cross winds may both create important problems in the design of pipe lines supported above ground. An analytic investigation, based on simple beam theory, shows that the flow of fluid in such a pipe line produces marked damping tendencies and thus may reduce the severity of loading encountered. The time dependence of the fundamental mode of a simply supported pipe line is calculated for a number of mass-flow rates, the damping being observed to increase rapidly and the frequency to remain nearly constant over the practically important range. A method is outlined for studying forced vibration, higher modes, and other end conditions. Finally the problem is discussed in terms of traveling waves on an "infinite" unsupported pipe line.**

## Statement of Problem

THE present investigation arose from a study of aerodynamically induced vibrations, which occurred at critical wind speed in a large above-ground oil pipe line operated by the Trans-Arabian Pipe Line Company. The vibrations were observed to be complicated in character and of small amplitude, decaying to rest after a few seconds. In view of the violence of the oscillations which critical winds induce in other circular-cylindrical beams (1),[3] one is led to suspect the presence of some agency that damps the pipe-line motion and tends to destroy its simple harmonic nature. The following analysis indicates that the flow of oil in the pipe line is such an agency and attempts to evaluate its effectiveness quantitatively.

As a model on which to base the theoretical study, consider a continuous pipe line of uniform, hollow, cylindrical section. Outside diameter is 30 in., and supports are spaced about 66 ft apart. Since alternate spans were observed to vibrate oppositely to one another, the condition of simple support is suggested. Each span appears to conform quite closely to the assumptions of simple beam theory with simply supported ends. Without fluid flowing, the free motion of any span is then governed by the differential equation

$$EI\,\frac{\partial^4 z}{\partial x^4} + m\,\frac{\partial^2 z}{\partial t^2} = 0 \qquad [1]$$

where

$EI$ = flexural stiffness
$m$ = mass per unit length
$z$ = lateral deflection of pipe line
$x$ = axial co-ordinate
$t$ = time co-ordinate

If $L$ represents the length of a span, Equation [1] must be combined with boundary conditions

$$\left.\begin{aligned} x = 0,\quad z &= \frac{\partial^2 z}{\partial x^2} = 0 \\ x = L,\quad z &= \frac{\partial^2 z}{\partial x^2} = 0 \end{aligned}\right\} \qquad [2]$$

The solutions of System [1]-[2] are well known to consist of simple harmonic vibrations with sinusoidal mode shapes and circular frequencies

$$\omega = \frac{n^2\pi^2}{L^2}\sqrt{EI/m},\quad n = 1, 2, 3, \ldots .$$

If incompressible fluid flows along the pipe line at flux rate $\sigma$ (mass per unit time), lateral motion induces a shear force $\sigma\,\frac{\partial z}{\partial t}$ on each section, as illustrated in Fig. 1. The magnitude of this shear may be affected by the development of eddies or systematic

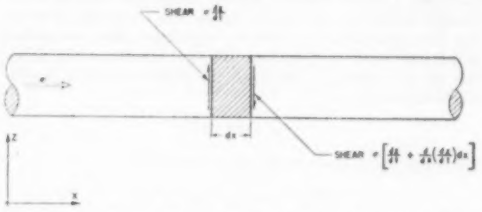


FIG. 1 SHEAR FORCES DUE TO FLUID FLOW IN A SECTION OF PIPE LINE

secondary circulation in the flow, and it would certainly be open to some question if the fluid were compressible, since then the center of mass of the fluid contained in any section would not be constrained to move laterally with the pipe. All these effects necessarily must be neglected in the present simple analysis. In order to set up the flexural vibration equation with mass flux $\sigma$ but with negligible rotatory inertia, apply Newton's law to an element $dx$ of the pipe. This has mass $m dx$ and acceleration $(\partial^2 z)/(\partial t^2)$. Elastic shears apply a force

$$-EI\,\frac{\partial^4 z}{\partial x^4}\,dx$$

Fig. 1 shows that the mass flux accounts for an additional unbalanced shear

$$= \sigma\,\frac{\partial z}{\partial t} - \sigma\left[\frac{\partial z}{\partial t} + \frac{\partial}{\partial x}\left(\frac{\partial z}{\partial t}\right)dx\right]$$

$$= -\sigma\,\frac{\partial^2 z}{\partial x \partial t}\,dx$$

[1] Assistant Professor, Department of Aeronautical Engineering, Massachusetts Institute of Technology.

[2] Research Assistant, Department of Aeronautical Engineering, Massachusetts Institute of Technology.

[3] Numbers in parentheses refer to the Bibliography at the end of the paper.

Contributed by the Applied Mechanics Division and presented at the Annual Meeting, New York, N. Y., November 27-December 2, 1949, of THE AMERICAN SOCIETY OF MECHANICAL ENGINEERS.

Discussion of this paper should be addressed to the Secretary, ASME, 29 West 39th Street, New York, N. Y., and will be accepted until October 10, 1950, for publication at a later date. Discussion received after the closing date will be returned.

NOTE: Statements and opinions advanced in papers are to be understood as individual expressions of their authors and not those of the Society. Paper No. 49—A-22.

Cancellation of common factor $dx$ produces the linear differential equation

$$EI\frac{\partial^4 z}{\partial x^4} + m\frac{\partial^2 z}{\partial t^2} + \sigma\frac{\partial^5 z}{\partial x \partial t} = 0 \quad [3]$$

Free motions of the pipe line can be studied by finding solutions of Equation [3], subject to boundary conditions [2], either with or without prescribed initial conditions. Permanent forced motion of the pipe line is described by a particular solution of System [3]–[2] with the given forcing function $F(x, t)$ per unit length inserted on the right of Equation [3]. In a cross-wind of velocity $v$, $F(x, t)$ is probably very nearly of the form $Pe^{i\omega_f t}$, $\omega_f$ being obtained from the experimental relation

$$\frac{\omega_f D}{v} \cong 2\pi(0.202)$$

when the Reynolds number based upon pipe diameter $D$ is less than about 400,000. Krzywoblocki (2) states that for greater Reynolds numbers, the wake of a cylinder still has a lateral periodic character that can be brought out by resonance between its frequency and a structural natural frequency of the cylinder. Therefore dangerous resonance cannot be ruled out completely. The same reference (2) shows that the empirical value of $\omega_f D/v$ increases with Reynolds number beyond 400,000, going toward infinity from its lower range magnitude near $2\pi$ (0.20).

Considerable light can be thrown on the forced-vibration problem by consideration of the simpler free-vibration problem represented by Equations [3] and [2]. The third term of Equation [3] is somewhat like the viscous-damping term which occurs in the equation of motion of a single-degree-of-freedom system; if the pipe line were externally damped it would be of the form $f(\partial z)/(\partial t)$. Hence damped natural modes of vibration are strongly suggested. It will be shown that no simple harmonic free vibrations can occur, since no "standing waves" are capable of being set up in the pipe line. Since linear differential Equation [3] has constant coefficients, the standard method of solution[4] is to assume that

$$z = Ce^{(\omega t + \alpha x)}$$

This substitution leads to the algebraic equation

$$EI\,\alpha^4 + \sigma\omega\alpha + m\omega^2 = 0$$

In theory this quartic can be solved for its four roots

$$\alpha_i(\omega) \quad i = 1, 2, 3, 4.$$

A solution of the form

$$z = e^{\omega t}\sum_{i=1}^{4} C_i e^{\alpha_i x}$$

is substituted into boundary conditions [2], producing four, homogeneous, linear equations for constants $C_i$. The coefficients in these equations are functions of $\omega$ and the beam properties. The characteristic values of $\omega$ can be found by setting the denominator determinant of these coefficients equal to zero.

While the process just outlined is relatively simple for beam problems with $\sigma = 0$, it is practically unworkable in the present case since it calls for analytic solution of a quartic, etc. Hence some straightforward approximate scheme is called for to find the natural modes. Since a Fourier series representation of the mode shape appears impossible in view of the natural modes at $\sigma = 0$, it was decided to resort to a power-series approximation.

[4] Reference (3), pp. 450–454.

## Solution by Power Series

In order to generalize the results and simplify numerical calculation, the problem is set up in terms of the following dimensionless quantities

$$\zeta = z/L$$
$$\xi = x/L$$
$$\tau = t\sqrt{EI/mL^4}$$

Substitution into System [3]–[2] produces the following forms

$$\frac{\partial^4 \zeta}{\partial \xi^4} + \frac{\partial^2 \zeta}{\partial \tau^2} + \mu\frac{\partial^2 \zeta}{\partial \xi \partial \tau} = 0 \quad [4]$$

$$\left.\begin{aligned} \xi = 0;\quad & \zeta = \frac{\partial^2 \zeta}{\partial \xi^2} = 0 \\ \xi = L;\quad & \zeta = \frac{\partial^2 \zeta}{\partial \xi^2} = 0 \end{aligned}\right\} \quad [5]$$

$\mu = \sigma L/\sqrt{mEI}$ is a dimensionless mass flux.

System [4]–[5] is solved by assuming

$$\zeta = F(\xi)e^{i\delta\tau} \quad [6]$$

with

$$F(\xi) = \sum_{n=0}^{\infty} a_n \xi^n \quad [7]$$

Insertion into Equation [4] produces an ordinary differential equation for $F$

$$\frac{d^4 F}{d\xi^4} + i\mu\delta\frac{dF}{d\xi} - \delta^2 F(\xi) = 0 \quad [8]$$

In the case of forced vibrations, a term $Pe^{i\omega_f t}$ on the right side of Equation [3] leads to

$$\frac{PL^3}{EI}e^{i\delta_f \tau}$$

on the right of Equation [4] with $\delta_f \tau = \omega_f t$. The constant $PL^3/EI$ would then appear on the right of Equation [6], and $\delta_f$ would replace $\delta$ throughout.

Substitution of power series [6] into Equation [8] and boundary conditions [5] gives a set of simultaneous equations for the coefficients $a_n$; $a_0$ and $a_2$ are at once determined to be zero, leaving the following equations

$$\left.\begin{aligned} &(a) \quad a_1 + \sum_{n=3}^{\infty} a_n = 0 \\ &(b) \quad \sum_{n=3}^{\infty} n(n-1)a_n = 0 \\ &(c) \quad 24a_4 + i\mu\delta a_1 = 0 \\ &(d) \quad 120a_5 - \delta^2 a_1 = 0 \\ &(e) \quad 360a_6 + 3i\mu\delta a_4 = 0 \end{aligned}\right\} \quad [9]$$

$$n(n-1)(n-2)(n-3)a_n + (n-3)i\mu\delta a_{n-3} - \delta^2 a_{n-4} = 0$$

$$\text{for } n = 7, 8, \ldots \qquad (f), (g), \ldots$$

For forced vibrations, the constant $PL^3/EI$ appears on the right of Equation [9c], while the others are unchanged. Convergence of the power series is easily demonstrated when $\mu = 0$ and certainly also holds for small positive values of $\mu$. Therefore a solution can be obtained by cutting off the power series above some finite $n$ and solving system [9]. For the free vibrations, values of

$\delta$ are determined by equating the denominator determinant of the system to zero. The mode shapes are then given by the relative magnitudes of the $a_n$. A study of the forced vibration could be carried out by plotting the response (deflection at mid-span, etc.) versus $\omega_f$ or $\delta_f$ for different values of $\mu$. Each point on such a plot would result from simultaneous solution of system [9] with appropriate $\mu$, $\delta_f$, and $PL^3/EI$ substituted.

The fundamental mode of free vibration of the pipe line has been calculated for values of $\mu$ from 0 to 0.25, which seem to cover the range to be encountered in practice. It was found by comparison with the known solution $\delta = \pi^2$ at $\mu = 0$ that terms up to $a_9$ must be included for satisfactory accuracy. This calculation involved determination of the proper root of a sixth-order complex polynomial in complex $\delta$. These roots were found graphically, using a simple iteration procedure which started from the known value of $\delta$, when $\mu = 0$. The results appear in Fig. 2. Since the time history of the motion is represented by

$$e^{i\delta\tau} = Exp\left[i\delta\sqrt{EI/mL^4}\,t\right]$$
$$= Exp\left\{\left[-\delta_I\sqrt{EI/mL^4} + i\delta_R\sqrt{EI/mL^4}\right]t\right\}$$

(with $\delta = \delta_R + i\delta_I$), it can be described by curves of dimensionless circular frequency

$$\delta_R = \omega\sqrt{mL^4/EI}$$

and dimensionless damping factor $-\delta_I$ versus dimensionless mass flux $\mu$. Very little change is seen to occur in the frequency of vibration over the practical range of $\mu$. The damping increases rapidly with $\mu$, however, confirming the suspected influence of mass flux on the vibrations. It is not expected that small values of $\mu$ will produce large changes in the mode shapes, but the fact that the values of $a_n$ will be complex shows that all points along a span will not reach maximum amplitude at the same instant. Thus waves will be observed to travel along the pipe. The appearance of such waves probably accounts in part for the complicated character of the motion actually observed in the Arabian pipe line.

The method proposed can be extended to study the higher harmonics of free vibration of the pipe line and to compute various types of forced motion. It is also suitable for systems with other boundary conditions, such as a clamped pipe.

### Numerical Example

Consider a pipe line with the following properties:

| | |
|---|---|
| Outside diameter | = 30 in. |
| Wall thickness | = 0.25 in. |
| Span between supports, $L$ | = 66 ft |

The bending stiffness of the steel pipe is given by

$$E = 30{,}000{,}000 \text{ psi}$$
$$I = 0.249 \text{ ft}^4$$
$$EI = 1.077 \times 10^9, \text{ lb-ft}^2$$

If the pipe line is full of oil with density 56.2 pcf, the mass per unit length of oil and pipe is

$$m = 10.77 \text{ slugs per ft}$$

At the high outside temperature to be expected, the viscosity of the oil will be low, and turbulent flow will occur inside the pipe. Hence a representative figure for the mean flow velocity of the oil is 15 fps and $\sigma = 124$ slugs per sec. This gives a dimensionless mass flux of $\mu = \sigma L/\sqrt{mEI} = 0.0761$

Fig. 2 gives the following values for dimensionless circular frequency and damping rate

$$\omega\sqrt{mL^4/EI} = 9.679$$
$$\delta_I = -0.163$$

From these it is easily calculated that the actual circular frequency of the fundamental mode of bending vibration is $\omega = 22.2$ radians per sec = 3.54 cycles per sec. The free vibration will damp to one half its initial amplitude in 1.86 sec, or 6.56 cycles. For a system of such large mass, external excitation would have to be applied by a very large force at almost exactly the natural frequency before a dangerous resonance condition

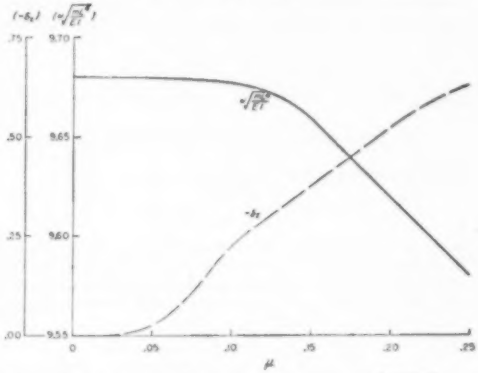


Fig. 2 Dimensionless Circular Frequency $\omega\sqrt{mL^4/EI}$ and Damping Factor $-\delta_I$ Versus Mass Flux Parameter $\mu = \sigma L/\sqrt{mEI}$ for Fundamental Vibration Mode of a Pipe Line

could occur. Any impulsive or transient excitation could be handled easily by the energy dissipation due to the fluid motion. Therefore it is not expected that aerodynamically induced vibrations of serious magnitude will be encountered.

### Traveling Waves in an Infinite Pipe Line

It is known from simple beam theory that traveling waves can occur in an unsupported beam of great extent. In fact, the natural vibrations of a finite span can be regarded as standing waves produced by traveling waves of equal wave length and amplitude proceeding in opposite directions. Only when waves of equal wave length travel in the two directions at the same velocity can such standing waves occur.[5]

Much light can be thrown on the vibrations of the pipe line with mass flux by considering its traveling waves. The form of these is found by changing variables in Equation [4] from $\tau$, $\xi$ to $\tau$ and $\eta - \mu\tau$, whereupon it assumes the form

$$\frac{\partial^4\zeta}{\partial\eta^4} + \frac{\partial^2\zeta}{\partial\tau^2} - \mu^2\frac{\partial^2\zeta}{\partial\eta^2} = 0 \qquad [10]$$

Equation [10] can be solved by separation of variables, letting

$$\zeta \sim e^{i(\delta\tau + \beta\eta)}$$

$\delta$ and $\beta$ are found to be related according to

$$\beta^4 + \mu^2\beta^2 - \delta^2 = 0$$

which has four roots

$$\beta = \pm\sqrt{-\frac{\mu^2}{2} \pm \tfrac{1}{2}\sqrt{\mu^4 + 4\delta^2}}$$

[5] Reference (4), vol. I, on waves in strings.

Simple harmonic traveling waves are represented only by those solutions in which $\beta$ and $\delta$ are real quantities. Thus two of the values of $\beta$ are excluded, leaving

$$\beta_1 = \sqrt{-\mu^2/2 + 1/2\sqrt{\mu^4 + 4\delta^2}}$$

$$\beta_2 = -\sqrt{-\mu^2/2 + 1/2\sqrt{\mu^4 + \mu\delta^2}}$$

In terms of the original variables $\tau$ and $\xi$ the two types of waves are represented by

$$\zeta_1 \sim Exp[i\beta_1\xi + i(\delta - \mu\beta_1)\tau]$$
$$= Exp[i\sqrt{\zeta} + i(\delta - \mu\sqrt{})\tau]$$
$$\zeta_2 \sim Exp[i\beta_2\xi + i(\delta - \mu\beta_2)\tau]$$
$$= Exp[-i\sqrt{\zeta} + i(\delta + \mu\sqrt{})\tau]$$

where

$$\sqrt{} = \sqrt{-\mu^2/2 + 1/2\sqrt{\mu^4 + 4\delta^2}}$$

Harmonic traveling waves are of the general form

$$Exp\left[i\frac{2\pi}{\lambda}(x - Vt)\right]$$

with $\lambda$ the wave length and $V$ the velocity of travel. A comparison between this expression and the forms of $\zeta_1$ and $\zeta_2$ leads to the following wave lengths and velocities of the two types

$$\left.\begin{aligned}\frac{\lambda_1}{L} &= \frac{2\pi}{\sqrt{1/2\sqrt{\mu^4 + 4\delta^2} - \mu^2/2}} \\ \sqrt{\frac{mL^3}{EI}}\,V_1 &= \mu - \frac{\delta}{\sqrt{1/2\sqrt{\mu^4 + 4\delta^2} - \mu^2/2}}\end{aligned}\right\} \quad \ldots [11]$$

$$\frac{\lambda_2}{L} = \frac{2\pi}{\sqrt{1/2\sqrt{\mu^4 + 4\delta^2} - \mu^2/2}} \quad \ldots [12]$$

$$\sqrt{\frac{mL^3}{EI}}\,V_2 = \mu + \frac{\delta}{\sqrt{1/2\sqrt{\mu^4 + 4\delta^2} - \mu^2/2}}$$

In Equations [11] and [12], $\delta$ is to be regarded as an intermediate parameter which can be used to calculate corresponding values of $V$ and $\lambda$. These values have been computed and are plotted in Figs. 3 and 4 in the dimensionless form $\sqrt{mL^3/EI}\,V_1$ versus $\lambda_1/L$; $L$ must here be regarded as some reference length.

It is evident from Figs. 3 and 4 that no standing waves can occur at any wave length unless $\mu = 0$. All of the curves preserve the rough inverse proportionality between $V$ and $\lambda$, which relation holds exactly at $\mu = 0$. However, for a given $\lambda$, the waves traveling in the positive $X$-direction move faster than the negative ones. This fact of course reflects a tendency of the flowing fluid to urge the positive waves along and retard the negative ones.

The true free vibrations of the finite pipe line must then be found by somehow superposing solutions of Equation [10], corresponding to imaginary or complex values of $\beta$. Such solutions will exhibit decaying or diverging characteristics with both $X$ and $t$, and they can only have physical validity over a limited range in space and time.

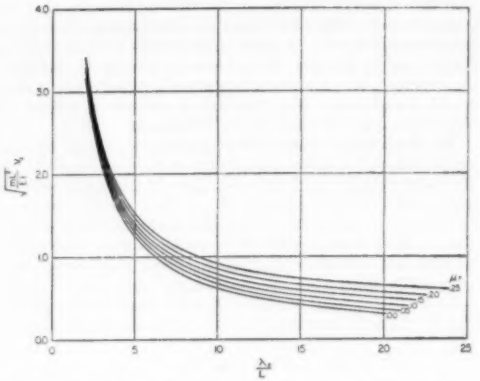


FIG. 3 $\sqrt{mL^3/EI}\,V_2$ VERSUS $\lambda_2/L$ FOR POSITIVE WAVES IN AN INFINITE PIPE LINE

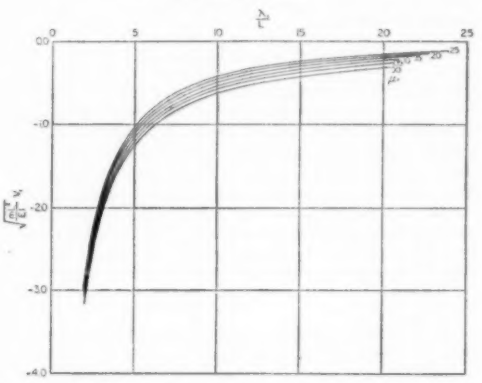


FIG. 4 $\sqrt{mL^3/EI}\,V_1$ VERSUS $\lambda_1/L$ FOR NEGATIVE WAVES IN AN INFINITE PIPE LINE

## BIBLIOGRAPHY

1 "Mechanical Vibrations," by J. P. Den Hartog, McGraw-Hill Book Company, Inc., New York, N. Y., 1940, chapt. 7.

2 "Investigation of the Wing-Wake Frequency With Application of the Strouhal Number," by M. Z. Krzywoblocki, *Journal of the Aeronautical Sciences*, vol. 12, January, 1945, pp. 51–62.

3 "Die Differential und Integralgleichungen der Mechanik und Physik," by Philipp Frank and Richard von Mises, Mary S. Rosenberg, New York, N. Y. (reprinted by authority of Alien Property Custodian), 1943, pp. 450–454.

4 "The Theory of Sound," by Baron Rayleigh, Dover Publications, New York, N. Y., vol. 1, 1945, chapt. 6.

# The Flow and Fracture of a Brittle Material

BY L. F. COFFIN, JR.,[1] SCHENECTADY, N. Y.

**The mechanism of flow and fracture of a gray cast iron can be understood if one considers the microstructure to consist of a ductile structure with a random dispersion of cracks due to the graphite flakes following the concept of Fisher. A notch effective stress can be calculated for a critically situated crack by a knowledge of the external stresses, a plastic stress-concentration factor of 3, and a residual tensile stress at the sharp edge of the crack, based upon either the "maximum-shear" theory or the "distortion-energy" theory. This allows the formulation of generalized plastic stress-strain relationships and renders gray cast iron applicable to the many known solutions for plastic flow of ductile metals. Fracture in the region of tension-tension and tension-compression can be evaluated by a similar analysis, using the same stress-concentration factor and the same residual stress. A combined stress-testing program is described wherein thin-walled cast-iron tubes are subjected to two-dimensional states of combined stress covering the complete two-dimensional field.**

## Nomenclature

The following nomenclature is used in this paper:

- $\sigma_1,\sigma_2,\sigma_3$ or $\sigma_r,\sigma_t,\sigma_z$ = principal stresses, psi (a second subscript refers to position)
- $\sigma_0$ = a residual stress
- $\sigma^*$ = effective stress, depending upon theory of strength used
- $\sigma_N{}^*$ = notch effective stress
- $\sigma_{Nf}{}^*$ = notch effective stress at fracture
- $\epsilon_1,\epsilon_2,\epsilon_3$ or $\epsilon_r,\epsilon_t,\epsilon_z$ = principal strains, in/in. (second subscript refers to position; subscript $p$ indicates a plastic strain; subscript $e$ indicates elastic strain)
- $\epsilon^*$ = effective strain, depending upon theory of strength used
- $E$ = modulus of elasticity, psi
- $\nu$ = Poisson's ratio
- $\nu_p$ = Poisson's ratio for plastic strains
- $A$, $D$ = variable coefficients depending upon degree of plastic flow
- $\omega_1 = 1 + D$
- $\omega_2 = \nu + D/2$
- $k$ = stress-concentration factor
- $K$ = constant

## Introduction

Mathematical formulation of the laws governing the deformation of an ideally plastic material under a monotonic combined stress state are well known (1)[2] and have been used with considerable success in numerous cases of static plastic flow and creep of ductile metals, such as the various steels, copper, aluminum, etc. In the formation of these relationships it is assumed that the material is isotropic, has only elastic compressibility, and that a generalized stress-strain relationship can be expressed of the form

$$\sigma^* = f(\epsilon^*) \quad \ldots\ldots [1]$$

where $\sigma^*$ is the effective stress, $\epsilon^*$ the effective strain defined as

$$\left.\begin{aligned} \sigma^* &= \frac{1}{\sqrt{2}}\sqrt{(\sigma_1-\sigma_2)^2+(\sigma_2-\sigma_3)^2+(\sigma_3-\sigma_1)^2} \\ \epsilon^* &= \frac{\sqrt{2}}{3}\sqrt{(\epsilon_1-\epsilon_2)^2+(\epsilon_2-\epsilon_3)^2+(\epsilon_3-\epsilon_1)^2} \end{aligned}\right\} \quad [2]$$

The basis of these effective stress-strain relations stem from the "distortion-energy" theory for plastic flow. Other simplified relations have been substituted for Equations [2] to facilitate analysis such as

$$\left.\begin{aligned} \sigma^* &= \sigma_{max} - \sigma_{min} \\ \epsilon^* &= \epsilon_{max} - \epsilon_{min} \end{aligned}\right\} \quad \ldots\ldots [3]$$

the basis of which is the "maximum-shear" theory. While Equations [3] lack the theoretical advantages of Equations [2], combined stress experiments by Davis (2) and Osgood (3) show that either is equally satisfactory, and further, that the validity of Equation [1] is good to about 10 per cent effective strain.

A generalized Hooke's law for plastic flow may then be written to include both elastic and plastic components of strain and has the form (4)

$$\left.\begin{aligned} E\epsilon_1 &= \omega_1\sigma_1 - \omega_2(\sigma_2+\sigma_3) \\ E\epsilon_2 &= \omega_1\sigma_2 - \omega_2(\sigma_3+\sigma_1) \\ E\epsilon_3 &= \omega_1\sigma_3 - \omega_2(\sigma_1+\sigma_2) \end{aligned}\right\} \quad \ldots\ldots [4]$$

where

$$\left.\begin{aligned} \omega_1 &= 1 + D \\ \omega_2 &= \nu + \frac{D}{2} \end{aligned}\right\} \quad \ldots\ldots [5]$$

Here $E$ and $\nu$ are the elastic constants (modulus of elasticity and Poisson's ratio) and $D$ is a variable, depending on the degree of flow. Equations [4] satisfy the law of constancy of plastic volume or

$$\epsilon_1 + \epsilon_2 + \epsilon_3 = \frac{1-2\nu}{E}(\sigma_1+\sigma_2+\sigma_3) \quad \ldots\ldots [6]$$

where the term of the right-hand side represents the elastic bulk modulus change. Also, Equations [4] satisfy the plastic-flow law regarding the constant proportionality of the stress differences to the strain differences or

$$\frac{\sigma_1-\sigma_2}{\epsilon_1-\epsilon_2} = \frac{\sigma_2-\sigma_3}{\epsilon_2-\epsilon_3} = \frac{\sigma_3-\sigma_1}{\epsilon_3-\epsilon_1} \quad \ldots\ldots [7]$$

The variable $D$ can be found in terms of the effective stress-

[1] Formerly Assistant Professor of Mechanical Engineering, Department of Mechanical Engineering, Massachusetts Institute of Technology, Cambridge, Mass.; now General Electric Research Laboratory. Mem. ASME.

Contributed by the Applied Mechanics Division and presented at the Annual Meeting, New York, N. Y., November 27–December 2, 1949, of The American Society of Mechanical Engineers.

Discussion of this paper should be addressed to the Secretary ASME, 29 West 39th Street, New York, N. Y., and will be accepted until October 10, 1950, for publication at a later date. Discussion received after the closing date will be returned

Note: Statements and opinions advanced in papers are to be understood as individual expressions of their authors and not those of the Society. Paper No. 49—A-24.

[2] Numbers in parentheses refer to the Bibliography at the end of the paper.

strain quantities by substitution of Equation [4] into the definition of $\epsilon^*$. Then

$$D = \frac{E\epsilon^*}{\sigma^*} - \frac{2}{3}(1 + \nu) \quad \ldots\ldots\ldots\ldots\ldots [8]$$

If one desires to use such relationships for a particular material, then certain experimentally observed characteristics must hold. By the nature of the Equations [1], [2], and [3], the simple tension stress-strain curve must be identical with the simple compression stress-strain curve. Furthermore, because of the condition of constancy of the plastic volume of the material, and isotropy, Poisson's ratio for plastic strains, both in compression and tension must be one half. Furthermore, by Equations [7], Mohr's stress circles must be proportional to Mohr's strain circle.

The foregoing characteristics are found to exist for the various so-called ductile materials such as iron, steel (except for ferritic steel at low temperatures and tool steels), copper, aluminum, lead, etc., at strains less than 10 per cent when the material is fairly free of directional effects. Brittle materials (those which show evidence of only slight flow in simple tension) in general do not show these characteristics. These include such substances as cast iron, concrete, pure magnesium, the glasses, beryllium, phosphor bronzes, etc. Generally, in these materials, the tensile characteristics are completely different for the compressive, showing for a particular stress a considerably larger plastic strain (except in the case of glass where no plastic flow is found). Further, the lateral-strain characteristics are markedly different in a tension and compression test, the tension test showing little lateral contraction, the compression test indicating considerable lateral expansion.

Because of these difficulties, the relationships of ideally plastic flow are completely invalid, and no success will be encountered in their use when a brittle material is considered. One of the purposes of this research is to investigate the behavior of a brittle material (cast iron) under combined stress, with an attempt to show what laws, if any, are followed when a brittle substance flows, and whether such laws can be formulated mathematically as in the case of ductile metals. This would be of considerable practical importance since low-ductility materials are commonly used in engineering applications and a complete understanding of their behavior should act to increase the scope of their application as well as the assurance of their present service.

Hand in hand with the problem of plastic flow in a brittle material is the problem of fracture (5 to 11). This is a complex problem and is not well understood. In a brittle structure the maximum stress theory is generally accepted as applying. That is to say, failure will occur when the maximum tensile stress reaches a certain critical value. This of course does not answer the problem when compressive stresses predominate in the loading. Experience seems to show that, under conditions of loading which are predominantly tensile, failure occurs along planes of maximum normal stress, while under simple compression, failure occurs by a shearing process on planes at about 45 deg to the loading direction.

Of particular interest in the problem of fracture of brittle materials is the influence of hydrostatic pr ssure. Th. von Kármán in his test on marble (6), and Bridgman (10) on various brittle materials, show that a superimposed hydrostatic pressure greatly increases the ductility of a brittle substance before fracture occurs. Bridgman has obtained in a tension specimen of beryllium a necking down to 48 per cent reduction in area by a high superimposed pressure of about 27,500 kg per sq cm.

The present-day concepts of the causes of brittleness in various substances stems from the theory of fracture proposed by Griffith (12), in which the structure is considered to be saturated with minute cracks having random orientation and causing stress concentrations of such magnitude as to account satisfactorily for the low strength and ductility. He further considered the effects of combined stress on this crack formation and arrived at a fracture criterion for combined stress in a completely brittle structure (no plastic flow), in which the fracture stress for compression was 8 times the fracture stress in tension, a ratio observed for certain brittle substances. This analysis also predicted normal plane fractures in tension, and oblique fractures in compression as observed.

The magnitude of the stress concentrations occurring varies considerably dependent on the size of the crack. Rowe and Gurney (13) calculated stress concentrations of the order of 600 for glass, while Fisher (14), explaining the tests of Grassi and Cornet (11) on cast iron, assumes the graphite flakes to act as sources of cracks and to cause a stress-concentrating effect of about 3. More will be said of the theory of Fisher later.

In the use of a brittle substance structurally the fracture conditions should be well understood because of the very low ductility usually present. The failure of a brittle structure when overstressed is not preceded by any of the danger signals exhibited in an overstressed ductile material such as local necking or large deformations, so that the stresses causing failure should be known with some precision. This investigation deals with the problems of fracture of cast iron as a brittle material with the purpose of formulating some mechanism to explain the fracture phemonenon in brittle materials and to propose a satisfactory law for engineering use.

## Experimental Program

The experimental phase of this investigation was devoted to the determination of stresses and strains up to fracture as found from thin-walled tubes of gray cast iron. Tubular specimens were chosen because of the simplicity in obtaining the various states of two-dimensional combined stress desired, because this type of specimen allowed the determination of the three principal strains independently, and because the stresses calculated from the applied loads depended only upon the equilibrium of the specimen and were independent of material constants.

Gray cast iron was selected for the material to be investigated principally because it represented an important engineering brittle material whose mechanical behavior was not well understood. At the same time it was felt that whatever was learned regarding its behavior might be extrapolated to apply to other brittle crystalline materials.

The material was supplied in the form of bars 12 in. long and 2 in. diam in an as-cast condition. The following chemical analysis was supplied: 3.08 per cent total C, 2.04 per cent Si, 0.56 per cent Mn, 0.112 per cent S, 0.33 per cent P. All bars were poured from the same ladle, and as much care as possible was furnished by the foundry to insure uniformity.

The bars were machined into thin-walled tubular specimens as shown in Fig. 1. The internal surface was honed, the external surface finished with crocus cloth so as to eliminate all surface irregularities. Three type of specimens were used. Those with threaded ends were used for states of combined stress involving circumferential tension and longitudinal tension or compression. Uniform cylindrical specimens were employed for tests involving both circumferential and axial compression. The thin-walled cylinder (lower left specimen in Fig. 1), was first used but resulted in premature buckling, making it necessary to thicken the wall and shorten the length to a more satisfactory type (shown at the lower right in Fig. 1). Prior to test, each specimen was measured carefully for internal and external diameter, wall thickness, and bore eccentricity. In general, due to the careful machining, the wall thickness varied less than 0.001 in. throughout each tube.

Special grips which were constructed for an earlier investigation

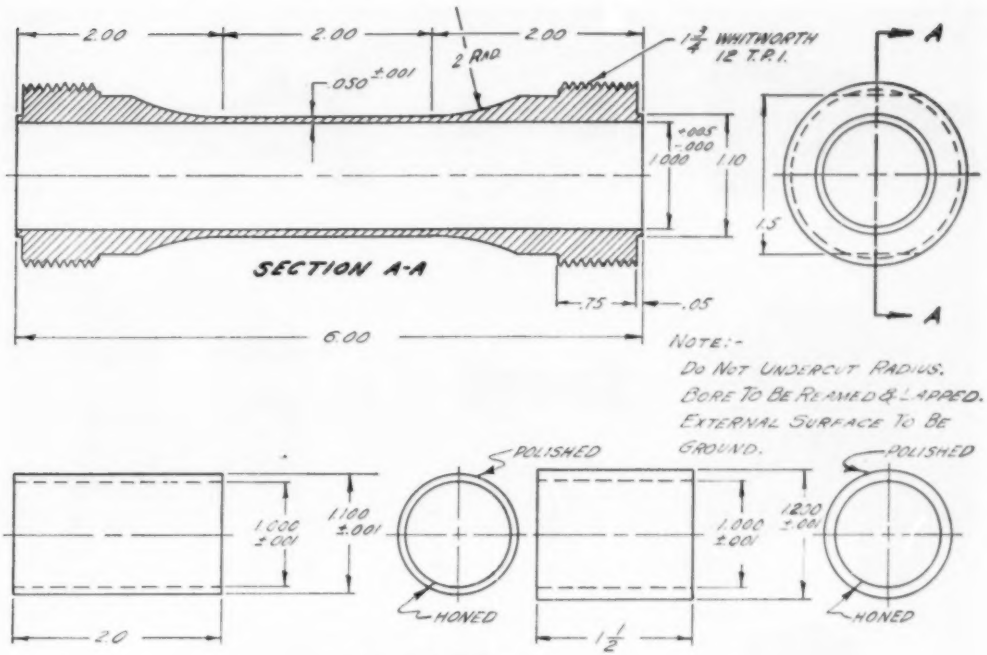


FIG. 1 TYPES OF TEST SPECIMENS

were modified to fit the cast-iron specimens to produce combined stress states of tension-tension and tension-compression. These are shown in Figs. 2 and 3. For the state of stress involving both axial and circumferential compression, external pressure was applied to the specimen which rested on a hardened base onto which was fitted a thick-walled cylinder. A plunger fitting the upper end of the cylinder supplied the longitudinal force. Sealing was accomplished by using neoprene washers. Fig. 4 shows an exploded view of this equipment.

Axial force, either tension or compression up to a maximum value of 60,000 lb was produced by a Baldwin-Southwark Universal hydraulic testing machine. Internal pressure was supplied by an Amsler pump and precision pendulum weighing system. This unit has the particularly desirable feature of an adjustable full scale range of pressure from 300 psi to 17,000 psi in infinite steps. Thus it is possible to use and maintain simple pressure-load ratios such as 1:1, 10:1, etc., by suitable adjustment of the pump scale. This makes for simplicity in supplying the correct constant stress ratio to the specimen throughout the test. For tests of the thicker-walled compression-compression specimens a similar Baldwin-Southwark machine of 200,000 lb capacity was used to supply longitudinal force.

In order to study the strain and density behavior of the material, it was necessary to measure independently the three principal strains in the tube. In so far as it is known to the author, this is the first time the independent measurement of the three principal strains during the actual test has been achieved. In studies of ductile materials, generally two principal strains are measured, the third being calculated by the law of constancy of volume. Since cast iron is not a ductile material and does not conform to a constant-volume law, such a procedure cannot be used.

The method finally decided upon to measure the principal strains depended upon the use of pairs of A-8, SR-4 resistance-wire strain gages cemented to the tube internally in the circumferential direction, and externally in the longitudinal and circumferential directions. By this procedure strains could be read up to fracture in most of the tubes tested since the gages would operate satisfactorily to strains of $20{,}000 \times 10^{-6}$ in./in. for most cases considerably above the limit of fracture strains. The proper interpretation of the internal circumferential gages when acted upon by pressure was the result of a considerable investigation which will be reported elsewhere (16). Initially an internal dilatation gage was investigated for the measurement of the internal tangential-strain readings, but was abandoned because of its inherent stiffness and inaccuracy for the more direct method of cementing gages to the internal-wall surface.

Knowing the internal and external circumferential strains, both the average radial strain and the average circumferential strain could be found since

$$\epsilon_r = \frac{\epsilon_{so}d_o - \epsilon_{si}d_i}{d_o - d_i} \quad \ldots\ldots [9]$$

$$\epsilon_t = \frac{\epsilon_{si} + \epsilon_{so}}{2} \quad \ldots\ldots [10]$$

also

$$\epsilon_z = \epsilon_{zo} \quad \ldots\ldots [11]$$

where the bared values are average strains, the unbared values the measured strains, and where the subscript refers to the inside or outside of the tube.

FIG. 2 TENSION-TENSION COMBINED STRESS GRIPS—EXPLODED VIEW

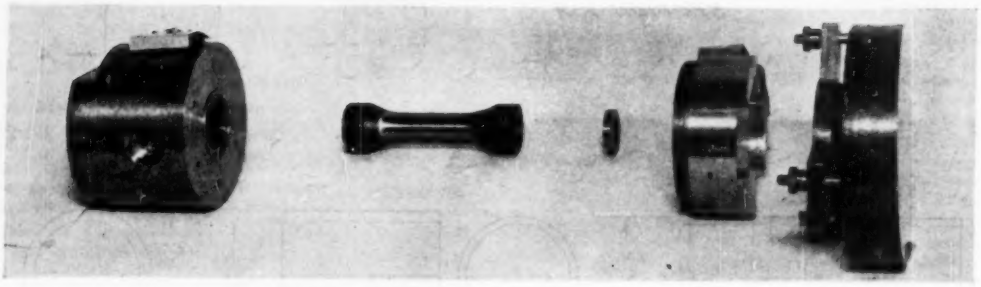

FIG. 3 TENSION-COMPRESSION COMBINED STRESS GRIPS—EXPLODED VIEW

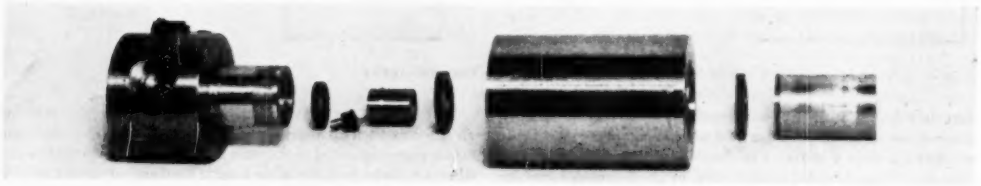

FIG. 4 COMPRESSION-COMPRESSION COMBINED STRESS GRIPS—EXPLODED VIEW

Each tube, when ready for test, had six A-8 gages attached, two each in series for each strain to be measured. Two additional gages mounted on a separate piece of cast iron served as a dummy for the external gages, while two other gages mounted on cast iron and subjected to the oil pressure acted as a dummy for the internal gages. Lead wires from the internal gages were soldered to a three-prong connector which could be attached to a mating connector on the grips to which in turn were soldered lead wires to the outside properly sealed to resist the pressure. Strains were measured by means of a SR-4 portable strain indicator.

The procedure in those tests in which strains were measured consisted of measuring the three strains as the load on the tube was increased by small increments (generally in increments of about 1000 psi or less of the largest stress). As the strain values became large and plastic flow ensued, some creeping of the tube was observed as the load was held fixed. In such cases sufficient time was allowed for the strain values to stabilize themselves so that during the time required to read gages there was negligible strain change. Strain readings could be taken directly to fracture in most cases (except in the compression-compression region). Stresses were calculated using the ordinary thin-walled expression for tubes acted on by internal-external pressure and end load.

Fracture-stress data were obtained on some 40 tubes subjected to various ratios of combined two-dimensional stress. Results of these fracture values are plotted in Fig. 5 for all the tubes tested,

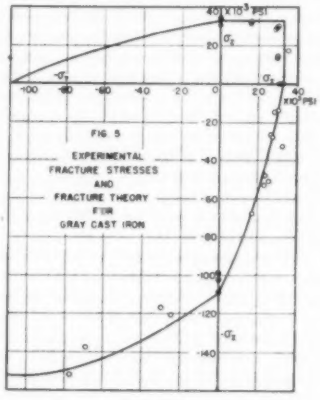


FIG. 5

except those which buckled or failed prematurely because of stress concentrations caused by the rejected dilatation gage. This is a two-dimensional representation of the axial stress versus the tangential stress. The radial stress (considered as acting on the mean diameter where it is $-p_i/2$ is not considered as having any bearing on this representation because of its small size. Complete strain data were obtained on about 12 tubes over a wide range of combined stress, using the technique just described.

Figs. 6 to 8 are included to show the appearance at fracture of some of the tubes. These tubes cover a wide range of two-dimen-

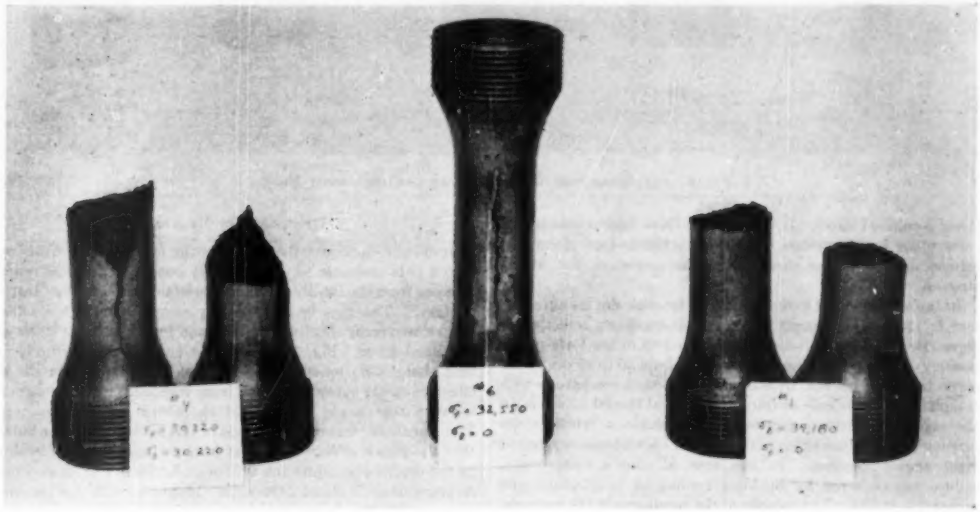

FIG. 6 FRACTURED SPECIMENS TENSION-TENSION REGION

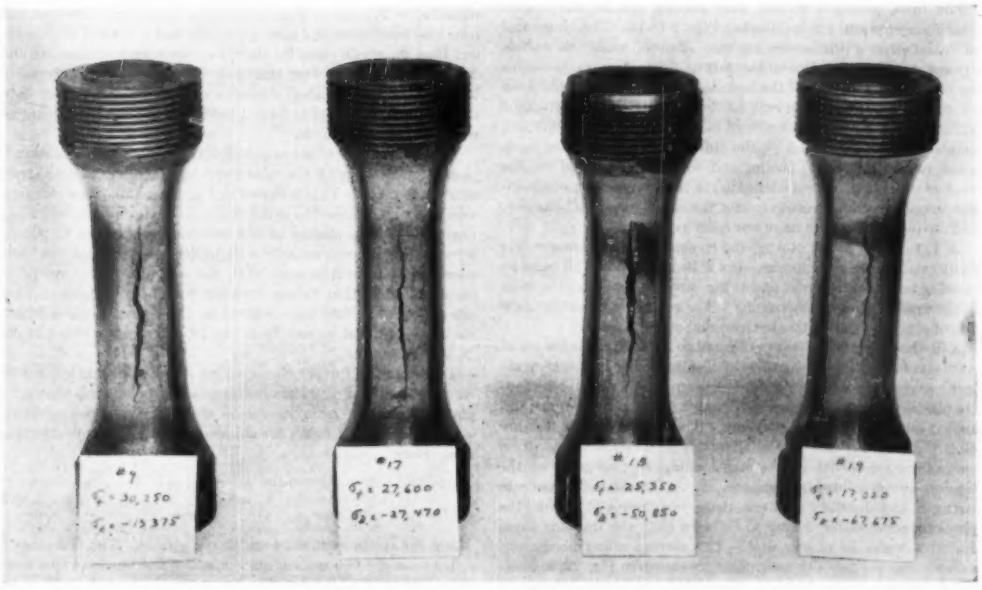

FIG. 7 FRACTURED SPECIMENS TENSION-COMPRESSION REGION

FIG. 8 FRACTURED SPECIMENS COMPRESSION-COMPRESSION REGION

sional combined stress. It is seen from these figures that in the cases where tensile stresses are present, a brittle type of crack is formed normal to the direction of the largest of the tensile stresses.

In the case of equal two-dimensional tension, the fracture surface in the four specimens tested at this condition consisted of three cracks, one longitudinal, the other two in the form of oppositely directed spirals making angles of from 30 to 45 deg. It is suspected that this is a necessary type of crack compatible with complete energy release at fracture for equal biaxial tension. In the region of tension-compression, the maximum tensile stress causing the crack decreases as the amount of compressive stress at right angles increases. In the case of simple compression, failure has occurred by buckling leading to longitudinal and transverse cracks. The balance of the specimens in the compression-compression range behaved in this fashion, failing due to an instability rather than because of complete separation along some plane.

The three principal strains were plotted against the largest principal stress and are included as Figs. 9 to 14. The tangential and axial stress-strain curves are very smooth, while the radial-strain curve shows considerable scatter. This of course is due to the inherent inaccuracy of the technique. Nevertheless, the data are sufficient to show with reasonable accuracy the magnitude of radial strain. For the tests carried out in simple compression and simple tension, Figs. 9 and 10, the radial strain was assumed to be equal to the tangential strain, and was not calculated by the method described. Tests conducted in the compression-compression range were not investigated for the complete strain behavior, and stress-strain curves have not been included.

In Figs. 15 to 20 are plotted the largest principal stress versus the permanent volume change. It will be noted that in all cases as yielding takes place, a permanent increase in volume occurs, even in the case of simple compression. The scatter in these curves is due of course to the scatter in the radial-strain data.

A further experiment was performed to indicate the influence of reversal of stress on the ductility of cast iron. Here a stress-strain test was performed first in compression to a point where considerable plastic strain had occurred, at which point the tube was unloaded and then tested in tension. The results of this test are plotted in Fig. 21. Also included in this figure is the stress-strain curve for tension with no previous loading, superimposed on the tension curve following compression. A marked difference in strength and ductility between these two curves is shown, the previous compression acting to increase both the fracture stress and the degree of plastic flow. The corresponding permanent volume changes for both specimens are shown in Fig. 22, indicating a return to zero volume change and less volume change in the tension region for the cycled specimen.

## DISCUSSION OF RESULTS

In order to interpret the results of the experiments of this research it is desirable to consider first how the cast iron tested deviates from the ideally plastic material discussed in the "Introduction." This may be done best by comparing curves of effective stress versus effective plastic strain for the various states of combined stress. Fig. 23 shows these curves. It is quite clear that there is no tendency for a uniqueness of effective stress-effective strain curve and there is an especially wide divergence between the simple tension and the simple compression test. There are other features of interest in this figure. It will be noted that the plastic effective strain at fracture increases considerably as the degree of compression is increased. In simple tension this fracture strain is about $2000 \times 10^{-6}$ in. per in. while for the case $\sigma_s = -\sigma_t$ this strain has increased to $2900 \times 10^{-6}$ in. per in. For the specimen tested at a stress ratio $\sigma_s = -2\,\sigma_t$ the plastic effective strain reaches $6310 \times 10^{-6}$ in. per in. (the limit of the gages).

Further, it should be noted that the biaxial compression specimens ($\sigma_s = 2\sigma_t$ and $\sigma_s = \sigma_t$) are nearly the same. However, before any conclusion is drawn from this fact it should be pointed out that the strain data for these two tests were incomplete and only the axial strains were recorded. Effective strains were calculated assuming constancy of plastic volume and isotropy of flow, assumptions suspected to be not too far from the actual behavior of cast iron in this region.

The assumption of incompressibility of plastic deformation is clearly violated in all the specimens in which a complete strain study was made. This is shown in Figs. 15 to 20. The compression test comes closest to satisfying such a criterion, undergoing a negligible volume change until a compressive stress of 52,000 psi is reached. There is actually a slight decrease in volume at lower stresses and, as will be seen later, this is plausible, but should be investigated further before drawing definite conclusions. Considerable plastic flow has occurred by the time a stress of 52,000 psi is reached, and, as seen from Fig. 10, this strain is about 24,000 $\times 10^{-6}$ in. per in.

To emphasize further the breaking down in plastic volume incompressibility, Fig. 24 has been prepared, in which is shown the plastic Poisson's ratio $\nu_p$ versus the effective stress quantity $\sigma_N^*$ (to be defined later) for simple tension and simple compression. Here

$$\nu_p = -\frac{\epsilon_{2p}}{\epsilon_{1p}} \qquad [12]$$

where the strain quantities are plastic strains. The difference of $\nu_p$ between the two tests is quite marked, the tension value never exceeding 0.12 while the compression value exceeds 0.50 at the higher stress values. This trend is of course consistent with in-

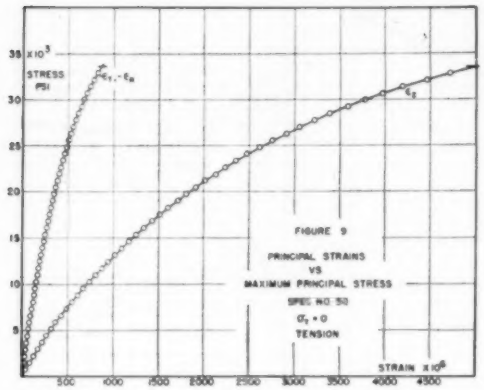


FIG. 9

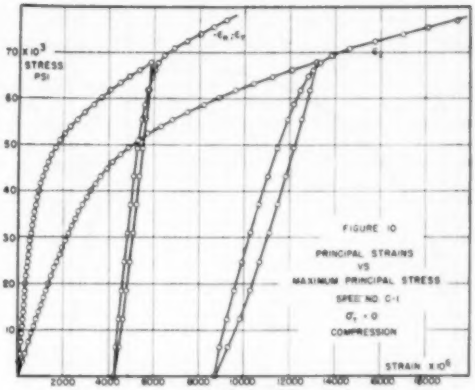


FIG. 10

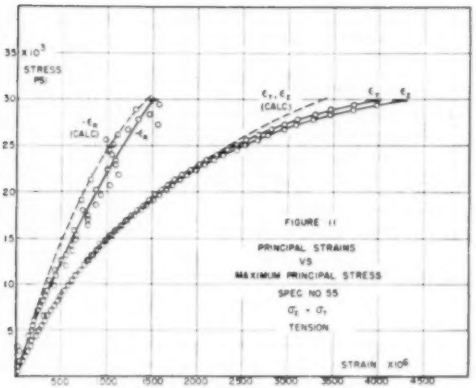


FIG. 11

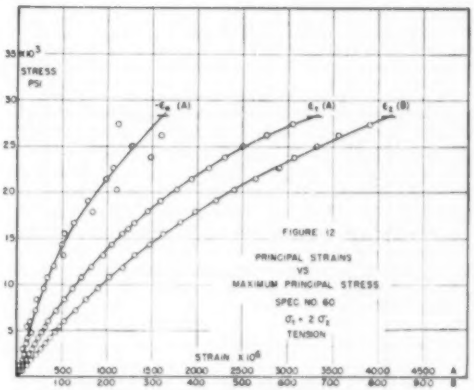


FIG. 12

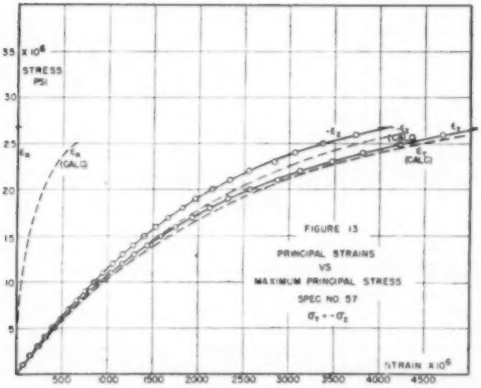


FIG. 13

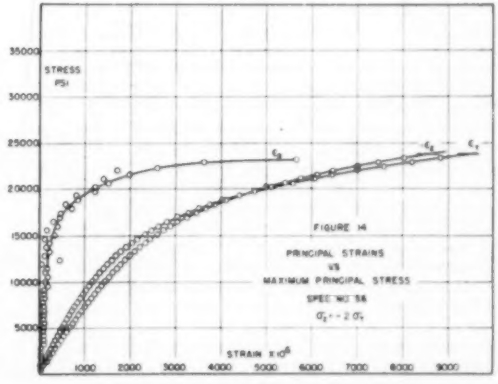


FIG. 14

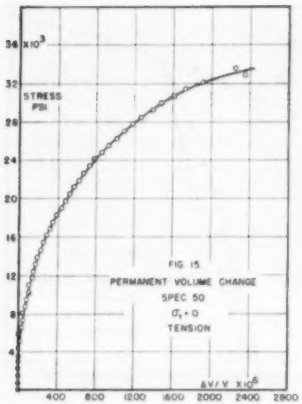


FIG. 15

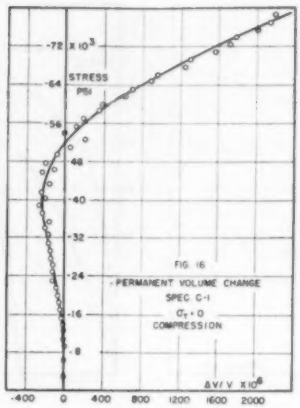


FIG. 16

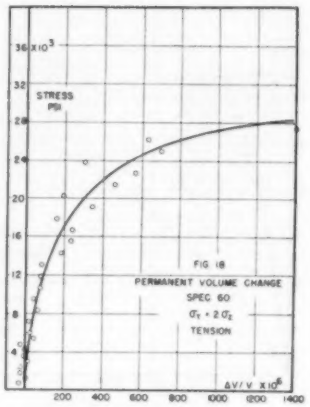


FIG. 18

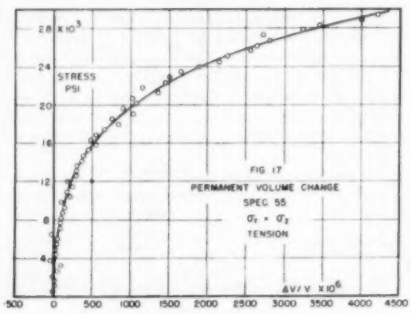


FIG. 17

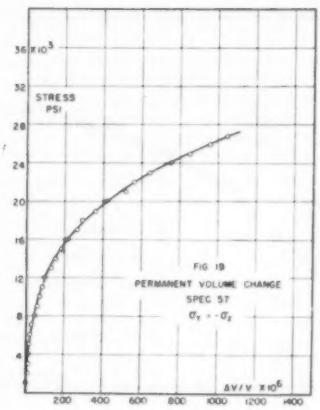


FIG. 19

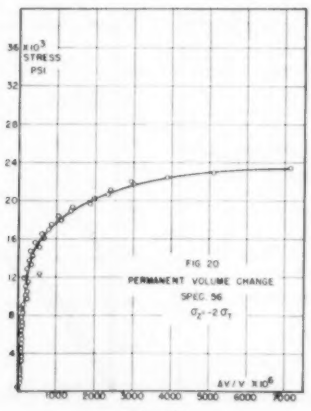


FIG. 20

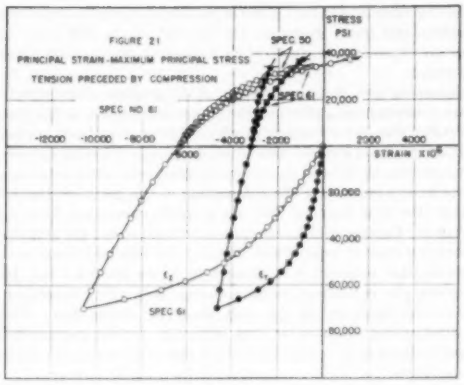


FIG. 21

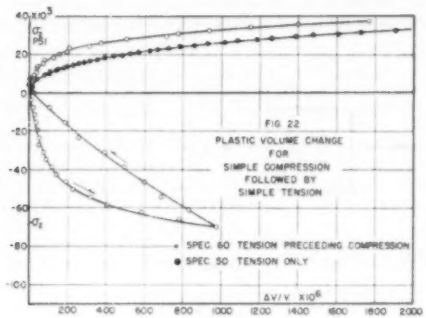


FIG. 22

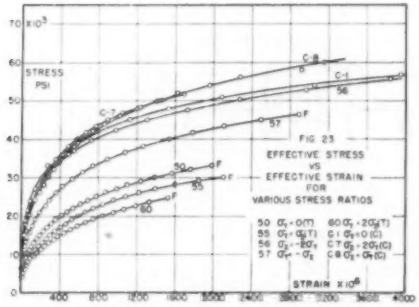


FIG. 23

crease in plastic volume in both tension and compression. For the ideally plastic material these quantities should at all times be 0.5.

To understand the peculiarities of cast iron and to establish a criterion for its behavior under stress, its metallurgical structure should be considered. A photomicrograph of the cast iron tested reveals a hypoeutectoid cast iron with a pearlitic matrix. The pearlite is medium to medium coarse and small amounts of iron-

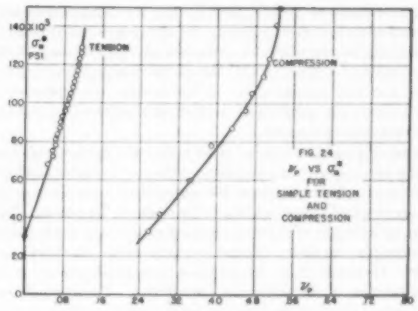


FIG. 24

iron phosphide eutectic are present. The graphite flakes are randomly oriented with a length to thickness ratio about 12 to 1. There is some enlargement of the apparent flake size due to the graphite flakes being torn out during the polishing and the pits enlarged. Classification of the flake size and distribution under the proposed Mahin-Hamilton classification is as follows:

No. 4. Flakes $^1/_2$ in. to 1 in. length at 100 magnification.
Type A Random orientation of flakes uniformly distributed.
The ASTM classification in view of the physical properties is probably No. 35.

The presence of graphite in a pearlitic matrix suggests the possibility that the graphite acts to produce a dispersion of cracks distributed throughout the structure. This concept is adopted by Fisher (14) in interpreting the tests of Grassi and Cornet (11) on the fracture of cast iron under combined stress. He assumes that the graphite plates can transmit compression without a stress-raising effect, while in tension the plate acts as an internal notch. Under states of combined stress the distortion-energy criterion is assumed to apply at the edge of the notch, leading to the resulting equations for the initiation of plastic flow depending upon the stress ratio

$$k\sigma_1 = \sigma^* \quad [13]$$

for tension-tension, and

$$\sqrt{(k\sigma_1)^2 - (k\sigma_1)(\sigma_2) + (\sigma_2)^2} = \sigma^* \quad [14]$$

for tension-compression, where $\sigma_1$ is the tensile stress, $\sigma_2$ the compressive stress, and for compression-compression

$$\sqrt{\sigma_1^2 - \sigma_1\sigma_2 + \sigma_2^2} = \sigma^* \quad [15]$$

In applying the foregoing relations to the tests of Grassi and Cornet for fracture, he assumed that their fracture data could be compared with these relations for initiation of plastic flow. He then could evaluate the constants $\sigma^*$ and $k$ and obtain a fairly good fit of Grassi and Cornet's data. It might be pointed out here that the tests of Grassi and Cornet are markedly similar to the fracture data of this paper as seen in Fig. 5.

Fisher's hypothesis was that plastic flow, no matter how small, preceded fracture, and Grassi and Cornet's tests were used to illustrate this. However, as is seen from the various stress-strain diagrams, considerable plastic flow of a definitely large-scale nature occurs in cast iron prior to fracture for all states of biaxial stress. Hence the correlation of a plastic-flow condition to fracture data is necessarily incompatible.

For example, the fracture stress in tension averaged about 33,000 psi, that in compression about 100,000 psi, giving a ratio of about 3 to 1 of compression to tension. Referring to Fig. 23, and taking

an effective strain of $2000 \times 10^{-6}$ in./in., the compressive stress (identical with the effective stress for this stress ratio) is 54,500 psi, while the tensile stress for this same effective strain is 33,000, giving a ratio of stress of 1.65. Hence the flow and fracture conditions are not comparable. Nevertheless, the concepts of Fisher's theory are quite useful in the hypothesis for flow and fracture proposed in this paper.

Considering again the point of view that the graphite plates in cast iron are sources of stress raisers acting in a similar fashion to the fine cracks found in glass, the assumption is made here that there are residual stresses acting at the edges of the plates. These stresses are thought of as being tensile in nature and act in a direction normal to the plate. Transverse stresses are also likely to be present. However, these are assumed to be small and are not included because of the additional complexity. There would seem to be a sound physical explanation for the presence of the stresses, inasmuch as there is a tendency for the graphite plates to be formed before the iron phase has solidified. Upon solidification, there is a considerable difference in the coefficients of thermal expansion of the iron ($0.119 \times 10^{-4}$ per deg C) and that of the graphite ($0.06 \times 10^{-4}$ per deg C). Hence, in cooling, the iron acts to compress the graphite plates, leading to a residual tensile stress at the edges of the plates. Other metallurgical explanations might be offered as to the nature of the surface forces between the graphite and iron; however, the concept of the difference in thermal expansions during cooling appears to be the most satisfactory.

Assuming now that the presence of the graphite plates acts to cause a stress-raising effect on the parent structure, it is felt that for initial flow the stress-raising effect is present for both tension and compression stresses normal to the plate. Yielding in compression, due to stresses normal to the plate, cannot occur to any great extent because of the compacting of the graphite, but for initial flow it is assumed that the graphite offers very little resistance. Because of the condition of internal stress, the graphite is under a state of compression initially and with additional compression due to stress it is thought to be compacted. Fig. 16, showing the permanent volume change in simple compression, shows this tendency in the early stages of plastic flow. This process cannot continue for long, obviously, for the graphite will soon begin to carry a full share of the normal stress as this stress is increased.

The state of applied stress plays an important role on the stress condition at the edge of the graphite plate. For the present discussion the distortion-energy criterion, Equations [2], is assumed as the law of yielding of the iron matrix. The state

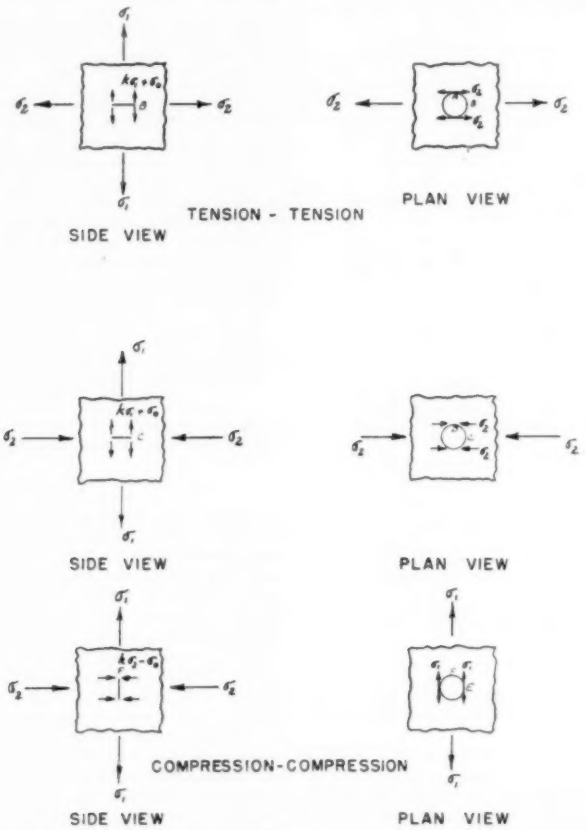


FIG. 25

of stress at the edge of plates normal to both principal stress directions is examined. The region where both principal stresses are tensile will be considered.

Referring to Fig. 25, if $\sigma_1 > \sigma_2$ the stresses at the edge of a graphite plate normal to $\sigma_1$ has the edge stresses $k\,\sigma_1 + \sigma_0$ in the 1-direction. Here $k$ is the stress-concentration factor due to the plate, and $\sigma_0$ is the edge residual tensile stress. At point $A$ in the plan view of the plate, there is a tensile stress $\sigma_2$, while at $B$, because of the presence of the plate, there is no transverse stress. For the flow of the metal, the greatest effective stress applies, and this will be at $B$, giving

$$\sigma_N{}^* = k\sigma_1 + \sigma_0 \quad [16]$$

where $\sigma_N{}^*$ is the notch effective stress. Plates located normal to the 2-direction will have a lower effective stress as long as $\sigma_1 > \sigma_2$.

When the state of stress is tension-compression, the plates normal to both principal directions must be considered. When the plate is normal to the 1-direction, the notch-edge stress is $k\,\sigma_1 + \sigma_0$ (considering stresses to be algebraic), while the transverse stress is 0 at $C$, and $\sigma_2$ at $D$. Consequently, the greatest effective stress now occurs at $D$ and this is

$$\sigma_N{}^* = \sqrt{(k\sigma_1 + \sigma_0)^2 - (k\sigma_1 + \sigma_0)(\sigma_2) + (\sigma_2)^2} \quad [17]$$

using the distortion-energy theory. When the plate is located normal to the 2-direction the greatest effective stress is

$$\sigma_N{}^* = \sqrt{\sigma_1{}^2 - \sigma_1\,(k\sigma_2 + \sigma_0) + (k\sigma_2 + \sigma_0)^2} \quad [18]$$

Whether Equation [17] or [18] is the flow criterion depends upon the magnitudes of $\sigma_1$ and $\sigma_2$.

When the state of stress is compression-compression, the criterion for initial flow is identical with that of tension-tension and Equation [16] is operative.

Graphical representation of the foregoing relations are shown in Fig. 26. Here $k = 3$ and $\sigma_0 = 30{,}000$ psi. Equations [17] and

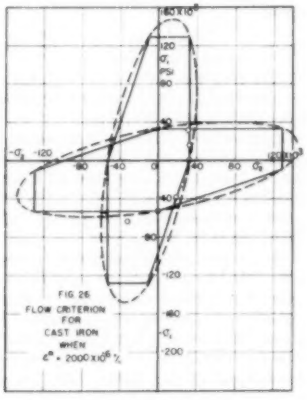


FIG. 26

[18] are ellipses which when plotted appear symmetrical with respect to a line 45 deg to the $\sigma_1$ and $\sigma_2$ co-ordinates. The flow criterion by the distortion-energy theory would be that curve as given by Equations [16] to [18] for the least stresses in any quadrant.

Because of the number and complexity of the equations given by the distortion-energy theory for flow at the edge of the graphite plates, a simpler criterion can be established if the maximum-shear law is applied to represent this flow. By this law, flow at the edge of graphite plates is governed by the difference between the maximum and minimum stresses (algebraically) at this point; hence

$$\sigma_N{}^* = k\sigma_{\max} + \sigma_0 - \sigma_{\min} \quad [19]$$

where $\sigma_{\max}$ is considered as the stress normal to the plate. Referring again to Fig. 25, where the region is tension-tension or compression-compression, $\sigma_{\max} = \sigma_1$ or $\sigma_2$ whichever is numerically the larger and $\sigma_{\min} = 0$. Hence for these two regions the distortion-energy theory and the maximum-shear theory are identical as regards flow at the edge of the plate. When the region is tension-compression, two equations exist, depending on whether $\sigma_1$ is numerically larger or smaller than $\sigma_2$. These are

$$\sigma_N{}^* = (k\sigma_1 + \sigma_0) - \sigma_2 \quad [20]$$

or

$$\sigma_N{}^* = (k\sigma_2 + \sigma_0) - \sigma_1 \quad [21]$$

Therefore the flow conditions at the plate edge by the maximum-shear theory are given by Equations [16], [20], or [21] depending on the state of biaxial stress. Graphically these equations form an eight-sided figure in a two-dimensional stress representation which is shown by the heavy line in Fig. 26. In the tension-compression zone, when tension predominates, the flow criterion is established at the edge of the plate normal to the tensile stress. For stress conditions when compression is considerably in excess of tension, the flow criterion is established by yielding at the edge of plates normal to the compressive stress.

Included in Fig. 26 are experimental points for various states of combined stress taken for an effective strain of $2000 \times 10^{-6}$ in. per in. The fit of the maximum-shear theory for flow at the graphite-plate edge is quite good for all cases, although there is some deviation in the compression-compression region. This deviation is plausible since at this strain the graphite plate is definitely transmitting compression and the hypothesis is somewhat in error.

In order to observe whether this criterion for flow of cast iron is satisfactory for all ranges of strain to failure, curves of $\sigma_N{}^*$ versus $\epsilon^*$ have been computed for all the ranges of combined stress investigated as Fig. 27. It is seen that, whereas in Fig. 23 there was no uniqueness of effective stress-effective strain, here a very satisfactory uniqueness of notch effective stress-effective strain exists. With the exception of specimen C-7, for the stress ratio $\sigma_x =$

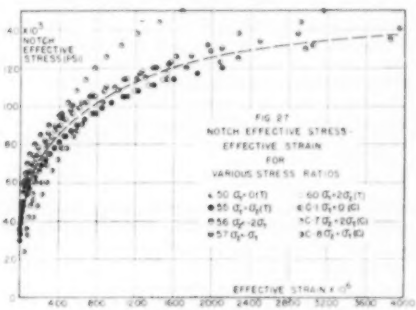


FIG. 27

$2\sigma_t(c)$ at effective strains ranging from $800 \times 10^{-6}$ in. per in. to $2400 \times 10^{-6}$ in. per in., there is a variation of about 5 per cent from the mean curve drawn as a dashed line. This mean curve may then be considered as a generalized stress-strain curve for

combined stress, and analysis of plastic flow in cast iron is then possible.

The fit is of course not exact, but within the limits of engineering design and mathematical analysis it is completely satisfactory. The compression-compression zone gives some deviation from the curve $\sigma_N^* = f(\epsilon^*)$, and this already has been explained. If large strains are to be examined in the compression-compression region more accuracy may be obtained if the conventional effective stress is used, rather than the notch effective stress. This has been shown in Fig. 19 for the three tests; $\sigma_t = 0\ (c)$, $\sigma_a = 2\,\sigma_t\,(c)$, and $\sigma_a = \sigma_t\,(c)$. Additional scatter is had in the early stages of flow, again attributed primarily to the compression-compression specimens. This is not considered as serious because of the inaccuracies in the plastic-strain values for initial flow.

Having obtained a generalized stress-strain law for gray cast iron, the next step to aid in the analysis of cast iron is to formulate a generalized Hooke's law for plastic as well as elastic strains. Because of the complexity of the plastic Poisson's ratio, the relationships will not be as simple as those applying to a ductile material. It is assumed in this derivation that the stresses act linearly in their influence on the strains and that there exist two distinct Poisson's ratios for plastic strains, one for tensile stresses, the other for compressive stresses, their magnitude being found from a simple tension test or a simple compression test having the same notch effective stress as the state of stress under investigation. With these assumptions, the following analysis is derived:

For a two-dimensional stress system the plastic portion of the total strains is assumed to be expressed in terms of the stresses as

$$\left.\begin{aligned} \epsilon_{p1} &= A\,[\sigma_1 - \nu_{p2}\sigma_2] \\ \epsilon_{p2} &= A\,[\sigma_2 - \nu_{p1}\sigma_1] \\ \epsilon_{p3} &= A\,[-\nu_{p1}\sigma_1 - \nu_{p2}\sigma_2] \end{aligned}\right\} \quad \ldots\ldots\ldots\ldots [22]$$

where $A$ is a variable coefficient depending on the degree of flow, $\nu_{p1}$ is the plastic Poisson's ratio depending on the sense of $\sigma_1$, and $\nu_{p2}$ is the plastic Poisson's ratio depending on the sense of $\sigma_2$. Substituting Equation [22] into the definition for effective strain, or

$$\epsilon_p^* = \frac{\sqrt{2}}{3}\sqrt{(\epsilon_{p1} - \epsilon_{p2})^2 + (\epsilon_{p2} - \epsilon_{p3})^2 + (\epsilon_{p3} - \epsilon_{p1})^2} \quad [23]$$

there results

$$\epsilon_p^* = \frac{2}{3}A$$

$$\sqrt{\sigma_1^2(1+\nu_{p1})^2 - \sigma_1\sigma_2(1+\nu_{p1})(1+\nu_{p2}) + \sigma_2^2(1+\nu_{p2})^2} \quad \ldots [24]$$

which may be written approximately as

$$\epsilon_p^* = \frac{2}{3}A\left\{\frac{(1+\nu_{p1})|\sigma_1| + (1+\nu_{p2})|\sigma_2|}{|\sigma_1| + |\sigma_2|}\right\}\sqrt{\sigma_1^2 - \sigma_1\sigma_2 + \sigma_2^2} \quad \ldots\ldots [25]$$

Calling the bracketed term $1 + \nu$ for simplicity, and noting that the radical is the ordinary effective stress, Equation [25] becomes

$$\epsilon_p^* = \frac{2}{3}A\,(1+\nu)\,\sigma^* \quad \ldots\ldots\ldots\ldots [26]$$

or

$$A = \frac{3}{2}\frac{\epsilon_p^*}{\sigma^*}\frac{1}{1+\nu} \quad \ldots\ldots\ldots\ldots [27]$$

Finally

$$\left.\begin{aligned} \epsilon_{p1} &= \frac{3}{2}\frac{\epsilon_p^*}{\sigma^*}\frac{1}{1+\nu}\,[\sigma_1 - \nu_{p2}\sigma_2] \\ \epsilon_{p2} &= \frac{3}{2}\frac{\epsilon_p^*}{\sigma^*}\frac{1}{1+\nu}\,[\sigma_2 - \nu_{p1}\sigma_1] \\ \epsilon_{p3} &= \frac{3}{2}\frac{\epsilon_p^*}{\sigma^*}\frac{1}{1+\nu}\,[-\nu_{p1}\sigma_1 - \nu_{p2}\sigma_2] \end{aligned}\right\} \quad \ldots\ldots\ldots [28]$$

The values of $\nu_{p1}$ and $\nu_{p2}$ are determined from the notch effective stress for the state of stress acting, and either the tensile or compressive values are used, depending upon the sign of $\sigma_1$ and $\sigma_2$. The numerical values of the plastic Poisson's ratio are determined graphically using Fig. 24. For any particular set of stresses $\sigma_1$ and $\sigma_2$, the quantity $\sigma_N^*$ is calculated from Equations [16], [20], or [21], and using this value $\epsilon^*$ is obtained from Fig. 27. Term $\sigma^*$ is readily calculated since it is the ordinary effective stress. The plastic strains given by Equations [28] are hence found. To these strains must be added the elastic strains or

$$\left.\begin{aligned} E\epsilon_{e1} &= \sigma_1 - \nu\sigma_2 \\ E\epsilon_{e2} &= \sigma_2 - \nu\sigma_1 \\ E\epsilon_{e3} &= -\nu\sigma_1 - \nu\sigma_2 \end{aligned}\right\} \quad \ldots\ldots\ldots\ldots [29]$$

to obtain the total strains. To check relations, Equations [28], calculated strains for the case $\sigma_a = \sigma_t\,(T)$ and $\sigma_c = -\sigma_t$ were obtained and plotted on Figs. 11 and 13. The mean curve in Fig. 27 was used for these calculations. It will be seen that agreement in all cases is very good.

To determine the constants $k$ and $\sigma_0$ in Equations [16], [20], and [21], a stress-concentration factor of 3 is assumed. From the data, if we chose a plastic effective strain of $\epsilon^* = 2000 \times 10^{-6}$ in. per in. the axial stress from the tension test is 33,000 psi; that of the compressive test is 53,000 psi. Then from Equation [16] in tension

$$\sigma_N^* = k\sigma_1 + \sigma_0 = (3)\ (33{,}000) + \sigma_0 = 99{,}000 + \sigma_0 \quad [30]$$

while in compression

$$-\sigma_N^* = k\sigma_1 - \sigma_0 = (3)(53{,}000) - \sigma_0 = 159{,}000 - \sigma_0 \quad [31]$$

Equating [30] and [31], we find that $\sigma_0 = 30{,}000$ psi, and the notch effective stress for $\epsilon^* = 2000 \times 10^{-6}$ in. per in. is 129,000 psi. There appears to be good justification (17, 18) for a stress-concentration factor of 3, despite the slenderness of the graphite flakes. With such sharp notches, some microplastic flow occurs for very low stresses which acts to reduce any higher stress-concentrating effects to this lower value. Hence the value $k = 3$ is actually a plastic stress-concentration factor. Materials like glass with finely dispersed cracks have very high values of $k$ [Gurney and Rowe (13) determined stress-concentration factors of the order of 600 for glass] do not have a crystalline structure, hence cannot undergo a slip process at the edge of the cracks, and fail in a brittle fashion with no plastic flow, regardless of the stress ratio, at extremely low stress values. Crystalline structures, however, can flow at crack edges because the slip process is characteristic of a crystalline structure, and the high stress-concentration factors can be reduced to the order of 3.

The volume increase with plastic flow for cast iron regardless of the stress ratio is quite satisfactorily explained by the presence of graphite flakes. The flow process at the flake edge causes an opening up of the crack when the stress across the flake is tension. When simple compression exists, flakes normal to the stress are closed up causing an initial decrease in volume, but as the flow continues, flakes oriented in the direction of the stress are opened by the lateral flow and the volume is increased. This excess lateral flow is reflected in the plastic Poisson's ratio for compression in Fig. 24. It is felt that this plastic volume increase is

characteristic of many brittle crystalline substances and is a result of the distribution of fine cracks throughout the structure. A ductile material does not have this distribution of cracks and flow occurs in the absence of plastic volume change.

The problem of fracture is indicated to be directly associated with the degree of opening of the cracks in the structure. With this point of view, fracture can be thought of as being the limit of the flow process at the edge of the cracks. A failure criterion is then possible with the aid of the foregoing analysis. It is proposed that failure will occur when a limiting energy of distortion is reached at the edge of the graphite flakes. This condition is similar to that of Fisher (14); however, the mechanism is quite different. If one assumes that there is a limiting notch effective stress at the edge of the crack, then, in the tension-tension region, this stress occurs at the edge of plates normal to the direction of the maximum tensile stress, and failure occurs normal to this stress as is indicated experimentally in Fig. 6. Further the criterion for fracture in this region is

$$\sigma_{Nf}^* = k\sigma_1 + \sigma_0 \quad \ldots\ldots\ldots\ldots\ldots\ldots [32]$$

as explained earlier. This condition is identical with the maximum-stress theory of Rankine. Here $\sigma_{Nf}^*$ is a constant depending on the type of cast iron.

In the region of tension-compression, plates oriented normal to the direction of compressive stress would be compacted during flow, and the notch effective stress would be reduced gradually to the ordinary effective stress away from the plate. Hence, since the greatest crack opening would occur for plates parallel to the direction of compression and normal to the direction of tension, the effective stress acting at the edge of these plates is critical. Hence in the tension-compression region (except for simple compression) failure occurs along a plane composed of these cracks or normal to the direction of the tensile stress. The fracture criterion would then be

$$\sigma_{Nf}^* = \sqrt{(k\sigma_1 + \sigma_0)^2 - \sigma_2 (k\sigma_1 + \sigma_0) + \sigma_2^2} \quad \ldots\ldots [33]$$

where $\sigma_1$ is the tensile stress, $\sigma_2$ the compressive.

At this point examination of the foregoing criteria with fracture data is in order. This is done in Fig. 5. Using for criteria Equations [32] and [33] values of $k = 3$ and $\sigma_0 = 30{,}000$ as obtained from the flow tests in simple tension and compression, it is seen that an extremely good fit is to be had with the various fracture points in the tension-tension and the tension-compression region. That the same constants give a good fit with the flow data as well as with the fracture data seem to place considerable emphasis on the validity of this form of analysis. The mechanism of a critical notch effective stress explains not only the mode of fracture in these regions but also analytically determines the fracture stresses.

The mechanism for fracture in the compression-compression region is not explained as satisfactorily. In this zone, fracture is observed to occur obliquely, consequently the opening of cracks parallel to the plane of the maximum compressive stress is not the cause of failure, but rather is due to some criterion along an oblique plane. This suggests the hypothesis of the Mohr envelope (19). In this theory the elastic limit and ultimate strength of a material are determined by the stresses in the planes of slip and of fracture. Further, the shearing stress in the planes of slip reaches at the limit a maximum value dependent on the normal stress acting on the same planes and on the properties of the material. Hence for fracture, the shearing stress on the fracture plane can be represented as some function of the normal stress on this plane. This function is established by constructing the largest Mohr's circle for each stress ratio at fracture and drawing the curve which is the envelope of these circles. Ros and Eichinger in their tests on cast iron (9) have substantiated this criterion for compression tests with an external hydrostatic pressure. However, the stress conditions there were quite different from the compression-compression tests of this paper.

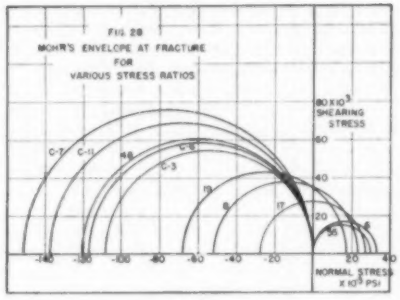


FIG. 28

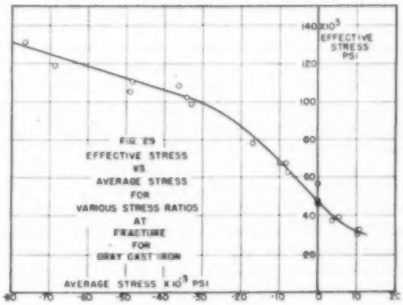


FIG. 29

In Fig. 28 is plotted the Mohr's circles for various tests in the compression-compression region, and the absence of any envelope is noted. Consequently the Mohr hypothesis is not valid. Further, the Mohr envelope is not substantiated in the tension-tension region or the tension-compression region since it does not predict the correct plane of failure.

The tests of Ros and Eichinger, however, give a result which seems to be of considerable application. By plotting the shearing stress on the octahedral plane, $\tau_a$ against the average stress $\sigma_a$ for the compression regions, a linear relation between the two was formed. A similar plot for the present data has been made and it will be seen Fig. 29, that a linearity also exists for the compression-compression tests. As a result the hypothesis

$$\sigma^* + \mu\sigma_a = K \quad \ldots\ldots\ldots\ldots\ldots [34]$$

seems to exist. Since $\sigma^*$ is equal to a constant times the octahedral shearing stress, Equation [34] can be interpreted as stating that when a critical shearing stress is reached on the octahedral plane, failure occurs. This shearing stress is equal to the algebraic sum of the octahedral shearing stress and an opposing shearing stress due to the frictional effects of the normal stress to this plane which is the average stress $\sigma_a$. As the state of stress becomes more nearly hydrostatic in compression $\sigma_a$ becomes large (negatively) in the relation to $\sigma^*$ and failure cannot take place until extremely large stresses have been reached. This is consistent with Bridgman's results (10).

When Equation [34] is applied to the present tests, as shown in

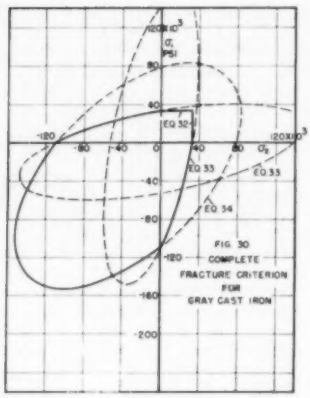


FIG. 30

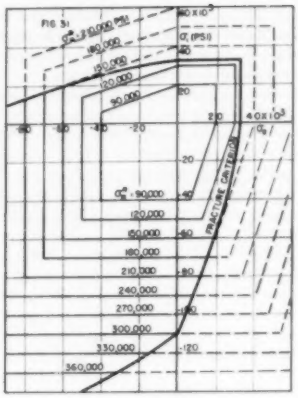


FIG. 31

Fig. 5, a reasonable agreement is found. This criterion, when plotted, is an ellipse; however, only the compression-compression quadrant is of interest. In plotting this ellipse in Fig. 5, the constants $\mu = 0.51$, and $K = 88{,}000$ psi were used.

The complete two-dimensional stress criterion for fracture is shown in Fig. 30. The complete ellipses for Equations [33] and [34] are shown, the solid line being the actual fracture criterion, the dashed line representing the balance of the various ellipses. In the tension-tension region Equation [32] is plotted giving two straight lines intersecting at right angles.

By combining the flow criterion with the fracture criterion as is done in Fig. 31, the degree of plastic flow prior to fracture may be observed. For each notch effective stress (in steps of 30,000 psi) the flow criterion is plotted using Equations [16], [20], and [21]. These are the solid and dashed lightweight lines. The fracture line is shown as the heavy curved line. Whenever the flow curve crosses the fracture curve, failure occurs, and the effective stress as well as the stresses causing this fracture are found.

Using Fig. 27, the effective strain can then be found, and this value can serve as an indication of fracture ductility. It will be seen that in the tension-tension region, the ductility for fracture is the same regardless of the stress ratio. In the tension-compression region, the ductility at fracture increases (because $\sigma_N{}^*$ increases) as the combined stress becomes more and more compressive. Finally, in the compression-compression region very large effective stresses and hence very large values for fracture ductility occur. It may be stated as a general criterion that the greater the average stress $(\sigma_1 + \sigma_2 + \sigma_3)/3$ compressively, the greater the fracture ductility. This is substantiated by the work of Bridgman on high-pressure effects on brittle materials with a superimposed tension or compression.

Finally, a discussion of the interesting results of a tensile loading following a compression loading, as shown in Figs. 21 and 22, is necessary. It is seen here that the previous compression loading up to a stress of —70,000 psi has increased the fracture stress and the fracture ductility over that obtained from a specimen with no previous loading. It is felt that this phenomenon may be explained adequately in the light of the stress-concentrating effects due to the graphite flakes.

When a compression specimen is deformed by the hypothesis of this paper, flow first occurs at the edges of graphite plates normal to the direction of compression due to the stress-concentrating effects of the crack. As flow continues, these cracks are compacted and closed while the cracks parallel to the direction of stress open up. At a stress level of 70,000 psi compression, the entire pearlite matrix has yielded and, as a result, the distribution of internal stress in the material has become quite uniform. The initial residual stress $\sigma_0$, therefore, has been completely relieved. Hence, when the specimen is unloaded, the cracks normal to the loading direction are without residual stress. During loading in tension, therefore, the cracks due to the graphite flakes should not open up until a higher stress value is reached and failure should be caused by a higher applied stress. That this is the case is seen from Figs. 21 and 22. The theoretical fracture stress in tension, from Equation [32] should be, in the absence of $\sigma_3$ a value $\sigma_1 = 129{,}000/3 = 43{,}000$ psi. The actual fracture value was 37,300 psi.

The slope of the stress-strain curves in the tension region (following compression) is considerably less than those of the previously undeformed tension test. This is due to the Bauschinger effect in the pearlitic matrix of the structure, the same effect being found in mild steel and all other ductile metals. Of further interest is the fact that the modulus of elasticity for unloading is considerably higher than for that of loading in the compression tests, indicating a general compacting of the structure due to the compression.

The permanent volume change with stress is shown in Fig. 22. The characteristic increase in volume with compression is observed, while during unloading the volume decreases. This seems quite curious since one would expect a constant plastic volume during unloading. However, the change in the unloading modulus over the loading modulus, and the difference in loading

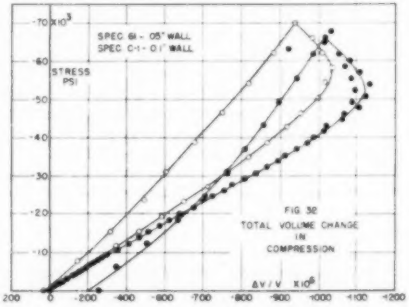


FIG. 32

and unloading of Poisson's ratio can account for this effect. During the loading, the elastic strains gave a modulus of elasticity of $E = 15.67 \times 10^6$ psi and a Poisson's ratio of $\nu = 0.248$. The measured values of $E$ and $\nu$ during unloading from Fig. 18 change to $19 \times 10^6$ psi and 0.34. It would appear from this behavior that cracks, which open up when loading, are again closed during unloading, leaving the net volume change very small when the stress has been reduced to zero. This interesting fact should be investigated for other stress ratios.

Because of the change in elastic constants during unloading the concept of plastic volume change (the difference between total volume change and elastic volume change using initial elastic constants) loses some of its significance. The total volume change during compressive loading and unloading seems to have greater practical value in studying the size change. Fig. 32 is included to show this effect for two compression tests. It is interesting to observe the sudden reversal in total volume decrease (due to elastic effects) as plastic flow takes place and the flakes parallel to the direction of stress open up. Further, the change in the slope of the unloading curve over that of the initial loading curve has decreased markedly, which is indicative of the change in unloading elastic constants. The inference here is that due to flow the geometry of the crack shape has changed. Cracks normal to the stress direction have been closed, causing a stiffer structure in the direction of stress, while cracks parallel to the stress have opened up causing a decrease in lateral stiffness.

## Conclusions

In the light of the experimental investigation and discussion connected with this research program, the following conclusions may be drawn:

1 The conventional mathematical relationships established for plastic flow of ductile metals cannot be applied to a brittle material such as gray cast iron. There is no uniqueness in the effective stress $\sigma^*$, effective strain $\epsilon^*$ relationship for various states of combined stress. The material is quite dissimilar in its reaction to stress in tension and compression tests. The law of constancy of volume for plastic flow is violated for all states of combined stress examined, and the plastic Poisson's number is considerably less than $^1/_2$ for tension, greater than $^1/_2$ for compression.

2 The structure of gray cast iron, consisting of graphite flakes in a pearlitic matrix may be considered as a ductile material with a random dispersion of fine cracks. From this point of view, flow and fracture may be considered to be governed by the mechanism for flow and fracture at the edge of the graphite flakes.

3 By assuming the graphite flakes to be in a state of residual compression, there results a tensile stress at the sharp corner of the crack in a direction normal to the plane of the flake. Upon the application of external stress, stress concentrations are caused by the sharp cracks.

4 Although a considerably higher stress concentration may exist initially, when plastic flow occurs at the crack edge this factor is reduced to 3.

5 Flow under any two-dimensional state of combined stress can be determined on the basis of a notch effective stress $\sigma_N^*$, the basis of which is the maximum shearing stress occurring in the metal at the crack edge. For predominantly tensile stresses, the critical flakes are those normal to the direction of maximum tensile stress. For states of stress predominantly compressive, the critical flakes are normal to the direction of the largest compressive stress. This criterion is expressed mathematically as Equations [16], [20], and [21].

6 With a stress-concentration factor of 3 and for an effective strain chosen at $2000 \times 10^{-6}$ in. per in. the residual tensile stress at the notch is 30,000 psi. With these values, and Equations [16], [20], and [21], a generalized stress-strain curve $\sigma_N^*$ versus $\epsilon^*$ may be constructed for all states of two-dimensional stress. Experiments on tubes under combined stress in which the three principal strains were measured independently are shown to give an extremely good verification of this concept of notch yielding. Fig. 27 shows the comparison.

7 In the compression-compression region, agreement of the theory with experiment is not quite as good for large strains, because of the compacting of the plates normal to the compressive stress, and the consequent reduction in the stress-concentration effect.

8 On the basis of the uniqueness of the notch effective stress-effective strain relationship, a generalized Hooke's law for plastic strains in gray cast iron can be written in which the strains are assumed to be linear functions of the stresses, and where two Poisson's ratios exist, one for tensile stresses, the other for compressive stresses. The total strains are found by including the elastic strains. The comparison of calculated strains with measured strain values was found to be quite good.

9 The concept of flow at the edge of cracks in gray cast iron serves as a satisfactory mechanism for the occurrence of volume increase under the states of combined stress examined. For tensile stress, cracks normal to the direction of stress open; for compressive stress, cracks parallel to the direction of stress open so that in all cases of stress (except hydrostatic pressure) there is volume increase for plastic flow.

10 In the tension-tension and the tension-compression regions, fracture occurs when a critical effective stress is reached at the edge of the graphite flakes. This critical stress is found on the basis of the distortion-energy criterion and can be formulated mathematically as seen in Equations [32] and [33]. The same constants $k$ and $\sigma_0$ are used as those which appeared in the flow relationships. Very good agreement with experimentally found fracture stresses is obtained as is seen in Fig. 5.

11 The mechanism of a limiting-flow value for fracture at the crack edge satisfactorily explains the fracture surface obtained in the tension-tension and tension-compression region. Except for the region in close proximity to pure compression, fracture occurs along planes normal to the direction of the largest tensile stress. These planes also contain the cracks which open up the most and can reach the critical effective stress for failure.

12 The Mohr envelope criterion for fracture of gray cast iron is not satisfactory. In the tension-tension and tension-compression regions, it does not predict the correct fracture surface. In the compression-compression region, the influence of the mean stress is clearly indicated. Whereas the Mohr envelope predicts a single Mohr circle for two-dimensional compression, such was found not to be the case.

13 A criterion for fracture in the compression-compression region can be established based on a critical shearing stress along the octahedral plane which depends both on the octahedral shearing stress and a frictional shearing stress proportional to the normal stress on the octahedral plane. Since the normal stress on the octahedral plane is the average stress, the average stress has a direct bearing on fracture. Mathematical formulation of this criterion is given in Equation [34].

14 Increasing ductility as the compression-compression region is approached is explained satisfactorily by the foregoing mechanisms of flow and fracture. Greater notch effective stresses can be maintained prior to fracture as the compression-compression region is approached, hence greater ductility.

15 Tension characteristics of cast iron when preceded by compression, are considerably altered. The fracture stress is increased by 10 per cent, and the ductility for fracture is increased by 50 per cent. This phenomenon can be explained by the removal of residual tensile stresses at the crack edges for plates

normal to the stress direction during compression loading, with the accompanying improvement in tension properties.

16 During unloading from plastic compression, cast iron has an increased modulus of elasticity and Poisson's ratio. The result is that when the stress is removed, the net volume change is very small. The plastic flow has changed the geometry of the crack shape to one which is stiffer in the direction of stress (because of the compacting of cracks normal to this direction), and less stiff laterally (because of the opening of cracks parallel to the stress direction).

## Acknowledgments

The author wishes to acknowledge the encouragement and driving force rendered him by his father, Mr. Louis F. Coffin, and his wife, Mary McCarthy Coffin, through the span of years over which this research was performed. Without their enthusiasm, this work might never have been completed. Another acknowledgment is due Prof. C. W. MacGregor for suggesting the problem, for helpful suggestions, and for arranging for the time and funds for the performance of the research program. Further thanks is due the Mechanical Engineering Department, Prof. C. R. Soderberg, Professor in Charge, for supplying the funds and materials for the work.

In the preparation of the paper, thanks are due to the following people for their help: Miss Marie Graham, who typed the manuscript, Miss Lillian Lawrie for drawing the figures, Mr. Arsen Tashjian who assisted with the photographs and figures, Mr. Lewis Eaton who also inked the figures, and Mr. Fredman Walcott who took the photographs. Dr. Maurice Shank made the photomicrographs and assisted with the tests. His aid is deeply appreciated.

## Bibliography

1 "Sur l'établissement des équations des mouvements intérieurs opérés dans les corps solides ductiles au delà des limites où l'élasticité pourrait les ramener à leur premier état," Barré de Saint Venant, Academie des Sciences, Comptes Rendus, Paris, France, vol. 70, 1870, pp. 473–480. For further references an excellent bibliography will be found in "The Flow of Metals Under Various Stress Conditions," by A. Nadai, Proceedings of The Institution of Mechanical Engineers, vol. 157, 1947, pp. 121–160.

2 "Yielding and Fracture of Medium-Carbon Steels Under Combined Stress," by E. A. Davis, Journal of Applied Mechanics, Trans. ASME, vol. 67, 1945, pp. A-13–24.

3 "Combined-Stress Tests on 24S-T Aluminum-Alloy Tubes," by W. R. Osgood, Journal of Applied Mechanics, Trans. ASME, vol. 69, 1947, pp. A-147–153.

4 "Partially Plastic Thick-Walled Tubes," by C. W. MacGregor, L. F. Coffin, Jr., and J. C. Fisher, *Journal of The Franklin Institute*, vol. 245, 1948, pp. 135–158.

5 By A. Föppl, *Mitteilungen aus dem Mechanisch Technischen Laboratorium*, München, no. 27, 1900.

6 By T. von Kármán, *Zeitschrift des Vereines deutscher Ingenieure*, 1911.

7 Dissertation, by R. Böker, Technischen Hochschule, Aachen, 1914.

8 "A Study of the Failure of Concrete Under Combined Compressive Stresses," by F. E. Richart, A. Brandtsaeg, and R. L. Brown, University of Illinois, Engineering Experiment Station, Bulletin no. 185, 1928, 102 pages.

9 "Versuche Zur Klärung der Frage der Bruchgefahr," by M. Ros and A. Eichinger, Laboratorie Fédéral d'Essai des Matériaux Annexe à l'École Polytechnique de Zürich, Diskussionsbericht Nr. 34, Zürich, Switzerland, February, 1929, 59 pages plus 4 folded sheets of tables.

10 "The Effect of Hydrostatic Pressure on the Fracture of Brittle Substances," by P. W. Bridgman, *Journal of Applied Physics*, vol. 18, 1947, pp. 246–258.

11 "Fracture of Gray-Cast-Iron Tubes Under Biaxial Stresses," by R. C. Grassi and I. Cornet, Journal of Applied Mechanics, June, 1949, Trans. ASME, vol. 71, pp. 178–182.

12 "The Theory of Rupture," by A. A. Griffith, Proceedings of the First International Congress for Applied Mechanics, 1924, part 1, pp. 55–63.

13 By G. Gurney and P. W. Rowe, Royal Aircraft Establishment, Farnsborough Report No. Mat. 5, May, 1945; and Report No. Mat. 8, November, 1945.

14 J. C. Fisher in an as yet unpublished paper.

15 "Combined Stress Experiments on a Nickel-Chrome-Molybdenum Steel," by J. M. Lessells and C. W. MacGregor, *Journal of The Franklin Institute*, vol. 230, 1940, pp. 163–181.

16 To be published in "Experimental Stress Analysis," 1950.

17 "Notch Brittleness and the Strength of Metals," by E. Orowan, Institution of Engineers and Shipbuilders, Scotland, vol. 89, 1945, pp. 165–215.

18 "Plasticity in Engineering," by F. K. Th. van Iterson, Blackie and Son, London, England, 1947, p. 33.

19 "Abhandlungen aus dem Bebiete der Technische Mechanik, by Otto Mohr, second edition, W. Ernst and Sohn, Berlin, Germany 1914.

# A Method for Determining Mode Shapes and Frequencies Above the Fundamental by Matrix Iteration

By H. I. FLOMENHOFT,[1] WASHINGTON, D. C.

**Recently, an increasing use has been made of the matrix-iteration method for determining mode shapes and frequencies, particularly with regard to dynamic problems in aircraft design. Its particular advantage is the relative ease with which it handles complex discontinuous structures whose elastic properties can be defined adequately only in terms of influence coefficients. The disadvantage of tedious calculations has been alleviated greatly by an "acceleration method" for convergence which has been described by Isakson.[2] The predominant disadvantage to matrix iteration, however, has been the difficulty in obtaining mode shapes and frequencies higher than the fundamental. The purpose of this paper is to establish a technique for accomplishing this in a manner that is practical for use in industry, as proved by its successful application to many problems of this type in the Aero-Elastic and Structures Research Laboratory at the Massachusetts Institute of Technology. This is accomplished by applying a device worked out by L. A. Pipes,[3] and extending it to the general case, at the same time organizing the computations in tabular form. Only a basic knowledge of matrix notation and dynamic systems is necessary to understand this development, and this can be obtained easily by a review of von Kármán and Biot's work[4] on this subject.**

## Nomenclature

The following nomenclature is used in the paper:

- $m_i$ = mass of $i$th element
- $(r)$ = superscript, indicates that the quantity is associated with the results of the $r$th mode
- $A_i$ = unknown or converging relative amplitude of the $i$th element in iteration process
- $\phi_i^{(r)}$ = known relative amplitude of the $i$th element in $r$th mode
- $[D_{ij}^{(r)}]$ = matrix whose fundamental mode is $r$th mode
- $[S^{(r)}]$ = sweeping[5] matrix derived from results of $r$th mode
- $[S^{(r)}]'$ = modified sweeping matrix containing only last row of $K_{ij}$
- $K_{ij}^{(r)}$ = sweeping constant derived from $r$th mode; element of $[S^{(r)}]$
- $\overset{?}{=}$ = "should equal"; used in check equations

## Introduction

The problem of determining vibration mode shapes and frequencies can always be reduced to the form of the following matrix equation

$$[D_{ij}]\{A_j\} = \lambda\{A_i\} \qquad [1]$$

Also, the typical orthogonality condition used for sweeping is of the form

$$\left.\begin{aligned} &\sum_i m_i \phi_i^{(r)} A_i^{(r+1)} = 0 \\ &\text{for the case of no dynamic coupling, and} \\ &\sum_i \sum_j m_{ij} \phi_j^{(r)} A_i^{(r+1)} = 0 \end{aligned}\right\} \qquad [2]$$

for the case when there is dynamic coupling, where $\phi$ represents the converged values of the $r$th mode and $A$ represents the unknown solution for the $(r+1)$th mode.

In more compact notation

$$\sum_i B_i^{(r)} A_i^{(r+1)} = 0$$

where

$$\left.\begin{aligned} B_i^{(r)} &= m_i \phi_i^{(r)} \\ &\text{for no dynamic coupling and} \\ B_i^{(r)} &= \sum_j m_{ij} \phi_j^{(r)} \end{aligned}\right\} \qquad [3]$$

for dynamic coupling.

If rigid body degrees of freedom are included in the analysis (such as the case of a wing free in space), the $A_i$ written previously may have to be modified by additional terms giving the displacements of these motions. In any case, the fundamental matrix equation and the orthogonality condition can be reduced to the form of Equations [1] and [3].

If the $[D_{ij}]$ matrix is derived from stiffness influence coefficients, it may be shown that $\lambda = \omega^2$. Conversely, if the $[D_{ij}]$ matrix is derived from flexibility influence coefficients, $\lambda = 1/\omega^2$, where $\omega$ is a natural frequency of the vibratory system.

In footnote 3, the orthogonality condition is stated in the following manner for the case where the first mode has been found, and the matrix for the second mode is to be determined

[1] Structural Loads Engineer of Structures Branch, Bureau of Aeronautics, Department of the Navy.

[2] "A Method for Accelerating the Convergence of an Iteration Procedure," by Gabriel Isakson, *Journal of the Aeronautical Sciences*, vol. 16, July, 1949, p. 443.

[3] "Applied Mathematics for Engineers and Physicists," by L. A. Pipes, McGraw-Hill Book Company, Inc., New York, N. Y., 1946, pp. 191–203.

[4] "Mathematical Methods in Engineering," by Th. von Kármán and M. A. Biot, McGraw-Hill Book Company, Inc., New York, N. Y., 1940, chapt. 5.

The statements contained herein are the opinions of the writer and are not to be construed as official or reflecting the views of the Department of the Navy or the Naval Service at large.

Contributed by the Applied Mechanics Division and presented at the Annual Meeting, New York, N. Y., November 27–December 2, 1949, of The American Society of Mechanical Engineers.

Discussion of this paper should be addressed to the Secretary, ASME, 29 West 39th Street, New York, N. Y., and will be accepted until October 10, 1950, for publication at a later date. Discussion received after the closing date will be returned.

Note: Statements and opinions advanced in papers are to be understood as individual expressions of their authors and not those of the Society. Paper No. 49—A-21.

[5] "Sweeping" is a term originated by L. Beskin and R. M. Rosenberg in "Higher Modes of Vibration by a Method of Sweeping," *Journal of the Aeronautical Sciences*, (Nov.) 1946, where the orthogonality restraint is applied to the Stodola method.

$$\left.\begin{aligned} A_1 &= -\frac{B_2^{(1)}}{B_1^{(1)}}A_2 - \frac{B_3^{(1)}}{B_1^{(1)}}A_3 - \cdots - \frac{B_n^{(1)}}{B_1^{(1)}}A_n \\ A_2 &= A_2 \\ A_3 &= A_3 \\ &\cdots \\ A_n &= A_n \end{aligned}\right\} \quad \ldots [4]$$

In matrix notation this set of equations can be written

$$\begin{bmatrix} A_1 \\ A_2 \\ \cdot \\ \cdot \\ \cdot \\ A_n \end{bmatrix} = \begin{bmatrix} 0 & K_{12}^{(1)} & K_{13}^{(1)} & \cdots & K_{1n}^{(1)} \\ 0 & 1 & 0 & \cdots & 0 \\ \cdot & 0 & 1 & \cdots & \\ \cdot & \cdot & \cdot & \cdots & \\ \cdot & \cdot & \cdot & \cdots & \\ 0 & 0 & 0 & \cdots & 1 \end{bmatrix} \begin{bmatrix} A_1 \\ A_2 \\ \cdot \\ \cdot \\ \cdot \\ A_n \end{bmatrix} \quad \ldots [5]$$

where

$$K_{1i}^{(1)} = -\frac{B_i^{(1)}}{B_1^{(1)}}$$

or, if the square array be designated by $[S^{(1)}]$

$$\{A_i\} = [S^{(1)}]\{A_i\} \quad \ldots [6]$$

If this result is substituted into Equation [1], the constraint represented by the orthogonality condition is introduced directly into the iteration process, so that the column of $A_i$ will converge to the second mode

$$[D_{ij}][S^{(1)}]\{A_j\} = \lambda\{A_i\} \quad \ldots [7]$$

It should be noticed that when $[D_{ij}]$ is multiplied by the sweeping matrix $[S^{(1)}]$, the first column of the resulting matrix is composed of all zeros, so that effectively the order of the matrix has been reduced by one. This is true because $A_1$ will then multiply zero in each row and therefore will have no effect upon the convergence of the iteration. Consequently, the first row and column can be omitted while iterating, and then, after convergence has been established, the final values of $A_2$ to $A_n$ are used with the first row to determine the final value of $A_1$. In this manner, sweeping to each successive mode reduces the order of the iteration matrix by one. While this makes the iteration process simpler as one proceeds to the higher modes, it also makes the accuracy of the results more critical since fewer variables become involved with each mode.

When finding the third mode two orthogonality conditions are known, and from these can be derived relations which express $A_1$ and $A_2$ each in terms of the remaining $A_i$. The sweeping matrix in this case will contain two rows of $K_{ij}$, and the first two columns will be all zeros, while the rest of the matrix will be equivalent to a unit matrix. Furthermore, the $K_{ij}$ cannot be expressed by so simple a relation as for the first mode. For each successive mode, then, a new row of $K_{ij}$ is added and at the same time the number of $K_{ij}$ in each row is reduced by one, since a new column of zeros is also added. However, it is shown later that only the last row of $K_{ij}$ need be used if it is combined with the matrix from which all previous modes have been swept.

As more orthogonality conditions become involved with each succeeding mode, the problem of determining the $K_{ij}$ in the sweeping matrix becomes increasingly laborious. Consequently, it is convenient to derive a general solution from which these constants can be evaluated for any mode. This is now done by a mode-by-mode process in which the constants obtained as a final result for one mode are used together with the new orthogonality condition to find the constants for the next mode.

### Determination of Constants of Sweeping Matrix for Eliminating the First $r$ Modes for System With $n$ Degrees of Freedom

Since $r$ modes have been found, $r$ orthogonality conditions are known, so that the problem is one of reducing these to a series of equations of the form

$$\left.\begin{aligned} A_i &= \sum_{j=r+1}^{n} K_{ij}^{(r)}A_j \quad i = 1, 2, 3, \ldots, r \\ A_p &= A_p \qquad\qquad p = r+1, r+2, \ldots, n \end{aligned}\right\} \quad \ldots [8]$$

In evaluating the elements $K_{ij}$ we assume that the constants used for sweeping the first $(r-1)$ modes are already known from previous calculations and are in the form of the following set of equations

$$\left.\begin{aligned} A_i &= \sum_{j=r}^{n} K_{ij}^{(r-1)}A_j \quad i = 1, 2, 3, \ldots, r-1 \\ A_p &= A_p \qquad\qquad p = r, r+1, r+2, \ldots, n \end{aligned}\right\} \quad \ldots [9]$$

Also, iteration of the $r$th mode yields the new orthogonality relation

$$\sum_{j=i}^{n} B_j^{(r)}A_j = 0 \quad \ldots [10]$$

If the expressions for the first $(r-1)$ values of $A_i$ from Equation [9] are substituted into Equation [10], it is possible to solve for $A_r$ in terms of $A_{r+1}$ to $A_n$. The coefficients of these $A_j$ are the elements $K_{rj}$, the last row of $K_{ij}$ in the sweeping matrix being determined. This substitution yields

$$\sum_{i=1}^{r-1}\sum_{j=r}^{n} B_i^{(r)}K_{ij}^{(r-1)}A_j + \sum_{j=r}^{n} B_j^{(r)}A_j = 0$$

Collecting coefficients of like $A_j$

$$\sum_{j=r}^{n}\left[\sum_{i=1}^{r-1} B_i^{(r)}K_{ij}^{(r-1)} + B_j^{(r)}\right]A_j = 0$$

Solving for $A_r$ gives

$$A_r = \sum_{j=r+1}^{n} K_{rj}^{(r)}A_j \quad \ldots [11]$$

where

$$K_{rj}^{(r)} = -\frac{\sum_{i=1}^{r-1} B_i^{(r)}K_{ij}^{(r-1)} + B_j^{(r)}}{\sum_{i=1}^{r-1} B_i^{(r)}K_{ir}^{(r-1)} + B_r^{(r)}} \qquad r+1 \le j \le n \quad \ldots [12]$$

Substituting Equation [11] into [9] eliminates the $A_r$ term in the first $(r-1)$ equations and yields the remaining $K_{ij}$ elements being determined

$$A_i = K_{ir}^{(r-1)}\sum_{j=r+1}^{n} K_{rj}^{(r)}A_j + \sum_{j=r+1}^{n} K_{ij}^{(r-1)}A_j$$

$$= \sum_{j=r+1}^{n}\left[K_{ir}^{(r-1)}K_{rj}^{(r)} + K_{ij}^{(r-1)}\right]A_j \quad \ldots [13]$$

Therefore

$$K_{ij}^{(r)} = K_{ir}^{(r-1)}K_{rj}^{(r)} + K_{ij}^{(r-1)} \quad \begin{matrix} i = 1 \text{ to } (r-1) \\ j = (r+1) \text{ to } n \end{matrix} \quad \ldots [14]$$

However, a saving in effort is attained by forming an abbreviated matrix using only one row of $K_{ij}$ in the $r$th row. These will be the elements given by Equation [12]. In every other row, unity is placed on the diagonal with zeros elsewhere. This matrix is multiplied by the sweeping matrix of the previous mode to give identically the same results as Equation [14]. For example, in sweeping the first three modes of a five-degree-of-freedom system, the second mode sweeping matrix can be combined with the results of Equation [12] in the following manner

$$[S^{(2)}][S^{(3)}]' = \begin{bmatrix} 0 & 0 & K_{13}^{(2)} & K_{14}^{(2)} & K_{15}^{(2)} \\ 0 & 0 & K_{23}^{(2)} & K_{24}^{(2)} & K_{25}^{(2)} \\ 0 & 0 & 1 & 0 & 0 \\ 0 & 0 & 0 & 1 & 0 \\ 0 & 0 & 0 & 0 & 1 \end{bmatrix} \begin{bmatrix} 1 & 0 & 0 & 0 & 0 \\ 0 & 1 & 0 & 0 & 0 \\ 0 & 0 & 0 & K_{34}^{(3)} & K_{35}^{(3)} \\ 0 & 0 & 0 & 1 & 0 \\ 0 & 0 & 0 & 0 & 1 \end{bmatrix}$$

$$= \begin{bmatrix} 0 & 0 & 0 & (K_{34}^{(3)}K_{13}^{(2)} + K_{14}^{(2)}) & (K_{35}^{(3)}K_{13}^{(2)} + K_{15}^{(2)}) \\ 0 & 0 & 0 & (K_{34}^{(3)}K_{23}^{(2)} + K_{24}^{(2)}) & (K_{35}^{(3)}K_{23}^{(2)} + K_{25}^{(2)}) \\ 0 & 0 & 0 & K_{34}^{(2)} & K_{35}^{(2)} \\ 0 & 0 & 0 & 1 & 0 \\ 0 & 0 & 0 & 0 & 1 \end{bmatrix} \quad \ldots [15]$$

The elements of this result can be seen to be the same as would be given by Equation [14]. Therefore the procedure to follow is to use the abbreviated sweeping matrix containing only the row $K_{rj}$ and to multiply it by the $[D_{ij}]$ matrix from which all previous modes have been swept and which was used to determine the $r$th mode.

Consequently, the following notation is useful

$$[D_{ij}^{(r)}][S^{(r)}]' = [D_{ij}^{(r+1)}] \quad \ldots [16]$$

### Check Method for Sweeping Operation

It is desirable to have a means of checking the computations performed in carrying out the functions of determining the sweeping constants without having to resort to the use of two computers working independently. A checking method is derived for this purpose, which can be adapted readily to the tables derived from Equations [12] and [14].

For the $r$th mode, the orthogonality condition is

$$\sum_j B_i^{(r)} A_i = 0$$

as given in Equations [3]. As in Equation [8], the recurrence formulas produced equations of the form

$$\left.\begin{aligned} A_1 &= \sum_{j=r+1}^{n} K_{1j}^{(r)} A_j \\ A_2 &= \sum_{j=r+1}^{n} K_{2j}^{(r)} A_j \\ &\vdots \\ A_r &= \sum_{j=r+1}^{n} K_{rj}^{(r)} A_j \end{aligned}\right\} \quad \ldots [17]$$

Any value which satisfies these equations must also satisfy Equations [3]. Therefore arbitrarily let all the $A_j$ from $A_r$ to $A_n$ equal unity, and evaluate $A_1$ to $A_r$ accordingly

$$\left.\begin{aligned} A_1' &= \sum_{j=r+1}^{n} K_{1j}^{(r)} \\ A_2' &= \sum_{j=r+1}^{n} K_{2j}^{(r)} \\ &\vdots \\ A_r' &= \sum_{j=r+1}^{n} K_{rj}^{(r)} \end{aligned}\right\} \quad \ldots [18]$$

Substituting these values into Equations [3] gives the check equation

$$B_1^{(r)} \sum_{j=r+1}^{n} K_{1j}^{(r)} + B_2^{(r)} \sum_{j=r+1}^{n} K_{2j}^{(r)} + \ldots + B_r^{(r)} \sum_{j=r+1}^{n} K_{rj}^{(r)} \stackrel{?}{=} \sum_{i=r+1}^{n} B_i^{(r)} \quad \ldots [19]$$

This form is very convenient, since, in the following tables, $B_1, B_2, \ldots B_r$ are listed in a column separate from $B_{r+1}, B_{r+2}, \ldots$ etc. The sum of the latter $B_i$ can then be listed clearly at the bottom of their column for use on the right-hand side of Equation [19]. The $K_{1j}$, $K_{2j}$, etc. are also tabulated in separate columns, with their sums at the bottom.

### Sweeping Tables

The general formulas that have been derived are now used to set up tables (Tables 1 and 2), giving each mode in order. The operations to be performed in obtaining any column may be indicated in the column itself by the literal notation or at the top of the column by numbers. In the latter case, each element of the column should be treated according to the operations indicated by the numbers.

Since sweeping modes from the original matrix is a critical part of the process of solving a system for its mode shapes and frequencies, accuracy becomes important. If small differences of large numbers are encountered, care must be taken to carry as many figures as are necessary to give accuracy to the same number of significant figures to which one expects to converge the iteration.

### Numerical Example

As the tables are set up, they are adapted for sweeping columns to zero successively from left to right. There are certain cases where it is desirable to do this, and for these the tables may be used directly. However, in other problems it may be necessary to sweep columns in an irregular fashion. A detailed discussion of the factors involved and the significance of these cases is given later.

A numerical example will now be presented to illustrate how

TABLE 1 TABLE FOR FINDING SWEEPING CONSTANTS FOR FIRST FOUR MODES

(Set up for five degrees of freedom.)

| Second Mode | | | Third Mode | | | | | | |
|---|---|---|---|---|---|---|---|---|---|
| ① | ② | ③ = -②/① | ④ | ⑤ | ⑥ | ⑦ | ⑧ = $B_1^{(2)}$⑤ + ⑥ | ⑨ = -⑧/⑦ | ⑩ = $K_{12}^{(1)}$⑨ + ⑧ |
| $B_1^{(1)}$ | | | $B_1^{(2)}$ | | $K_{12}^{(1)}$ | $K_{12}^{(1)}B_1^{(2)}$ | | | |
| | $B_2^{(1)}$ | $K_{12}^{(1)}$ | $B_2^{(2)}$ | | | $B_2^{(2)}$ | | | |
| | $B_3^{(1)}$ | $K_{13}^{(1)}$ | | $B_3^{(2)}$ | $K_{13}^{(1)}$ | ↓ | $B_1^{(2)}K_{13}^{(1)} + B_3^{(2)}$ | $K_{23}^{(2)}$ | $K_{13}^{(2)}$ |
| | $B_4^{(1)}$ | $K_{14}^{(1)}$ | | $B_4^{(2)}$ | $K_{14}^{(1)}$ | Σ ⑦ | $B_1^{(2)}K_{14}^{(1)} + B_4^{(2)}$ | $K_{24}^{(2)}$ | $K_{14}^{(2)}$ |
| | $B_5^{(1)}$ | $K_{15}^{(1)}$ | | $B_5^{(2)}$ | $K_{15}^{(1)}$ | $K_{12}^{(1)}B_1^{(2)}$ | $B_1^{(2)}K_{15}^{(1)} + B_5^{(2)}$ | $K_{25}^{(2)}$ | $K_{15}^{(2)}$ |
| | ⋮ | ⋮ | | ⋮ | ⋮ | $+ B_2^{(2)}$ | ⋮ | ⋮ | ⋮ |
| | $\Sigma B_i^{(1)}$ | $\Sigma K_{1i}^{(1)}$ | | $\Sigma B_i^{(2)}$ | | | | $\Sigma K_{2i}^{(2)}$ | $\Sigma K_{1i}^{(2)}$ |

Check Equation- $B_1^{(1)} \Sigma K_{1i}^{(1)} \stackrel{?}{=} -\Sigma B_i^{(2)}$

Check Equation- $B_1^{(2)} \Sigma K_{1i}^{(2)} + B_2^{(2)} \Sigma K_{2i}^{(2)} \stackrel{?}{=} -\Sigma B_i^{(2)}$

| Fourth Mode | | | | | | | | |
|---|---|---|---|---|---|---|---|---|
| ⑪ | ⑫ | ⑬ = -⑫/① | ⑭ | ⑮ | ⑯ | ⑰ | ⑱ | ⑲ = -⑱/Σ⑯ |
| $B_1^{(3)}$ | | $K_{13}^{(2)}$ | | $K_{13}^{(2)}B_1^{(3)}$ | | | | |
| $B_2^{(3)}$ | | | $K_{23}^{(2)}$ | $K_{23}^{(2)}B_2^{(3)}$ | | | ⑯ + | |
| $B_3^{(3)}$ | | | | $B_3^{(3)}$ | | | ⑰ + | |
| | $B_4^{(3)}$ | $K_{14}^{(2)}$ | $K_{24}^{(2)}$ | ↓ | $B_1^{(3)}K_{14}^{(2)}$ | $B_2^{(3)}K_{24}^{(2)}$ | ⑫ | $K_{34}^{(3)}$ |
| | $B_5^{(3)}$ | $K_{15}^{(2)}$ | $K_{25}^{(2)}$ | Σ ⑮ | $B_1^{(3)}K_{15}^{(2)}$ | $B_2^{(3)}K_{25}^{(2)}$ | | $K_{35}^{(3)}$ |
| | ⋮ | ⋮ | ⋮ | | ⋮ | ⋮ | | ⋮ |
| | $\Sigma B_i^{(3)}$ | | | | | | | $\Sigma K_{3i}^{(3)}$ |

Check Equation- $B_1^{(3)} \Sigma K_{1i}^{(3)} + B_2^{(3)} \Sigma K_{2i}^{(3)} + B_3^{(3)} \Sigma K_{3i}^{(3)} \stackrel{?}{=} -\Sigma B_i^{(3)}$

| ⑳ = $K_{13}^{(2)}$⑱ + ⑭ | ㉑ = $K_{23}^{(2)}$⑱ + ⑭ |
|---|---|
| | |
| | |
| | |
| $K_{14}^{(3)}$ | $K_{24}^{(3)}$ |
| $K_{15}^{(3)}$ | $K_{25}^{(3)}$ |
| ⋮ | ⋮ |
| $\Sigma K_{1i}^{(3)}$ | $\Sigma K_{2i}^{(3)}$ |
| | |

TABLE 2 TABLE FOR FINDING SWEEPING CONSTANTS FOR FIFTH MODE
(Set up for five degrees of freedom.)

| Fifth Mode | | | | | | | | | |
|---|---|---|---|---|---|---|---|---|---|
| (22) | (23) | (24) | (25) | (26) | (27) | (28) | (29) | (30) | (31) |
| $B_1^{(4)}$ | | $K_{14}^{(2)}$ | | | $K_{14}^{(2)}B_1^{(4)}$ | | | | |
| $B_2^{(4)}$ | | | $K_{24}^{(2)}$ | | $K_{24}^{(2)}B_2^{(4)}$ | | | | |
| $B_3^{(4)}$ | | | | $K_{34}^{(2)}$ | $K_{34}^{(2)}B_3^{(4)}$ | | | | (23) + |
| $B_4^{(4)}$ | | | | | $B_4^{(4)}$ | | | | (28) + |
| | $B_5^{(4)}$ | $K_{15}^{(2)}$ | $K_{25}^{(2)}$ | $K_{35}^{(2)}$ | $\Sigma$ (27) | $B_1^{(4)}K_{15}^{(2)}$ | $B_2^{(4)}K_{25}^{(2)}$ | $B_3^{(4)}K_{35}^{(2)}$ | (29) + |
| | ⋮ | ⋮ | ⋮ | ⋮ | | ⋮ | ⋮ | ⋮ | (30) |
| | $\Sigma B_i^{(4)}$ | | | | | | | | |
| | | | | | | | | | |
| | | | | | | | | | |
| (32) = −(31)/(27) | (33) = $K_{14}^{(2)}$ (32) + (24) | | | | (34) = $K_{24}^{(2)}$ (32) + (25) | | | (35) = $K_{34}^{(2)}$ (32) + (26) | |
| | | | | | | | | | |
| | | | | | | | | | |
| | | | | | | | | | |
| | | | | | | | | | |
| $K_{48}^{(4)}$ | $K_{18}^{(4)}$ | | | | $K_{28}^{(4)}$ | | | $K_{38}^{(4)}$ | |
| ⋮ | ⋮ | | | | ⋮ | | | ⋮ | |
| $\Sigma K_{1i}^{(4)}$ | $\Sigma K_{1i}^{(4)}$ | | | | $\Sigma K_{2i}^{(4)}$ | | | $\Sigma K_{3i}^{(4)}$ | |
| Check Equation— $B_1^{(4)}\Sigma K_{1i}^{(4)} + B_2^{(4)}\Sigma K_{2i}^{(4)} + B_3^{(4)}\Sigma K_{3i}^{(4)} + B_4^{(4)}\Sigma K_{4i}^{(4)} \stackrel{?}{=} -\Sigma B_i^{(4)}$ | | | | | | | | | |

the sweeping tables are used for the latter situation, and each operation will be explained to show how it corresponds to the operation indicated by the table. The technique can be reduced to a simple rule, however. This is, that the most desirable arrangement is to make the row of $K_{rj}$ as small as possible, which is accomplished by inserting the largest $B$ into the first column of the table for each mode.

In this example, a fourteen degree-of-freedom system derived from the properties of a full-size airplane wing, the method by which the modal columns are found will not be shown, but will be assumed to have been calculated by a standard iteration procedure. The determination of the $B_i$ by Equations [3] is also assumed to have been carried out, since the primary interest here is the method of using these quantities in the table. Therefore let us assume that the first mode and the associated $B_i^{(1)}$ have been determined. They are now tabulated as in Table 3, the *largest* $B$ being placed in column ①, rather than $B_1^{(1)}$.

As desired, all the $K_{ij}^{(1)}$ are less than unity, and since $B_6^{(1)}$ was put into column ①, the row $K_{6i}^{(1)}$ is placed in row six of the sweeping matrix, reducing column six of $[D_{ij}^{(1)}]$ to zero and resulting in the matrix $[D_{ij}^{(2)}]$. Iteration is now applied to this matrix to obtain the second modal column.

Using these results to fill out the "Third Mode" table (Table 4)

TABLE 3 SECOND MODE

| | ① | ② | ③ = −②/① $K_{6i}^{(1)}$ |
|---|---|---|---|
| 1 | | 15.0043 | −0.161490 |
| 2 | | 15.0306 | −0.161773 |
| 3 | | 13.4711 | −0.144988 |
| 4 | | 13.8001 | −0.148529 |
| 5 | | 89.7399 | −0.965859 |
| 6 | 92.9119 | | |
| 7 | | 10.6973 | −0.115133 |
| 8 | | 12.7415 | −0.137135 |
| 9 | | 73.9942 | −0.796360 |
| 10 | | 24.2217 | −0.260695 |
| 11 | | 25.4800 | −0.274238 |
| 12 | | 3.27070 | −0.0352021 |
| 13 | | 2.87011 | −0.0308906 |
| 14 | | − 2.63475 | 0.0283575 |
| | | Σ 297.6865 | −3.203964 |

*Check Equation:* $B_6^{(1)}\Sigma K_i^{(1)} \stackrel{?}{=} -\Sigma B_i^{(1)}$

$(92.9119)(-3.203964) = -297.6865$ Checks
$(-297.6865)$

becomes a more complicated process. The first step is to fill out column ④, $B_6^{(2)}$ being entered first in the sixth position. This quantity actually performs the function that is indicated by $B_1^{(2)}$ in the standard table, since $B_6^{(1)}$ was used to perform the function of $B_1^{(1)}$ in the "First Mode" table. $B_9^{(2)}$ is now placed in

TABLE 4 THIRD MODE

| Third Mode: | | $B_i^{(3)}$ | $K_{6i}^{(3)}$ | | $B_6^{(3)}$ ⑥ + ⑦ | $K_{9i}^{(3)}$ -④/⑧ | $K_{6i}^{(3)}$ $K_{6i}^{(2)}$ ⑨ + ⑥ |
|---|---|---|---|---|---|---|---|
| | ④ | ⑤ | ⑥ | ⑦ | ⑧ | ⑨ | ⑩ |
| 1 | | -9.26570 | -.161493 | | -10.4426 | .0154493 | -.197685 |
| 2 | | -8.21653 | -.161773 | | - 9.19510 | .0130541 | -.180132 |
| 3 | | -10.7728 | -.166988 | | -11.6498 | .0126735 | -.180156 |
| 4 | | -.693141 | -.148569 | | - 1.76159 | .0794380 | -.154860 |
| 5 | | -60.5607 | -.965859 | | -60.4032 | .0046650 | -1.200515 |
| 6 | 6.04901 | -------- | -.796390* | -4.81737 | ---------- | ---------- | -------- |
| 7 | | -12.9052 | -.115133 | | -13.6016 | .0083542 | -.163198 |
| 8 | | 23.2456 | -.127435 | | 20.0961 | -.0104434 | -.0555178 |
| 9 | 230.180 | -------- | -------- | 230.180 | -------- | ---------- | -------- |
| 10 | | -37.4763 | -.600695 | | -39.9532 | .0173490 | -.398701 |
| 11 | | 23.3475 | -.074238 | | 21.0686 | -.0080443 | -.197665 |
| 12 | | -12.3074 | -.0352021 | | -12.5203 | .0055561 | -.0794464 |
| 13 | | 16.7452 | -.0303906 | | 16.5583 | -.0034739 | .0478433 |
| 14 | | 110.819 | .0483575 | ------- | 110.991 | -.0434499 | .0020574 |
| | Σ | 26.4195 | | 225.363 | | -25.6117 | -2.365664 |

Check Equation- $B_6^{(2)}\sum K_{61}^{(2)} + B_9^{(2)}\sum K_{91}^{(2)} \doteq -\sum B_i^{(2)}$

(6.04901)(-2.36566) + (230.180)(-.0526117) ≐ -26.4201 (-26.4195) Checks.

* Transferred from position 9

column ④ rather than $B_2^{(2)}$, since it is the largest of the remaining elements. The remaining $B_i$ are now placed in their proper position in column ⑤. The $K_{6i}$ from the previous mode are then entered in regular order, except that $K_{66}^{(1)}$ is transferred from block nine to six so that it multiplies the correct $B$. The calculating operations are carried out as indicated in the standard table giving numerical results as in Table 4.

The constants $K_{9i}^{(3)}$ resulting from this table go into row nine of the modified sweeping matrix $[S^{(2)}]'$, which multiplies $[D_{ij}^{(2)}]$ to produce $[D_{ij}^{(3)}]$ which converges to the third modal column when iteration is applied to it. The values $B_i^{(3)}$ are then determined.

In preparing the table (Table 5) for determining the constants for $[S^{(3)}]'$, column ⑩ is filled out first. $B_6^{(3)}$ and $B_9^{(3)}$ are put into this column because $B_6^{(2)}$ and $B_9^{(2)}$ were placed in the corresponding column of the preceding table. Then, $B_{14}^{(3)}$ is also entered in column ⑩ because it is the largest of the remaining elements. After these three numbers have been taken out, the other $B_i$ are put into column ⑫. The $K_{ij}^{(3)}$ are then entered in columns ⑬ and ⑭. Here it must be noticed that $K_{ij}^{(2)}$ is transferred to the sixth position and $K_{9,14}^{(2)}$ to the ninth position, so that they multiply the appropriate $B$ according to Equation [12].

The constants $K_{14,i}^{(3)}$ make up the fourteenth row of $[S^{(3)}]'$, which multiplies the matrix $[D_{ij}^{(3)}]$ to produce $[D_{ij}^{(4)}]$. This matrix converges directly to the fourth mode when iteration is applied to it. Still higher modes can be found by continuing this procedure.

## Discussion

A distinct characteristic of systems involving the coupling of normal modes of elastic structures, where the coupling effect is small, is that each individual degree of freedom will dominate in determining the roots of the coupled system. Also, the largest element of the vector corresponding to each root will be mainly the result of these individual degrees of freedom. In the computing process this is indicated by the fact that the diagonal elements of the given matrix have the strongest effect in producing the largest element. In general, the largest element of the fundamental mode usually lies in the same row as the largest diagonal element of the given matrix. In fact, the root may be very nearly the value of the largest diagonal element.

Consequently one can define the "dominant" degree of freedom in any system, even where coupling effects are large, as the one corresponding to the largest element of the column of $B_i$ derived from the mass system and the results of the iteration process. This concept is important with regard to accuracy when the orthogonality condition is used for sweeping previously determined modes, especially in the case of coupling normal modes where coupling is small and the determination of all roots is required. It is best to apply the constraint of orthogonality to the dominant degree of freedom, which results in sweeping out the column which contains the largest diagonal element. The sweeping constants will then tend to be relatively small, so that there will be less likelihood of small differences of large numbers, particularly on the diagonal.

In one case involving the analysis of an airplane wing this was not done during preliminary calculations and very small differences of large numbers resulted in obtaining the matrix for the second mode. Errors grew steadily worse with each mode. Later these calculations were repeated, taking care to sweep out the dominant modes. This not only reduced greatly the incidence of small differences of large numbers, but it became possible to satisfy all the orthogonality conditions to exactly the number of significant figures to which convergence of the iteration process was carried. This was due to the fact that the two terms involving the dominant degree of freedom of each mode were the most important in satisfying the orthogonality condition. Thus when the results of iteration were tested for orthogonality, errors were removed by adjusting a value which had negligible effect upon the others. The adjusted results also satisfied the original matrix very closely.

TABLE 5 FOURTH MODE

| Fourth Mode: | | $B_1^{(2)}$ | $K_{01}^{(2)}$ | $K_{91}^{(2)}$ | | $B_0^{(3)}$ (13) | $B_9^{(2)}$ (14) | (16)+(17)+(18) | $K_{14,1}^{(2)}$ (19)/(15) | $K_{0,1}^{(2)}$ $K_{0,14}^{(3)}$ (13)+(20) | $K_{9,1}^{(2)}$ $K_{9,14}^{(2)}$ (14)+(20) |
|---|---|---|---|---|---|---|---|---|---|---|---|
| | (11) | (12) | (13) | (14) | (15) | (16) | (17) | (18) | (19) | (20) | (21) |
| 1 | | 11.2514 | -.197685 | .0456493 | | -6.03972 | | | | | |
| 2 | | -89.4222 | -.180132 | .0430521 | | -5.84058 | .476199 | 5.31779 | -.0211386 | -.206983 | .0563378 |
| 3 | | 7.74460 | -.186156 | .0510935 | | -6.03530 | .421485 | -75.3213 | .311900 | -.0689534 | -.130558 |
| 4 | | 6.81971 | -.154860 | .0374498 | | -5.02117 | .541520 | 2.29022 | -.0095156 | -.190161 | .0563829 |
| 5 | | 37.3139 | -1.220515 | .494650 | | -38.9454 | .0834789 | 1.88182 | -.00784364 | -.158150 | .0113029 |
| 6 | 32.4239 | ------- | .4205778 | ------- | 13.0308 | -------- | 3.08664 | 1.47514 | -.00613487 | -1.69309 | .297670 |
| 7 | | 3.54181 | -.163148 | .0603564 | | -5.49152 | -------- | ------- | ---------- | ---------- | ---------- |
| 8 | | 1.30074 | -.0555178 | -.10.464 | | -1.80010 | .632446 | -1.11746 | .00464582 | -.161264 | .0583661 |
| 9 | 10.4756 | ------- | -------- | -.494499* | - 5.15302 | -------- | -1.07358 | -1.57490 | .00653956 | -.0547674 | -.135705 |
| 10 | | - 4.33474 | -.398701 | .173499 | | -12.9474 | ------- | ------- | ---------- | -------- | -------- |
| 11 | | 13.2654 | -.197665 | -.0961498 | | -6.40907 | 1.81532 | -15.4668 | .0642115 | -.371695 | .141666 |
| 12 | | - 8.68418 | -.0734464 | .0555561 | | -2.57576 | -1.00743 | 5.84910 | -.0243175 | -.207832 | -.0841735 |
| 13 | | 14.2954 | .0276233 | -.0734739 | | .895655 | .581983 | -10.678 | .0443945 | -.0607750 | .0338919 |
| 14 | 232.0523 | ------- | -------- | -------- | 436.928 | ------- | -.769683 | 14.4614 | -.0599568 | .0004073 | -.0859451 |
| | | Σ 43.1362 | | | 440.530 | | ------ | ------ | ---------- | ---------- | ---------- |
| | | | | | | | | | Σ .3018304 | -2.6593041 | .291236 |

* Transferred from position 44

Check Equation- $B_0^{(3)}\sum B_{0,1}^{(3)} + B_9^{(3)}\sum K_{9,1}^{(3)} + B_{14}^{(3)}\sum K_{14,1}^{(3)} = -\sum B_1^{(3)}$

$(32.4239)(-2.65930) + (10.4756)(.291236) + (232.0523)(.301830) = \underset{(-13.1338)}{-13.1336}$ Checks.

## Conclusion

The conclusions may be drawn that in setting up the matrix for a system representing coupled normal modes, the rows and columns should be arranged such that the diagonal elements go in decreasing order of magnitude from the upper left to the lower right. Thus dominant modes will be swept successively from the left automatically when the sweeping tables are applied. For an elastic system such as a wing structure with large concentrated masses, however, it is desirable to number the lumped masses in regular order which scatters the dominant modes throughout the matrix. For the higher modes of this system, the sweeping tables must be applied with care as shown in the numerical example, since the various elements do not lie in the regular order in which the tables are given.

Caution must be exercised with the resultant $K_{ij}$ to put them into the proper row of the sweeping matrix so that they will multiply the corresponding row and column of the given matrix. This means that columns will not be reduced to zeros from left to right in successive order, but rather, wherever the dominant mode may be situated. An alternative to this method is to rearrange rows and columns of the given matrix in order to place dominant modes in successive positions from the top. The disadvantage to this scheme is that such rearranging and recopying is a constant source of error.

When it is necessary to determine all the mode shapes and frequencies of a given system, accuracy becomes an especially important problem. There appears to be a tendency for significantly more errors in the determination of the last mode than n any of the preceding ones. It is obvious that the single column of sweeping constants determined for this mode is identically the solution. It may be checked first by sweeping the two-column matrix that was used just previously. The single column that results should be the same as the sweeping constants each multiplied by the $n$th root of the equation. Another check involves substitution of the whole column into the original equation. This is equivalent to sweeping out all modes but the last from the $n$ by $n$ matrix. Of course if none of these methods gives satisfactory results, the original matrix can be inverted and iteration applied to it, since the first mode of the reciprocal is equivalent to the last of the given matrix, this usually giving the greatest accuracy. The general rule that has often been applied stating that one significant figure is lost in the determination of each new mode appears to be too severe a limitation to be justified by the experience encountered in the numerical work that was done in the present research. There are too many variables involved to allow any such simple rule, and the number of significant figures to be used is mostly a matter of the judgment of the engineer in each case, taking into account relative orders of magnitude and situations where two roots lie very close together. However, if dominant modes are noted carefully and swept as discussed previously, six significant figures appear to be reasonable, in the absence of any other determining factors.

This discussion on numerical accuracy was based upon the work involved in applying the matrix iteration method to the determination of free-free mode shapes and frequencies of the wings of two full-scale airplanes and three model wings built dynamically similar to full-scale aircraft.

## Acknowledgment

The work described in this paper was done originally when the author worked on a Navy research project at the Massachusetts Institute of Technology in 1947, under the direction of Prof. R. L. Bisplinghoff. Also, the author would like to express his appreciation to Dr. Theodore H. H. Pian for many helpful suggestions.

# Approximate Solutions of Problems of Plane Plastic Flow[1]

By P. G. HODGE, JR.,[2] LOS ANGELES, CALIF.

**A method of approximating the stress and velocity fields in problems of plane plastic flow is presented. A general procedure for finding the deformed pattern of an originally square grid is devised and applied to two examples. The results are compared with known continuous solutions and with experiments.**

## Introduction

THE problems considered in this paper are concerned with the behavior of a perfectly plastic material in a state of plane plastic flow. It is assumed that the material remains rigid for stresses which do not satisfy the yield condition, and flows under constant maximum shearing stress if the yield condition is fulfilled. Under these conditions, the solution of the problem is reduced to the determination of the three stress components $\sigma_x$, $\sigma_y$, and $\tau_{xy}$, and the two velocity components $u$ and $v$.

At any point in a known stress field, orthogonal first and second principal directions may be defined as the directions across which the tensile stress is a maximum and minimum, respectively. The elements at 45 deg to the principal directions will be in the directions of maximum shearing stress. In particular, the direction obtained by a 45-deg counterclockwise rotation of the first principal direction will be denoted by the first shear direction. Lines which are everywhere in the direction of the first or second shear direction will be denoted by first and second slip lines, respectively. Along the slip lines the following relations are known to hold (1)[3]

$$\left.\begin{aligned} \omega - \theta &= \text{const along a first slip line} \\ \omega + \theta &= \text{const along a second slip line} \end{aligned}\right\} \quad \ldots\ldots [1]$$

Here $2k\omega$ is the mean normal stress ($k$ is the yield stress in pure shear), and $\theta$ is the angle between the first slip line and the negative $y$-axis. In terms of $\omega$ and $\theta$, the stress components are given by

$$\left.\begin{aligned} \sigma_x &= 2k\omega + k \sin 2\theta \\ \sigma_y &= 2k\omega - k \sin 2\theta \\ \tau_{xy} &= -k \cos 2\theta \end{aligned}\right\} \quad \ldots\ldots [2]$$

Therefore the determination of the pattern of slip lines in a given region is equivalent to the determination of the stress components.

If the material is assumed to flow according to the Saint Venant-Mises stress-strain law, then the slip lines are also in the direction of maximum shear strain. The following relations then hold (1)

$$\frac{dV_1}{ds_1} - \frac{V_2}{R_1} = 0, \qquad \frac{dV_2}{ds_2} - \frac{V_1}{R_2} = 0 \quad \ldots\ldots [3]$$

Here the subscripts 1 and 2 refer to the first and second slip lines, respectively; $V$ is the velocity component, $ds$ the element of arc length, and $R$ the radius of curvature. In particular, the velocity component directed along a straight slip line is constant. Also, if $V_1$ vanishes along a second slip line, $V_2$ is constant along this line, while if $V_2$ vanishes along a first slip line, $V_1$ is constant along this line. Finally, it follows that a region at rest must always be bounded by slip lines.

In some cases it may happen that the boundary conditions imposed cannot all be satisfied by a continuous solution, but that a solution may be obtained if certain discontinuities are introduced. Prager (2) has shown that if a line of discontinuity (shock) separates two regions of perfectly plastic material, then the following relations between the stress components must be valid

$$\left.\begin{aligned} \theta_1 + \theta_2 &= 2\alpha_{12} \\ \omega_2 - \omega_1 &= \sin(\theta_1 - \theta_2) \end{aligned}\right\} \quad \ldots\ldots [4]$$

Here the subscripts 1 and 2 refer to opposite sides of the shock, and $\alpha_{12}$ is the angle between the shock and the negative $y$-axis. Geometrically, the first Equation [1] means that the shock must bisect the intersecting slip lines of either family. In addition, conservation of mass requires that the velocity component normal to the shock be continuous across the shock.

Winzer and Carrier (3) have shown that a discontinuous solution is possible in some cases which admit a continuous solution. In the present paper this concept will be extended further, and the results of continuous and discontinuous solutions compared in detail. The good agreement found will seem to justify the use of discontinuous solutions as a computational device.

The body of this paper is concerned with problems of plastic flow in which the motion of the boundaries is taken into account. First, however, an elementary "instantaneous state" problem will be considered. Here the stress and incipient-velocity fields can be determined, even though the motion of the boundaries is neglected. The classical solution, which is continuous, will be compared with some conceivable discontinuous solutions. The results of this instantaneous state solution will then be used in developing the problems of plastic motion in the remainder of the paper.

## Example of an Instantaneous State Problem

The problem to be considered is that of a uniform pressure applied to one side of a semi-infinite wedge of a perfectly plastic material. The continuous slip-line pattern for this problem was first given by Prandtl (4) in 1923. The isosceles right triangles $ABC_1$ and $ADC_2$, Fig. 1, are regions of constant $\omega$ and $\theta$ (and hence of constant $\sigma_x$, $\sigma_y$, and $\tau_{xy}$), and will be referred to as regions of constant state. In the circular segment $C_1AC_2$, the first family of slip lines (solid lines) consists of straight lines

---

[1] The results presented in this paper were obtained in the course of research conducted at Brown University under Contract N7onr-358 sponsored jointly by the Office of Naval Research and the Bureau of Ships.

[2] Assistant Professor of Mathematics, University of California.

[3] Numbers in parentheses refer to Bibliography at end of paper.

Contributed by the Applied Mechanics Division and presented at the Annual Meeting, New York, N. Y., November 27–December 2, 1949, of The American Society of Mechanical Engineers.

Discussion of this paper should be addressed to the Secretary, ASME, 29 West 39th Street, New York, N. Y., and will be accepted until October 10, 1950, for publication at a later date. Discussion received after the closing date will be returned.

Note: Statements and opinions advanced in papers are to be understood as individual expressions of their authors and not those of the Society. Paper No. 49—A-10.

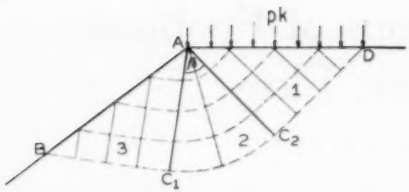


FIG. 1

through the point $A$, while the second slip lines (dotted lines) are a family of circular arcs. Such a region will be called a "centered fan."

The pressure $p$ necessary to achieve this configuration is easily computed. The yield condition[4]

$$\left(\frac{\sigma_x - \sigma_y}{2}\right)^2 + \tau_{xy}^2 = k^2 \quad \ldots\ldots [5]$$

must be satisfied throughout the plastic domain. Therefore[5]

$$\left.\begin{aligned} \sigma_a &= \sigma_y = -pk, \quad \sigma_t = \sigma_x = k(2 - p) \\ \omega &= {}^1/_2(1 - p), \quad \theta = \pi/4 \end{aligned}\right\} \quad \ldots\ldots [6]$$

on $AD$, and

$$\sigma_a = 0, \quad \sigma_t = -2k, \quad \omega = -{}^1/_2, \quad \theta = \frac{\pi}{4} - \beta \quad \ldots\ldots [7]$$

on $AB$. Since $\omega + \theta$ is constant along a second slip line, it follows that

$$p = 2(1 + \beta) \quad \ldots\ldots [8]$$

The incipient velocity solution for this problem is indeterminate. One possible solution is to demand that the vertical velocity along $AD$ be uniform. If the rigid-plastic boundary is some second slip line such as $BC_1C_2D$, then continuity demands that $V_1 = 0$ along this boundary. The first slip lines being straight, it follows that $V_1 = 0$ throughout the plastic domain. Therefore $V_2 = v_0\sqrt{2}$, where $v_0$ is the prescribed vertical velocity of $AD$.

A discontinuous solution to a similar problem has been given by Winzer and Carrier (3). In terms of the present example, the constant-state regions are continued up to the line $AC$, which bisects the angle $BAD$ (Fig. 2). Across $AC$ the tangential stress is discontinuous, hence this line is a shock.

Equations [6] and [7] are still valid; if they are substituted into Equations [4] the necessary pressure is

$$p_1 = 2(1 + \sin\beta) \quad \ldots\ldots [9]$$

[4] For the plane-strain problem, both the Mises and Tresca yield conditions reduce to Equation [5].

[5] An alternative solution is to reverse the first and second slip lines in Fig. 1. However, this would lead to a negative pressure, i.e., to a tension.

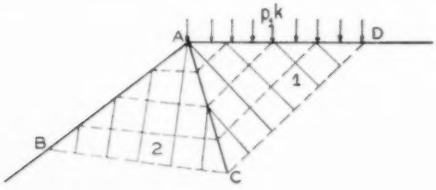


FIG. 2

Therefore the predicted pressure is less for the discontinuous solution. Fig. 3 shows the variation of $p$ and $p_1$ with the angle $\beta$. For small $\beta$ the agreement is seen to be quite good.

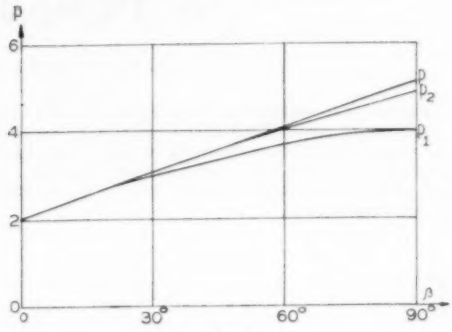


FIG. 3

If the vertical velocity along $AD$ is prescribed constant as before, then

$$V_1 = 0, \qquad V_2 = v_0\sqrt{2}$$

throughout the plastic domain. Since the second slip lines do not have continuous slopes at the shock, this implies that the velocity is discontinuous across $AC$.[6] However, the normal component of velocity is continuous, as required.

The discontinuous solution indicated in Fig. 2 is not by any means the only one possible for this problem. In fact, the fan $C_1AC_2$ in the continuous solution, Fig. 1, may be divided into any number of regions of constant state, separated by shocks. A two-shock configuration is shown in Fig. 4. Let $\alpha_1$, $\alpha_2$, and $\alpha_3$

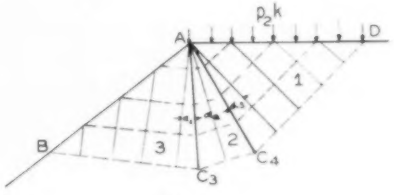


FIG. 4

denote the angles as indicated in Fig. 4. Then, in view of Equations [4]

$$\theta_3 = \pi/4, \quad \theta_2 = \pi/4 - 2\alpha_3, \quad \theta_1 = \pi/4 - 2\alpha_2$$

Since

$$\theta_1 = \pi/4 - \beta, \text{ where } \beta = \alpha_1 + \alpha_2 + \alpha_3$$

it follows that

$$\alpha_2 = \alpha_1 + \alpha_3 = \beta/2$$

Symmetry would indicate that $\alpha_1 = \alpha_3$, but there appears to be no necessity for this restriction. The pressure for this distribution is found to be

[6] It should be noted that a discontinuous tangential velocity component does not necessarily imply a discontinuous displacement. Therefore the material need not exhibit rupture or sliding in the neighborhood of the shock.

$$p = 2[1 + \sin 2\alpha_1 + \sin (\beta - 2\alpha_1)]$$

This pressure lies between the pressure necessary for a continuous stress field and a single-shock stress field. In particular, if $\alpha_1 = \beta/4$, the pressure is given by

$$p_2 = 2[1 + 2 \sin \beta/2]$$

The value of $p_2$ as a function of $\beta$ is plotted in Fig. 3.

A similar computation may be carried out for any number of shocks. As the number of shocks is increased, the pressure tends asymptotically to the continuous pressure, as would be expected.

### Indentation of a Plastic Mass by a Rigid Wedge—Single-Shock Solution

As a first example, consider a smooth rigid wedge pressed into a semi-infinite perfectly plastic material under conditions of plane strain. Hill, Lee, and Tupper (5) have shown that the continuous slip-line pattern consists of three regions on either side of the wedge. Regions 1 and 3, Fig. 5, are regions of constant state,

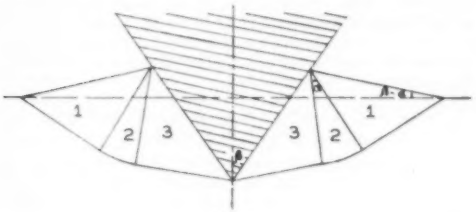


Fig. 5

bounded by straight lines intersecting the lip and the wedge, respectively, at 45-deg angles. Region 2 is a centered fan whose angle $\alpha$ is related to the wedge angle $2\beta$ by

$$\cos (2\beta - \alpha) = \frac{\cos \alpha}{1 + \sin \alpha} \quad \ldots\ldots\ldots\ldots [10]$$

This distribution obviously satisfies the stress-boundary conditions. In view of Equation [10], it can be shown to satisfy the condition of incompressibility which requires that the volume of the lip equal the volume displaced by the wedge. Finally, Hill, Lee, and Tupper have shown that the motion of the plastic material is "pseudo steady," i.e., as the wedge is further indented, the angle $\alpha$ remains constant, and the configuration merely changes in scale.

To compare theoretical and experimental results, it is desirable to calculate the deformation of an originally square grid. The procedure of Hill, Lee, and Tupper (5) for doing this is easily formulated, but the actual calculations for any given example involve numerical integration and are quite laborious. However, it is found that if the continuous solution illustrated in Fig. 5 is replaced by a discontinuous solution, then the deformed grid can be calculated very simply.

In analogy with the example of the previous section, the single-shock discontinuous solution is obtained by continuing the constant-state regions 1 and 3 until they meet at the center of the fan, Fig. 6. The shape of the pattern is entirely determined by Equation [10], and the given wedge angle $2\beta$. Therefore the equations of the lines $AD$, $AC$, $CD$, . . . may all be regarded as known functions of the depth of penetration $OD$. It will be shown later that it is not necessary to evaluate these equations explicitly. Since inertia effects are neglected, according to the Saint Venant-Mises theory of plastic flow, the wedge may be assumed to penetrate at unit speed, so that $\overline{OD} = t$.

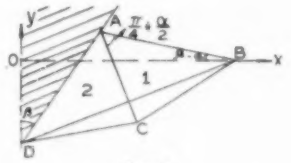


Fig. 6

The material below $BCD$ is assumed rigid. Therefore the velocity vector $\mathbf{q}_1 = u_1, v_1$ in $ABC$ is parallel to $BC$, while in $ACD$, $\mathbf{q}_2 = u_2, v_2$ is parallel to $DC$. The magnitude of the velocity vector is $\sqrt{2} \sin \beta$ in both regions. Thus the normal component of velocity is continuous across the shock $AC$, but the tangential component is reversed in sign. However, as noted previously, the displacements themselves are continuous.

As the wedge is indented into the plastic material, an element at a point $r = x, y$ will remain fixed in space until one of the lines $BC$ or $CD$ passes across it. Let $r_1$ denote the position vector of an arbitrary point which enters the plastic domain across $BC$, and let $t_1 = t_1(r_1)$ be the time at which this occurs. Similarly, let $r_2$ be a point which enters the plastic domain across $CD$ at time $t_2 = t_2(r_2)$.

Once a point is in region 2, it will move with constant velocity $\mathbf{q}_2$. Therefore, if $\overrightarrow{\rho_2} = \xi_2, \eta_2$ is the position vector at time $t$ of a point initially at $r_2$

$$\left.\begin{aligned} \overrightarrow{\rho_2} &= r_2 \qquad\qquad\qquad \text{for } t \leq t_2 \\ \overrightarrow{\rho_2} &= r_2 + \mathbf{q}_2(t - t_2) \quad \text{for } t_2 < t \end{aligned}\right\} \quad \ldots\ldots\ldots [11]$$

However, a point which enters region 1 will move with uniform velocity $\mathbf{q}_1$ until it is overtaken by the shock $AC$, and will thereafter move with velocity $\mathbf{q}_2$. Let $t_{12} = t_{12}(r_1)$ be the time at which the element passes through the shock. Then its position vector at time $t$ is

$$\left.\begin{aligned} \overrightarrow{\rho_1} &= r_1 \qquad\qquad\qquad\qquad\qquad\qquad \text{for } t \leq t_1 \\ \overrightarrow{\rho} &= r_1 + \mathbf{q}_1(t - t_1) \qquad\qquad\qquad \text{for } t_1 < t \leq t_{12} \\ \overrightarrow{\rho_1} &= r_1 + \mathbf{q}_1(t_{12} - t_1) + \mathbf{q}_2(t - t_{12}) \quad \text{for } t_{12} < t \end{aligned}\right\} \quad \ldots [12]$$

The functions $t_1$, $t_2$, and $t_{12}$ may be determined in the following manner: Since each of the lines $AC$, $BC$, and $CD$ is straight, and since the pattern is similar at any stage of the indentation, each line is a linear function of the co-ordinates and the depth of penetration $t$. Thus $CD$, for example, will have an equation of the form

$$a\xi + b\eta + ct + d = 0 \quad \ldots\ldots\ldots\ldots [13]$$

Now at the instant a particle is on $CD$

$$\xi = x, \quad \eta = y, \quad t = t_2$$

where $x$, $y$ are the original co-ordinates of the particle. Therefore Equations [13] can be solved to yield $t_2$ as a linear function of $x$ and $y$. The same procedure determines $t_1$ as a linear function of $x$ and $y$. Finally, for a point instantaneously on $AC$, it follows from the second Equation [12] that

$$\xi = x + u_1(t_{12} - t_1), \quad \eta = y + v_1(t_{12} - t_1), \quad t = t_{12}$$

The substitution of these values, along with the computed values of $t_1$ and $t_2$ into Equation [13] shows that $t_{12}$ is also a linear function of $x$ and $y$.

If the values of $t_1$, $t_2$, and $t_{12}$ so found are substituted back into Equations [11] and [12], the position vector of a point is found as a function of its original co-ordinates and the time $t$. Each of

these equations will be linear in $x$, $y$, and $t$, hence they may be written in the form

$$\left.\begin{array}{l} \left.\begin{array}{l} \xi = x \\ \eta = y \end{array}\right\} t \le t_2 \\ \left.\begin{array}{l} \xi = a_{22}x + b_{22}y + u_2 t \\ \eta = c_{22}x + d_{22}y + v_2 t \end{array}\right\} t_2 < t \end{array}\right\} t_2 \le t_1$$

$$\left.\begin{array}{l} \left.\begin{array}{l} \xi = x \\ \eta = y \end{array}\right\} t \le t_1 \\ \left.\begin{array}{l} \xi = a_{11}x + b_{11}y + u_1 t \\ \eta = c_{11}x + d_{11}y + v_1 t \end{array}\right\} t_1 < t \le t_{12} \\ \left.\begin{array}{l} \xi = a_{12}x + b_{12}y + u_2 t \\ \eta = c_{12}x + d_{12}y + v_2 t \end{array}\right\} t_{12} < t \end{array}\right\} t_1 < t_2 \quad \ldots [14]$$

The coefficients $a_{ij}$, $b_{ij}$, $c_{ij}$, $d_{ij}$ may all be determined from the geometry of the figure (Fig. 6). However, certain interesting conclusions may be drawn directly from the linear form of Equations [14]. First, the entire plastic stress field at any instant may be divided into three regions: material which entered the plastic domain across *BC* and is still in region 1, material which entered the plastic domain across *BC* but is now in region 2, and material which entered the plastic domain across *CD* and is still in region 2. These domains may be conveniently designated by $\Delta_{11}$, $\Delta_{12}$, and $\Delta_{22}$, respectively. Furthermore, since the process of deformation is 1 to 1, a domain $D_{ij}$ in the undeformed material prior to penetration may be associated with each domain $\Delta_{ij}$. The mapping of any particular domain $D_{ij}$ into $\Delta_{ij}$ is given by a particular pair of Equations [14], i. e., by an affine transformation of the form

$$\xi = a_{ij}x + b_{ij}y + u_j t$$
$$\eta = c_{ij}x + d_{ij}y + v_j t$$

It is a well-known theorem concerning affine transformations (see, for instance reference 6) that a family of equispaced parallel lines is mapped into a family of equispaced parallel lines. Therefore, to determine the deformed pattern of an originally square grid, it is necessary to determine only the three regions $\Delta_{11}$, $\Delta_{12}$, and $\Delta_{22}$, and the deformed position of one vertical and one horizontal line in each.

It is readily seen that these results are not limited to the particular example considered, but are, in fact, quite general. Therefore, without further proof, the following theorem will be stated:

*Theorem 1.* Let a stress field be composed entirely of regions of constant state, each of which moves instantaneously as a rigid body. Let these regions be numbered 1, 2, 3, . . . . At any fixed time $t$ in the process of deformation, let $D_{ijk\ldots ms}$ denote the initial position, and $\Delta_{ijk\ldots ms}$ the final position of that set of points which first became plastic in region $i$, then passed successively through regions $j$, $k$, . . . , $m$, and finally occupied region $n$ at time $t$.

*Conclusion.* A set of equispaced parallel lines in $D_{ijk\ldots ms}$ is deformed into a set of equispaced parallel lines in $\Delta_{ijk\ldots mns}$.

In the present example, the regions are defined as follows: Let the parallel to *CD* through *O* intersect *AD* at *E*, and let the parallel to *BC* through *A* intersect *OB* at *F*, Fig. 7. Then the material initially in triangle *OCD* ($D_{22}$) is moved into triangle *ECD* ($\Delta_{22}$) by a process of pure shear parallel to *CD*. Similarly, the material initially in triangle *FCB* ($D_{11}$) has been moved into triangle *ACB* ($\Delta_{11}$) by a process of pure shear parallel to *BC*. Therefore the deformed grid patterns in these two regions may be constructed by inspection. Finally, the material initially in triangle *OCF* ($D_{12}$) is in triangle *ECA* ($\Delta_{12}$) at time $t$. The deformed grid in this region is constructed by joining the end points of corresponding segments from the deformed pattern in $\Delta_{11}$ and $\Delta_{22}$.

The deformed grid for the particular case where $\beta = 30$ deg is shown in Fig. 8. For comparison, Fig. 9 shows the deformed grid for the continuous solution obtained by Hill, Lee, and

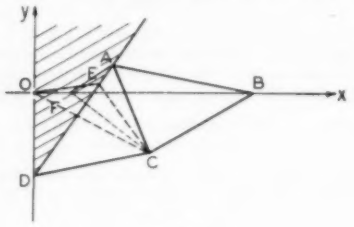


FIG. 7

Tupper (5). Both these solutions may be compared with experimental results obtained by Hill, Lee, and Tupper (Fig. 10). It is seen that the variation between the two computed solutions is of the same order as the variation between the computed solution and the experimental solution.

### INDENTATION OF A PLASTIC MASS BY A RIGID WEDGE—DOUBLE-SHOCK SOLUTION

A closer approximation to the continuous solution may be obtained if the fan in Fig. 5 is replaced by several regions of constant state, separated by shocks. The method will be illustrated by two shocks, but is applicable to any number.

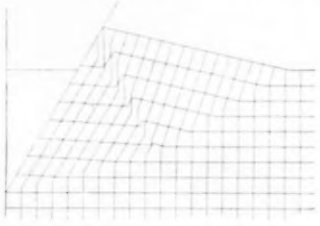

FIG. 8

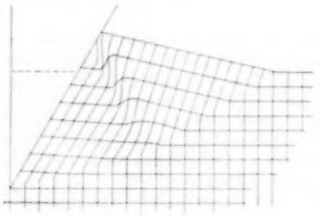

FIG. 9

Let $AC_1$ and $AC_2$, Fig. 11, be the two shocks. In analogy with the results already obtained, the angle $C_1AC_2$ is $\alpha/2$ where $\alpha$ is related to the wedge angle by Equation [10], and the shocks are symmetrically located so that regions 1 and 3 are congruent. As in the case of one shock, the magnitude of the velocity vector is $\sqrt{2}\sin\beta$ throughout the plastic field. Since the normal component must be continuous across the rigid-plastic

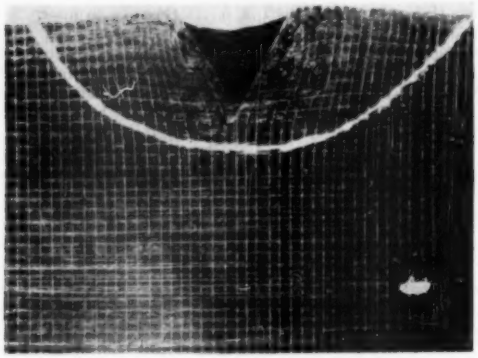

FIG. 10

boundary $BC_1C_2D$, the velocity vector in each region must be parallel to the boundary of the region.

Obviously, this problem satisfies the conditions of Theorem 1. To determine the various domains, locate the points $E$ and $F$ as before, and construct the lines $OC_1$, $OC_2$, $FC_1$, $EC_2$, Fig. 12. Material initially in triangle $OC_2D$ ($D_{21}$) is moved into triangle $EC_2D(\Delta_{22})$ by a pure shear parallel to $DC_2$. Material initially in triangle $FC_1B(D_{11})$ is moved into triangle $AC_1B(\Delta_{11})$ by a pure shear parallel to $BC_1$. The deformed grid in these two regions will coincide with the single-shock pattern.

The material originally in triangle $C_1OC_2$ entered the plastic domain in region 2. However, part of this material is still in region 2, while the remainder has been overtaken by $AC_2$ and is now in region 3. To determine the dividing lines between these two parts, it is necessary to find the deformed position of the line $OC_1$. This is most easily done by means of a "unit diagram," introduced by Hill, Lee, and Tupper (5).

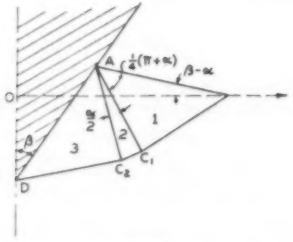


FIG. 11

Consider Fig. 12 as the configuration when the depth of penetration is unity. Let the vector of a point in this unit diagram be $\mathbf{r}'$. Then, at any other depth of penetration $t$, the vector of the corresponding point is

$$\mathbf{r} = t\mathbf{r}'$$

The differentiation of this expression with respect to $t$ leads to

$$t\frac{d\mathbf{r}'}{dt} = \frac{d\mathbf{r}}{dt} - \mathbf{r}' = \mathbf{q} - \mathbf{r}'$$

Since the velocity vector $\mathbf{q}$ has constant magnitude $\sqrt{2}\sin\beta$, all vectors $\mathbf{q}$ must lie on a circle with center at $O$ and radius

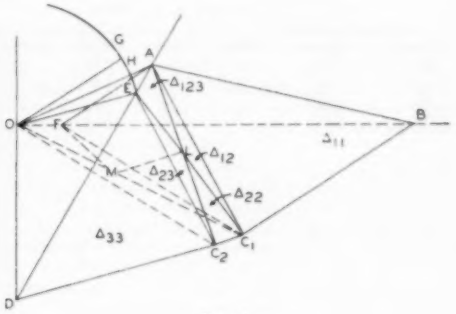


FIG. 12

$\sqrt{2}\sin\beta$. This circle will pass through $E$, hence the velocity vector in region 3 is represented by the point $E$. The points $G$ and $H$, representing the velocity vectors in 1 and 2, respectively, are easily found by drawing lines through $O$ parallel to $BC_1$ and $C_1C_2$, respectively. It is readily verified that $H$ is the intersection of the circle with $OA$.

For any point $P$ in the unit diagram, the vector $d\mathbf{r}'/dt$ is the vector from $P$ to the point $G$, $H$, or $E$, according as $P$ is in region 1, 2, or 3, respectively. Since this vector is in the direction of the velocity vector at $P$, the trajectory of a point in relation to the shock configuration is readily constructed.

As the penetration is increased from 0 to $t$, the locus of points $C_1$, representing the juncture of regions 1 and 2 and the rigid material, is the straight line $OC_1$. The locus of the position of all such points at unit time is the broken line $C_1LE$, where $L$ is the intersection of $C_1H$ and $AC_2$ (Fig. 12). Therefore the deformed position of $OC_1$ is $ELC_1$.

It follows that the material in triangle $C_1LC_2$ ($\Delta_{22}$) has always been in region 2. Therefore the point $M$, representing the initial position of $L$, is the intersection of $OC_1$ with a parallel to $C_1C_2$ through $L$. The various domains are now easily identified. They are summarized in Table 1.

As previously indicated, the deformed grid in $\Delta_{11}$ and $\Delta_{33}$ is the same as for a single shock and may be constructed immediately. In addition to the grid lines the deformed positions of the initially vertical and horizontal lines through $M$ should be constructed (these are indicated by dotted lines in Fig. 13). Since these lines must go through $L$, one grid line of each family is determined in $\Delta_{12}$ and $\Delta_{23}$. In view of Theorem 1, and the fact that one end point of the grid lines is known, this is sufficient to determine the deformed grid in $\Delta_{12}$ and $\Delta_{23}$. Finally, the grid is completed in $\Delta_{22}$ and $\Delta_{123}$ by joining the end points of corresponding segments.

The final pattern is shown in Fig. 13. The agreement with the continuous solution, Fig. 9, is seen to be extremely close.

### Pressing of a Plastic Mass Between Two Rough Plates

As a final example, consider an infinitely long plastic bar which is being pressed between two rough plates. Prandtl (4) has shown that the continuous slip lines are cycloids enveloped by the plates. Geiringer (7) has indicated a numerical method of obtaining the velocity streamlines, but still further numerical work would be necessary to find the pattern of a deformed grid. Lee and Hill (8) have found the stress and velocity distributions for a finite bar, and have shown that Prandtl's solution is a good approximation except near the ends.

A discontinuous solution is obtained as follows: In the exact solutions it is found that there exist two curvilinear triangles

TABLE 1 SUMMARY OF DOMAINS

| Initial conditions | | | Final conditions | | |
|---|---|---|---|---|---|
| Domain | Triangle | Region | Region | Triangle | Domain |
| $D_{11}$ | $FBC_1$ | 1 | 1 | $ABC_1$ | $\Delta_{11}$ |
| $D_{22}$ | $C_1MC_2$ | 2 | 2 | $C_1LC_2$ | $\Delta_{22}$ |
| $D_{33}$ | $C_2OD$ | 3 | 3 | $C_2ED$ | $\Delta_{33}$ |
| $D_{12}$ | $C_1MF$ | 1 | 2 | $C_1LA$ | $\Delta_{12}$ |
| $D_{23}$ | $C_2MO$ | 2 | 3 | $C_2LE$ | $\Delta_{23}$ |
| $D_{123}$ | $OMF$ | 1 | 3 | $ELA$ | $\Delta_{123}$ |

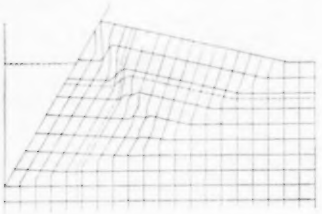

FIG. 13

which do not exhibit plastic flow. These are indicated by the shaded regions 0 in Fig. 14. For the discontinuous solution, these curvilinear triangles will be replaced by linear triangles whose sides make an angle $\beta$ with the horizontal, Fig. 15. Since the sides of the triangles are the boundaries between the rigid and plastic domains, they must be slip lines. Therefore the total angle at $P_0$ (Fig. 15), must be a right angle, and it follows from symmetry that $\beta = \pi/4$.

By hypothesis the pressing plates are perfectly rough. Therefore the slip lines must be everywhere tangent or perpendicular to them, and it is necessary to introduce a shock at $P_1$. In view of Equation [4], this shock must bisect angle $P_0P_1P_2$, hence the shock makes an angle of $\pi/8$ with the negative $y$-axis. A similar consideration shows that a shock must originate at $P_1'$, making an angle of $7\pi/8$ with the negative $y$-axis, and intersecting the first shock at a point $P_2$ on the $x$-axis.

Winzer and Carrier (3) have shown that if two shocks intersect at a point in a plastic domain, there must be at least two more shocks emanating from that point. They have also established interaction conditions. In a symmetrical case, these are most simply stated by the requirement that one pair of opposite angles be right angles. Therefore the shocks $P_2P_3$ and $P_2P_3'$ make angles of $5\pi/8$ and $3\pi/8$, respectively, with the negative $y$-axis.

At the point $P_3$, the shock must "reflect" off the pressing plate. In this case, the Winzer-Carrier relations require that the angle $P_3P_4P_4$ be a right angle. Therefore $P_3P_4$ is parallel to $P_1P_2$, and it follows that the shock configuration at $P_4$ is the same as that at $P_2$. The pattern can thus be continued indefinitely, and of course reflected in the $y$-axis to obtain the pattern for $x$

FIG. 14

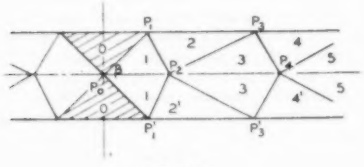


FIG. 15

less than zero. In regions 1, 3, 5, ... (Fig. 15), symmetry demands that the slip lines be inclined to the axes at 45 deg, while in regions 2, 4, 6, ..., 2', 4', 6', ... the boundary conditions on the plate require them to be parallel to the axes. In Fig. 16 the first and second slip lines are represented by solid and dotted lines, respectively, while the shocks are given by heavy lines.

It is readily verified that the solution just defined satisfies the first Equation [4] across each shock. The second Equation [4] may be used to determine the pressure variation along the plate. Let $p_2k$ be the pressure over region 2. Since the slip lines coincide with the axes

$$\sigma_x = \sigma_y = -p_2k, \quad \omega_2 = -p_2/2, \quad \theta_2 = 0$$

In view of the second Equation [4]

$$\omega_3 = \omega_2 + \sin(\theta_2 - \theta_3) = -p_2/2 + \sqrt{2}/2$$

$$\omega_4 = \omega_3 + \sin(\theta_3 - \theta_4) = -p_2/2 + \sqrt{2}$$

$$\omega_5 = -p_2/2 + 3\sqrt{2}/2, \quad \omega_6 = -p_2/2 + 2\sqrt{2}, \ldots$$

Therefore the pressure distribution is given by

$$p_4 = -2\omega_4 = p_2 - 2\sqrt{2}$$

$$p_5 = -2\omega_5 = p_2 - 4\sqrt{2}, \ldots$$

For an infinite bar, $p_2$ represents an arbitrary hydrostatic pressure; for a finite bar it may be determined by the end conditions.

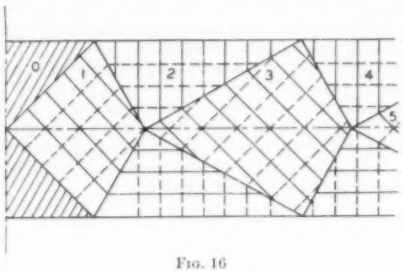


FIG. 16

The pressure distribution according to Prandtl may be written

$$p = p_0 - x/h$$

where $p_0$ represents an arbitrary hydrostatic pressure, and $2h$ is the height of the bar. The two pressure distributions are compared in Fig. 17.

Let the plates be pressed together so that each moves with unit speed with respect to the center line. The velocities in each region may then be determined. In region 0 (Fig. 16), the material is moving downward with unit speed, hence

$$u_0 = 0, \quad v_0 = -1$$

Since the normal component of velocity must be continuous across $P_1P_3$, the component of velocity along the first slip lines in region 1 is $\sqrt{2}$. From symmetry considerations, the velocity along the second slip lines is also $\sqrt{2}$, hence

$$u_1 = 1, \quad v_1 = 0$$

In region 2, let the normal and tangential components of velocity along the shock $P_1P_2$ be $q_n$ and $q_t$, respectively. Then the horizontal and vertical components may be written

$$u_2 = q_n \cos \pi/8 + q_t \sin \pi/8$$

$$v_2 = q_n \sin \pi/8 - q_t \cos \pi/8$$

The components $q_n$ and $q_t$ may be determined from the conditions that $q_n$ is continuous across $P_1P_2$, and $v_2 = -1$. Thus

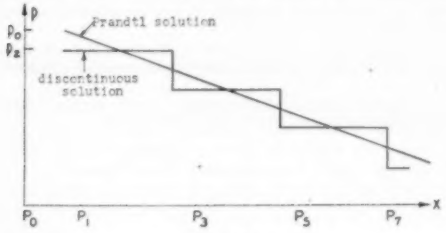


FIG. 17

$$q_n = \cos \pi/8, \quad q_t = \sin \pi/8 - \sec \pi/8$$

and hence

$$u_2 = \sqrt{2}, \quad v_2 = -1$$

Similar computations may be carried out for the remaining regions.

In each region the condition that $q_n$ be continuous across the shock furnishes one boundary condition. The other boundary condition is given by symmetry in regions 1, 3, 5, ... ($v_2 = 0$), and by the prescribed plate velocity in regions 2, 4, 6, ... ($v_2 = -1$). A summary of the results is given in Table 2.

TABLE 2 SUMMARY OF BOUNDARY CONDITIONS

| Region | Velocity component | |
|---|---|---|
| | Horizontal | Vertical |
| 0 | 0 | −1 |
| 1 | $\sqrt{2}$ | 0 |
| 2 | $1 + 2\sqrt{2}$ | −1 |
| 3 | $3\sqrt{2}$ | 0 |
| 4 | $1 + 4\sqrt{2}$ | −1 |
| ... | ... | ... |
| $2n - 1$ | $(2n - 1)\sqrt{2}$ | 0 |
| $2n$ | $1 + 2n\sqrt{2}$ | −1 |

At any stage of the deformation, the slip-line pattern is geometrically similar. Therefore, considered as a stress problem, the solution is pseudo steady. However, this will not be true of the deformed grid pattern, which will change as the deformation progresses. At any particular stage of the compression the deformed grid may be constructed directly, since the problem satisfies the conditions of Theorem 1.

To illustrate the method, let the initial semiheight of the bar be unity, and let the compression be 10 per cent. The separate stress regions in the first quadrant, before and after compression, are represented by solid lines in Figs. 18 and 19, respectively. The dotted lines represent the divisions into separate domains as required by Theorem 1. In Fig. 19 the points $\Pi_i$ represent the position at time $t = 0.1$ of particles initially at the point $P_i$; the lines $\Pi_i \Lambda_{i+1}$ are parallel to the lines $P_iP_{i+1}'$. In Fig. 18 the points $Q_i$ represent the initial positions of particles which deform into $P_i'$; the points $L_i$ are the initial positions of particles which deform into $\Lambda_i$. All of these points are easily constructed with the aid of Table 2.

The deformed grid may now be constructed directly. The final pattern for the first quadrant is shown in Fig. 20. Unfortunately, this cannot be compared with the continuous solution, since the deformed grid for the latter case has not been computed. Experimental results have been obtained by Nye (9) and Odqvist (10). The agreement between Fig. 20 and Nye's results is not very good, possibly owing to the fact that his experiments were carried out with lead blocks, and lead is not a perfectly plastic material. Odqvist, however, used plasticine blocks and observed a region of great shear strain, (Fig. 21), similar to that which occurs in $\Delta_{12}$ (Figs. 19 and 20).

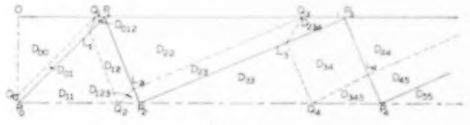

FIG. 18

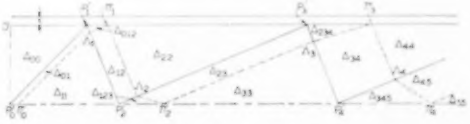

FIG. 19

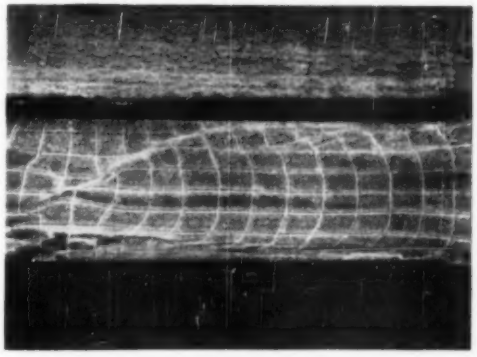

FIG. 21

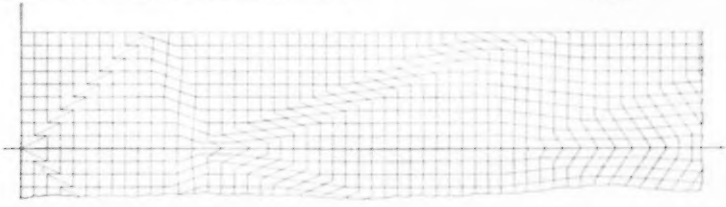

FIG. 20

## BIBLIOGRAPHY

1 "Plasticity for the Aerodynamicist," by W. Prager, *Journal of the Aeronautical Sciences*, vol. 15, 1948, pp. 253–262.

2 "Discontinuous Solutions in the Theory of Plasticity," by W. Prager, Courant Anniversary Volume, Interscience Publishers, New York, N. Y., 1948, pp. 289–299.

3 "The Interaction of Discontinuity Surfaces in Plastic Fields of Stress," by A. Winzer and G. F. Carrier, JOURNAL OF APPLIED MECHANICS, Trans. ASME, vol. 70, 1948, p. A-261.

4 "Anwendungsbeispiele zu einem Henckyschen Satz über des plastische Gleichgewicht," by L. Prandtl, *Zeit. für angewandte Mathematik und Mechanik*, vol. 3, 1923, pp. 401–407.

5 "The Theory of Wedge Indentation of Ductile Metals," by R. Hill, E. H. Lee, and S. J. Tupper, Proceedings of the Royal Society of London, series A, vol. 188, 1947, pp. 273–289.

6 "Differential and Integral Calculus," by R. Courant, Nordeman Publishing Company, New York, N. Y., vol. 2, 1945.

7 "Fondements mathématiques de la théorie des corps plastiques isotropes," by H. Geiringer, Mémorial Sci. Math., no. 86, Gauthiers-Villars, Paris, France, 1937.

8 "The Solution of Plane Strain Problems in the Plastic Flow of Metals Under Large Strains," by E. H. Lee and R. Hill, Proceedings of the 6th International Congress of Applied Mechanics, Paris, France, 1946.

9 "Experiments on the Compression of a Body Between Rough Plates," by J..F. Nye, Armament Research Report 39/47 (England), 1947.

10 "Plasticitetsteori med tillaempigar," by F. Odqvist, Ingenioervetenskaps-Akademien, Stockholm, Sweden, 1934.

# Thermoelastic Stress Around a Cylindrical Inclusion of Elliptic Cross Section

By RAYMOND D. MINDLIN[1] and HILDA L. COOPER,[2] MURRAY HILL, N. J.

**The two-dimensional equations of thermoelasticity are solved for the case of a uniform temperature change of an infinite medium containing a cylindrical inclusion of elliptic cross section. The problem is treated as one of plane strain in elliptic co-ordinates, and the solution is given in closed form. Formulas and curves are given for the maximum values of various components of stress at the interface between the inclusion and the surrounding medium.**

## Introduction

IF an elastic body containing an elastic inclusion is heated, uniformly or not, an elastic state of stress is induced if the inclusion has a coefficient of linear thermal expansion different from that of the surrounding material. The problem considered here is one of uniform heating, or cooling, of a body composed of an infinite elastic medium in which is embedded an infinitely long cylinder of elliptic cross section. The cylinder and the surrounding medium have not only different coefficients of thermal expansion, but also different constants of elasticity. The displacement and traction, across the interface between the two materials, are assumed to be continuous. The problem is treated as one of plane strain in elliptic co-ordinates.

## Elliptic Co-Ordinates

We shall use elliptic co-ordinates $\xi$, $\eta$ defined, in terms of rectangular co-ordinates $x$, $y$, by[3]

$$x + iy = c \cosh (\xi + i\eta) = c \cosh \zeta$$

so that $c$ is one half the distance between the foci of the family of confocal ellipses $\xi$ = const and the orthogonal family of confocal hyperbolas $\eta$ = const, Fig. 1. The co-ordinate $\xi$ is restricted to be positive with the same value assigned to the whole of one ellipse.

The elliptic boundary between the inner and outer bodies is taken as the curve $\xi = \xi_0$. Hence if $b$ and $a$ are, respectively, the minor and major semiaxes of the boundary, their ratio is given by

$$\gamma = b/a = \tanh \xi_0$$

The stretch ratio $J$, and the angle, $\varphi$, which the tangent to $\eta$ = const makes with the $x$-axis, are given by $Je^{i\varphi} = d(x + iy)/d\zeta$,

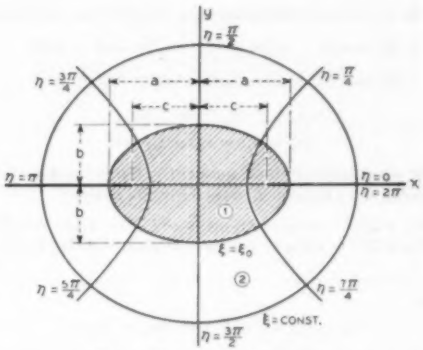


FIG. 1 ELLIPTIC CO-ORDINATES

so that

$$2J^2 = c^2 (\cosh 2\xi - \cos 2\eta)$$

$$\tan \varphi = \coth \xi \tan \eta$$

## Formulas for Stress, Strain, and Displacement

The components of stress are expressed in terms of Airy's stress function $\chi$ by the usual formulas[4]

$$\sigma_\xi = \frac{1}{J^2}\frac{\partial^2 \chi}{\partial \eta^2} + \frac{1}{J^3}\left(\frac{\partial \chi}{\partial \xi}\frac{\partial J}{\partial \xi} - \frac{\partial \chi}{\partial \eta}\frac{\partial J}{\partial \eta}\right)$$

$$\sigma_\eta = \frac{1}{J^2}\frac{\partial^2 \chi}{\partial \xi^2} + \frac{1}{J^3}\left(\frac{\partial \chi}{\partial \eta}\frac{\partial J}{\partial \eta} - \frac{\partial \chi}{\partial \xi}\frac{\partial J}{\partial \xi}\right)$$

$$\tau_{\xi\eta} = -\frac{1}{J^2}\frac{\partial^2 \chi}{\partial \xi \partial \eta} + \frac{1}{J^3}\left(\frac{\partial \chi}{\partial \xi}\frac{\partial J}{\partial \eta} + \frac{\partial \chi}{\partial \eta}\frac{\partial J}{\partial \xi}\right)$$

so that

$$\sigma_\xi + \sigma_\eta = \frac{1}{J^2}\left(\frac{\partial^2 \chi}{\partial \xi^2} + \frac{\partial^2 \chi}{\partial \eta^2}\right) = \nabla^2 \chi$$

and

$$\nabla^4 \chi = 0 \qquad [1]$$

The stress-strain relation is expressed, in rectangular co-ordinates, by three equations of the type

$$E\epsilon_x = \sigma_x - \nu(\sigma_y + \sigma_z) + E\alpha T$$

and three of the type

$$G\gamma_{xy} = \tau_{xy}$$

where $E$ is Young's modulus, $G$ is the shear modulus, $\nu$ is Poisson's ratio, $\alpha$ is the coefficient of linear thermal expansion, and $T$

---

[1] Columbia University, New York, N. Y., and Consultant, Bell Telephone Laboratories. Mem. ASME.

[2] Bell Telephone Laboratories.

[3] "A Treatise on Photo-Elasticity," by E. G. Coker and L. N. G. Filon, Cambridge University Press, London, England, 1931, p. 159.

Contributed by the Applied Mechanics Division and presented at the Annual Meeting, New York, N. Y., November 27–December 2, 1949, of THE AMERICAN SOCIETY OF MECHANICAL ENGINEERS.

Discussion of this paper should be addressed to the Secretary, ASME, 29 West 39th Street, New York, N. Y., and will be accepted until October 10, 1950, for publication at a later date. Discussion received after the closing date will be returned.

NOTE: Statements and opinions advanced in papers are to be understood as individual expressions of their authors and not those of the Society. Paper No. 49—A-20.

[4] Ibid., p. 163.

is the temperature above a uniform initial temperature. For plane strain

$$\gamma_{xz} = \gamma_{yz} = 0$$

and we may take

$$\epsilon_z = k = \text{const}$$

Then

$$\sigma_z = \nu(\sigma_x + \sigma_y) - E\alpha T + Ek$$

and the stress-strain relation becomes, in curvilinear co-ordinates

$$2G\,\epsilon_\xi = (1-\nu)(\sigma_\xi + \sigma_\eta) - \sigma_\eta + E\alpha T - 2\nu Gk$$

$$2G\,\epsilon_\eta = (1-\nu)(\sigma_\xi + \sigma_\eta) - \sigma_\xi + E\alpha T - 2\nu Gk$$

$$\epsilon_z = k, \quad G\gamma_{\xi\eta} = \tau_{\xi\eta}$$

$$\gamma_{\eta z} = \gamma_{z\xi} = \tau_{\eta z} = \tau_{z\xi} = 0$$

The components of displacement, $U_\xi$, $U_\eta$, in the directions $\xi$ increasing and $\eta$ increasing, respectively, are given by

$$\left.\begin{aligned} 4GJU_\xi &= 2(1-\nu)Ju_\xi - 2\partial\chi/\partial\xi + c^2(E\alpha T - 2\nu Gk)\sinh 2\xi \\ 4GJU_\eta &= 2(1-\nu)Ju_\eta - 2\partial\chi/\partial\eta - c^2(E\alpha T - 2\nu Gk)\sin 2\eta \end{aligned}\right\} \quad \ldots\ldots\ldots [2]$$

where

$$u_\xi + iu_\eta = e^{i\varphi}\int J e^{i\varphi}\,(\nabla^2\chi + iR)d\zeta$$

and $R$ is the conjugate of $\nabla^2\chi$. Equations [2] are the usual forms[5] with the addition of the terms containing $E\alpha T - 2\nu Gk$, which account for the thermal dilatation and axial strain.

We shall designate the portion within the elliptic boundary as Region 1 and the surrounding medium as Region 2. Quantities associated with Region 1 will be identified by primes, and those of Region 2 by double primes.

## Boundary Conditions

In view of the assumptions of continuity of traction and displacement across the common boundary of Regions 1 and 2, we require

$$\sigma_\xi' = \sigma_\xi'', \ \tau_{\xi\eta}' = \tau_{\xi\eta}'' \text{ on } \xi = \xi_0 \quad \ldots\ldots\ldots [\text{I}]$$

$$U_\xi' = U_\xi'', \ U_\eta' = U_\eta'', \ U_z' = U_z'' \text{ on } \xi = \xi_0 \quad \ldots [\text{II}]$$

At points in Region 2 far from its inner boundary, the stress must vanish, that is

$$\lim_{\xi\to\infty}\ (\sigma_\xi'', \sigma_\eta'', \sigma_z'', \tau_{\xi\eta}'') = 0 \quad \ldots\ldots\ldots [\text{III}]$$

If, as is likely in practice, the composite body is bounded by two traction-free planes $z$ = const, the solution to be given should not be used if $E' >> E''$ and, in any case, not within a distance $a$ from the intersections of the cylindrical surface $\xi = \xi_0$ with the two planes $z$ = const. These restrictions arise from the assumption of plane strain in which we can require, at the most, on $z$ = const

$$\int_0^{2\pi}\int_0^{\xi_0} \sigma_z'\,J^2 d\xi d\eta + \lim_{\xi_0\to\infty}\int_0^{2\pi}\int_{\xi_0}^{\xi_0} \sigma_z''\,J^2\,d\xi d\eta = 0 \quad [\text{IV}]$$

[5] Ibid., p. 166.

The third of Conditions [II] requires

$$\epsilon_z' = k' = \epsilon_z'' = k'' = k \text{ (say)}$$

and Condition [III] requires

$$k = \alpha'' T$$

If the components of stress and displacement are derived from stress functions which are solutions of Equation [1], and if Boundary Conditions [I, II, III] are satisfied, Condition [IV] will be satisfied identically.

## Stress Function

The appropriate Airy functions, $\chi'$ for Region 1 and $\chi''$ for Region 2, were selected from a list[6] of biharmonic functions in elliptic co-ordinates, leading to single-valued displacements. The possibility that the solution might be expressed in closed form was indicated by Donnell's solution[7] of a similar problem. The functions which generate the solution of the present problem are

$$\left.\begin{aligned} \chi' &= A\cosh 2\xi\cos 2\eta + B(\cosh 2\xi + \cos 2\eta) \\ \chi'' &= De^{-2\xi}\cos 2\eta + F\xi + H(e^{-2\xi} + \cos 2\eta) \end{aligned}\right\} \quad \ldots [3]$$

where $A$, $B$, $D$, $F$, $H$ are constants whose values are found, from the boundary conditions, to be

$$\left.\begin{aligned} A &= c^2\delta(1-\gamma^2)\gamma^{-1}K/4 = A_0c^2/4 \\ B &= [n\gamma - (1+\gamma)^2](1-\gamma^2)^{-1}A = B_0c^2/4 \\ D &= -2\gamma(1-\gamma)^{-2}A = D_0c^2/4 \\ F &= 2[n(1+\gamma^2) - 2(1+\gamma)^2]\gamma(1-\gamma^2)^{-2}A \\ H &= n\gamma(1-\gamma^2)^{-1}A = H_0c^2/4 \end{aligned}\right\} \quad \ldots [4]$$

in which

$$K = \frac{(2m'+1)(m''+1)^2(2m''+1)^{-1}}{n[n(m'-1) - 4(m'+1) + 2(m''+1)] - 2(m''+1-n)\gamma^{-1}(1+\gamma)^2}$$

$$m' = \nu'/(1-\nu'), \qquad m'' = \nu''/(1-\nu'')$$

$$n = (1 - G''/G')/(1-\nu''), \quad \delta = E''(\alpha'' - \alpha')/T$$

This completes the formal solution of the problem as stated, and we proceed to the computation of the important components of stress.

## Boundary Stress

On the boundary $\xi = \xi_0$, the components of stress (identified by overbars) are found to be

$$\left.\begin{aligned} \bar\sigma_\xi' &= \bar\sigma_\xi'' = B_0 + A_0\Phi \\ \bar\sigma_\eta' &= B_0 - A_0\Phi \\ \bar\sigma_\eta'' &= H_0(1 - 2\Psi) - D_0(\Phi + \Psi\cos 2\eta) \\ \bar\tau_{\xi\eta}' &= \tau_{\xi\eta}'' = A_0\Psi\sin 2\eta \\ \bar\sigma_z' &= (E'/E'')\delta + 2\nu' B_0 \\ \bar\sigma_z'' &= 2\nu'' H_0(1-\Psi) \end{aligned}\right\} \quad \ldots\ldots [5]$$

where

$$\Phi = \frac{1 - \gamma^2 - (1+\gamma^2)\cos 2\eta}{1 + \gamma^2 - (1-\gamma^2)\cos 2\eta}$$

$$\Psi = \frac{2\gamma}{1 + \gamma^2 - (1-\gamma^2)\cos 2\eta}$$

and $A_0$, $B_0$, $D_0$, $H_0$ are defined in Equations [4].

[6] Ibid., p. 536.

[7] "Stress Concentrations Due to Elliptical Discontinuities in Plates Under Edge Forces," by L. H. Donnell, Th. von Kármán Anniversary Volume, California Institute of Technology, 1941.

The principal stresses on $\xi = \xi_0$ are given by the formulas

$$p, q = \frac{1}{2}(\sigma_\xi + \sigma_\eta) \pm \frac{1}{2}[(\sigma_\xi - \sigma_\eta)^2 + 4\tau_{\xi\eta}^2]^{1/2} \quad \ldots\ldots [6]$$

where $p$ is associated with the $+$ sign and is, hence, always the algebraically larger of the two principal stresses. Both $p$ and $q$ are found to be independent of $\eta$ within the boundary (Region 1) and dependent on $\eta$ outside the boundary (Region 2).

Substituting the expressions for $\sigma_\xi{}^\sigma$, $\sigma_\eta{}^\sigma$, $\tau_{\xi\eta}{}^\sigma$ from Equations [5] into Equations [6] and setting the derivatives, with respect to $\eta$, of the resulting expressions for $p^\sigma$ and $q^\sigma$ equal to zero, we find that both $p^\sigma$ and $q^\sigma$ have stationary values at[8] $\eta = 0, \pi/2, \eta_0$ where

$$\cos 2\eta_0 = \frac{1}{1-\gamma^2}\left[1 + \gamma^2 - \frac{2n\gamma^2(2 \pm n^{1/2})}{(1+\gamma)^2 - n\gamma}\right] \quad \ldots [7]$$

When using Equation [7] the following must be noted:

($a$) It applies only if $n \geq 0$.

($b$) It applies only if $n$ and $\gamma$ have such values that the right-hand side lies between $-1$ and $+1$.

($c$) If $\delta > 0$, the plus sign applies to $q$ and the minus sign to $p$.

($d$) If $\delta < 0$, the plus sign applies to $p$ and the minus sign to $q$.

The magnitudes of the stationary values of $p^\sigma$ and $q^\sigma$ are found by substituting $\eta = 0, \pi/2, \eta_0$ into Equations [6], with the following results

$$p^\sigma{}_{\eta=0,\,\delta>0} = -q^\sigma{}_{\eta=0,\,\delta<0} = K|\delta|[n - 2(1+\gamma^{-1})]$$

$$q^\sigma{}_{\eta=0,\,\delta>0} = -p^\sigma{}_{\eta=0,\,\delta<0} = K|\delta|[n(1-2\gamma^{-1}) + 2(1+\gamma^{-1})]$$

$$p^\sigma{}_{\eta=\pi/2,\,\delta>0} = -q^\sigma{}_{\eta=\pi/2,\,\delta<0} = K|\delta|[n - 2(1+\gamma)]$$

$$q^\sigma{}_{\eta=\pi/2,\,\delta>0} = -p^\sigma{}_{\eta=\pi/2,\,\delta<0} = K|\delta|[n(1-2\gamma) + 2(1+\gamma)]$$

$$p^\sigma{}_{\eta=\eta_0,\,\delta>0} = -q^\sigma{}_{\eta=\eta_0,\,\delta<0} = K|\delta|\left[n - \frac{2[(1+\gamma)^2 - n\gamma]}{(2-n^{1/2})\gamma n^{1/2}}\right]$$

$$q^\sigma{}_{\eta=\eta_0,\,\delta>0} = -p^\sigma{}_{\eta=\eta_0,\,\delta<0} = K|\delta|\left[n + \frac{2[(1+\gamma)^2 - n\gamma]}{(2+n^{1/2})\gamma n^{1/2}}\right]$$

where $|\delta|$ denotes the absolute value of $\delta$.

### Maximum Tension in Outer Region

Of special interest is the algebraically largest of the values of $p^\sigma$ given by the preceding formulas. This value, denoted by $p_{max}{}^\sigma$ is plotted in Fig. 2 for $\delta > 0$, and in Fig. 3 for $\delta < 0$, with $\nu' = \nu^\sigma = 0.3$. It is found that $p_{max}{}^\sigma$ is always a tension, whereas the other stationary values of $p^\sigma$ may be positive or negative. When Equation [7] is applicable, $p_{max}{}^\sigma$ occurs at $\eta = \eta_0$, otherwise it occurs at $\eta = 0$. The dashed curve in each of Figs. 2 and 3 is the locus of combinations of $b/a$ and $E'/E^\sigma$ for which $p_{max}{}^\sigma$ shifts from $\eta = 0$ to $\eta = \eta_0$. Below and to the left of the dashed curves, $p_{max}{}^\sigma$ occurs at $\eta = 0$; above and to the right of the dashed curves, $p_{max}{}^\sigma$ occurs at $\eta = \eta_0$. For $b/a = 0$, $p_{max}{}^\sigma$ occurs at $\eta = 0$ for all values of $E'/E^\sigma$.

For $\delta > 0$, the largest deviation of $\eta_0$ from zero is only about 0.03 radians and the largest deviation of $p_{max}{}^\sigma$ from $p^\sigma{}_{\eta=0,\,\delta>0}$ is less than 1 per cent. However, when $\delta < 0$, $p_{max}{}^\sigma$ may occur at any value of $\eta$, and may have values considerably larger (algebraically) than $p^\sigma{}_{\eta=0,\,\delta<0}$. In fact, when $\delta < 0$, both principal stresses at $\eta = 0$ may be compressive over a wide range of $b/a$ and $E'/E^\sigma$; but, in such cases, $p_{max}{}^\sigma$ occurs at $\eta = \eta_0$ and is tensile. This is contrary to the usual rule that the most dangerous stress occurs where the boundary has the sharpest curvature.

[8] Because of symmetry it is necessary to consider only one quadrant of the $x$, $y$-plane.

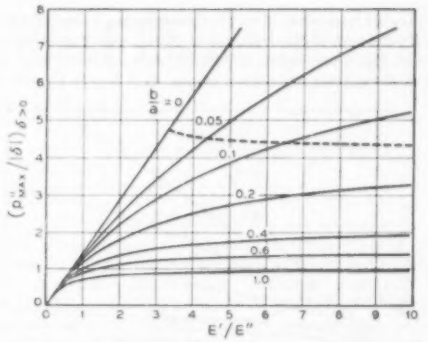


Fig. 2 Maximum Tension in Outer Medium at Interface When Inclusion Tends to Expand Less, or Contract More, Than Surrounding-Medium ($\delta > 0$)

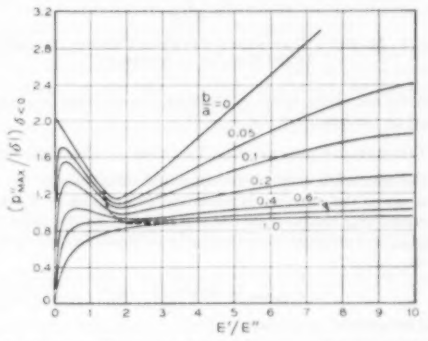


Fig. 3 Maximum Tension in Outer Medium at Interface When Inclusion Tends to Expand More, or Contract Less, Than Surrounding Medium ($\delta < 0$)

### Principal Stress Difference in Outer Region

The difference between the principal stresses is of interest as it is proportional to one of the simplest measurements that can be made with the photoelastic technique. Stationary values of $p^\sigma - q^\sigma$ on $\xi = \xi_0$ in Region 2 occur at $\eta = 0, \pi/2, \eta_1$, where

$$\cos 2\eta_1 = \frac{1}{1-\gamma^2}\left[1 + \gamma^2 - \frac{n\gamma^2(4-n)}{(1+\gamma)^2 - n\gamma}\right]$$

The magnitudes of the stationary values of $p^\sigma - q^\sigma$ are

$$(p^\sigma - q^\sigma)_{\eta=0} = 2K|\delta|\gamma^{-1}[n - 2(1+\gamma)]$$

$$(p^\sigma - q^\sigma)_{\eta=\pi/2} = 2K|\delta|\gamma[n - 2(1+\gamma^{-1})]$$

$$(p^\sigma - q^\sigma)_{\eta=\eta_1} = 4K|\delta|\gamma^{-1}[(1+\gamma)^2 - n\gamma][n(4-n)]^{-1/2}$$

The algebraically largest value of these quantities, denoted by $(p^\sigma - q^\sigma)_{max}$, is plotted in Fig. 4 for the case $\nu' = \nu^\sigma = 0.3$. Here, again, the dashed curve is the locus of combinations of the parameters $b/a$ and $E'/E^\sigma$ for which $(p^\sigma - q^\sigma)_{max}$ shifts from $\eta = 0$ to $\eta = \eta_1$. To the left and below the dashed curve, $(p^\sigma - q^\sigma)_{max}$ occurs at $\eta = 0$; to the right and above the dashed curve, $(p^\sigma - q^\sigma)_{max}$ occurs at $\eta = \eta_1$.

It should be noticed that, for corresponding values of $b/a$ and $E'/E''$, the sum of the ordinates in Figs. 2 and 3 gives the ordinate in Fig. 4 only when all three points fall below and to the left of the appropriate dashed curves, as it is only in such cases

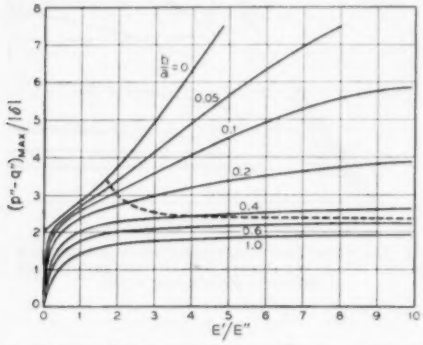


FIG. 4 MAXIMUM DIFFERENCE BETWEEN PRINCIPAL STRESSES IN OUTER MEDIUM AT INTERFACE

that the maximum values of the three stresses occur at the same point on the boundary (i.e., $\eta = 0$).

### TANGENTIAL COMPONENT OF TRACTION ACROSS INTERFACE

The maximum value of the tangential component of the traction across the interface between the two regions is of interest in considering the possibility of slip. This quantity, denoted by $(\bar{\tau}_{\xi\eta})_{max}$ and obtained from the fourth of Equations [5], is found to be

$$(\tau_{\xi\eta})_{max} = K\delta\gamma^{-1}(1-\gamma)^2 \quad \ldots\ldots\ldots\ldots\ldots\ldots [8]$$

and occurs at $\eta = \eta_2$ where

$$\cos 2\eta_2 = (1-\gamma^2)(1+\gamma^2)^{-1}$$

Equation [8] is plotted in Fig. 5 for $\nu' = \nu'' = 0.3$.

### STRESS IN INNER REGION

The state of stress in Region 1 is very simple. This may be recognized by transforming the first of Equations [3] to rectangular co-ordinates, obtaining

$$\chi' = A[2c^{-2}(x^2-y^2)-1] + 2Bc^{-2}(x^2+y^2)$$

It is readily seen that the stress is homogeneous throughout Region 1, the principal stresses being parallel to the principal axes

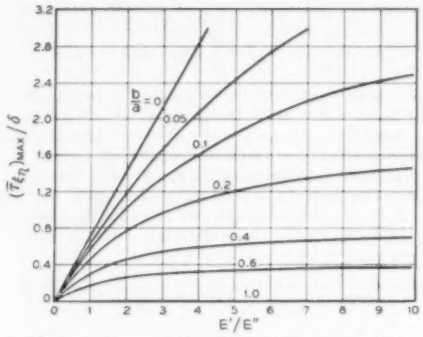


FIG. 5 MAXIMUM VALUE OF TANGENTIAL COMPONENT OF TRACTION ACROSS INTERFACE

of the ellipse. When $\delta > 0$, the algebraically larger principal stress is a tension of magnitude

$$p'_{\delta>0} = K|\delta|[n - 2(1+\gamma^{-1})] = p''_{\eta=0,\,\delta>0}$$

Hence for $\nu' = \nu'' = 0.3$, Fig. 2 gives $p'_{\delta>0}$ exactly to the left and below the dashed curve and to within 1 per cent over the remainder. When $\delta < 0$, the algebraically larger principal stress in Region 1 is a compression.

The principal stress difference throughout Region 1 is of course constant and equal to the maximum value of the tangential component of traction across the interface. Thus

$$p' - q' = 2(\tau_{\xi\eta})_{max}$$

where $(\tau_{\xi\eta})_{max}$ is given by Equation [8] and is plotted in Fig. 5 for $\nu' = \nu'' = 0.3$.

### AXIAL STRESS

The components of stress parallel to the axis of the cylinder are given by the last two of Equations [5]. The formula given for $\sigma_z'$ is valid throughout Region 1 and, as may be seen, $\sigma_z'$ is a constant. The formula given for $\sigma_z''$ pertains only to the boundary $\xi = \xi_0$. The stationary values of $\sigma_z''$ occur at $\eta = 0, \pi/2$, with magnitudes

$$(\sigma_z'')_{\eta=0} = 2\nu''K\delta n(1-\gamma^{-1})$$

$$(\sigma_z'')_{\eta=\pi/2} = 2\nu''K\delta n(1-\gamma)$$

Whereas, for the cylinder of circular cross section ($\gamma = 1$), $\sigma_z''$ is zero throughout, it may become very large at the ends of the major axis of an elongated elliptic cross section.

# Bending of an Elliptical Plate by Edge Loading

By W. A. NASH,[1] SOUTH BEND, IND.

**A series solution is presented for the problem of the small deflections of a thin elliptical plate with the following boundary conditions: (a) The edge of the plate is supported and is given a small prescribed deflection in a direction perpendicular to the middle plane of the plate. (b) The external load applied to the plate consists of a general distribution of bending moments acting around the edge of the plate. Since the loading consists of moments distributed around the edge of the plate, the general Lagrange differential equation for the middle surface of the plate reduces to the biharmonic equation. Elliptic coordinates are used and the problem reduces to finding a solution of the biharmonic equation, in elliptic co-ordinates, which satisfies the boundary conditions. Solutions to this equation are of two types: (a) harmonic functions, and (b) biharmonic functions which are not harmonic. Functions of type (a) are found by the method of separation of variables in Laplace's equation expressed in elliptic co-ordinates. Functions of type (b) are found by the use of complex variable theory.**

## Nomenclature

The following nomenclature is used in the paper:

$c$ = distance from center of ellipse to either focus

$D$ = flexural rigidity of plate = $\dfrac{Et^3}{12(1-\nu^2)}$

$E$ = Young's modulus

$\xi, \eta$ = elliptic co-ordinate directions

$M_x, M_y$ = bending moments, per unit length of middle surface of plate, in rectangular co-ordinates

$M_{xy}, M_{yx}$ = twisting moments, per unit length of middle surface of plate, in rectangular co-ordinates

$Q_x, Q_y$ = shearing forces, per unit length of middle surface of plate, parallel to the $z$-axis

$M_\xi, M_\eta$ = bending moments, per unit length of middle surface of plate, in elliptic co-ordinates

$M_{\xi\eta}, M_{\eta\xi}$ = twisting moments, per unit length of middle surface of plate, in elliptic co-ordinates

$Q_\xi, Q_\eta$ = shearing forces, per unit length of middle surface of plate, parallel to $z$-axis

$q$ = normal load per unit area acting on face of plate

$t$ = thickness of plate

$w$ = $z$-component of displacement of particle originally in middle plane of plate

$\nu$ = Poisson's ratio = 0.3

## Introduction

The solutions of only a few problems involving plates of elliptical or semielliptical contour are known. They are: (*a*) Uniformly loaded elliptical plate with a clamped edge (1);[2] (*b*) uniformly varying pressure acting on an elliptical plate clamped at the edge (2); (*c*) uniformly loaded elliptical plate with a simply supported edge (3); (*d*) uniformly loaded semielliptical plate simply supported along either the major or minor axis and clamped along the elliptical boundary (3); (*e*) edge loading acting on a hollow plate with confocal elliptical boundaries (4); and (*f*) concentrated load acting at any point on the straight line joining the foci of a clamped-edge elliptical plate (5).

Mushelisvili (6, 7), and Lechnitsky (8) have made use of complex variables in solving plate problems. This method has been applied to the problem of a linearly varying load acting on a nonisotropic elliptical plate with a clamped edge (9).

The theory developed here is subject to the following restrictions:

1 The plate is composed of a material which is elastically homogeneous and isotropic.

2 The material follows Hooke's law.

3 The deflection of the plate is small compared to the thickness.

4 The thickness of the plate is small compared to its lateral dimensions.

*Fundamental Equations.* The expressions in rectangular co-ordinates for bending and twisting moments, per unit length of the middle surface of the plate, are (1)

$$M_x = -D\left(\frac{\partial^2 w}{\partial x^2} + \nu\frac{\partial^2 w}{\partial y^2}\right) \quad [1]$$

$$M_y = -D\left(\frac{\partial^2 w}{\partial y^2} + \nu\frac{\partial^2 w}{\partial x^2}\right) \quad [2]$$

$$M_{xy} = -M_{yx} = D(1-\nu)\frac{\partial^2 w}{\partial x \partial y} \quad [3]$$

where $\nu$ is Poisson's ratio, and $D$ is the flexural rigidity of the plate. Here, $w$ denotes the $z$-component of displacement of a particle originally in the middle plane of the plate. The quantity $w$ is called the deflection of the plate.

The differential equation of the middle surface of the plate is (1)

$$\frac{\partial^4 w}{\partial x^4} + 2\frac{\partial^4 w}{\partial x^2 \partial y^2} + \frac{\partial^4 w}{\partial y^4} = \frac{q}{D} \quad [4]$$

or

$$\left(\frac{\partial^2}{\partial x^2} + \frac{\partial^2}{\partial y^2}\right)\left(\frac{\partial^2 w}{\partial x^2} + \frac{\partial^2 w}{\partial y^2}\right) = \frac{q}{D} \quad [5]$$

Here, $q$ is the normal load per unit area acting on the face of the plate. If $q$ is zero, Equation [4] is called the biharmonic equation. Solutions to this equation are known as biharmonic functions.

[1] Assistant Professor, Department of Engineering Mechanics, University of Notre Dame. Jun. ASME.

Contributed by the Applied Mechanics Division and presented at the Annual Meeting, New York, N. Y., November 27–December 2, 1949, of The American Society of Mechanical Engineers.

Discussion of this paper should be addressed to the Secretary, ASME, 29 West 39th Street, New York, N. Y., and will be accepted until October 10, 1950, for publication at a later date. Discussion received after the closing date will be returned.

Note: Statements and opinions advanced in papers are to be understood as individual expressions of their authors and not those of the Society. Paper No. 49—A-4.

[2] Numbers in parentheses refer to the Bibliography at the end of the paper.

Equation [5] may be written in the form

$$\nabla^4 w = \frac{q}{D} \quad \ldots\ldots [6]$$

where $\nabla^2$ is the Laplace operator

$$\nabla^2 = \frac{\partial^2}{\partial x^2} + \frac{\partial^2}{\partial y^2}$$

## Elliptic Co-Ordinates

The problem to be treated in this paper is that of a plate of elliptical contour. Hence elliptic co-ordinates will be used. The equations relating rectangular Cartesian co-ordinates $(x, y)$ to elliptic co-ordinates $(\xi, \eta)$ are

$$\left.\begin{aligned} x &= c \cosh \xi \cos \eta \\ y &= c \sinh \xi \sin \eta \end{aligned}\right\} \quad \ldots\ldots [7]$$

Elimination of $\eta$ between Equations [7] yields

$$\frac{x^2}{c^2 \cosh^2 \xi} + \frac{y^2}{c^2 \sinh^2 \xi} = 1 \quad \ldots\ldots [8]$$

From Equation [8] it follows that the family of curves $\xi$ = const are confocal ellipses, the distance between the foci being $2c$.

Elimination of $\xi$ between Equations [7] yields

$$\frac{x^2}{c^2 \cos^2 \eta} - \frac{y^2}{c^2 \sin^2 \eta} = 1 \quad \ldots\ldots [9]$$

From Equation [9] it follows that the family of curves $\eta$ = const are confocal hyperbolas, the distance between the foci being $2c$. This family of hyperbolas is orthogonal to the family of ellipses. The two orthogonal families of curves are shown in Fig. 1. They are the parametric lines of the elliptic co-ordinates $\xi$, $\eta$.

*Some Transformations.* By means of Equations [7], the Laplacian operator may be expressed in terms of elliptic co-ordinates. It is

$$\nabla^2 = \frac{2}{c^2(\cosh 2\xi - \cos 2\eta)} \left( \frac{\partial^2}{\partial \xi^2} + \frac{\partial^2}{\partial \eta^2} \right) \quad \ldots\ldots [10]$$

Thus the differential equation of the middle surface of the plate, expressed in elliptic co-ordinates, is

$$\left[ \frac{2}{c^2(\cosh 2\xi - \cos 2\eta)} \left( \frac{\partial^2}{\partial \xi^2} + \frac{\partial^2}{\partial \eta^2} \right) \right]^2 w = \frac{q}{D} \quad \ldots [11]$$

The solution of the problem of the bending of a plate of elliptical contour, when a resultant normal load $q$ per unit area acts on the faces of the plate and the edges are loaded by bending moments, twisting moments, and shearing forces, thus reduces to the integration of Equation [11], subject to certain boundary conditions.

*Expressions for Bending and Twisting Moments in Elliptic Co-Ordinates.* In the elliptic co-ordinate system, the bending moments, per unit length of the middle surface of the plate, are denoted by $M_\xi$ and $M_\eta$, and the twisting moments, per unit length of the middle surface, by $M_{\xi\eta}$ and $M_{\eta\xi}$. The shearing forces, also per unit length of the middle surface, parallel to the $z$-axis are denoted by $Q_\xi$ and $Q_\eta$. The positive directions of each of these quantities is represented by a vector in Fig. 2.

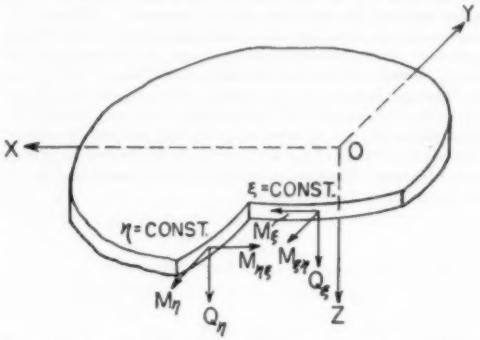


Fig. 2 Bending Moments, Twisting Moments, and Shearing Forces in Elliptic Co-Ordinate System

The expressions for the various partial derivatives of $w$ with respect to $x$ and $y$ may be obtained from Equations [7]. If these values are substituted in Equations [1], [2], and [3], the following expressions are obtained

$$M_\xi = -\frac{2D}{c^2(\cosh 2\xi - \cos 2\eta)} \left[ \frac{\partial^2 w}{\partial \xi^2} + \nu \cdot \frac{\partial^2 w}{\partial \eta^2} - \frac{(1-\nu)\sinh 2\xi}{(\cosh 2\xi - \cos 2\eta)} \cdot \frac{\partial w}{\partial \xi} + \frac{(1-\nu)\sin 2\eta}{(\cosh 2\xi - \cos 2\eta)} \cdot \frac{\partial w}{\partial \eta} \right] \quad [12]$$

$$M_\eta = -\frac{2D}{c^2(\cosh 2\xi - \cos 2\eta)} \left[ \nu \cdot \frac{\partial^2 w}{\partial \xi^2} + \frac{\partial^2 w}{\partial \eta^2} + \frac{(1-\nu)\sinh 2\xi}{(\cosh 2\xi - \cos 2\eta)} \cdot \frac{\partial w}{\partial \xi} - \frac{(1-\nu)\sin 2\eta}{(\cosh 2\xi - \cos 2\eta)} \cdot \frac{\partial w}{\partial \eta} \right] \quad [13]$$

$$M_{\xi\eta} = -M_{\eta\xi} = \frac{D(1-\nu)}{c^2(\cosh 2\xi - \cos 2\eta)^2} \left[ \frac{\partial w}{\partial \xi} \cdot \sin 2\eta + \frac{\partial w}{\partial \eta} \cdot \sinh 2\xi - \frac{\partial^2 w}{\partial \xi \partial \eta} (\cosh 2\xi - \cos 2\eta) \right] \quad [14]$$

*Singular Points in Elliptic Co-Ordinate System.* The locus of the points $\xi = 0$ is that part of the major axis between the foci of the ellipse. Any point on this portion of the major axis may be represented either by the elliptic co-ordinates $(0, \phi)$ or $(0, -\phi)$, where $0 \leqslant \phi \leqslant \pi$. Hence each of these points is a singular point of the elliptic co-ordinate system, and the locus of the points $\xi = 0$ is a line of singular points.

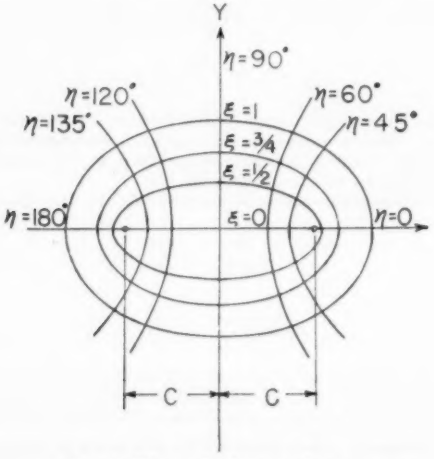


Fig. 1 Elliptic Co-Ordinate System

It is necessary that the conditions of continuity of deflection and gradient prevail across the line of singular points of the plate.

Let $w$ be any function of $\xi$, $\eta$. Then, if $w$ is to be continuous at the line of singular points, the following condition must hold:

$$\lim_{\substack{\epsilon_1 \to 0+ \\ \epsilon_2 \to 0}} w(\epsilon_1, \phi + \epsilon_2) = \lim_{\substack{\epsilon_3 \to 0+ \\ \epsilon_4 \to 0}} w(\epsilon_3, -\phi + \epsilon_4), \quad (0 \leq \phi \leq \pi) \quad [15]$$

Similarly, if $w$ is to have a continuous directional derivative at the line of singular points, two more relations must be true. They are as follows

$$\lim_{\substack{\epsilon_1 \to 0+ \\ \epsilon_2 \to 0}} \frac{\partial w}{\partial \xi}(\epsilon_1, \phi + \epsilon_2) = -\lim_{\substack{\epsilon_3 \to 0+ \\ \epsilon_4 \to 0}} \frac{\partial w}{\partial \xi}(\epsilon_3, -\phi + \epsilon_4) \quad [16]$$

$$\lim_{\substack{\epsilon_1 \to 0+ \\ \epsilon_2 \to 0}} \frac{\partial w}{\partial \eta}(\epsilon_1, \phi + \epsilon_2) = -\lim_{\substack{\epsilon_3 \to 0+ \\ \epsilon_4 \to 0}} \frac{\partial w}{\partial \eta}(\epsilon_3, -\phi + \epsilon_4) \quad [17]$$

There are similar relations involving the higher derivatives. They will have the same form as Equations [16] and [17] except that the minus sign on the right will be present only in those relations involving derivatives of odd order. Equations [15], [16], and [17] will henceforth be referred to as the "continuity conditions."

## The Biharmonic Equation

The differential equation of the middle surface of a plate has already been found in elliptic co-ordinates for the case when a resultant normal load $q$ per unit area acts on the faces of the plate, and the edges are loaded by bending moments, twisting moments, and shearing forces. This is Equation [11].

If the external forces acting on the plate are applied only to the edges, the faces being free, then $q = 0$ and the foregoing equation reduces to

$$\left[\frac{1}{(\cosh 2\xi - \cos 2\eta)}\left(\frac{\partial^2}{\partial \xi^2} + \frac{\partial^2}{\partial \eta^2}\right)\right]^2 w = 0 \quad [18]$$

This is the biharmonic equation expressed in elliptic co-ordinates. Biharmonic functions $w(\xi, \eta)$ that satisfy this equation are of two general types as follows:

1 Those which are harmonic, i.e., they satisfy Laplace's equation $\nabla^2 w = 0$.

2 Those which are biharmonic, but are not harmonic.

*Harmonic Functions in Elliptic Co-Ordinates.* Functions of type 1 are readily found from Laplace's equation by the method of separation of variables. This procedure leads to the harmonic functions

$$\left.\begin{array}{c} 1,\ \xi,\ \eta, \\ \left.\begin{array}{l} \sinh n\xi \sin n\eta,\ \sinh n\xi \cos n\eta \\ \cosh n\xi \sin n\eta,\ \cosh n\xi \cos n\eta \end{array}\right] n = 1, 2, \cdots \end{array}\right\} \quad [19]$$

*Biharmonic Functions Which Are Not Harmonic in Elliptic Co-Ordinates.* Functions of the type sought here can be obtained by the use of complex variables. Any biharmonic function can be expressed in the form $xu_1 + u_2$, where $u_1$ and $u_2$ are harmonic functions of the rectangular Cartesian co-ordinates[3] $x$, $y$. Let $z$ denote the complex variable defined by the relation $z = x + iy$, and let $\bar{z}$ be the complex conjugate, $\bar{z} = x - iy$. The function $z^n$ is analytic for all positive integral values of $n$. It is necessary to consider only those integral values of $n$ greater than 1. Thus the real and imaginary parts of

$$z\bar{z}^{n-1}, \quad n = 2, 3, \cdots, \quad [20]$$

are biharmonic. Equation [20] may be written in the form

$$\tfrac{1}{2}(z + \bar{z})\bar{z}^{n-1} \quad [21]$$

Since the objective here is to find biharmonic functions which are not harmonic, the harmonic term $(^1/_2)\bar{z}^n$ in Equation [21] can be discarded. We shall then investigate the biharmonic functions $\psi_n$ and $\chi_n$ defined by the relation

$$\phi_n = \psi_n + i\chi_n = z\bar{z}^{n-1} \quad [22]$$

The relation [7] between rectangular and elliptic co-ordinates may be written in the form

$$z = c\cosh(\xi + i\eta) \quad [23]$$

Let $\alpha = e^{\xi}$, $\beta = e^{i\eta}$. Then Equation [23] becomes

$$z = \frac{c}{2}\left(\alpha\beta + \frac{1}{\alpha\beta}\right) \quad [24]$$

Thus Equation [22] becomes

$$\phi_n = \frac{c^n}{2^n\alpha^n}\sum_{r=0}^{n-1} {}_{n-1}C_r\alpha^{2r}[\alpha^2\beta^{2r-n} + \beta^{2r-n+2}] \quad [25]$$

The function $\phi_n$ can also be expressed as a Fourier series[4] in the form

$$\phi_n = \sum_{p=-\infty}^{\infty} c_{np}\beta^p \quad [26]$$

where $c_{np}$ are the Fourier coefficients given by the relation

$$c_{np} = \frac{1}{2\pi}\int_0^{2\pi} \phi_n e^{-ip\eta}\, d\eta \quad [27]$$

Let $\gamma$ denote the unit circle with center at the origin of the co-ordinate system. Since $\beta = e^{i\eta}$, then Equation [27] may be written in the form

$$c_{np} = \frac{1}{2\pi i}\int_\gamma \phi_n \frac{d\beta}{\beta^{p+1}} \quad [28]$$

The integral in Equation [27] is thus transformed into a contour integral around a unit circle in a complex plane.

In general, we have

$$\int_\gamma \frac{d\beta}{\beta^m} = \begin{bmatrix} 0 & \text{if} \quad m \neq 1 \\ 2\pi i & \text{if} \quad m = 1 \end{bmatrix} \quad [29]$$

The value of $\phi_n$ as given by Equation [25] may now be substituted in Equation [28], and this integral evaluated by the use of Equation [29]. With the values of the Fourier coefficients known, $\phi_n$ is now given by Equation [26]. By equating the coefficients of the real parts of Equations [22] and [26] we are lead to the sequence of biharmonic functions

$$\cosh(n+2)\xi\cos n\eta + \cosh n\xi\cos(n+2)\eta,\ n = 0, 1, 2\cdots, \quad [30]$$

In an analogous manner, by considering the function $\chi_n$, which is the coefficient of the imaginary part of the function $\phi_n$ given by Equation [26], we get the sequence of biharmonic functions

$$\sinh(n+2)\xi\sin n\eta + \sinh n\xi\sin(n+2)\eta,\ n = 1, 2\cdots, \quad [31]$$

## A Particular Problem in the Bending of Elliptical Plates

Let us consider the small deflections of a thin elliptical plate with the following boundary conditions:

[3] Bibliography reference (2), p. 492.

[4] Bibliography reference (7), p. 34.

1 The edge of the plate is supported and is given a small prescribed deflection in a direction perpendicular to the middle plane of the plate.

2 The external load applied to the plate consists only of a general distribution of bending moments acting around the edge of the plate.

The deflection $w(\xi, \eta)$ in addition to satisfying the boundary conditions, must be biharmonic and analytic. Let us assume for $w$ a general linear combination of the biharmonic functions which satisfy the conditions of continuity of deflection and gradient at the line of singular points. Thus let us take

$$\left.\begin{aligned} w = &\sum_{n=2}^{\infty} A_n \cosh n\xi \cos n\eta + \sum_{n=3}^{\infty} B_n \sinh n\xi \sin n\eta \\ &+ \sum_{n=0}^{\infty} C_n[\cosh (n+2)\xi \cos n\eta + \cosh n\xi \cos (n+2)\eta] \\ &+ \sum_{n=1}^{\infty} D_n[\sinh (n+2)\xi \sin n\eta + \sinh n\xi \sin (n+2)\eta] \end{aligned}\right\} \quad . . [32]$$

where $A_n$, $B_n$, $C_n$, and $D_n$ are constants to be determined from the boundary conditions.

(*a*) *First Boundary Condition.* Let the edge of the plate be denoted by $\xi = \xi_0$. The prescribed deflection of any point on the neutral axis of the edge of the plate may be represented by the Fourier series

$$[w]_{\xi=\xi_0} = \frac{a_0}{2} + \sum_{n=1}^{\infty} (a_n \cos n\eta + b_n \sin n\eta) . . . . . [33]$$

where $a_0$, $a_n$, and $b_n$ are known Fourier coefficients. This boundary condition may be applied to the value of $w$ given by Equation [32] to yield an identity in $\eta$. Coefficients of corresponding sine and cosine terms in this identity are then equated to give one infinite set of equations containing the $A_n$, $C_n$, and another infinite set of equations containing the $B_n$, $D_n$.

(*b*) *Second Boundary Condition.* The expression for the bending moment $M_\xi$ at any point in an elliptical plate is given by Equation [12]. Let $M$ denote this applied moment at the edge $\xi = \xi_0$. Thus we have

$$\begin{aligned} -\frac{Mc^2(\cosh 2\xi_0 - \cos 2\eta)^2}{2D} = &\left\{ (\cosh 2\xi_0 - \cos 2\eta) \left[\frac{\partial^2 w}{\partial \xi^2}\right]_{\xi=\xi_0} \right. \\ &+ \nu(\cosh 2\xi_0 - \cos 2\eta) \left[\frac{\partial^2 w}{\partial \eta^2}\right]_{\xi=\xi_0} - (1-\nu) \sinh 2\xi_0 \left[\frac{\partial w}{\partial \xi}\right]_{\xi=\xi_0} \\ &\left. + (1-\nu) \sin 2\eta \left[\frac{\partial w}{\partial \eta}\right]_{\xi=\xi_0} \right\} . . . . [34] \end{aligned}$$

Also, $M$ may be expanded in a Fourier series of the form

$$-\frac{Mc^2(\cosh 2\xi_0 - \cos 2\eta)^2}{2D} = \frac{c_0}{2} + \sum_{n=1}^{\infty} (c_n \cos n\eta + d_n \sin n\eta) . . . . . [35]$$

where $c_0$, $c_n$, and $d_n$ are known Fourier coefficients. Again, using the value of $w$ given by Equation [32], coefficients of corresponding sine and cosine terms in the right sides of Equations [34] and [35] may be equated to yield one infinite set of equations containing the $A_n$, $C_n$, and another infinite set of equations containing the $B_n$, $D_n$.

*Determination of Coefficients in the Assumed Series.* The four sets of equations resulting from the boundary conditions may be grouped in the following manner

$$\left.\begin{aligned} C_0 T_{12}' &= a_0/2 \\ C_1 T_{13}' &= a_1 \\ A_2 T_{12}' + C_0 T_{10}' + C_2 T_{14}' &= a_2 \\ A_2 P_{20} + C_0 P_{02} + C_2 P_{70} &= c_0/2 \\ A_3 T_{13}' + C_1 T_{11}' + C_3 T_{15}' &= a_3 \\ A_3 P_{21} + C_1 P_{01} + C_3 P_{71} &= c_1 \\ A_4 T_{14}' + C_2 T_{12}' + C_4 T_{16}' &= a_4 \\ A_4 P_{22} + C_2 P_{02} + C_4 P_{72} + A_2 P_{22} + C_0 P_{52} &= c_2 \\ A_5 T_{15}' + C_3 T_{13}' + C_5 T_{17}' &= a_5 \\ A_5 P_{23} + C_3 P_{03} + C_5 P_{73} + A_3 P_{23} + C_1 P_{53} &= c_3 \\ A_{n+2} T_{1,n+2}' + C_n T_{1n}' + C_{n+2} T_{1,n+4}' &= a_{n+2} \\ A_{n-2} P_{1n} + A_n P_{2n} + A_{n+2} P_{0n} + C_{n-4} P_{4n} + C_{n-2} P_{1n} & \\ + C_n P_{0n} + C_{n+2} P_{7n} &= c_n \end{aligned}\right\} n = 4, 5, \cdots \quad . . [36]$$

$$\left.\begin{aligned} D_1 S_{13}' &= b_1 \\ D_2 S_{14}' &= b_2 \\ B_2 S_{12}' + D_1 S_{11}' + D_3 S_{15}' &= b_3 \\ B_2 Q_{21} + D_1 Q_{01} + D_3 Q_{71} &= d_1 \\ B_4 S_{14}' + D_2 S_{12}' + D_4 S_{16}' &= b_4 \\ B_4 Q_{22} + D_2 Q_{02} + D_4 Q_{72} &= d_2 \\ B_5 S_{15}' + D_3 S_{13}' + D_5 S_{17}' &= b_5 \\ B_5 Q_{23} + D_3 Q_{03} + D_5 Q_{73} + B_3 Q_{23} + D_1 Q_{53} &= d_3 \\ B_6 S_{16}' + D_4 S_{14}' + D_6 S_{18}' &= b_6 \\ B_6 Q_{24} + D_4 Q_{04} + D_6 Q_{74} + B_4 Q_{24} + D_2 Q_{54} &= d_4 \\ B_{n+2} S_{1,n+2}' + D_n S_{1n}' + D_{n+2} S_{1',n+4}' &= b_{n+2} \\ B_{n-2} Q_{1n} + B_n Q_{2n} + B_{n+2} Q_{0n} + D_{n-4} Q_{4n} + D_{n-2} Q_{5n} & \\ + D_n Q_{6n} + D_{n+2} Q_{7n} &= d_n \end{aligned}\right\} n = 5, 6, \cdots \quad . . [37]$$

where $P_{mn}$, $Q_{mn}$ are known constants give by the relations

$$
\begin{aligned}
P_{30} &= -R_3T_{12} + R_4T_{13} + R_5T_{14} \\
P_{50} &= R_1S_{12} - R_3T_{32} + R_3T_{34} + R_5T_{32} \\
P_{70} &= -R_3T_{32} + R_4T_{44} + R_5T_{43} \\
P_{31} &= -R_3T_{13} + R_4T_{23} + R_5T_{24} \\
P_{51} &= R_1S_{13} - R_3T_{33} + R_2T_{43} + R_4T_{41} + R_5T_{31} + R_5T_{43} \\
&\qquad + R_4T_{23} - R_3T_{21} + R_5T_{42} \\
P_{71} &= -R_3T_{23} + R_4T_{43} + R_5T_{42} \\
P_{32} &= R_1S_{13} + R_3T_{42} + R_5T_{43} \\
P_{52} &= -R_3T_{14} + R_4T_{44} + R_5T_{44} \\
P_{72} &= R_4T_{43} + R_5T_{52} \\
P_{33} &= R_1S_{14} - R_3T_{34} + R_3T_{44} + R_4T_{42} + R_5T_{42} + R_5T_{34} \\
P_{73} &= -R_3T_{24} + R_4T_{45} + R_5T_{44} \\
P_{13} &= R_2T_{11} + R_4T_{41} + R_5T_{41} \\
P_{23} &= R_1S_{12} + R_3T_{41} + R_5T_{42} \\
P_{33} &= -R_3T_{15} + R_4T_{45} + R_5T_{45} \\
P_{53} &= R_1S_{11} + R_3T_{21} + R_3T_{41} + R_4T_{42} + R_5T_{23} + R_5T_{41} \\
P_{63} &= R_1S_{14} - R_3T_{35} + R_3T_{45} + R_4T_{43} + R_4T_{43} + R_5T_{45} \\
P_{73} &= -R_3T_{25} + R_4T_{47} + R_5T_{43} \\
P_{1n} &= R_2T_{1,n-2} + R_4T_{4,n-2} + R_5T_{4,n-2} \\
P_{2n} &= R_1S_{1n} + R_3T_{4n} + R_5T_{4n} \\
P_{3n} &= -R_2T_{1,n+2} + R_4T_{4,n+2} + R_5T_{4,n+2} \\
P_{4n} &= R_4T_{4,n-4} + R_5T_{5,n-2} + R_5T_{5,n-2} \\
P_{5n} &= R_1S_{1,n-2} + R_2T_{2,n-2} + R_3T_{4,n-2} + R_4T_{4n} \\
&\qquad + R_4T_{5n} + R_5T_{5,n-2} \\
P_{6n} &= R_1S_{1,n+2} - R_2T_{3,n+2} + R_3T_{4,n+2} + R_4T_{6n} \\
&\qquad + R_5T_{6n} + R_5T_{5,n+2} \\
P_{7n} &= -R_3T_{2,n+2} + R_4T_{5,n+4} + R_5T_{6,n+2}
\end{aligned}
\Bigg\} \ldots [38]
$$

$n = 4, 5 \cdots$

$$
\begin{aligned}
Q_{21} &= -R_2S_{13} + R_4S_{23} + R_5S_{23} \\
Q_{41} &= R_1T_{12} + R_2S_{21} - R_2S_{32} + R_2S_{43} - R_4S_{43} + R_4S_{31} \\
&\qquad + R_4S_{23} - R_5S_{31} + R_5S_{32} \\
Q_{71} &= -R_2S_{23} + R_4S_{45} + R_5S_{43} \\
Q_{22} &= R_1T_{13} + R_2S_{42} + R_5S_{42} \\
Q_{42} &= -R_2S_{14} + R_4S_{44} + R_5S_{44} \\
Q_{62} &= R_1T_{14} - R_2S_{34} + R_2S_{44} + R_4S_{42} + R_5S_{42} + R_5S_{44} \\
Q_{72} &= -R_2S_{24} + R_4S_{46} + R_5S_{44} \\
Q_{12} &= R_2S_{11} + R_4S_{41} + R_5S_{41} \\
Q_{32} &= R_1T_{13} + R_2S_{42} + R_4S_{42} \\
Q_{52} &= -R_2S_{15} + R_4S_{45} + R_5S_{45} \\
Q_{82} &= R_1T_{11} + R_2S_{21} + R_2S_{41} + R_4S_{43} + R_4S_{43} + R_5S_{43} \\
Q_{62} &= R_1T_{15} - R_2S_{35} + R_2S_{45} + R_4S_{43} + R_4S_{43} + R_5S_{45} \\
Q_{72} &= -R_2S_{25} + R_4S_{47} + R_5S_{45} \\
Q_{14} &= R_2S_{12} + R_4S_{42} + R_5S_{42} \\
Q_{34} &= R_1T_{14} + R_2S_{44} + R_4S_{44} \\
Q_{54} &= -R_2S_{16} + R_4S_{46} + R_5S_{46} \\
Q_{84} &= R_1T_{12} + R_2S_{22} + R_2S_{42} + R_4S_{44} + R_4S_{44} + R_5S_{42} \\
Q_{64} &= R_1T_{16} - R_2S_{36} + R_2S_{46} + R_4S_{44} + R_4S_{44} + R_5S_{46} \\
Q_{74} &= -R_2S_{26} + R_4S_{48} + R_5S_{46} \\
Q_{1n} &= R_2S_{1,n-2} + R_4S_{4,n-2} + R_5S_{4,n-2} \\
Q_{2n} &= R_1T_{1n} + R_2S_{4n} + R_4S_{4n} \\
Q_{3n} &= -R_2S_{1,n+2} + R_4S_{4,n+2} + R_5S_{4,n+2} \\
Q_{4n} &= R_4S_{4,n-4} + R_5S_{5,n-2} + R_5S_{5,n-2} \\
Q_{5n} &= R_1T_{1,n-2} + R_2S_{2,n-2} + R_3S_{4,n-2} + R_4S_{4n} + R_4S_{5n} \\
&\qquad + R_5S_{5,n-2} \\
Q_{6n} &= R_1T_{1,n+2} - R_2S_{3,n+2} + R_3S_{4,n+2} + R_4S_{6n} + R_4S_{5n} \\
&\qquad + R_5S_{5,n+2} \\
Q_{7n} &= -R_2S_{2,n+2} + R_4S_{5,n+4} + R_5S_{6,n+2}
\end{aligned}
\Bigg\} \ldots [39]
$$

the constants $R_m$, $S_{mn}$, and $T_{mn}$ being given by the relations

$$\left.\begin{aligned} R_1 &= -(1-\nu)\sinh 2\xi_0 \\ R_2 &= \frac{1}{2}(1-\nu) \\ R_3 &= \cosh 2\xi_0 \\ R_4 &= -\frac{1}{2} \\ R_5 &= -\nu\cosh 2\xi_0 \\ R_6 &= \frac{\nu}{2} \end{aligned}\right\} \quad \ldots\ldots\ldots\ldots [40]$$

$$\left.\begin{aligned} S_{1n} &= n\sinh n\xi_0 \\ S_{2n} &= n\sinh (n+2)\xi_0 \\ S_{3n} &= n\sinh (n-2)\xi_0 \\ S_{4n} &= n^2\sinh n\xi_0 \\ S_{5n} &= n^2\sinh (n-2)\xi_0 \\ S_{6n} &= n^2\sinh (n+2)\xi_0 \end{aligned}\right\} \quad \ldots\ldots\ldots\ldots [41]$$

$$\left.\begin{aligned} T_{1n} &= n\cosh n\xi_0 \\ T_{2n} &= n\cosh (n+2)\xi_0 \\ T_{3n} &= n\cosh (n-2)\xi_0 \\ T_{4n} &= n^2\cosh n\xi_0 \\ T_{5n} &= n^2\cosh (n-2)\xi_0 \\ T_{6n} &= n^2\cosh (n+2)\xi_0 \end{aligned}\right\} \quad \ldots\ldots\ldots\ldots [42]$$

Also

$$\left.\begin{aligned} S_{1n}' &= \sinh n\xi_0 \\ T_{1n}' &= \cosh n\xi_0 \end{aligned}\right\} \quad \ldots\ldots\ldots\ldots [43]$$

Equations [36] are an infinite set of equations for the infinite set of unknowns $A_n$, $C_n$. Equations [37] are an infinite set of equations for the infinite set of unknowns $B_n$, $D_n$. In these equations the quantities $a_m$, $b_m$, $c_m$, and $d_m$ are known Fourier coefficients of the prescribed edge deflection and edge bending moment. Thus Equations [36] and [37] may readily be solved for the coefficients of the terms appearing in Equation [32].

*Convergence of the Solution.* The series given by Equation [32] converge absolutely and uniformly in both variables throughout the entire plate, including the boundary.

## A Numerical Example

*Statement of Problem.* Let us consider the following special case of the problem just discussed. The boundary conditions are:

(*a*) The edge of the plate is supported and does not deflect in the direction perpendicular to the middle plane of the plate.

(*b*) The external load applied to the plate consists of a uniform distribution of bending moments acting around the edge of the plate.

Let the boundary of the plate be given by the parameter $\xi_0 = {}^1/_2$. For this case, the ratio of the length of the major axis to the length of the minor axis of the plate is 2.16465 to five decimal places. Also, let us take Poisson's ratio $\nu = 0.3$.

*Numerical Results.* The deflection $w$ of the plate is given by Equation [32] in which $A_n$, $B_n$, $C_n$, and $D_n$ are constants to be determined from Equations [36] and [37]. In these equations the constant coefficients $P_{mn}$, $Q_{mn}$ are defined by Equations [38] and [39] in terms of the known constants $R_m$, $S_{mn}$, and $T_{mn}$ defined by Equations [40], [41], and [42].

The first step is to determine the Fourier coefficients which are defined by Equations [33] and [35].

The next step is to determine the constants $R_m$. After that the values of the quantities $S_{mn}$ and $T_{mn}$ may be computed. With these values known, the quantities $P_{mn}$ and $Q_{mn}$ may be computed.

From these results the equation of the middle surface of the elliptical plate is found to be

$$\left.\begin{aligned} w = \frac{Mc^2}{D}\,[&+ 0.08084\cosh 2\xi\cos 2\eta \\ &+ 0.00341\cosh 4\xi\cos 4\eta + 0.00027\cosh 6\xi\cos 6\eta \\ &+ 0.00010\cosh 8\xi\cos 8\eta - 0.10396(\cosh 2\xi + \cos 2\eta) \\ &- 0.00553(\cosh 4\xi\cos 2\eta + \cosh 2\xi\cos 4\eta) \\ &- 0.00043(\cosh 6\xi\cos 4\eta + \cosh 4\xi\cos 6\eta) \\ &- 0.00004(\cosh 8\xi\cos 6\eta + \cosh 6\xi\cos 8\eta) \\ &- 0.00003(\cosh 10\xi\cos 8\eta + \cosh 8\xi\cos 10\eta) + \ldots] \end{aligned}\right\} \quad \ldots [44]$$

From Equation [44] the maximum deflection at the center of the plate is found to be

$$w_{max} = 0.552\,\frac{Ma^2}{Et^3} \quad \ldots\ldots\ldots\ldots [45]$$

where $a$ is the semimajor axis of the ellipse. The addition of the terms having coefficients $A_3$ and $C_3$ changes the value of the maximum deflection by only 0.12 per cent, which indicates that the nine terms on the right side of Equation [44] represent $w$ with sufficient accuracy for all practical purposes.

The value of the bending moment $M_\xi$ at any point in the plate is given by Equation [12]. The maximum value of this moment will occur at a point on the minor axis of the plate, since the maximum curvature of the middle surface along that axis is greater than the maximum along the major axis. The variation of this moment along the minor axis of the elliptical plate is shown in Fig. 3, where $M$ is the prescribed bending moment per unit length applied along the edge of the plate. The addition of the terms having coefficients $A_3$ and $C_3$ changes the value of the ratio $M_\xi/M$ by at most 5 per cent.

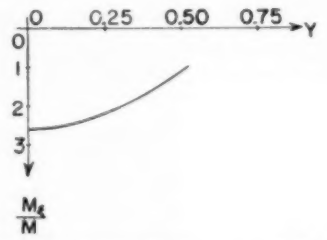


Fig. 3 Variation of Bending Moment $M_\xi$ Along Minor Axis of Plate

## BIBLIOGRAPHY

1 "Theory of Plates and Shells," by S. P. Timoshenko, McGraw-Hill Book Company, Inc., New York, N. Y., 1940, p. 88.

2 "Mathematical Theory of Elasticity," by A. E. H. Love, fourth edition, Dover Publications, New York, N. Y., 1944, p. 485.

3 "Adaptation of Curvilinear Isothermal Coordinates to Integrate the Equations of Equilibrium of Elastic Plates," by B. G. Galerkin, *Messenger of Mathematics*, vol. 52, 1923, p. 99.

4 "Die Airysche Funktion für den Ellipsenring," by A. Timpe, *Mathematische Zeitschrift*, Berlin, Germany, vol. 17, 1923, p. 189.

5 "On the Bending of an Elliptical Plate Under Certain Distribution of Load," by H. M. Sengupta, Bulletin of the Calcutta Mathematical Society, vol. 40, 1948, p. 17.

6 N. I. Mushelisvili, Bulletin Academie de l' URSS, 1919, pp. 663–668.

7 "Mathematical Theory of Elasticity," by I. S. Sokolnikoff, mimeographed lecture notes, Brown University, Providence, R. I., 1941, p. 244.

8 S. G. Lechnitsky, *Applied Mathematics and Mechanics*, Leningrad, USSR, vol. 2, 1939, p. 181.

9 "On the Deflection of Anisotropic Thin Plates," by V. Morkovin, *Quarterly of Applied Mathematics*, vol. 1, 1943, p. 116.

# Torsion of Noncylindrical Shafts of Circular Cross Section

By H. J. REISSNER[1] and G. J. WENNAGEL[2]

**The theory of torsion of noncylindrical bodies of revolution, initiated by J. H. Michell[3] and A. Föppl,[4] is stated by a basic differential equation of the circumferential displacement and by a boundary condition of the shear stress along the generator surface. The solution of these two equations by the "direct" method of first assuming the boundary shape has not lent itself to closed solutions in terms of elementary functions, so that only approximation, infinite series, and experimental methods have been applied. A semi-inverse method analogous to Saint Venant's semi-inverse method for cylindrical bodies has the disadvantage of the restriction to special boundary shapes but the advantage of exact solutions by means of elementary functions. By this method, bodies of conical, ellipsoidal, and hyperbolic boundary shapes have been obtained in a simple analysis. One class of integrals leading to other boundary shapes seems not to have been analyzed up to now, namely, the integrals in the form of a product of two functions of, respectively, axial ($z$) and radial ($r$) co-ordinates. A first suggestion of this possibility was given in Love's treatise on the mathematical theory of elasticity.[5] In the present paper, the classes of boundary shapes, displacements, and stress distributions are investigated analytically and numerically. The extent of the numerical investigation contains only the results of single-term integrals for full and hollow cross sections of technical interest. The detailed analysis of the boundary shapes, following from series integrals, presents essential mathematical obstacles. Overcoming these difficulties might lead to a multitude of solutions of interesting boundary shapes, and stress and strain distribution.**

## Nomenclature

The following nomenclature is used in the paper:

$r$ = radial co-ordinate
$\theta$ = angular co-ordinate
$z$ = axial co-ordinate
$\sigma$ = normal stress
$\tau$ = shear stress
$\epsilon$ = extensional strain
$\gamma$ = shear strain
$\omega = \omega(r, z)$ = angular displacement
$u$ = radial displacement
$v$ = circumferential displacement
$w$ = axial displacement
$G$ = shear modulus
$M$ = twisting moment (torque)
$J_p(x)$ = Bessel function of first kind
$N_p(x)$ = Bessel function of second kind
$1/q$ = a reference length

## Displacements

"Pure torsion" for shafts of varying circular cross section, as introduced by J. H. Michell[3] and A. Föppl,[4] is defined by the condition that there are no surface tractions on the generator (mantle) surface, and by the following consistent state of displacement

$$u = 0, \quad w = 0, \quad v = r\omega(r, z) \qquad [1]$$

## Strains and Stresses

The displacements, when introduced into the strain-displacement relations, lead to the following strain values

$$\left.\begin{aligned} \epsilon_r &= \frac{\partial u}{\partial r} = 0 & \gamma_{r\theta} &= \frac{\partial v}{\partial r} - \frac{v}{r} + \frac{1}{r}\frac{\partial u}{\partial \theta} = r\frac{\partial \omega}{\partial r} \\ \epsilon_\theta &= \frac{1}{r}\frac{\partial v}{\partial \theta} + \frac{u}{r} = 0 & \gamma_{\theta z} &= \frac{1}{r}\frac{\partial w}{\partial \theta} + \frac{\partial v}{\partial z} = r\frac{\partial \omega}{\partial z} \\ \epsilon_z &= \frac{\partial w}{\partial z} = 0 & \gamma_{rz} &= \frac{\partial u}{\partial z} + \frac{\partial w}{\partial r} = 0 \end{aligned}\right\} \qquad [2]$$

The linear stress-strain relations give the stresses in the form

$$\left.\begin{aligned} \sigma_r &= 0 & \tau_{r\theta} &= Gr\frac{\partial \omega}{\partial r} \\ \sigma_\theta &= 0 & \tau_{\theta z} &= Gr\frac{\partial \omega}{\partial z} \\ \sigma_z &= 0 & \tau_{rz} &= 0 \end{aligned}\right\} \qquad [3]$$

## Equilibrium Equation

Fig. 1 shows a shaft of circular varying cross section with the stresses acting upon a body element of the shaft. On account of the relations, Equations [3], only the equilibrium condition for the shear stresses in the circumferential direction ($\tau_{r\theta}$ and $\tau_{\theta z}$) and their equivalents ($\tau_\theta$, and $\tau_{\theta z}$) lead to a significant relation. This relation is

$$\frac{\partial \tau_{r\theta}}{\partial r} + \frac{\partial \tau_{z\theta}}{\partial z} + 2\frac{\tau_{r\theta}}{r} = 0$$

Substitution of relations, Equations [3], into this equation gives the equilibrium condition in terms of the derivatives of the angular displacement $\omega$, $\partial\omega/\partial r$, and $\partial\omega/\partial z$ in the form

$$\frac{\partial}{\partial r}\left(r\frac{\partial \omega}{\partial r}\right) + 2\frac{\partial \omega}{\partial r} + r\frac{\partial^2 \omega}{\partial z^2} = 0 \qquad [4]$$

[1] Professor of Aerodynamics and Aero Structures, Polytechnic Institute of Brooklyn, Brooklyn, N. Y. Mem. ASME.

[2] Structural Engineer, Grumman Aviation Engineering Corporation, Bethpage, L. I., N. Y.

[3] "Uniform Torsion and Flexure of Incomplete Tores With Application to Helical Springs," by J. H. Michell, Proceedings of the London Mathematical Society, vol. 31, 1900, pp. 141–146.

[4] "Über die Torsion von runden Stäben mit Veränderlichem Durchmesser," by A. Föppl, *Sitzungsberichte bayerische Akademie der Wissenschaften*, vol. 35, 1905, pp. 249–262.

[5] "Theory of Elasticity," by A. E. H. Love, Cambridge University Press, London, England, 1927, sect. 226A.

Contributed by the Applied Mechanics Division and presented at the Annual Meeting, New York, N. Y., November 27–December 2, 1949, of The American Society of Mechanical Engineers.

Discussion of this paper should be addressed to the Secretary, ASME, 29 West 39th Street, New York, N. Y., and will be accepted until October 10, 1950, for publication at a later date. Discussion received after the closing date will be returned.

Note: Statements and opinions advanced in papers are to be understood as individual expressions of their authors and not those of the Society. Paper No. 49—A-12.

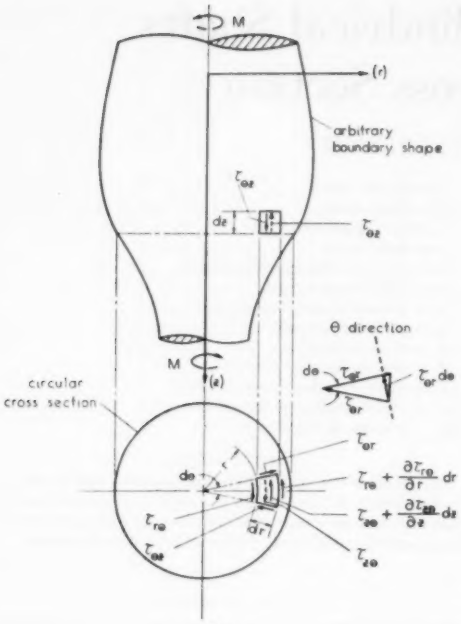


FIG. 1

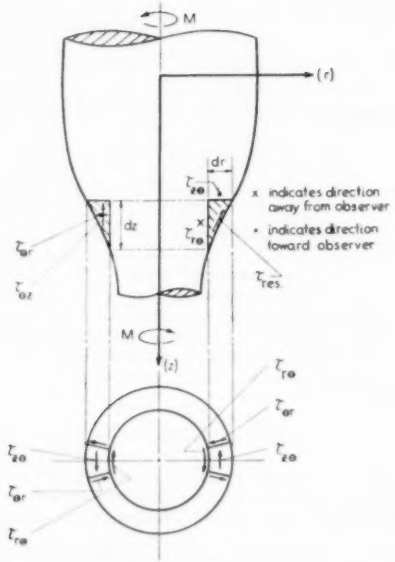


FIG. 2

### BOUNDARY CONDITION

It is required by the boundary condition that the mantle (generatrix) surface shall be free from surface stress. In Fig. 2 an annular volume element of triangular cross section is shown. Summing the moments about the $z$-axis, caused by the shear stresses on its sides, one obtains the following equilibrium condition

$$\tau_{z\theta}\, r\, dr = \tau_{\theta r}\, dz$$

This condition signifies that at the boundary the resultant stress

$$\tau_{res}^2 = \tau_{\theta r}^2 + \tau_{\theta z}^2$$

runs parallel to the generatrix. It can be expressed in terms of the twist-angle derivatives by using the stress expressions of Equations [3]

$$\frac{\partial \omega}{\partial z}\, dr = \frac{\partial \omega}{\partial r}\, dz \quad \text{or} \quad \frac{dz}{dr} = \frac{\partial \omega / \partial z}{\partial \omega / \partial r} \qquad [5]$$

Hence, in addition to satisfying Equation [4], $\omega = \omega(r, z)$ must satisfy the foregoing condition at the boundary.

### SEMI-INVERSE METHOD OF SOLUTION

All stress, strain, and displacement components have been expressed as functions of $\omega$ and its derivatives. The function $\omega$ must now be determined as an integral of Equation [4] which then must satisfy the boundary condition, Equations [5]. In a direct method of solution, the shape of the boundary generatrix of the shaft would be prescribed and an integral of Equation [4] satisfying the boundary condition, Equation [5], would have to be adapted to it. This method, however, has been found to be very difficult. Saint Venant, in his theory of torsion of cylindrical shafts, has developed a semi-inverse method. It will here be utilized for a class of integrals of Equation [4] which seems not to have been investigated previously. It has, however, been mentioned by A. E. H. Love[5] and treated more in detail in the elasticity courses of the first-named author of this paper.[6]

### CLASS OF INTEGRALS CHOSEN

The general expression for the class of integrals chosen in this paper is

$$\omega = m\sum\, n\sum\, e^{(q_m + i q_n)z}\, R(r)$$

It may be represented here by means of the two subclasses

$$\omega_a = n\sum\, e^{q_n z}\, R_a(r) \qquad [6a]$$

$$\omega_b = n\sum \begin{matrix}\sin\\ \cos\end{matrix} (q_n z) R_b(r) \qquad [6b]$$

where $q_n$ signifies an arbitrary, constant, reciprocal reference length.

If the functions

$$Z_{a,b} = r \cdot R_{a,b}(r)$$

are introduced, Equation [4] leads to the standard forms of the differential equations of the Bessel function of real and imaginary argument, namely

$$\frac{d^2 Z_a}{dr^2} + r^{-1}\frac{dZ_a}{dr} + (q^2 - r^{-2})Z_a = 0 \qquad [7a]$$

$$\frac{d^2 Z_b}{dr^2} + r^{-1}\frac{dZ_b}{dr} - (q^2 + r^{-2})Z_b = 0 \qquad [7b]$$

where $q$ has been written for $q_n$.

[6] Notes for the graduate course entitled "Theory of Elasticity," Polytechnic Institute of Brooklyn, Brooklyn, N. Y.

The solutions of Equations [7] are

$$Z_a = Z_1(qr) = AJ_1(qr) + BN_1(qr) \quad [8a]$$

$$Z_b = Z_1(iqr) = CJ_1(iqr) + DN_1(iqr) \quad [8b]$$

so that

$$\omega_a = e^{qz}\, r^{-1}\, Z_1(qr) \quad [9a]$$

$$\omega_b = \begin{matrix}\sin\\ \cos\end{matrix} (q\,z) r^{-1}\, Z_1\,(iqr) \quad [9b]$$

The displacements follow directly from Equations [9] and [1]

$$v_a = \omega_a r = e^{qz}\, Z_1(qr) \quad [10a]$$

$$v_b = \omega_b r = \begin{matrix}\sin\\ \cos\end{matrix} (qz) Z_1(iqr) \quad [10b]$$

The stresses, known from Equations [9] and [3], are

$$\left.\begin{aligned} (\tau_{r\theta})_a &= -qG\, e^{qz}\, Z_2(qr)\\ (\tau_{z\theta})_a &= +qG\, e^{qz}\, Z_1(qr)\\ (\tau_{r\theta})_b &= -iqG \begin{matrix}\sin\\ \cos\end{matrix} (qz)\, Z_2(iqr)\\ (\tau_{z\theta})_b &= +qG \begin{matrix}+\cos\\ -\sin\end{matrix} (qz)\, Z_1(iqr) \end{aligned}\right\} \quad [11]$$

where the relation

$$\frac{\partial}{\partial r}\,[r^{-1}\, Z_1(\alpha r)] = -\alpha r^{-1}\, Z_2(\alpha r)$$

has been used. In the quite general case, the Expressions [9] for $\omega_a$ and $\omega_b$, and the boundary condition, Equations [5], lead to the following equations for the shaft generatrices

$$\left(\frac{dz}{dr}\right)_a = \frac{n\sum q_n\, e^{q_n z}\, r^{-1}\, Z_1(q_n r)}{n\sum -q_n\, e^{q_n z}\, r^{-1}\, Z_2(q_n r)} \quad [12a]$$

$$\left(\frac{dz}{dr}\right)_b = \frac{n\sum \begin{matrix}+\cos\\ -\sin\end{matrix} (q_n z)\, r^{-1} q_n\, Z_1(iq_n r)}{n\sum -\begin{matrix}\sin\\ \cos\end{matrix} (q_n z) r^{-1}\, iq_n\, Z_2(iq_n r)} \quad [12b]$$

The solution of these general differential equations of the boundary curves would require very involved integrations. Therefore it seemed advisable to consider, in this paper, only the cases of single terms, so that the subscript $n$ will not appear any more in the text

$$\left(\frac{dz}{dr}\right)_a = -\frac{Z_1(qr)}{Z_2(qr)} \quad [13a]$$

$$\left(\frac{dz}{dr}\right)_b = \begin{matrix}+\cot\\ -\tan\end{matrix} (qz)\, \frac{iZ_1(iqr)}{Z_2(iqr)} \quad [13b]$$

Integration gives, for case $(a)$

$$z = -\int \frac{Z_1(qr)}{Z_2(qr)}\, dr \quad [14a]$$

and for case $(b)$

$$\int \begin{matrix}+\tan\\ -\cot\end{matrix} (qz) dz = \int \frac{iZ_1(iqr)}{Z_2(iqr)}\, dr$$

$$z = \frac{1}{q} \begin{matrix}\arccos\\ \arcsin\end{matrix} \left[e^{-iq\int \frac{Z_1(iqr)}{Z_2(iqr)}\, dr}\right] \quad [14b]$$

*The Twisting Moments.* On each shaft equal and opposite twisting moments must be applied on external surfaces other than the generatrix surface. These external surfaces, for technical applications, can be produced by cutting plane or curved end cross sections, by drilling bores through the body of the shaft, and so forth. It is then only necessary to assume those stresses which result from stress Equations [11] as acting on these surfaces to produce surface tractions. This requirement concerning the stress distribution on the external surfaces means the same restriction as in the theory of torsion of cylindrical shafts. In this latter case it has been shown that the errors following from the difference of the practical and the theoretical stress distributions of the applied twisting moments are small, except quite near the surface tractions. This is a significant example of Saint Venant's "principle of elastic equivalence of statically equipollent systems of load," which seems also to be acceptable in the case of shafts with varying circular cross section.

### Case of the Integral $\omega = e^{qz}\, Z_1(qr)$

The explicit form of Case [9a] was given by

$$\omega = e^{qz}\, r^{-1}\, [AJ_1(qr) + BN_1(qr)] \quad [9a]$$

The Bessel function of real argument and of the second kind, $N_1(qr)$, goes to infinity as $r$ approaches zero. It follows that for full shafts, the integration constant $B$ must be zero. For hollow shafts, it will be necessary to determine the value of $B$ by means of a prescribed stress or displacement value.

Only two separate assumptions will be treated in this paper, namely

$$A \neq 0, \quad B = 0, \quad \text{and} \quad A = 0, \quad B \neq 0$$

The more general case wherein $A$ and $B$ are both different from zero does not present any further difficulty, but is left out for the sake of brevity and simplicity.[7]

*Solid Shafts.* The function $\omega$, which gives the distribution of the angle of twist and of the circumferential displacement, $v(r, z) = r\omega(r, z)$, follows from Equation [9a] with $B = 0$

$$\omega = Ae^{qz}\, r^{-1}\, J_1(qr) \quad [9a_1]$$

According to Equation [14a], the generatrix curve of the surface is

$$qz = -\int_0^{qr} \frac{J_1(qr)}{J_2(qr)}\, d(qr) \quad [14a_1]$$

The form of this relation makes it advisable to introduce the dimensionless variables $(qr)$ and $(qz)$ as co-ordinates. A graphical integration is preferred since an analytical integration seemed to become too involved. This is done by means of the available tabulations of Bessel functions.[8] Fig. 3 shows a plot of $J_1(qr)/J_2(qr)$ for a $(qr)$ range extending from asymptote $(qr) = 0$ to asymptote $(qr) = 11.62$. The solution of Equation $[14a_1]$ contains an arbitrary constant of integration which can be chosen such that $(qz) = 0$ when $(qr)$ has any convenient value, say, $(qr)_1$.

Fig. 4 shows the boundary shapes which result from $(qr)_1$ values of 3.832, 7.0156, and 10.1735. The portions of these curves which lie between $(qr) = 3.832$ and $(qr) = 5.136$, and between $(qr) = 7.0156$ and $(qr) = 8.417$, have not been included as part of the boundary shapes. They will appear and be discussed later when hollow shafts are considered.

Equations [1], [3], and [9a] are sufficient to determine the displacements and stresses

[7] An appropriate procedure would be to compare the geometric consequences of cases with a number of different $B/A$ ratios.

[8] "Tables of Functions," by E. Jahnke and F. Emde, Dover Publications, New York, N. Y. 1945

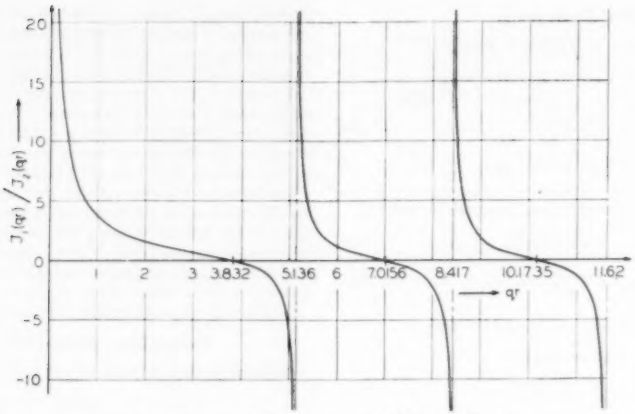


$\omega = R\,e^{qz}$ CURVE OF $J_1(qr)/J_2(qr)$ VS. $(qr)$

FIG. 3

$$\left.\begin{aligned} \omega &= Ae^{qz}\, r^{-1}\, J_1(qr) \\ v &= Ae^{qz}\, J_1(qr) \\ \tau_{r\theta} &= GAqe^{qz}\, J_1(qr) \\ \tau_{r\theta} &= -GAqe^{qz}\, J_2(qr) \end{aligned}\right\} \quad \ldots\ldots\ldots\ldots [15]$$

The distribution of the shear stress on the end sections of a shaft gives the manner in which the external twisting moment should be applied. Obviously, it is convenient to assume these end sections as planes at prescribed $(qz)$ values. Fig. 5 shows the $\tau_{r\theta}$, $v$, and $\omega$ distributions at cross sections determined by $(qz) = 0$ and $(qz) = 3.5$, for the boundary shape corresponding to $(qr)_1 = 3.832$ (see Fig. 4).

Up to this point, all stresses, displacements, and the angle of twist have been given in terms of the constant $A$. The value of $A$ will be calculated by developing an expression for the known, externally applied, twisting moment. In the case of shafts with plane end sections at given $(qz)$ values, $M$ is expressed by the following equation where the subscript $e$ denotes co-ordinates of the shaft generatrix

$$M = \frac{1}{q^2}\int_0^{(qr)_e} 2\pi\tau_{r\theta}\,(qr)^2 d(qr) \quad \ldots\ldots\ldots\ldots [16]$$

The $\tau_{r\theta}$ value of Equations [15] gives

$$M = 2\pi GAq^{-2}\, e^{qz}\,[(qr)_e^2\, J_2(qr)_e] \quad \ldots\ldots\ldots\ldots [16a]$$

This expression must hold at any cross section. Hence any corresponding values of $(qr)_e$ and $(qz)$, which determine a point on the boundary shape, can be selected and used to solve for $A$

$$A = +Mq^2/(11.8)\pi G$$

for the boundary in Fig. 4 corresponding to $(qr)_1 = 3.832$.

$$A = -Mq^2/(29.6)\pi G$$

for the boundary in Fig. 4 corresponding to $(qr)_1 = 7.0156$.

$$A = +Mq^2/(51.6)\pi G$$

for the boundary in Fig. 4 corresponding to $(qr)_1 = 10.1735$.

The shear-stress distribution in Fig. 5, which corresponds to the bottom boundary curve in Fig. 4, is obtained from the $\tau_{r\theta}$ expression of Equations [15]. The same formula can be used to

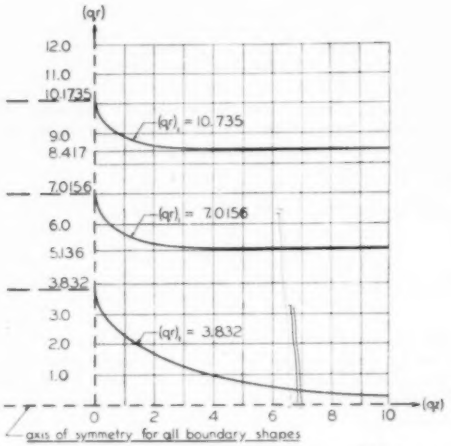


BOUNDARY SHAPES OBTAINED FROM $qz = -\int \frac{J_1(qr)}{J_2(qr)}\, d(qr)$

$\omega = R\,e^{qz}$

FIG. 4

determine the manner in which the external moments are applied for the other two boundary shapes in Fig. 4. However, as $(qr)$ exceeds 3.832 (the first zero of $J_1(qr)$), $\tau_{r\theta}$ changes sign; this indicates that $\tau_{r\theta}$ changes direction. For this reason, the upper two boundary shapes in Fig. 4 are of theoretical rather than practical interest, where torque and partial counter torque are in the same cross section.

*Hollow Shafts Derived From Bessel Functions of the First Kind.* The portions of the boundary shapes which lie between $(qr)$ values of 3.832 to 5.136, 7.0156 to 8.417, and 10.1735 to 11.62, have not been included in Fig. 4. As $(qr)$ increases from zero to 3.832, $(qz)$ decreases; as $(qr)$ exceeds 3.832, $(qz)$ increases, and the boundary line approaches the asymptote, $(qr) = 5.136$. In

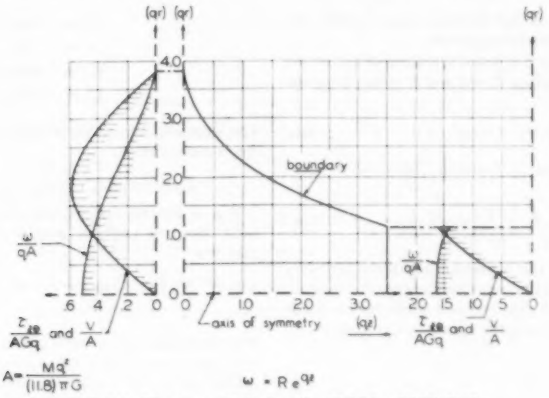


FIG. 5

a similar manner, the other two boundaries in Fig. 4 approach the asymptotes $(qr) = 8.417$ and $(qr) = 11.62$. The full boundary line obtained by continuing, for example, the thinnest boundary shape in Fig. 4, defines the hollow shaft in Fig. 6. *In other words, what was a shaft before* (in Fig. 4) *has now become a bore, and the continued boundary lines define* hollow *instead of solid shafts.*

Equations [15] represent the solution for the stresses and displacements of the hollow as well as the solid shafts, since Equations [4] and [5] remain satisfied. Fig. 6 includes the $v$, $\omega$, and $\tau_{z\theta}$ distributions at the cross section determined by $(qz) = 8$. The value of the constant $A$ is not the same for corresponding hollow and solid shafts. In the case of a hollow shaft, $A$ must be determined from a prescribed stress or displacement value at a given radius, and no longer can be calculated from an expression for the twisting moment. The external torque must be applied in accordance with the $\tau_{z\theta}$ distribution, and since the mantle surface of the shaft is free of external stress, this distribution (on any cross section) must consist of two equal and opposite twisting moments. Letting the subscripts $i$ and $e$ designate internal and external $(qr)$ values of the mantle surface, respectively, the moment on a plane cross section at any given $(qz)$ value is

$$M = \frac{1}{q^3}\int_{(qr)_i}^{(qr)_e} 2\pi\tau_{z\theta}\,(qr)^3 d(qr) = 2\pi\, GAq^{-3}e^{qz}[(qr)^3 J_3(qr)]_{(qr)_i}^{(qr)_e} \qquad \ldots\ldots\ldots [16a]$$

The conclusion that $M$ is zero is confirmed for any value of $A$ because the quantity

$$[(qr)^3 J_3(qr)]_{(qr)_i}^{(qr)_e}$$

can be shown to be zero at all cross sections of the hollow shaft.

*Hollow Shafts Derived From Bessel Functions of the Second Kind.* In the discussion of solid shafts, the constant $B$ had to be taken as zero in order that $\omega$ be finite at $(qr) = 0$. This con-

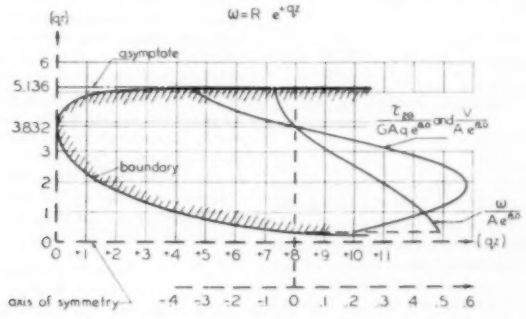


FIG. 6

dition for $B$ is not binding for hollow shafts because the shaft material does not reach the points where $(qr) = 0$.

The shafts corresponding to the Bessel functions of the second kind can be investigated by taking $A = 0$ and $B \neq 0$ in Equation [9a]

$$\omega = Be^{qz} r^{-1} N_1(qr) \quad \ldots\ldots [9a_2]$$

The generatrix curve is given by Equation [14a] with $A = 0$

$$qz = -\int \frac{N_1(qr)}{N_2(qr)} d(qr) \quad \ldots\ldots [14a_2]$$

A graphical integration of this expression yields the boundary shapes in Fig. 7. For the upper generatrix curve, the constant of integration was chosen such that $(qz) = 0$ where $(qr) = 5.428$; the integration constant for the lower boundary was chosen such

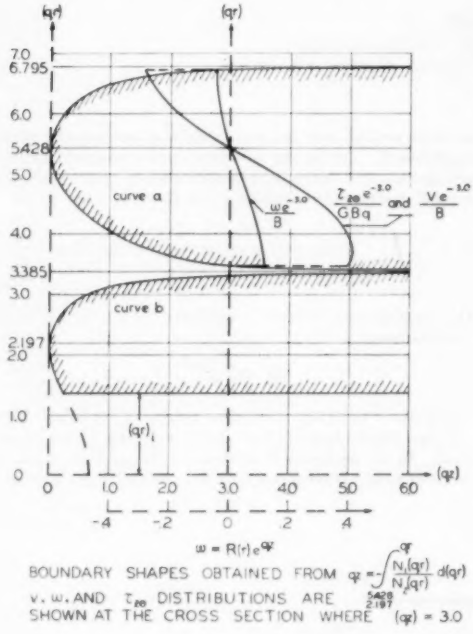


FIG. 7

that $(qz) = 0$, where $(qr) = 2.197$. (These values are convenient because the integrand becomes zero at $qr = 5.428$ and $qr = 2.197$.) In the latter case (curve $b$), material must be drilled out of the shaft so that the shaft body does not reach the axis of symmetry and so that the stresses and displacements remain finite. ($N_1[qr] = \infty$, where $qr = 0$.) This can be accomplished, for example, by drilling an axial bore of radius ratio $(qr)_1$ through the shaft as indicated in Fig. 7. In the first case (curve $a$), a bore need not be drilled out; on any cross section the moment then consists of two equal and opposite parts. However, if a bore is drilled parallel to the axis of symmetry, the case can be made analogous to curve ($b$), except that the bore is larger.

The stresses and displacements are known from Equations [1], [3], and [9a$_2$]

$$\left.\begin{aligned} \omega &= Be^{qz} r^{-1} N_1(qr) \\ v &= Be^{qz} N_1(qr) \\ \tau_{z\theta} &= GBe^{qz} q N_1(qr) \\ \tau_{r\theta} &= -GBe^{qz} N_2(qr) \end{aligned}\right\} \quad \ldots\ldots [17]$$

The constant $B$ must be determined from a prescribed stress or displacement value.

### Case of the Integral $\omega = r^{-1} \sin(qz)\, Z_1(qr)$

If $\omega = R(r) \sin(qz)$ is introduced into the equation of equilibrium, then the angle of twist is explicitly given by expression [9b], viz

$$\omega = r^{-1} \sin(qz)\, Z_1(iqr) = r^{-1} \sin(qz)\, [CJ_1(iqr) + DN_1(iqr)] \quad \ldots\ldots [9b]$$

The particular solution for $\omega$, which results when $C$ is taken as zero, is not applicable for a solid shaft, since $N_1(iqr)$ becomes infinite at $(qr) = 0$. On the other hand, if a bore along the axis of symmetry is assumed, the case of a flat ellipsoidal shape is found such that on the drilled out (inner) surface the resultant couples of the shear stresses give torque and counter torque. This case is considered of minor technical importance and will not be presented here in detail. The other particular solution for $\omega$, obtained by assuming $D$ as zero, will be investigated now

$$\omega = C \sin(qz)\, r^{-1} J_1(iqr) \quad \ldots\ldots [9b_1]$$

Equation [14b], with $D = 0$, represents the generatrix curve obtained by introducing $\omega$ into the boundary condition, Equation [5]

$$qz = \arccos e^{-i\int \frac{J_1(iqr)}{J_2(iqr)} d(qr)} \quad \ldots\ldots [14b_1]$$

The right-hand side of the foregoing equation would be difficult to integrate by analytical means, and therefore a graphical integration is again used to obtain the boundary shapes. It is found convenient to choose the constant of integration as

$$+ \ln(K \cos qz) - \int_0^{0.5} \frac{-iJ_1(iqr)}{-J_2(iqr)} d(qr) \quad \ldots\ldots [14b_2]$$

so that $(qz) = 0.5$ for $K = 1.0$ and $(qz) = 0$. (The quantities $-iJ_1(iqr)$ and $-J_2(iqr)$ are real and positive.) For several values of the constant $K$, the boundary curves represented by Equation [14b$_2$] were evaluated graphically by means of the tabulated Bessel functions and are shown in Fig. 8. Since $K$ is arbitrary, it is evident that an infinite number of boundary shapes can be obtained. The solution can be interpreted as follows: All generatrix curves in Fig. 8 approach the asymptotes $(qz) = \pm\pi/2$. Outside of these asymptotes there are no real values until $(qz)$ reaches the values of $\pm(3/2)\pi$. Then the same set of curves repeats itself as shown in Fig. 8($a$).

From Equations [1], [3], and [9b$_2$], the stresses and displacements are known. In order to express these quantities in terms of real factors, let $C = -Pi$

$$\left.\begin{aligned} \omega &= Pr^{-1} \sin qz\, [-iJ_1(iqr)] \\ v &= P \sin qz\, [-iJ_1(iqr)] \\ \tau_{z\theta} &= GPq \cos qz\, [-iJ_1(iqr)] \\ \tau_{r\theta} &= -GPq \sin qz\, [-J_2(iqr)] \end{aligned}\right\} \quad \ldots\ldots [18]$$

For the boundary shape corresponding to $K = 1.0$ (see Fig. 8), the stress and displacement distributions are shown in Fig. 9 at the cross sections determined by $(qz)$ values of 0.80 and 1.50. The angular displacement function $\omega$, and the circumferential displacement $v$, are zero for all $(qr)$ values at the section where

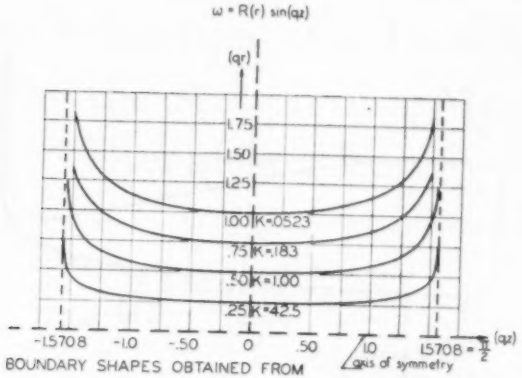


FIG. 8

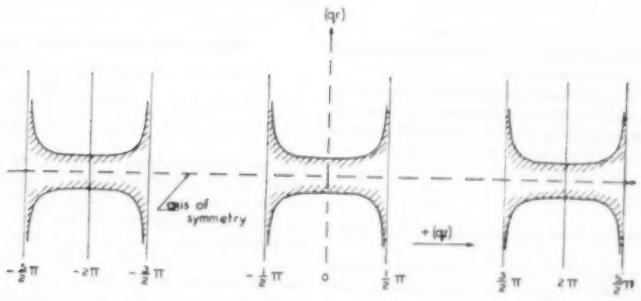


REPETITION OF BOUNDARY SHAPES OBTAINED FROM FORMULA ON FIG. 8

FIG. 8(a)

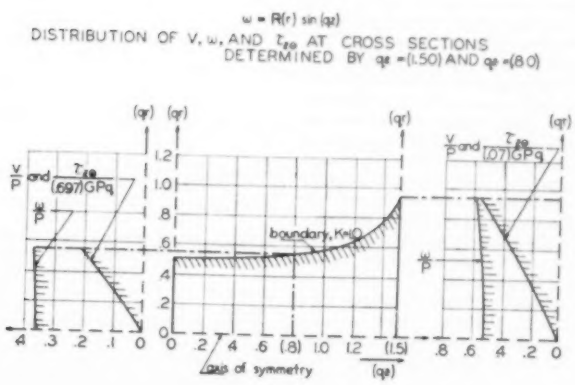


FIG. 9

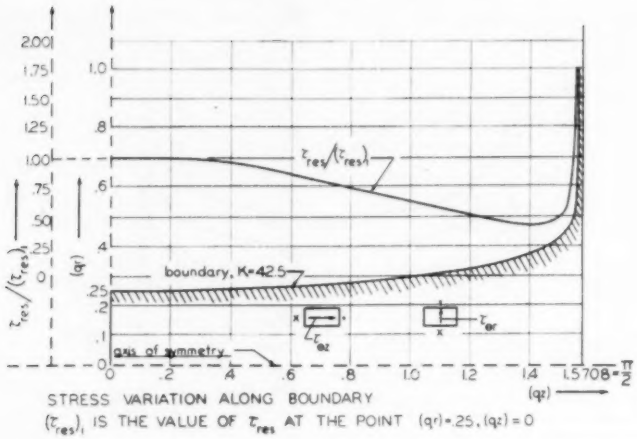


FIG. 10

$(qz) = 0$; this is as it should be since the shaft is symmetrical with respect to the $(qz) = 0$ cross section.

The constant $P$ is determined from an expression for the known external moment. Previously, this expression has been stated for the case of plane end sections by Equation [16], and is evaluated for the $\tau_{z\theta}$ expression of Equations [18] in the form

$$M = \int_0^{(qr)_a} \tau_{z\theta}\, 2\pi r^2 d(qr) = 2\pi GCq^{-3} i^{-1} \cos(qz)(qr)_a^2 J_2(iqr)_a \ldots\ldots [16b]$$

This relation must be valid for all cross sections, and therefore the $(qr)_a$ and $(qz)$ co-ordinates of any point on the boundary shape (conveniently at $qz = 0$) can be used to solve for $P$. A different value of $P$ results for each boundary shape (each $K$ value) as follows:

When $K = 0.0523$: $P = +\ (3.68)\ M\ q^3/(\pi G)$

When $K = 0.1830$: $P = +\ (12.08)\ M\ q^3/(\pi G)$

When $K = 1.000$: $P = +\ (62.695)\ M\ q^3/(\pi G)$

When $K = 42.50$: $P = +\ (1038.96)\ M\ q^3/(\pi G)$

*Stress Variation Along Boundary.* At any given $(qz)$ value, the shear stresses of Equations [18] are a maximum at the boundary as can be seen from the character of the Bessel functions. The variation of resultant stress along the boundary can be obtained by plotting $\tau_{res}/(\tau_{res})_1$, where $(\tau_{res})_1$ is the value of $\tau_{res}$ at the point where $(qz) = 0$ and $(qr) = 0.25$. (This point has been chosen because here the shaft is nearly cylindrical and the value of 0.25 indicates the case of the most slender shaft in Fig. 8.) For the boundary shape corresponding to $K = 42.50$, the variation of the resultant stress along the generatrix is shown in Fig. 10.

# Transverse Vibration of a Two-Span Beam Under the Action of a Moving Alternating Force

By R. S. AYRE[1] and L. S. JACOBSEN,[2] STANFORD UNIVERSITY, CALIF.

**An alternating force (for example, due to unbalance in a locomotive driving apparatus) moves across a symmetrical two-span beam (or equivalent bridge) with uniform velocity. The stress-time equations for the three time eras of the problem have been derived by classical methods. The experimental part of the investigation employs a mechanical system with wire resistance strain gages. Resonances from the first through the sixth mode have been investigated. There is good agreement between theory and experiment in so far as number and location of resonances are concerned. The discrepancy in amplitude is to be expected due to the omission of damping in the theory. The most important observation is the "multiplicity of resonances" associated with "each" natural mode.**

## Nomenclature

The following nomenclature is used in the paper:

- $x$ = horizontal co-ordinate
- $\sigma$ = dynamic flexural stress at lower surface of beam at a given location, $x$
- $\sigma_i$ = contribution of the $i$th term to $\sigma$
- $\sigma_0 = 2.0048 \frac{P_e l}{\pi^2 Z}$, flexural stress at lower surface of two-span beam at mid-point of a span due to the force $P_e$ when $P_e$ is fixed at the mid-point of the same span (static)
- $t$ = time
- $l$ = length of each span
- $E$ = modulus of elasticity for bending
- $I$ = moment of inertia of beam cross section with reference to its neutral axis
- $Z$ = section modulus of beam
- $A$ = cross-sectional area of beam
- $\gamma$ = weight of material of beam per unit of volume
- $g$ = acceleration due to gravity
- $P_e \cos \omega_0 t$ = alternating force
- $C = \frac{P_e l}{2\pi^2 Z}$, constant having dimensions of stress; note that $C \approx \frac{1}{4}\sigma_0$
- $v$ = uniform horizontal velocity of point of application of alternating force
- $\omega_0 = \frac{m\pi v}{l}$, circular frequency of alternating force
- $\omega = \frac{\pi v}{l}$, a circular frequency relating to horizontal movement of alternating force
- $m = \frac{\omega_0}{\omega}$, number of cycles which force makes in crossing two spans (for purposes of simplification, $m$ has been restricted to even integer numbers)
- $r$ = radius of a wheel which rolls along beam
- $i$ = number of a natural mode
- $n_i\pi$ = the $i$th root of frequency equation
- $p_i$ = $n_i^2 p_1$, circular natural frequency of the $i$th mode
- $p_1 = \frac{\pi^2}{l^2}\sqrt{\frac{EIg}{A\gamma}}$, circular natural frequency of fundamental mode
- $\tau_1 = \frac{2\pi}{p_1}$, natural period of fundamental mode
- $N_i = \frac{\sin n_i\pi}{\sinh n_i\pi} = \frac{\cos n_i\pi}{\cosh n_i\pi}$, constant for $i$th term, where $i = 2, 4, 6, \ldots$; $N_2 = -0.0279$; $N_4 = +0.00121$; $N_6 = -0.0000526, \ldots$.

## Introduction

This investigation is the second of a series which relates to the effects of traveling loads on beams of more than one span. While the first was concerned with the action of a "constant" force traversing a symmetrical two-span beam with uniform velocity (1),[3] the present deals with an "alternating" force which moves with uniform velocity along the beam. The problem has practical importance in the study of the effects of unbalanced driving mechanisms in vehicles of various types. The histories of the two problems are quite similar. The principal references in the present case are to S. P. Timoshenko (2, 3) and Sir Charles E. Inglis (4, 5), who deal with beams of a single span. To our knowledge there has been nothing published on the effect of an alternating force moving across a beam of more than one span.

It is assumed, as in the previous case, that the beam is of uniform mass and cross section, is free to rotate at all supports, is of slender proportions (shear distortions and rotatory inertia may be neglected), contains negligible damping, and that there is no mass associated with the disturbing force. The basic mathematics of the two problems are similar, involving application of Lagrange's equations of motion (3). Hence the mathematics of the present paper has been limited to a presentation of the

[1] Acting Associate Professor of Mechanical Engineering, Stanford University.

[2] Professor of Mechanical Engineering, Stanford University. Mem. ASME.

Presented at the Conference of the Applied Mechanics Division, Purdue University, Lafayette, Ind., June 22–24, 1950, of The American Society of Mechanical Engineers.

Discussion of this paper should be addressed to the Secretary, ASME, 29 West 39th Street, New York, N. Y., and will be accepted until October 10, 1950, for publication at a later date. Discussion received after the closing date will be returned.

Note: Statements and opinions advanced in papers are to be understood as individual expressions of their authors and not those of the Society. Manuscript received by the Applied Mechanics Division July 29, 1949. Paper No. 50—APM-2.

[3] Numbers in parentheses refer to the Bibliography at the end of the paper.

stress equations. The experimental apparatus, employing electrical recording of strain, is essentially the same as in the earlier problem with the exception of the loading device.

As may be expected, a moving alternating force has, in general, a greater dynamic effect than a moving constant force. Moreover, these effects manifest themselves at much lower velocities and are therefore of greater practical importance. Probably the most interesting feature of the problem is the multiplicity of resonances associated with each natural mode. It is shown that there are two resonance peaks related to the fundamental mode; three peaks to the second mode; two peaks to the third; four peaks to the fourth; two peaks to the fifth; five peaks to the sixth; etc.

## Theory

*The Problem.* An alternating force $P_e \cos \omega_0 t$ moves across the beam with a uniform velocity $v$. In the general case a phase angle will be associated with the force; however, the omission of the phase angle simplifies the equations and results in no significant error in the stress maxima provided that a reasonably large number of force cycles occur in crossing each span of the beam, say, 5. In many practical cases the alternating force is the vertical component of a centrifugal force which arises from an unbalance in a vehicle driving mechanism rolling along the beam; the forcing frequencies are then proportional to the velocity and inversely proportional to the radius of the wheel. The first-order forcing frequencies are therefore

$$\omega_0 = \frac{v}{r} = m\omega$$

The parameter $m$ is one of the important variables; it has been restricted to even integer numbers in order to eliminate further complications due to phase angles. Since from the practical standpoint values of $m$ equal to 10 or greater are of interest, the limitation does not result in important gaps in the investigation. It will appear later that resonance stresses are approximately proportional to $m$.

*The Stress Equations.* The terms of the stress series are given by Equations [1*a*, 1*b*, 2*a*, 2*b*, and 3*a*, 3*b*]; the co-ordinate system is shown in Fig. 1. The functions of $x$, appearing at the ends of the equations, describe variation in stress with location; they are characteristic of the natural modes.[4] These functions, called location functions, all have for the even-numbered modes an absolute maximum value equal to $\sqrt{2}$ in contrast with those for the odd-numbered modes which have a maximum of unity. The remaining functions include time functions, the two resonance functions $R_1$ and $R_2$, and in the case of the free vibration era (*c*) a term ($\sin p_i \pi/\omega$ or $\cos p_i \pi/\omega$), which determines whether or not the beam will continue to vibrate after the force has passed over.

*Discussion of Limiting Cases:*

1 If $v \to \infty$, $\omega \to \infty$, $\omega_0 \to \infty$; the stresses approach zero.

2 If $v$, $\omega$, $\omega_0$ are small quantities, the problem becomes a "static" one in which a sinusoidally varying force of maximum value $P_e$ slowly crosses the beam.

3 If $0 < v < \infty$, $0 < \omega < \infty$; $\omega_0 = 0$, i.e., $m = 0$; the alternating force becomes a constant, and the problem reduces to that of the constant moving force.[5]

4 If $v = 0$, $\omega = 0$; $0 < \omega_0 < \infty$; a steady-state problem results with a stationary alternating force of frequency $\omega_0$ acting at some fixed location.

*Resonance.* The conditions of resonance are as follows:

$$\text{Lower translatory resonance, } \frac{\omega}{p_i} = \frac{1}{m + n_i}$$

$$\text{Upper translatory resonance, } \frac{\omega}{p_i} = \frac{1}{m - n_i}$$

The term "translatory resonance" identifies these resonances with their physical origin, namely, the translation of the alternating disturbing force along the beam. Intuition tells us, although the equations do not show it explicitly, that the condition of stationary resonance, $\omega_0/p_i = 1$, must also be of importance. The term "stationary resonance" has been adopted since it involves only the frequency $\omega_0$ of the alternating force; in the related problem of the stationary alternating force it is the only resonance. We may also write, since $\omega_0 = m\omega$

$$\text{Stationary resonance, } \frac{\omega}{p_i} = \frac{1}{m}$$

Thus the stationary resonance lies between the two translatory resonances. The differences in frequencies are akin to positive and negative Doppler shifts.

*Translatory Resonance Stress.* The maximum resonance stresses may be derived from Equations [3*a*] and [3*b*]. Those for the odd-numbered modes are given by

$$\left|\sigma_i\right|_{\substack{\text{res}\\\text{max}}} = \frac{C\pi(m \pm n_i)}{{n_i}^2} \quad \ldots\ldots [4]$$

where $i = 1, 3, 5, \ldots$, and where the positive sign relates to the lower translatory resonance, and the negative sign to the upper. The fundamental mode is by far the most important of the odd-numbered modes; these resonances occur at $\omega/p_1 = 1/(m \pm 1)$, with maximum stresses given by

$$\left|\sigma_1\right|_{\substack{\text{res}\\\text{max}}} = C\pi(m \pm 1) \quad \ldots\ldots [4a]$$

Note that if $m$ is large the stress is approximately proportional to $m$. Expressions relating to the translatory resonances in the even-numbered modes are not of sufficient interest to warrant including them here.

*Stationary Resonance Stress.* In the case of the two-span beam the stationary resonance is of particular interest only in the second-mode term where it results in nearly an absolute maximum stress of

$$\left|\sigma_2\right|_{\substack{\text{res}\\\text{max}}} \approx 3.45\, Cm \quad \ldots\ldots [5]$$

Equation [5] is an approximation derived from Equation [3*b*]; it is correct within 1 per cent for practical values of $m$ and shows that the resonance response in the second mode at $\omega_0/p_2 = 1$ is directly proportional to the number of forcing cycles.

A comparison of Equations [4*a*] and [5] leads to the important conclusion that resonance with the second mode may result in stresses which are as great as those due to resonance with the fundamental mode. A similar conclusion has been drawn in the investigation of the constant-moving-force problem (1). On the other hand, the second-mode resonance responses in the "single-span" case are relatively less important, being about one fourth of those due to the fundamental. Furthermore, the second natural frequency of the single-span beam is 4 times the fundamental while the second of the two-span beam is only 1.56 times the fundamental. Thus second-mode resonance in the two-span case occurs at a value of velocity $v$ which is about 40 per cent

[4] See Fig. 2 in reference (1).

[5] Compare with stress equations [9*a*,*b*], [10*a*,*b*], [11*a*,*b*] reference (1).

STRESS COMPONENTS $m = 2, 4, 6, \ldots$

Odd Modes $i = 1, 3, 5, \ldots$; $n_i = 1, 2, 3, \ldots$

Force crossing span a (era a)

1a)* $\sigma_{ia} = \frac{C}{n_i^2}\left(R_1 \sin(m+n_i)\omega t + R_2 \sin(m-n_i)\omega t + R_3 \sin p_i t\right) f_1(x)$, $0 \le t \le \frac{\pi}{\omega}$

Force crossing span b (era b)

2a)* $\sigma_{ib} = \frac{C}{n_i^2}\left(R_1 \sin(m+n_i)\omega t + R_2 \sin(m-n_i)\omega t + R_3 \sin p_i t\right) f_1(x)$, $\frac{\pi}{\omega} \le t \le \frac{2\pi}{\omega}$

Force passed beyond the beam (era c)

3a) $\sigma_{ic} = \frac{2C}{n_i^2} R_3 \sin\frac{p_i\pi}{\omega} \cdot \cos\left(p_i t - \frac{p_i\pi}{\omega}\right) \cdot f_1(x)$, $\frac{2\pi}{\omega} \le t < \infty$

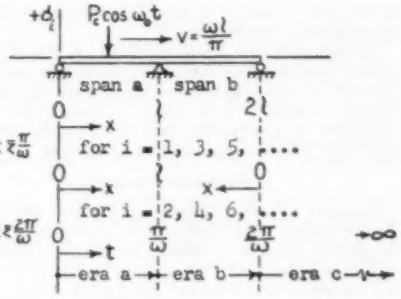


FIGURE 1

Even Modes $i = 2, 4, 6, \ldots$; $n_i = 5/4, 9/4, 13/4, \ldots$ (within 1/100 of 1 %)

Force crossing span a (era a)

1b) $\sigma_{ia} = \frac{C}{n_i^2(1-N_i^2)}\left(R_1 \sin(m+n_i)\omega t + R_2 \sin(m-n_i)\omega t + S_1 \sinh n_i\omega t \cdot \cos m\omega t + S_2 \cosh n_i\omega t \cdot \sin m\omega t + (R_3+S_3)\sin p_i t\right) f_2(x)$, $0 \le t \le \frac{\pi}{\omega}$

Force crossing span b (era b)

2b) $\sigma_{ib} = \frac{C}{n_i^2(1-N_i^2)}\left(R_1 \cos(m+n_i)\omega t - R_2 \cos(m-n_i)\omega t + S_1 \sinh(2n_i\pi - n_i\omega t)\cdot\cos m\omega t - S_2 \cosh(2n_i\pi - n_i\omega t)\cdot\sin m\omega t\right.$

$\left. + (R_3+S_3)\sin p_i t - 2(R_3 \cos n_i\pi + S_3 \cosh n_i\pi)\sin\left(p_i t - \frac{p_i\pi}{\omega}\right)\right) f_2(x)$, $\frac{\pi}{\omega} \le t \le \frac{2\pi}{\omega}$

Force passed beyond the beam (era c)

3b) $\sigma_{ic} = \frac{2C}{n_i^2(1-N_i^2)}\left((R_3+S_3)\cos\frac{p_i\pi}{\omega} - R_3 \cos n_i\pi - S_3 \cosh n_i\pi\right)\sin\left(p_i t - \frac{p_i\pi}{\omega}\right) \cdot f_2(x)$, $\frac{2\pi}{\omega} \le t < \infty$

where:

$$R_1 = \frac{1}{1 - \frac{\omega^2(m+n_i)^2}{p_i^2}}, \quad R_2 = \frac{-1}{1 - \frac{\omega^2(m-n_i)^2}{p_i^2}}, \quad R_3 = -R_1\frac{\omega(m+n_i)}{p_i} - R_2\frac{\omega(m-n_i)}{p_i}.$$

$$S_1 = -N_i\left(D_1\left(1+\frac{m\omega}{p_i}\right) + D_2\left(1-\frac{m\omega}{p_i}\right)\right), \quad S_2 = N_i\frac{n_i\omega}{p_i}(D_1 - D_2), \quad S_3 = N_i\frac{n_i\omega}{p_i}(D_1 + D_2),$$

$$D_1 = \frac{1}{\left(\frac{n_i\omega}{p_i}\right)^2 + \left(1+\frac{m\omega}{p_i}\right)^2}, \quad D_2 = \frac{1}{\left(\frac{n_i\omega}{p_i}\right)^2 + \left(1-\frac{m\omega}{p_i}\right)^2}.$$

$$f_1(x) = \sin\frac{n_i\pi x}{l}, \; 0 \le x \le 2l; \qquad f_2(x) = \sin\frac{n_i\pi x}{l} + N_i \sinh\frac{n_i\pi x}{l}, \; 0 \le x \le l.$$

* Note that equations 1a and 2a are identical.

of the velocity required for second-mode resonance in the corresponding single-span system.

*Comparison With a Simple Oscillator.* It is well known that an undamped simple oscillator, when subjected to a sinusoidal disturbance of finite duration, has a resonance response which is directly proportional to the number of cycles in the disturbance. This provides a comparison with the beam, for which similar proportionalities have been shown by Equations [4*a*] and [5].

## Experimental Method

*Superposition and Separation of Constant and Alternating-Force Problems.* The experimentally applied force must always be positive, therefore, a combined loading, $P + P_e \cos \omega_e t$ where $P > P_e$, has been used. The effects of the two parts of the loading are separable due to the principle of superposition. The separation of the effects presents no serious problem for the following reasons: (*a*) The alternating-force component of the loading sets up large response in a particular mode at a much lower velocity than does the constant-force component. (*b*) The resonant magnification caused by the alternating-force term is much greater than that due to the constant-force term. (*c*) If resonance effects due to the two components do overlap, they will have widely different and easily distinguishable frequencies.

A purely alternating loading of a mechanical nature seldom occurs in practice; it is generally associated with some constant loading. The foregoing considerations regarding separation of the two superimposed effects are therefore important.

The "loading device" is the only part of the apparatus which will be described in detail, Fig. 2.[6] The constant force $P$, maintained by the spring $h$, was 3 lb; the centrifugal force $P_e$ was kept at known values, of approximately 2 lb, by adjusting the size of the unbalanced weight $g$, to suit the velocity. The static moment of the unbalanced weight could be determined directly by an accurate lever-and-slider weighing device temporarily attached to the wheel. The effective mass of the loading arm, wheel, unbalanced weight, and so forth, compared to the total mass of the beam, varied from about 2 per cent, at the lowest velocities, to 0.5 per cent, at the highest velocities. The disturbing forces were therefore essentially "massless." Some extraneous vibration problems arose in the development of the force-carriage pulling-cord system. They were minimized by the addition of a balancing wheel *i*, and a friction pad *m*.

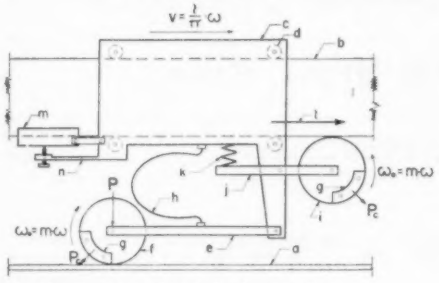


*a* portion of two-span beam (length of each span = *l*)
*b* guide rail
*c* frame of force carriage
*d* carriage guide rollers (4)
*e* loading arm
*f* loading wheel of circumference $2\pi r = \frac{2l}{m}$
*g* unbalanced weight for creating centrifugal force $P_e$
*h* multiple-wire, low-modulus spring to create constant force $P > P_e$
*i* balancing wheel of circumference $2\pi r$; phase adjusted to cancel horizontal component of $P_e$
*j* carrying arm for balancing wheel
*k* pressure spring for balancing wheel
*l* carriage pulling cord; to winding drum, or to elastic nylon cord for high speeds
*m* friction pad for reducing horizontal oscillation of carriage-pulling cord system caused by large starting acceleration
*n* loading spring for friction pad

Fig. 2 Schematic Diagram of Loading Device

[6] See appendix, reference (1), for complete description of remainder of apparatus and of recording system.

## Experimental Results; Comparison With Theory

The results have been presented in four sets of diagrams in which stress ratios have been plotted as functions of a frequency ratio. About seventy theoretical values of the natural-mode components have been computed. The experimental work represents 1350 tests, the large number being required in order to define the many resonance peaks (there are eighteen peaks within the first six modes). The experimental points have been shown only in one typical case.

*Maxima Due to Location: Maxima Due to Time.* It should be kept in mind that there are two sources of stress maxima, one of which is due to the functions of location $x$, while the other is due to the functions of time. Wherever the natural-mode components are shown, the stresses are absolute maxima, the time and the location functions both being taken at their maximum values. The total stresses, on the other hand, are maxima only with relation to time. The locations of maximum stress in the natural modes are readily determined from theory (1), but the location of maximum total stress depends on the relative importance of the natural-mode terms at each value of forcing velocity. For example, at resonance with the fundamental mode the total stress will be a maximum at a location near a mid-span point, but the exact location cannot be detetermined without consideration of the higher modes. At resonance with the second mode the total stress will be a maximum at or very close to the mid-support. Resonance with the third mode will result in maximum total stress near a quarter-point. It would be extremely laborious, even with the experimental apparatus, to determine total stress maxima with relation to time and to location. Therefore the locations have been restricted to the three of greatest practical interest, the mid-span points and the mid-support.

*Damping.* It is obvious that damping is important, particularly in the resonance regions, and that account must be taken of it in a quantitative manner in practical applications. A qualitative remark can, however, be made. At resonance there is an appreciable longitudinal translation at the end supports. It can be shown that the effect of a coulomb or constant damping arising from this translation is approximately inversely proportional to $n_i^2$. Thus relatively greater damping effects can be expected at resonance with the lower modes than at resonance with the higher modes. This general trend is in agreement with the experimental results.

*Phase of Forcing Function.* In the initial statement of "The Problem," a question was raised concerning the phase of the forcing function. The alternating force has been taken as $P_e \cos \omega_e t$, i.e., when the force starts to cross the beam it is acting downward at its maximum value. The first step in the experimental part of the investigation was to determine if phase is of practical importance when the number of forcing cycles is reasonably large, say, five per span ($m = 10$). This question is a tedious one to answer theoretically. A phase angle was introduced experimentally into the alternating force and given values of 0 deg (as in the theory), 90 deg, and 180 deg. There is no significant difference in the stresses even at resonance.

*Comparison of Experiment and Theory; Fundamental Component* (Fig. 3). Near the peaks, the maxima occur in era *c*, i.e., during the free vibration after the force has left the beam, or near the end of era *b*. The experimental work confirms the existence

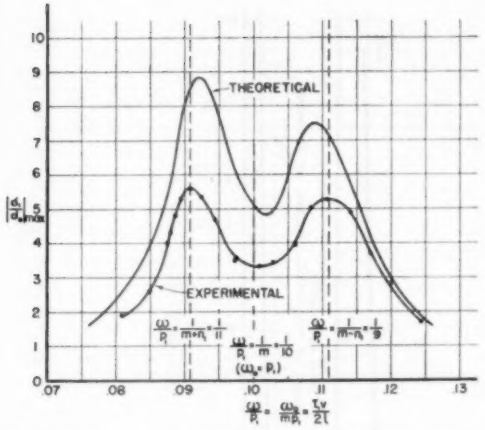


FIG. 3 COMPARISON OF EXPERIMENTAL AND THEORETICAL MAXIMUM STRESSES FUNDAMENTAL-MODE COMPONENT, REGION OF RESONANCE

(Total number of cycles, $m = 10$. At locations giving maximum stresses [mid-span points, i.e., $x = \frac{l}{2}, \frac{3l}{2}$].)

of two resonance peaks in the fundamental mode; they relate to the translatory resonances. Note that the stationary resonance is unimportant in this case. The poor agreement in amplitude is to be expected due to the omission of damping in the theory; the discrepancy will generally be greater at larger values of $m$ and smaller at lower values of $m$. The experimental method of separating the natural-mode components is explained in reference (1).

*Fundamental, Second, and Third-Mode Resonance Regions* (Fig. 4). Notice the existence of two resonance peaks (corresponding to the translatory resonances) in the fundamental and in the third modes, and of one major and two minor peaks in the second mode (the major peak is related to the stationary resonance). As the number of forcing cycles $m$, is increased, the resonant velocities decrease and the required "tuning" becomes sharper. The left-hand resonance peaks for the fundamental and third modes are theoretically higher than the right-hand peaks; the reversal of this relationship in the case, $m = 20$, fundamental mode, is due to experimental difficulties arising from the sharp tuning.

The curves of theoretical resonance maxima for the fundamental and third modes have been drawn through the maxima arising when

$$\frac{\omega}{p_1} = \left(\frac{1}{m+1}\right)_{i=1}, \quad \left(\frac{4}{m+2}\right)_{i=3}$$

(Equation [4]), and for the second mode through the maxima corresponding to

$$\frac{\omega}{p_1} = \left(\frac{1.56}{m}\right)_{i=2}$$

(Equation [5]). As $m$ increases the curves tend to infinity. If damping were included in the theory, the curves would drop to a level in better agreement with the experimental resonance maxima and would no longer tend to infinity. The agreement between theory and experiment at resonance is somewhat better in the second mode than in the fundamental and there is good agreement in the third mode.

*Another Method of Comparing Resonance Regions* (Fig. 5). The resonance regions may be compared in a more condensed manner than is possible in Fig. 4, if it is noted that the resonances are grouped about the value of the frequency ratio, $\omega_0/p_i = 1$ (stationary resonance). The vertical dashed ($m = 10$) and dotted ($m = 20$) lines lie at the translatory-resonance frequencies, $\omega_0/p_i = m/(m \pm n_i)$ (see Equation [4]). The experimental work was not carried to velocities high enough to complete the data in the fifth and sixth modes when $m = 10$.

The maximum stress at the lower and upper translatory resonances is a good approximation to the greatest maximum in the first, third, and fifth modes. In the second mode the stress at the stationary resonance is very nearly equal to the greatest maximum. In the fourth and sixth modes, the relationship is more complex, and simple resonance calculations are not of great value. The width of the resonance band increases as the number of the mode increases.

The magnitude and position of the peaks relating to the even modes may be determined from Equation [3b]. In the region of resonance the maximum stress is given approximately by

$$\left|\sigma_{ic}\right|_{\max} \approx \frac{2\sqrt{2C}}{n_i^2} \cdot \frac{n_i\omega}{p_i} \left[\frac{\cos n_i\pi - \cos \frac{p_i\pi}{\omega}}{\left(\frac{n_i\omega}{p_i}\right)^2 - \left(1 - \frac{m\omega}{p_i}\right)^2} + \frac{\cos n_i\pi}{\left(\frac{n_i\omega}{p_i}\right)^2 + \left(1 - \frac{m\omega}{p_i}\right)^2}\right] \quad \ldots [6]$$

where $i = 2, 4, 6, \ldots$.

where the location function has been taken at its maximum value, $= \sqrt{2}$, and where the time function has its maximum value of unity. Of the two terms within the bracket, the first term alone can be used to determine the positions of the peaks. Only in the case of the second mode are the peaks very closely related to the two translatory resonances and the stationary resonance. It has been shown by calculations based upon the foregoing analysis that there are three, four, and five peaks associated with the second, fourth, and sixth modes, respectively. A consideration which is more important than the exact number of peaks is the relative width of the resonance band. An estimate of the width and location of the band can be determined very easily by calculating the translatory resonant velocities.

*Comparison of Component Stresses With Total Stresses* (Fig. 6). The upper diagram shows a further comparison of theory and experiment. There is good agreement in the third, fourth, and fifth modes; damping did not strongly affect the response. The fundamental and second-mode resonance regions overlap each other slightly ($p_2 = 1.56\ p_1$). The overlapping of resonance in the third and fourth modes is much more pronounced ($p_4 = 1.26\ p_3$. The fifth and sixth modes can be expected to overlap still more ($p_6 = 1.17\ p_5$).

The "total" stresses at mid-span are composed mainly of the fundamental and second modes, except that at very high velocities the fifth mode also becomes important. It is to be expected that the stress pictures at the two mid-span points should be similar, but they will not be identical due to the transient nature of the phenomenon. The total stresses at mid-support are made up only of the even-numbered components, and of these the second mode is by far the most important except at velocities in the region of resonance with the fourth mode.

At the peak corresponding to the lower resonance in the fundamental mode the value of the experimental total stress ratio at mid-span is about 6.2, while the "fundamental"-mode stress ratio has a value of 5.7. The difference is about 10 per cent and

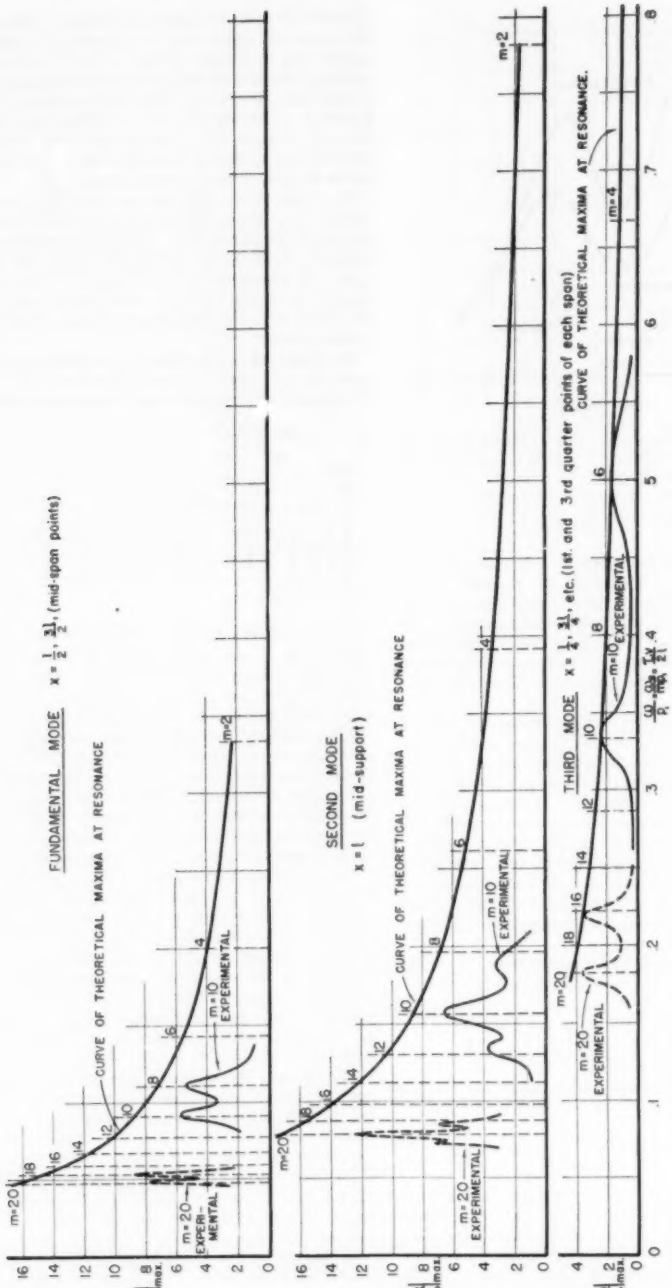


FIG. 4

1 EXPERIMENTAL COMPARISON OF STRESSES IN FUNDAMENTAL, SECOND, AND THIRD-MODE RESONANCE REGIONS
2 EXPERIMENTAL COMPARISON OF STRESS FOR $m = 10$ WITH STRESS FOR $m = 20$
3 CURVES OF THEORETICAL RESONANCE MAXIMA FOR VARIOUS VALUES OF $m$
(At locations giving maximum stresses.)

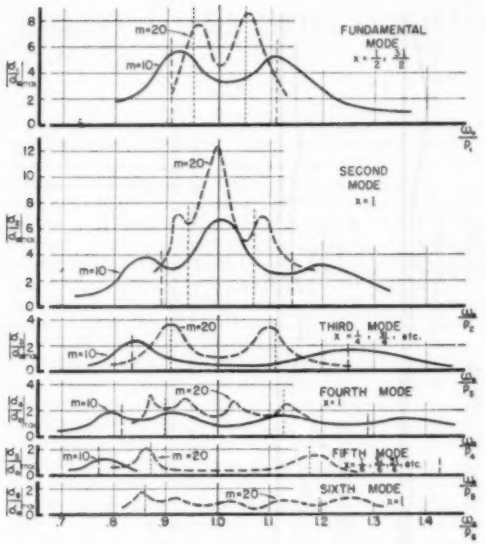


FIG. 5 EXPERIMENTAL COMPARISON OF RESONANCE REGIONS, MODES 1 TO 6, $m$ = 10, 20

(Stress maxima as functions of $\omega/p_1$. At locations giving maximum stresses.)

is due mainly to the presence of the second mode. At the peak corresponding to the stationary resonance in the second mode the total stress ratio at mid-support is 6.5; this is also the ratio for second-mode stress alone. The fourth mode, which is the next contributor to total stress at mid-support, contributes very little stress in this velocity range. Within the limits of measurement the total stress is composed entirely of the second-mode component.

The peaks of the fourth-mode component appear approximately in full value in the diagram of total stress at mid-support and to about one fourth their value, as would be expected, at mid-span. The third mode makes no contribution at either a mid-span point or at mid-support. If total stress had been measured at a first- or third-quarter point, the third mode would have appeared prominently. Note that a mode as high as the fifth can be traced into the total stress diagrams.

Fig. 6 provides an answer to the question: How many, and which, natural modes must be included in a "practical" calculation of total stress? The answer depends mainly upon location and upon resonance.

*Example.* Assume a two-span continuous girder bridge with span lengths $l$ = 200 feet and with a fundamental natural period $\tau_1$ = 0.30 sec. A locomotive with an unbalanced driving mechanism and with driving wheels of 20 ft circumference rolls across the bridge and in doing so sets up a total number of forcing cycles $m$ = 20. Looking at Fig. 4, we see that if $\omega/p_1 = (\tau_1 v)/(2l)$ lies in the approximate range 0.04 to 0.10, resonance with either the fundamental or the second mode may result. The corresponding range in miles per hour is 36 to 91. One means of avoiding resonance would be to operate at speeds above this range, but this has the obvious disadvantage that the unbalanced force $P_c$ would be greatly increased since, in general, it varies as the square of the velocity.

An important comparison can be drawn between single-span and two-span continuous bridges. The fundamental modes of the two types correspond, but the "second" mode of the single-span system is comparable to the "third" mode of the two-span system (1). The lower-resonance region for the 200-ft single-span bridge would then be approximately $\omega/p_1$ = 0.04 to 0.065, or 36 to 59 mph.

## CONCLUSIONS

1 The maximum stress at resonance is approximately proportional to the number of cycles which the alternating force makes in crossing the beam.

2 There may be several resonances associated with each natural mode; the number of resonances depends on the number of the mode and on the number of spans in the beam. For example, in the case of the two-span beam there is a total of five resonances associated with the first two modes.

3 The first two natural modes are both of primary importance in the two-span beam, in contrast with the already known fact that the fundamental mode alone usually gives satisfactory answers for the single-span case. The question of which modes to consider depends on the forcing frequency, i.e., on the velocity with which the alternating force crosses the beam, and on the location at which stress is being calculated. In the near neighborhood of resonance, the resonant mode alone often gives sufficiently accurate answers.

4 When there is more than one span there is an overlapping of resonances. In the single-span case, the second-mode resonances occur at velocities about 4 times the resonant velocity of the fundamental mode, but in the two-span case the second-mode resonant velocities are only about 50 per cent higher than the fundamental.

5 There are two principal limitations on applying the results of the investigation to practical cases, namely, that damping in the beam and in the loading device must be taken into account, and that some mass is always associated with the alternating force vehicle. If the moving mass is a fairly large percentage of the mass of the beam the natural frequencies of the system will vary as the load moves across the beam. The general effect will be a reduction of resonance response. It is planned to investigate these limitations in the future.

## ACKNOWLEDGMENT

The authors are indebted to the following graduate students in Mechanical Engineering: Dr. George Ford for the derivation of the stress equations (6), Mr. Rune Evaldson for assistance in the experiments, and particularly to Mr. C. S. Hsu for assistance in the experiments, calculations, and analysis of the results. This investigation is a part of a contract held by Stanford University and sponsored by the Office of Naval Research.

## BIBLIOGRAPHY

1 "Transverse Vibration of a Two-Span Beam Under Action of a Moving Constant Force," by R. S. Ayre, George Ford, and L. S. Jacobsen, presented at the Semi-Annual Meeting, San Francisco, Calif., June 27–30, 1949, of THE AMERICAN SOCIETY OF MECHANICAL ENGINEERS (Paper No. 49—SA-4).

2 "On the Forced Vibration of Bridges," by S. P. Timoshenko, *Philosophical Magazine*, vol. 43, 1922, p. 1018.

3 "Vibration Problems in Engineering," by S. P. Timoshenko, D. Van Nostrand Company, Inc., New York, N. Y., 1937.

4 "Theory of Transverse Oscillations in Girders and Its Relation to Live Load and Impact Allowances," by Sir Charles E. Inglis, Proceedings of the Institution of Civil Engineers, London, England, vol. 218, 1924, p. 255.

5 "A Mathematical Treatise on Vibrations in Railway Bridges," by Sir Charles E. Inglis, Cambridge University Press, London, England, 1934.

6 "Transverse Vibration of a Two-Span Beam Under the Action of a Moving Force," by George Ford, doctoral dissertation, Stanford University, June, 1948.

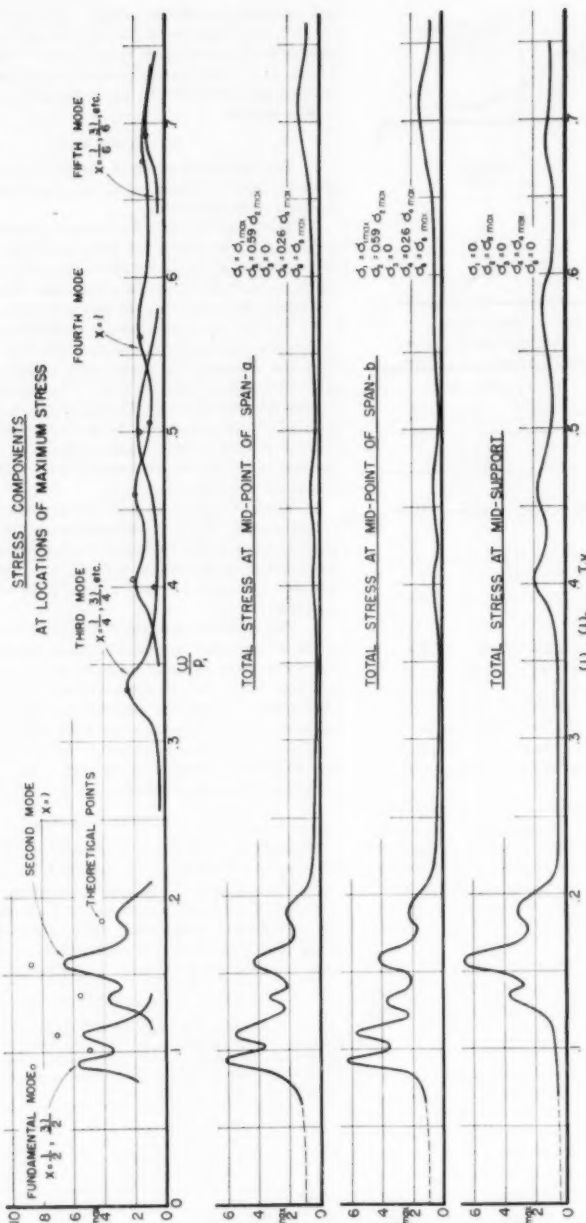


FIG. 6

1 COMPARISON OF EXPERIMENTAL CURVES AND THEORETICAL POINTS FOR FIRST FIVE NATURAL MODES AT LOCATIONS OF MAXIMUM STRESS

2 EXPERIMENTAL COMPARISON OF NATURAL-MODE STRESSES (COMPONENT STRESSES) WITH TOTAL STRESSES AT MID-SPAN AND AT MID-SUPPORT (Number of forcing cycles, $m = 10$.)

# Soap-Film and Sandbed-Mapper Techniques

By A. D. MOORE,[1] ANN ARBOR, MICH.

**A new photographic method for indirect measurement of a soap film is presented. Only one photograph is taken of a spiderweb grid as reflected by the film; the picture is analyzed to find contour lines and lines of maximum slope. Thus the film need last only long enough to be photographed. A fluid mapper of the isolated sandbed type is shown to be an analog for the soap film and, therefore, for the torsional stress situation in a shaft of like boundary. Thus sandbed techniques might replace soap-film techniques. The sandbed mapper also is an analog for other noncircular two-dimensional distributed source situations, such as the following: Field of a space charge; heat flow, with uniform heat production in the volume, the boundary being an isothermal; eddy currents in a plate (or section of lamination) uniformly pierced by a changing flux; magnetic flux in a volume of iron of constant permeability, the iron being (axially) a conductor of uniformly distributed current; streamline fluid flow in a long straight tube (sandbed isopressure lines corresponding to the tube's isovelocity lines); and chemical diffusion, with the diffusing material uniformly appearing or disappearing throughout the volume. Since the sandbed is an analog for the soap film, the soap film is also an analog for these other situations.**

## Introduction

IN a shaft of arbitrary section, finding the torsional stresses can be very difficult. If a slightly inflated soap film is formed on a plane base (film boundary being a copy of shaft boundary), the contour lines correspond to lines of maximum shear. This is a brief statement of the well-known "soap-film analogy." However, the matter of measuring the film offers its own difficulties.

In 1944 the author invented a photographic method for measuring the film, but only recently has time been available for perfecting the method. This method will be described first.

## Apparatus for Soap-Film Photography

The apparatus is shown in Fig. 1. Above the table is a piece of masonite, with the spiderweb-grid drawing attached. The illuminated grid, Fig. 2, has 16 radials, and concentric circles lettered *A* to *J*. On the table is laid a drawing of radial lines only, matching the grid radials and located directly below them. Plate glass rests on the drawing.

The ring for supporting the soap film, Fig. 3, is made of 1-in-wide brass strip, bent to the boundary shape, with ends meeting and soldered. The upper outer edge of the ring is beveled to provide a thin lip. The ring has a bottom and a nipple for tak-

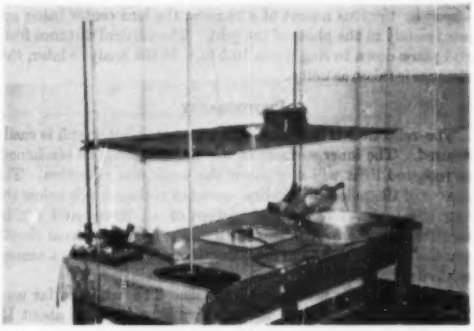

Fig. 1 Apparatus for Photographing Grid Reflection in Soap Film

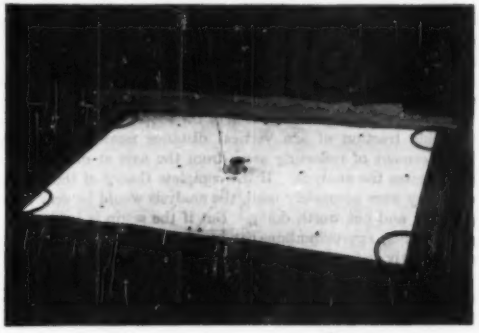

Fig. 2 Looking Up at Spiderweb Grid (Camera lens shows in center hole.)

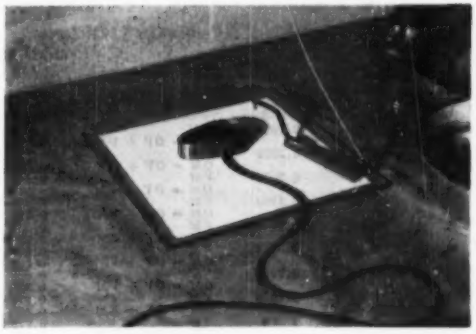

Fig. 3 Soap-Film Can, Pin Gage, Plate Glass, and Drawing of Radial Lines Matching Grid Radials

[1] Department of Electrical Engineering, College of Engineering, University of Michigan.

Contributed by the Applied Mechanics Division and presented at the Semi-Annual Meeting, St. Louis, Mo., June 19–23, 1950, of The American Society of Mechanical Engineers.

Discussion of this paper should be addressed to the Secretary, ASME, 29 West 39th Street, New York, N. Y., and will be accepted until October 10, 1950, for publication at a later date. Discussion received after the closing date will be returned.

Note: Statements and opinions advanced in papers are to be understood as individual expressions of their authors and not those of the Society. Manuscript received at ASME Headquarters, March 27, 1950. Manuscript received by the Applied Mechanics Division August 4, 1949. Paper No. 50—SA-15.

ing the inflating tube. The ring is inverted, dipped in soap solution, and set upright on the plate. After inflation, the tube is clamped. A gage with a pin soldered to the screw can slide on the plate and be used to inflate to a given film peak elevation.

Looking down through the hole in the grid mount, one sees the film and its warped grid reflection. The eye is then replaced by the lens mount of a camera, the lens center being approximately in the plane of the grid. The vertical distance from grid plane down to ring top is 16.5 in. In the analysis later, this distance is taken as unity.

## Photography

The reflection is weak, but an adequate photograph is easily secured. The inner surfaces of the ring box must be blackened, or reflected light will overpower the weak film reflection. The images of the reflected grid lines occur at various levels below the soap film; therefore a sharp picture of all lines could not be secured with the 5 × 7 camera initially tried; its focal length was too great. The 5-cm focal length of a 35-mm Exacta camera worked very well.

A large print is needed for analysis. The prints so far used have been blown up from the negative by a factor of about 15. The trick in printing is to get the lines dark enough, yet leave the soap-film area light enough to facilitate the graphical work.

## Ideal Versus Actual Possibilities

Ideally, the soap film would be placed on the camera axis, with its greatest dimension made very small compared to the distance from soap film to lens. It is easily seen that then a reflected grid circle would be a line of constant slope for the film. But the photographic image would be very small, and it is doubtful if emulsion grain size will permit an ideal setup to be approached.

Therefore the largest dimension of the soap film must be a considerable fraction of the vertical distance named previously. Displacement of reflecting areas from the axis at once greatly complicates the analysis. If the complete theory of the optical geometry were accurately used, the analysis would be very complicated, and not worth doing. But if the setup is held within given limits, approximations can be adopted by which the analysis is greatly compressed; yet high accuracy is retained.

Approximation (1) consists in ignoring the elevation of a soap-film point above the film base, in the analysis. The error thus introduced is very small.

*Grid-Circle Radii and Nominal-Slope Values.* In Fig. 4 let $OU$, the 16.5-in. distance from grid plane to soap-film base, be taken as unity. A point on the film surface on the axis at $U$, if tilted by the angle $\theta$, reflects a point $N$ of the grid, along $OU$, to the lens. $ON$ is tan $2\theta$, and film slope is tan $\theta$. A grid circle of radius $ON$ then has tan $\theta$ as its "nominal slope value." When $N$ is seen at $U$ where there is no lateral displacement, the actual slope is identical with the nominal slope for the $N$-circle.

Convenient nominal slopes are adopted as in column 2, Table 1. Corresponding values of tan $2\theta$, column 3, are found, and used for drawing circles $A$, $B$, $C$, etc., on the grid.

*Displacement of Film Surface Parallel to ON.* Now consider the film surface at $S$, Fig. 4, displaced by $US$ from the axis, reflecting a grid point $N$ to the lens. Point $S$ is in the vertical plane $OUSN$, with its axis of tilt normal to this plane. It would appear to have the nominal slope of the $N$-circle, but its actual slope is less. What is its slope?

$SV$ is vertical. $ON - OV = \tan \alpha$. Thus $\alpha$ can be found. $OV$ is tan $\beta$, thus $\beta$ can be found. $SM$ is the bisector of angle $OSN$, and is normal to the film at $S$. Angle $VMS$ is $1/2\ (\alpha - \beta)$, and $VM = \tan 1/2\ (\alpha - \beta)$. $VM$ is the desired slope.

Adopt convenient values of displacement $OV$, as at the column heads, last seven columns, Table 1. $VM$-values for all such, and for all $A$- to $J$-circles, are worked out. Since $OM = OV + VM$, all corresponding values of $OM$ are found and given in the table.

A chart of $OM$:$OV$ (not included herein) was prepared, with a curve of $OM$ versus $OV$ for each circle. Any desired $OM$-value was then readily found.

*Further Displacement of Film, Normal to Plane OUSN.* A further displacement $SR$, Fig. 5, normal to the vertical plane, is next allowed. The film at $R$ now reflects $N$ to the lens. The plane $ORN$ is normal to the film at $R$; and $RM'$, the bisector of

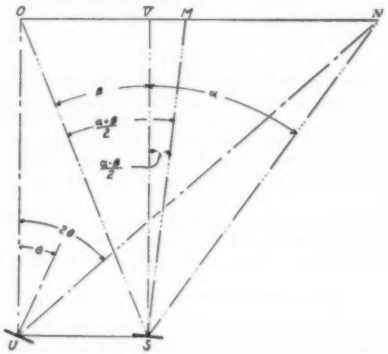


Fig. 4 Reflecting Film Surface Displaced From Axis but Kept in Vertical Plane $OUN$

TABLE 1

| Grid circle letter | Nominal slopes. Adopted values of tan $\theta$ | Grid circle radii tan $2\theta$ | $OV \rightarrow$ | −0.3 | −0.2 | −0.1 | 0 | 0.1 | 0.2 | 0.3 |
|---|---|---|---|---|---|---|---|---|---|---|
| A | 0.05 | 0.1004 | $VM$ | 0.350 | 0.250 | 0.150 | 0.050 | −0.050 | −0.150 | −0.250 |
| | | | $OM = OV + VM$ | 0.050 | 0.050 | 0.050 | 0.050 | 0.050 | 0.050 | 0.050 |
| B | 0.10 | 0.2022 | $VM$ | 0.398 | 0.299 | 0.199 | 0.100 | 0.001 | −0.098 | −0.197 |
| | | | $OM = OV + VM$ | 0.098 | 0.099 | 0.099 | 0.100 | 0.101 | 0.102 | 0.103 |
| C | 0.15 | 0.3070 | $VM$ | 0.445 | 0.346 | 0.248 | 0.150 | 0.052 | −0.046 | −0.143 |
| | | | $OM = OV + VM$ | 0.145 | 0.146 | 0.148 | 0.150 | 0.152 | 0.154 | 0.157 |
| D | 0.20 | 0.4169 | $VM$ | 0.491 | 0.394 | 0.297 | 0.200 | 0.104 | 0.008 | −0.088 |
| | | | $OM = OV + VM$ | 0.191 | 0.194 | 0.197 | 0.200 | 0.204 | 0.208 | 0.212 |
| E | 0.25 | 0.5332 | $VM$ | 0.537 | 0.441 | 0.345 | 0.250 | 0.155 | 0.062 | −0.031 |
| | | | $OM = OV + VM$ | 0.237 | 0.241 | 0.245 | 0.250 | 0.255 | 0.262 | 0.269 |
| F | 0.30 | 0.6594 | $VM$ | 0.583 | 0.486 | 0.392 | 0.300 | 0.208 | 0.117 | 0.027 |
| | | | $OM = OV + VM$ | 0.283 | 0.286 | 0.292 | 0.300 | 0.308 | 0.317 | 0.327 |
| G | 0.35 | 0.7983 | $VM$ | 0.630 | 0.535 | 0.441 | 0.350 | 0.260 | 0.173 | 0.086 |
| | | | $OM = OV + VM$ | 0.330 | 0.335 | 0.341 | 0.350 | 0.360 | 0.373 | 0.386 |
| H | 0.40 | 0.9523 | $VM$ | 0.676 | 0.581 | 0.490 | 0.400 | 0.314 | 0.229 | 0.144 |
| | | | $OM = OV + VM$ | 0.376 | 0.381 | 0.390 | 0.400 | 0.414 | 0.429 | 0.444 |
| I | 0.45 | 1.129 | $VM$ | 0.723 | 0.629 | 0.538 | 0.450 | 0.365 | 0.283 | 0.203 |
| | | | $OM = OV + VM$ | 0.423 | 0.429 | 0.438 | 0.450 | 0.465 | 0.483 | 0.503 |
| J | 0.50 | 1.333 | $VM$ | 0.770 | 0.677 | 0.586 | 0.500 | 0.417 | 0.337 | 0.261 |
| | | | $OM = OV + VM$ | 0.470 | 0.477 | 0.486 | 0.500 | 0.517 | 0.537 | 0.561 |

angle *ORN*, is normal to the film. *RP* is vertical; angle *M'RP* is the angle of tilt from horizontal; the film's slope is *PM'*. Also, *PM'* viewed from above is the horizontal direction of the film's line of maximum slope at *R*.

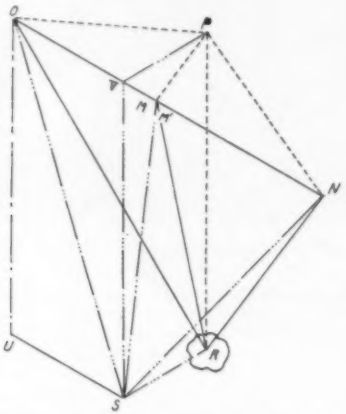


FIG. 5 REFLECTING FILM DISPLACED AS IN FIG. 4, AND FURTHER DISPLACED NORMAL TO PLANE *OUN*

*Approximation (2): M and M' Taken as Coincident.* The two bisectors locate *M* and *M'* as separate points. But analysis is greatly shortened if they are taken as coincident. The author finds that for *VP* of 0.2 or less, with *OV* held between —0.3 and 0.3, and with the *J*-circle as the largest reflected, slope error due to approximation (2) is less than 1 per cent. Point *M'* is then dropped from consideration. *PM* rather than *PM'* is taken as the slope, and as giving the direction of greatest slope.

*Special Scale.* A special scale, hereafter called the "scale," can be drawn on bristol board; it saves a great deal of time. *OU* was taken as unity. If the photographic print were made just full size, one scale unit would be equal to the actual *OU*, or 16.5 in. for this case. With a print larger than full size, the scale unit is longer, being dimension *OU* times the enlargement factor. Herein, the greatest film-ring dimension was 4.5 in., but the same dimension on the picture used was 9.55 in. The scale unit was then (9.55/4.5) × 16.5, or 35.0 in. long. Only that part from zero to 0.45 was needed.

*Film Analysis for Slopes.* Fig. 6 shows part of the reflection of Fig. 7, and part of the undistorted grid. For instance, grid point *N* as reflected at *R* and seen at *P*, is the intersection of circle *A* with radial 1. The grid circles are drawn here to present the theory; they are omitted in actual analysis.

Lay the scale along *ON*, with its zero at *O*. Place a right-angle triangle against it, sliding it until the edge goes through *P*. Read *OV*. Go to the *OM:OV* chart, apply *OV*, read *OM*, apply *OM* to the scale, mark point *M* on Fig. 6. Shift the scale to read *PM*. *PM* is the slope and it gives the slope direction.

In this case, the 11 × 14 photographic paper was mounted on 22 × 28 bristol board; all of the graphical work fell within the area thus provided.

*Approximation (3); Taking OM Equal to Nominal Slope Value.* Much of the analysis work lies in finding *OM*-values, and laying them out. Table 1 shows that for the smaller circles and smaller values of *OV*, *OM*-values nearly agree with nominal-slope values in column 2. By holding *OV* to, say, —0.1 to 0.1, and by limiting film inflation to reflect smaller circles only, *OM* could be held

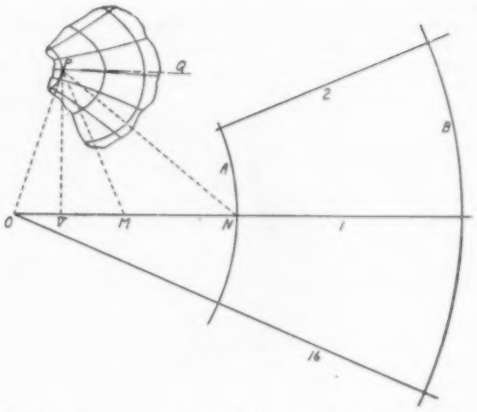


FIG. 6 CONSTRUCTION AS USED IN ANALYSIS OF SOAP-FILM PHOTOGRAPH

to within less than about 2 per cent of the nominal slope. This might bring in a 3 or 4 per cent error in *PM*, at most. If such errors are accepted, or if reduced by still narrower limitations, the *OM:OV* chart and its use are eliminated, and *OM*-values are not plotted. Instead, on the layout, circles are drawn whose radii are the nominal slope values for the grid circles, radii being measured with the scale. Circle intersections with the straight radials give the *M*-positions for finding *PM*-slopes and directions. Much of the work drops out.

Herein, approximation (3) was not used; the range in this setup was such that slope errors of some 12 per cent would have entered in.

*Lines of Greatest Slope.* The *PM* or slope directions at reflected intersections can be indicated by short lines. Curves can be started at the film edge and made to follow these trend lines. These are lines of maximum slope, which converge at the film peak, and are orthogonal to the contour lines. As is seen later, such a line pattern is obtained directly from the sandbed fluid mapper.

*Film Elevations Along Reflected Radials.* In Fig. 6, *PQ* is tangent to the reflected radial at *P*. Since the film's greatest slope is *PM* and in the *PM*-direction, its slope in the *PQ*-direction is less; it is equal to *PM* cos $\phi$, where $\phi$ is angle *MPQ*. The angle is measured and the cosine found; or, use of a cosine chart will save time. The mean of the two *PQ*-slopes for adjacent intersections, times the measured distance, very nearly gives the difference in elevation, if the grid is no coarser than that used here. Elevation differences along a reflected radial are added successively, so that an elevation curve can be plotted. With 16 radials there will be 8 elevation curves; for radials 1 and 9, for example, are continuations of each other. Time is saved by using equal spacings for plotting. When used to get contour lines, positions taken from the elevation curves are put back on the photograph by interpolation.

Using the scale is the quick way to measure distances along reflected radials. However, these are short distances. It is more accurate to use a good commercial scale and convert.

*Soap-Film Contour Lines.* Contour-line data can be read from the elevation curves and used to plot contour-line points on the photograph, Fig. 7. The contour lines shown are for levels at 0.1, 0.3, and 0.7 down from peak to base.

*Soap-Film Peak.* Find the peak elevations of all elevation

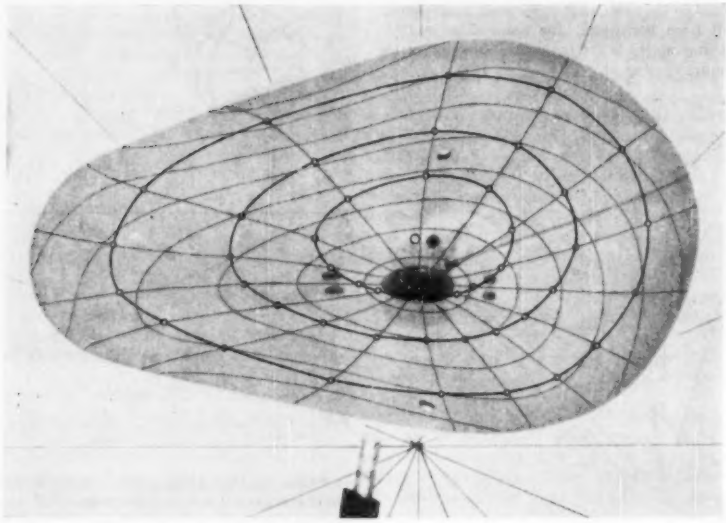

FIG. 7 PHOTOGRAPH OF GRID REFLECTED BY SOAP FILM
(Contour lines and film peak secured by analysis. Camera lens, as reflected, is dark oval near center.)

curves. Plot, at equal intervals, numbering the abscissa points with the grid radial numbers. Draw a smooth curve; this curve's peak gives the film-peak elevation. By inspection, one can tell with good accuracy where to spot the film peak (small circle), Fig. 7.

*Discussion of Soap-Film Analyzed.* Now, instead of thinking of using the elevation curves to find the peak elevation above the film base, think of going down: use them to find how far the film base is below the peak. They should all indicate the same difference in level, namely, 0.170 in., since the gage was used for inflating the peak to this level before photographing. Close agreement was obtained from the curves for where the soap film behaved itself by springing from the lip of the ring, or nearly so. Some disagreement should have been obtained—and was—for where the film was imperfect. With a ring of this design, pull-down is unavoidable; the sharper the ring curvature, the more the film base is pulled down below the ring lip.

This also means that the contour lines shown are for the actual and somewhat imperfect soap film, rather than for an ideal film springing from a plane base.

## THE SANDBED MAPPER

A half-century ago in England, Professor Hele-Shaw[2] did a great deal of splendid pioneering work, proving that streamline flow of a real (viscous) fluid could stimulate magnetic and other fields, and carrying out experimental verifications. He created a very thin uniform flow space between two rectangular pieces of plate glass, the long sides being sealed. Injection of dye streams made streamlines visible. With an unmodified flow space, the flow would be rectilinear. But then, Hele-Shaw modified the thickness of flow space at will, by means of paraffin applied to one plate and scraped down as desired. Two-dimensional curved flow resulted, the fluid tending to avoid the thinner space, and to gather into the thicker space. Magnetic fields through regions of differing permeabilities were thus accurately simulated.

Desiring to go beyond Hele-Shaw's work and to make fluid flow portray the difficult phenomena concerned with a "distributed source," the author invented the "sandbed" form of fluid source in 1943. Also, Hele-Shaw's techniques were inflexible and costly, which may be why they died soon after birth; and the author wished to develop flexible and cheap techniques. Time was found for these developments in 1948–1949. The lower Hele-Shaw plate has been replaced by a slab of artificial stone, and the sandbed techniques have also been worked out. These new "fluid mappers" are described in an earlier paper,[3] which may be consulted for details not included here. In the sandbed type of fluid source, a permeable bed of constant depth provides a uniformly distributed source of fluid in the flow space.

The ring box in Fig. 3 now becomes a sandbed receptacle. It has a level screen, mounted about halfway down. The 70-mesh screen supports the sandbed. The screen is in turn supported by spaced brass rods. There is a plenum chamber below.

The box bottom may be metal, soldered in place, but the author has found an easier bottoming technique. Mix some dental stone plaster (see earlier paper[3]) and spread it on plate glass to a thickness of $^1/_{16}$ in. or a little more. Place the ring down on the plate through the plaster, using it as a cookie cutter. Tap it to settle the plaster. When plaster sets, immerse, slip off the plate, break off outside plaster, and the box is ready.

In Fig. 8 the tray bottom is covered with white paper, to assist the photography. On it is plate glass, invisible. The box sits on the lower plate, as do three brass posts, all as high as the ring. The plenum chamber of the box has been connected to the tank, a corner of which shows at the left. Tray water has been poured in to a depth to cover the upper plate when it will have been placed. Air has been cleared from the tube, and air under the screen has been sucked up through it.

[2] "Lines of Induction in a Magnetic Field," by H. S. Hele-Shaw and Alfred Hay, Philosophical Transactions, series A, vol. 195, 1901, pp. 303–328.

[3] "Fields From Fluid Mappers," by A. D. Moore, *Journal of Applied Physics*, vol. 20, August, 1949, pp. 790–804.

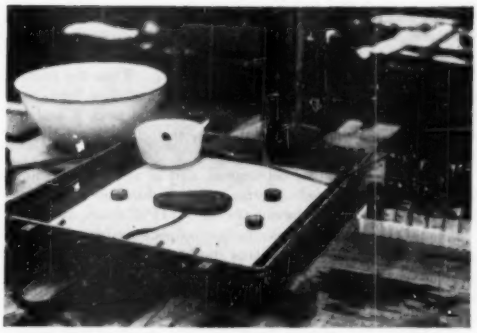

FIG. 8 PREPARING TO BUILD A SHOTTED NICKEL SANDBED

The "sand" used here is a nickel shot, some 18 mils in diameter (at this writing, nickel is still unobtainable on the open market—copper shot is usable and can be had). Shot has been poured in, about enough to fill. Preliminary leveling is done with a small piece of plate glass. The medicine dropper (see earlier paper[3]) is used to remove or add small amounts, until, when the test plate rests on the ring and is moved, nearly all top grains move slightly.

Spacers (three washers checked for equal thickness) are laid on the posts. These will give a flow space of about 37 mils between the sandbed surface and plate, when the top plate is placed on the spacers. Any uniform spacing of around 25 to 50 mils will do for the present sandbed. These "isolated" sandbeds are very easy to build.

*Demonstration and Test of Sandbed.* Potassium-permanganate crystals are sprinkled, which sink to the sandbed and rest thereon. The plate is placed over the bed, on the spacers. With tank water above tray water, upflow occurs through the sandbed, and fluid uniformly appears on top—only to flow away in all directions in the flow space, arriving orthogonally at the isopressure boundary. The pattern appears at once. The colored flow lines are on the bottom of flow, hence are somewhat disturbed and broadened by the sandbed grains. However, this is a quick method for demonstration purposes; and it is a quick test for defects; such as an air bubble under the screen.

*Producing a Sharp Pattern.* A sharp pattern, with the lines and the kernel clearly delineated, is obtained by forming colored streamlines on the flow ceiling. A template is made of bristol board, it being a copy of the boundary. Place it on the (dry) upper plate. Clear "nail polish" (Cutex) is applied to the plate, around the template. Crystals are sprinkled on it while sticky. Place the plate so that the ring of crystals occurs all around the boundary. Lower the tank to make the sandbed become a uniform sink.

Methylene blue in the form of hard little lumpy crystals will give very sharp lines—such having been used in Fig. 9. (The author is still ardently seeking a source of supply for this material. His personal supply was recently increased by a few grams, when a bacteriologist friend unearthed an old bottle which he thinks came from Germany in 1914.)

*Similarity Between Sandbed, Soap Film, and Other Phenomena.* Comparing the film-contour lines in Fig. 7 with the flow lines in Fig. 9, one would suspect orthogonality. This can be proved by the Laplacian theory, or by the following simple argument: Begin with a part of a soap film, referring to Fig. 10. Here is any narrow element of the film running from the peak at $O$ out to the base, confined between maximum slope lines. Taking any part from $O$ out to an arc of width $w$ (the arc being part of a contour line) this part is in equilibrium. Tension forces on the curved radial sides are horizontal; having no vertical components, they are ignored for our purposes. With low inflation, the upward force, closely, is due to the uniform inflation pressure, and $I$ is proportional to the area considered. The downward force equals, approximately, the tension acting on the width $w$, times the slope

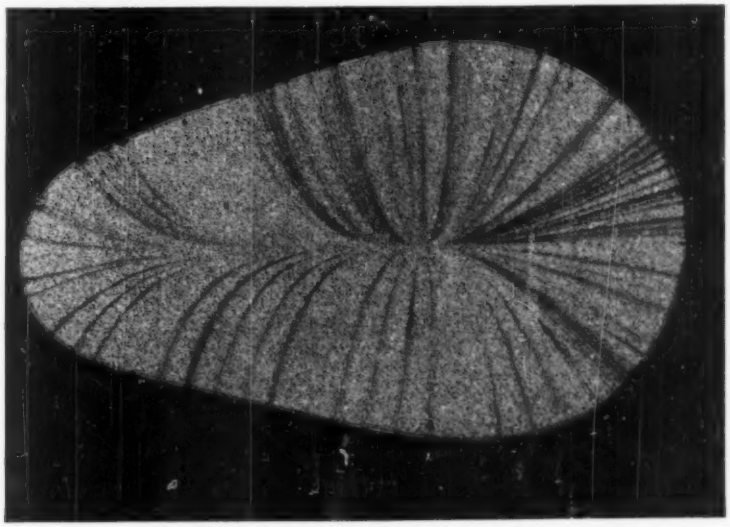

FIG. 9 SANDBED OPERATING AS A SINK
(Visible flow lines colored by methylene blue crystals at edge, stuck to plate.)

at arc $w$; the slope being $dy/dr$, $dy$ being normal to the paper. We then say

$$\text{Area } \alpha\ (dy/dr)w \quad \ldots\ldots [1]$$

Next consider, in a sandbed mapper of like boundary, a narrow flow sector from the kernel at $O$, Fig. 10, to the edge. Fluid crossing the isopressure arc $w$ uniformly appears over the area from $O$ to $w$, the rate at $w$ being in proportion to the area out to $w$. Pressure drop $dp$ over the fluid path length $dr$ at $w$ is proportional to $dr/w$ and to the rate of flow. Thus

$$(\text{Area})\ (dr/w)\ \alpha\ dp$$

or

$$\text{Area } \alpha\ (dp/dr)w \quad \ldots\ldots [2]$$

Consider a heat-flow case, the boundary again being like that just given. Let heat appear uniformly throughout the volume, the boundary being an isothermal. The element, Fig. 10, now represents two-dimensional flow beginning at the hot spot $O$, bounded by two heat-flow lines, and going to the boundary. For a given slice normal to the axis, the heat crossing $w$ is in proportion to the originating area from $O$ to $w$. The temperature drop $dt$, for $dr$, is

$$(\text{Area})\ (dr/w)\ \alpha\ dt$$

or

$$\text{Area } \alpha\ (dt/dr)w \quad \ldots\ldots [3]$$

The identical form of these equations shows that similarity prevails; and the argument can be extended to cover other physical phenomena mentioned early in the paper.

FIG. 10 NARROW CURVED SECTORIAL ELEMENT OF SOAP FILM, BETWEEN MAXIMUM SLOPE LINES; OR, ELEMENT OF SANDBED FLUID FLOW, BETWEEN FLOW LINES; OR, ELEMENT OF FLOW IN A HEAT-FLOW CASE

*Sandbed Flow Lines Orthogonal to Film-Contour Lines.* In Fig. 11 the contour lines were traced from Fig. 7. Then the tracing was placed over the flow pattern, Fig. 9, and flow lines were traced. The close agreement between the film peak $T$ and the sandbed kernel $K$ meets a rather severe test of the similarity involved.

The systems should be orthogonal, and at most intersections this condition is well met. Among many factors tending to spoil the perfection, three will be mentioned: (1) Pull-down, and additional observed imperfections at the soap-film edge, made the film imperfect. (2) Lack of true flatness of the screen caused perhaps 4 per cent variation in sandbed depth, with like variation in uniformity of the fluid source. (3) In printing, the sandbed picture came out 1 per cent larger than the soap-film picture.

*Theory for Flow-Pattern Analysis.* The sandbed picture can be analyzed to find the isopressure lines. In Fig. 11 consider the flow tube $KAB$. Enlarged, this tube appears in Fig. 12, copied from an extra big enlargement. Beginning at $AB$, the tube has been filled in with a number of "curvilinear squares." For example, square 1 is bounded by $AB$ and arc 1 for two sides, and by the flow lines for the other two sides.

For those not familiar with "field mapping," some theory is in order. Assume for the moment that the area described is a curvilinear square. Let $ab$ be drawn, this being a mid-isopressure line; its pressure is halfway between that of arc 1, and $AB$. Also let a mid-flow line be drawn, dividing the flow equally. The original area has been carved into four areas. Continue with such regular subdivision; in the next stage, 16 areas appear, and so on. If, in the limit, the infinitesimal areas approach true squares, then the original was a curvilinear square.

A curvilinear square always represents a volume in the field, taking the axial dimension into account. Curvilinear square volumes have this property; in two-dimensional cases of heat-conduction fields, electric-current flow, magnetic fields, fluid flow in fluid mappers, etc.—all the volumes, irrespective of size or shape of curvilinear square areas, have, within a given field, the same thermal conductance, or the same electrical resistance, or the same magnetic permeance, and so on.

*Drawing Curvilinear Squares.* For quick approximate work, curvilinear squares are sketched in, freehand. For better work, either method about to be described will give good

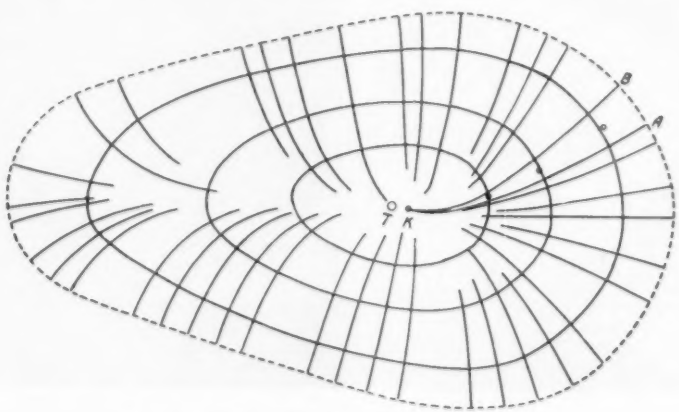


FIG. 11 FILM-CONTOUR LINES AND SANDBED FLOW LINES

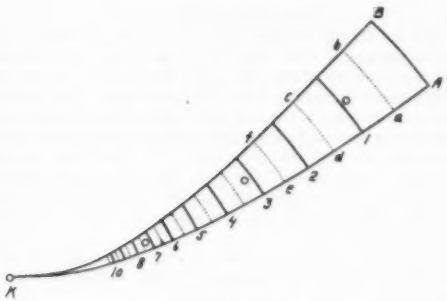


FIG. 12 A FLOW TUBE
(Curvilinear squares have been drawn and tube is ready for analysis.)

TABLE 2

| 1 Arc or square no. | 2 Arc length | 3 (2)² Areas | 4 (3) Σ Up | 5 (4) Σ Down |
|---|---|---|---|---|
| 1 | 10.8 | 116.7 | 326.7 | 326.7 |
| 2 | 8.6 | 74.0 | 210.0 | 536.7 |
| 3 | 6.8 | 46.3 | 136.0 | 672.7 |
| 4 | 5.4 | 29.2 | 89.7 | 762.4 |
| 5 | 4.4 | 19.4 | 60.5 | 822.9 |
| 6 | 3.5 | 12.3 | 41.1 | 864.0 |
| 7 | 2.9 | 8.4 | 28.8 | 892.8 |
| 8 | 2.2 | 4.8 | 20.4 | 913.2 |
| 9 | 1.9 | 3.6 | 15.6 | 928.8 |
| 10 | 1.5 | 2.2 | 12.0 | 940.8 + 60 for remainder |
| Remainder, $\frac{1}{2}(15 \times 1.3) =$ | | | 9.8 | 1000.8 |

accuracy, for curvilinear squares no more distorted away from being true squares than are those of Fig. 12. (1) The average length of two opposite sides will nearly equal that of the other two; a little "fiddling" with a compass enables one to mark off good areas with fair speed. (2) Recommended; the author developed the "circling-in" method in recent years, using the Lietz circle guide. Fit a circle into the outer end of the tube, Fig. 12, touching at 3 places. Draw arc 1 to touch the circle. Continue likewise for square 2, and so on.

In this tube, there was room to put in 10 squares, before the last one became too small for good accuracy. The undivided remainder would hold an infinite number of squares; it will not be forgotten. The dotted arcs *ab*, *cd*, etc., are shown here to help present the theory; in actual work, they are omitted; also in routine work, the solid arcs 1, 2, 3, etc., need not be completed — marking their positions when circling-in is sufficient.

*Flow-Pattern Analysis.* Since all squares represent the same flow resistance, the pressure drop over a square is in proportion to the rate at which fluid passes across it. Now, fluid crossing *AB* out of square 1 is greater than fluid crossing arc 1 into square 1, since some flow originates within square 1. But nearly enough, for narrow tubes, we may take the fluid crossing square 1 as constant, and equal to that originating in the area *Kab*; that for square 2 originates in area *Kcd*, and so on.

The area *abcd* (also a curvilinear square!) is closely found by squaring the chord length of arc 1. In Table 2, column 1, the numbers of squares and arcs are listed; chord lengths, measured in any desired units (0.1 in. being used here) are in column 2, with their squares in column 3. The remainder area is treated as a triangle, measuring the altitude along the curved path. The adding machine is used to fill column 4, by summing column 3 from the bottom up. For example, the area causing flow across square 5 is found to be 60.5, being the remainder area, plus areas around the 5 inner arcs. The figure opposite a square number in column 4 is the relative pressure drop over that individual square.

Column 5 is filled by summing column 4 downward, giving the "total" relative pressures at the arc positions, the base *AB* being taken as at zero pressure.

The pressure drop for the remainder poses a special problem. To solve it, assume that the flow in the region from *K* to arc 8 is the same as if the curved triangle were an undistorted triangle—or simple radial flow over a circular distributed source. The drop in pressure from *K* out then varies with the square of the radius (corresponding to a parabolic soap film, with change of elevation from the peak varying with radius squared). By measuring the curved radii from *K* to arcs 10 and 8, from knowing the drop between these two arcs, and by using the law just cited, the drop from *K* to arc 10 is yielded by a quadratic equation. It came out to be 60.0; which, added to 940.8 for arc 10, gave a relative kernel pressure of 1000.8. The total relative pressures plotted against positions, Fig. 13, give a smooth curve.

At the left end of Fig. 11 some tubes occur in which a remainder may be so very long and slim that it cannot be safely treated, alone, by the foregoing triangle method. In such cases, analyze two or more adjacent tubes by filling inward as far as good squares can be drawn; then throw a common isopressure arc across them; combine the remainders into a single tube, and

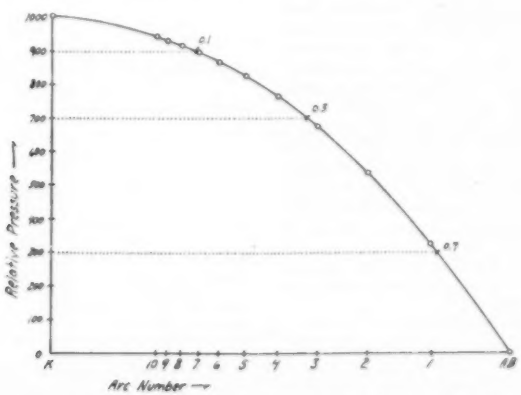


FIG. 13 RELATIVE PRESSURE CURVE FOR FLOW TUBE IN FIG. 12

start a new series of squares; the remainder may then be amenable to triangle treatment. If not, take another combining step.

*Isopressure-Line Locations.* The film-contour lines were found at the 0.1, 0.3, and 0.7 levels, going from peak to base. If we go to Fig. 13 and find points that are at like fractional vertical distances from the peak pressure level, the corresponding isopressure points of the flow tube are located. These have been spotted in by interpolation, Fig. 12, and transferred by proportion to the *KAB* tube, Fig. 11. The agreement is close.

*Limited Analysis.* By either method—soap film or sandbed—it is not required that the entire region be analyzed if the main interest is in local regions of high stress, high density, etc. Only that curved sector running out from the peak or the kernel, and taken broad enough to cover the region of interest, may need analysis.

## Comparison of Methods

Very few appear to have done much by way of direct soap-film measurement. The difficulties in repeating the production of defect-free films of like inflations (when the film breaks) plus measurement difficulties, must be discouraging. As between direct measurement of the soap film; photographic measurement as described here; and the sandbed method, for solving problems by analog, the author's experience is too limited to warrant making a final choice. However, sandbed-pattern analysis does appear to be simpler than analysis of the soap-film photograph. Moreover, the soap-film analogy holds accurately only for near-zero inflation.

In practice, soap-film slopes are kept moderate, but they probably are permitted at times to be large enough to bring in considerable error.

# An Investigation of Ejector Design by Analysis and Experiment

By J. H. KEENAN,[1] E. P. NEUMANN,[2] AND F. LUSTWERK,[3] CAMBRIDGE, MASS.

**A one-dimensional method of analysis of jet pumps or ejectors is presented. The analysis considers mixing of the primary and secondary streams at constant pressure, and mixing of the streams at constant area. For the analytical conditions considered, better performance can be obtained when constant-pressure mixing is employed. A comparison between experimental and analytical results shows good agreement over a broad range of variables. Some experimental data on the length of tube required for mixing of the two streams are presented. A method for jet-pump design is given.**

## Nomenclature

The following nomenclature is used in the paper:

- $a$ = area, sq ft
- $c_p$ = specific heat at constant pressure (ft-lb/lb F) (186.79 for air)
- $c_v$ = specific heat at constant volume (ft-lb/lb F)
- $D$ = minimum diameter of mixing tube
- $d$ = minimum diameter of primary nozzle
- $g$ = acceleration given to a unit mass by a unit force (32.17 ft-$lb_m$/sec$^2$ $lb_f$)
- $h$ = enthalpy (ft-lb/lb)
- $k$ = ratio of specific heats, $c_p/c_v$ (1.4 for air)
- $L$ = length of constant-area section
- $\mathsf{M}$ = Mach number (stream velocity divided by local velocity of sound)
- $\mathsf{M}^*$ = stream velocity divided by velocity of sound obtained with isentropic expansion from local stagnation conditions
- $p$ = pressure, psfa
- $R$ = gas constant (1545 ft-lb/F lb-mole divided by molecular weight)
- $T$ = temperature, deg F abs
- $T_{stag}$ = stagnation temperature, deg F abs
- $V$ = mean stream velocity, fps
- $v$ = specific volume ft$^3$/lb
- $w$ = mass rate of flow, lb per sec
- $x$ = distance from primary nozzle exit
- $y$ = distance from primary nozzle exit to beginning of constant-area portion of mixing tube
- $\alpha$ = ratio of area of mixed streams to area of primary nozzle throat ($a_2/a_t$)
- $\omega$ = ratio of mass rates of flow, secondary stream to primary stream $w''/w'$
- $r$ = ratio of stagnation temperatures, secondary stream to primary stream

*Subscripts (refer also to Fig. 4):*

- $c$ = minimum cross section of diffuser
- $i$ = initial stagnation state of primary stream
- $t$ = cross section at minimum area of primary nozzle
- $x$ = cross section at exit of primary nozzle (for constant-area mixing $x$ and 1 coincide)
- $o$ = initial stagnation state of secondary stream
- 1 = cross section at beginning of minimum area of mixing tube
- 2 = cross section at end of minimum area of mixing tube (state where streams are completely mixed)
- 3 = stagnation state of mixed streams

*Superscripts:*

- $'$ = refers to primary stream
- $''$ = refers to secondary stream

## Introduction

A one-dimensional analysis of the mixing of two gas streams consisting of the application of the equations of continuity, momentum, and energy to the design of ejectors was made by Flügel (1).[4] He considered mixing at constant cross-sectional area and at constant pressure, but the published results of his calculations were meager. Keenan and Neumann (2) applied the same method of analysis to ejectors with large ratios of mixing-tube area to primary-nozzle area and relatively small ratios of primary-inlet pressure to secondary-inlet pressure. They showed in some detail the good agreement between analytical and experimental results.

The present investigation consists of an extension of the comparison of analytical and experimental results for a greater range of variables than that presented in reference (2). The calculated results presented here are almost wholly confined to the special cases which are referred to as *constant-area mixing* and *constant-pressure mixing*.

Assumptions other than constant-area and constant-pressure mixing might be made and might well give superior results for certain conditions. However, all other cases investigated have complicated the analysis to such a degree that the results were open to serious question. No analytical device has been found for determining under all circumstances the mixing process corresponding to optimum ejector performance.

The assumptions selected have yielded a manageable analysis, the results of which are in good agreement with experimental data over the range investigated. By comparison of a few experiments with the analytical results it is possible to design ejectors to accomplish a given purpose.

## Description of Apparatus

The arrangement of the test apparatus is shown in Figs. 1 and

[1] Professor of Mechanical Engineering, Massachusetts Institute of Technology. Mem. ASME.

[2] Associate Professor of Mechanical Engineering, Massachusetts Institute of Technology. Mem. ASME.

[3] Research Associate, Department of Mechanical Engineering, Massachusetts Institute of Technology. Jun. ASME.

Contributed by the Applied Mechanics Division and presented at the Annual Meeting, New York, N. Y., November 27–December 2, 1949, of The American Society of Mechanical Engineers.

Discussion of this paper should be addressed to the Secretary, ASME, 29 West 39th Street, New York, N. Y., and will be accepted until October 10, 1950, for publication at a later date. Discussion received after the closing date will be returned.

Note: Statements and opinions advanced in papers are to be understood as individual expressions of their authors and not those of the Society. Paper No. 49—A-25.

[4] Numbers in parentheses refer to the Bibliography at the end of the paper.

2. Air is supplied to the primary nozzle by a two-stage compressor. Between the compressor and the primary nozzle is a large receiver to smooth out fluctuations in flow and a strainer to remove any solid or liquid particles carried by the air stream. A length of straight pipe is used to reduce disturbances in the air stream before it enters the primary nozzle. Attached to the wall of the secondary chamber is a device for changing the position of the primary nozzle with respect to the mixing tube.

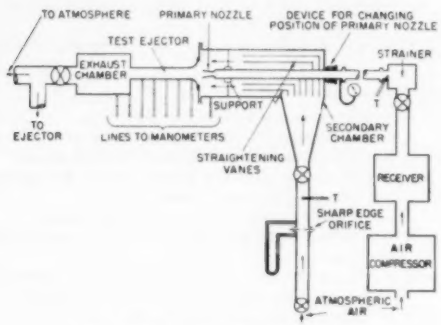


FIG. 1 DIAGRAM OF TEST APPARATUS

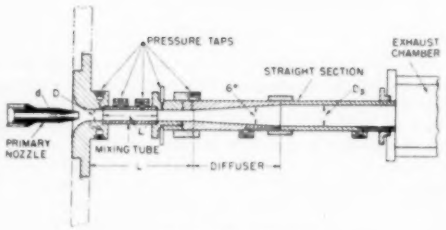


FIG. 2 TEST EJECTOR

The secondary air enters the mixing tube from a large chamber which is provided with straightening vanes. Air enters the chamber through control valves and a sharp-edged metering orifice.

Calibration of the orifices used in the secondary line by means of a gasometer gave results within 1 per cent of ASME values. Flow coefficients for the primary nozzle were obtained by calibrating the nozzle against the secondary metering orifices. The primary nozzle was then used as the metering nozzle for its own flow. The uncertainty in the flows is less than 1 per cent. The flow-ratio uncertainty is slightly more than 1 per cent.

The primary and secondary streams mix in the test ejector and are discharged into an exhaust chamber. The air may be discharged to the atmosphere or to a booster ejector so that back pressures lower than atmospheric may be attained. The pressure in the exhaust chamber is controlled by means of a valve at the chamber exit.

Small holes for measuring static pressure are distributed along the length of the test ejector.

Different values of the length-diameter ratio of the constant-area section are obtained by changing the length $L'$ shown in Fig. 2.

Values of the ratio of cross-sectional area of mixed streams to primary-nozzle throat area of 4, 9, 16, 25, and 100 were obtained by using constant-area sections of 0.400, 0.600, and 1.000 in. diam with primary nozzles of 0.100 and 0.200 in. throat diam.

Fig. 3 shows some of the entrance profiles used in the tests.

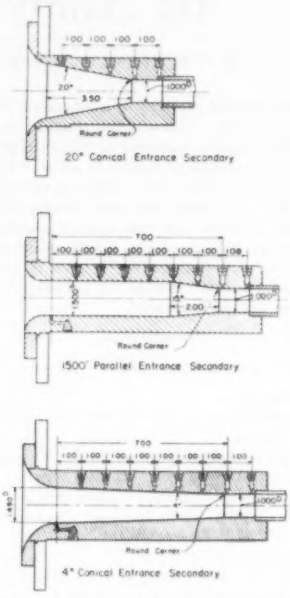


FIG. 3 SOME SECONDARY ENTRANCES USED FOR TESTS

## METHOD OF ANALYSIS

Unless otherwise stated, the analysis employed here is for an ejector of the type shown in Fig. 4. Both streams are assumed to have the same molecular weight and the same ratio of specific heats. Shear forces between the streams and the walls are assumed to be zero. The primary stream is supplied at zero velocity in state $i$ and secondary stream at zero velocity in state $o$. Between sections $i$ and $x$ for the primary stream and $o$ and $x$ for the secondary stream, the processes are isentropic. At section $x$ the two streams meet, and the pressure at this section is assumed to be uniform. For the constant-pressure case, mixing occurs between sections $x$ and 1, for the constant-area case mixing occurs between 1 and 2, and sections $x$ and 1 coincide. Mixing is always complete at section 2. Transverse shocks may occur between sections 1 and 2. At section 3 the velocity is zero and the process between 2 and 3 or $c$ and 3 is isentropic.

A one-dimensional analysis is applied to the mixing of two

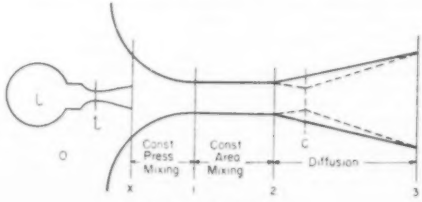


FIG. 4 EJECTOR

streams between section $a$, where they are first exposed to each other, and section $b$, where mixing is complete. Equations [1], [2], [3], [4], and [5] which follow apply to either constant-pressure or constant-area mixing

Momentum equation

$$\Sigma \left(\frac{w}{g} V\right)_a - \left(\frac{w}{g} V\right)_b + (p_a - p_b)a_b = 0 \quad [1]$$

Energy equation

$$\Sigma \left[w\left(h + \frac{V^2}{2g}\right)\right]_a - \left[w\left(h + \frac{V^2}{2g}\right)\right]_b = 0 \quad [2]$$

Continuity equation

$$\Sigma \left(\frac{Va}{v}\right)_a - \left(\frac{Va}{v}\right)_b = 0 \quad [3]$$

Perfect-gas relations

$$pv = RT \quad [4]$$

$$h = c_p T \quad [5]$$

*Constant-Pressure Mixing.* Here section ($a$) becomes ($x$) of Fig. 4, and ($b$) becomes 1, also $p_x = p_1 = p_b$. Equations [1], [2], [3], [4], and [5] can then be combined to obtain a solution for $V_1$ as a function of $p_x$

$$V_1 = -\frac{b}{2}\left(1 \pm \sqrt{1 - \frac{4c}{b^2}}\right) \quad [6]$$

where

$$b = \frac{-\left[2gc_p(T_x - T_o) + \frac{2gk}{k-1}\frac{p_x a_1}{w'} V''_x\right]}{V'_x - V''_x + \frac{2gk}{k-1}\frac{p_x a_1}{w'}}$$

and

$$c = \frac{2gc_p(T_x V''_x - T_o V'_x)}{V'_x - V''_x + \frac{2gk}{k-1}\frac{p_x a_1}{w'}}$$

Equation [6] with the other known quantities ($p_o$, $p_i$, $T_i$, $T_o$, $a_i$, and $a_1$) and the assumptions that processes $i - x$ and $o - x$ are reversible and adiabatic defines state 1. The equation may also be solved in terms of dimensionless quantities, thus

$$\mathbf{M}_1^* = \frac{\mathbf{M}'^*_x + \omega \mathbf{M}''^*_x \sqrt{\tau}}{\sqrt{(1+\omega\tau)(1+\omega)}} \quad [7]$$

where

$$\mathbf{M}^* = \frac{V}{\sqrt{gkRT_{stag}\left(\frac{2}{k+1}\right)}}$$

and

$$\tau = \frac{T_o}{T_i}$$

Values of $\mathbf{M}^*$ have been tabulated for a wide range of values of $k$ and pressure ratios in references (3, 4, 5).

*Diffuser Analysis.* After the completely mixed state has been located at 1, the analytical method for process 1-2-3 depends upon the nature of the diffuser assumed. For example, the conventional relation for pressure rise obtained from reversible adiabatic diffusion would take the form

$$\frac{p_2}{p_1} = \left(\frac{V_1^2}{2gc_pT_1} + 1\right)^{\frac{k}{k-1}} = \left(\frac{k-1}{2}\mathbf{M}_1^2 + 1\right)^{\frac{k}{k-1}} \quad [8]$$

Equation [8] adequately represents experimental results when the velocity at section 1 is subsonic. However, when $V_1$ is supersonic (i.e., $V_1 > \sqrt{gkRT_1}$), Equation [8] no longer gives an adequate approximation to experimental results obtained for supersonic diffusers. Reference (6) shows experimental results for supersonic diffusers.

When supersonic flow exists at section 1 and a transverse compression shock precedes section 2, the pressure rise between sections 1 and 2 can be computed by combining Equations [1], [2], [3], [4], and [5] with the definition of Mach number $\mathbf{M}$, for the case where section $a$ becomes section 1, and section $b$ becomes section 2. Then

$$\frac{p_2}{p_1} = \frac{2k}{k+1}\mathbf{M}_1^2 - \left(\frac{k-1}{k+1}\right) \quad [9]$$

The pressure rise between sections 2 and 3 can then be computed by assuming reversible adiabatic diffusion as in Equation [8].

*Constant-Area Mixing.* Equations [1], [2], [3], [4], and [5] can be applied to constant-area mixing for the case where $a_1 = a_2$. Here section $a$ becomes section 1 of Fig. 1, and section $b$ becomes section (2). A solution for $\mathbf{M}^*_2$ may be obtained in terms of known quantities

$$(\mathbf{M}^*_2)^2 - \mathbf{M}^*_2 \left\{ \frac{k(\mathbf{M}'_1)^* + \omega k\sqrt{\tau}\,(\mathbf{M}''_1)^* + \alpha\left(\frac{k+1}{2}\right)^{\frac{k}{k-1}}\left[1 - \frac{k-1}{k+1}(\mathbf{M}''^*_1)^2\right]^{\frac{k}{k-1}}}{\sqrt{(1+\omega)(1+\omega\tau)}} \right\} + 1 = 0 \quad [10]$$

The analytical results for intermediate values of area ratio ($a_2/a_1$) and pressure ratio ($p_2/p_o$) are shown qualitatively in Fig. 5. The ordinate is either the static pressure ratio $p_2/p_o$, or the stagnation pressure ratio $p_3/p_o$. These curves show the calculated performance with and without a transverse compression shock preceding section 2.

The term shock is used here to denote the standing wave of compression which is characteristic of supersonic flow. The two roots of Equation [6], if neither is imaginary, correspond to the two conditions on either side of a shock.

To attain the pressure corresponding to zero velocity without shock, a convergent-divergent diffuser must follow section 2. Thus, to attain a stagnation pressure at 3 equivalent to that before a shock, the diffuser must take the form of the dashed lines in Fig. 4.

In Fig. 5 the dashed curves show the performance for constant-area mixing, that is, the primary-nozzle exit is at section 1. The solid curves show the performance for constant-pressure mixing, that is, the velocity is uniform at section 1, and the constant-area passage between sections 1 and 2 either serves no purpose or serves as a shock-type diffuser (6).

In Fig. 5, point $A$ on the curve for the static pressure after mixing (constant-pressure case) corresponds to the condition for

which the stream issuing from the primary nozzle fills the cross-sectional area $a_1$ with no secondary flow. Sections $x$ and 1 may then be considered to coincide. Moving along this curve to the right from $A$ corresponds to increasing the area $a_x$. Because of the divergence of the primary stream in attaining the area $a_1$, for condition $A$, the pressure at 1 may be low enough to cause supersonic velocities of the secondary fluid if it expands from $p_o$ to $p_1$. Thus when the area $a_x$ is made larger than $a_1$, the secondary velocities at $x$ are at first supersonic.

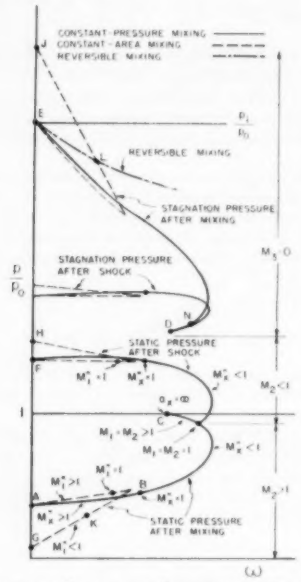


FIG. 5 ANALYTICAL RESULTS FOR INTERMEDIATE PRESSURE RATIOS SHOWN QUALITATIVELY

As the area available to the secondary stream at $x$ increases, the velocity at $x$ decreases until at point $B$ it becomes the sonic value. Further increase in $a_x$ results in subsonic secondary velocities and finally, at point $C$, zero secondary velocity occurs when $a_x$ is infinite. At this point sections $o$ and $x$ coincide and since

$$p_o = p_x = p_1 = p_2$$

it follows that $p_2/p_o$ is unity.

Between $B$ and $C$ the curve usually passes through a point of maximum flow ratio $\omega$. This is the result of the opposing effects of increasing area available to the secondary stream at $x$ and decreasing mass velocity there because $p_x$ is approaching $p_o$.

Since at $x$ the velocity of the primary stream is higher than that of the secondary stream, the velocity of the mixture at 1 can be supersonic when the secondary velocity at $x$ is subsonic. The transition from supersonic to subsonic velocity at 1 is indicated on the curve by the point marked

$$\mathbf{M}_1 = \mathbf{M}_2 = 1$$

If velocities at 1 are supersonic, a shock with a resultant rise in pressure may occur between 1 and 2. The corresponding curve for $p_2/p_o$ is labeled "static pressure after shock" in Fig. 5. The curve labeled "stagnation pressure after mixing" shows by its ordinate the value of $p_2/p_o$ corresponding to reversible diffusion from the section where mixing is complete, to zero velocity. The point $D$ on this line corresponds to point $C$ and the point $E$ to point $A$. The point $E$ represents reversible expansion of the primary stream to the area $a_1$ followed by reversible diffusion back to zero velocity. The pressure $p_2$ is therefore equal to $p_1$ and

$$\frac{p_2}{p_o} = \frac{p_1}{p_o}$$

The curve labeled "stagnation pressure after shock" shows by its ordinate the value of $p_2/p_o$ obtained when a shock is present immediately after mixing. The difference between the stagnation pressure before and after a shock results from irreversibility in the shock.

The point

$$\mathbf{M}_1 = \mathbf{M}_2 = 1$$

moves to a higher pressure ratio as the area ratio $a_2/a_x$ is decreased, or as the pressure ratio $p_1/p_o$ is increased. For a sufficient decrease in area ratio or increase in pressure ratio, the point $C$ corresponds to supersonic velocity at section 2. Fig. 6 illustrates the case where the velocity at point $C$ is supersonic. Point $C'$ corresponds to point $C$ when a shock occurs between sections 1 and 2.

The dashed curves in Fig. 5 (constant-area mixing), show the values of the static pressure, $p_2/p_o$; the curve at the bottom of the figure ($GA$), corresponds to no shock and the curve above, ($HF$), corresponds to a shock between sections 1 and 2. The curves at the top of the figure show the corresponding values of the stagnation pressure, $p_2/p_o$. For no secondary flow with the primary-nozzle exit filling section 1, the constant-area and constant-pressure conditions become identical, as indicated at points $A$, $F$, and $E$.

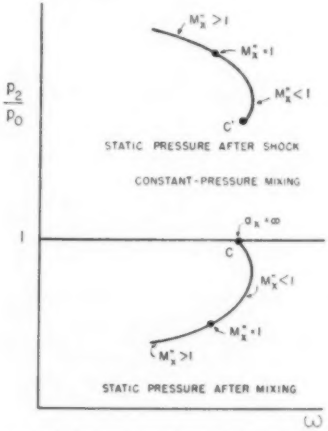


FIG. 6 ANALYTICAL RESULTS FOR LARGE PRESSURE RATIOS SHOWN QUALITATIVELY

Another condition of zero secondary flow is that for which the primary-nozzle exit area is less than $a_1$, but the pressure $p_1$ is equal to $p_o$. This condition is represented by the points $G$, $H$, and $J$. The point $J$ indicates a value of $p_2/p_o$ in excess of $p_i/p_o$, which indicates an adiabatic change of the primary stream from state $i$ to a state 3 of higher pressure and the same enthalpy. State 3 is evidently a state of lower entropy than state $i$ and the condition

corresponding to point $J$ is therefore an impossible one in view of the second law of thermodynamics. Since the entropy does not change between the condition corresponding to point $G$ and that for point $J$, it follows that the condition for point $G$ is also an impossible one.

Somewhere along the constant-area curve between $G$ and $A$, or between $E$ and $J$, is a point marking the boundary between impossible and possible conditions of flow. This point has not been determined accurately. At the points $K$ and $L$ the entropy at sections 2 and 3 is identical with the sum of the incoming entropies at $i$ and $o$. This condition must lie in the impossible region because the mixing process, being irreversible, must cause an increase in entropy. Thus the boundary point must lie between $K$ and $A$ on the curve of $p_2/p_o$ and between $L$ and $E$ on the curve of $p_3/p_o$.

Although the condition for point $H$ cannot be reached by shock from the condition for point $G$, since $G$ represents an impossible condition, nevertheless the condition for point $H$ might be attained by some other procedure. An example of such a procedure would be a shock in the primary stream after leaving the nozzle and before it had spread to fill area $a_1$, followed by spreading at subsonic velocity. Further evidence of the possibility of the condition for $H$ is found in experiments for which values of $p_2/p_o$ closely approximating those for point $H$ have been observed.

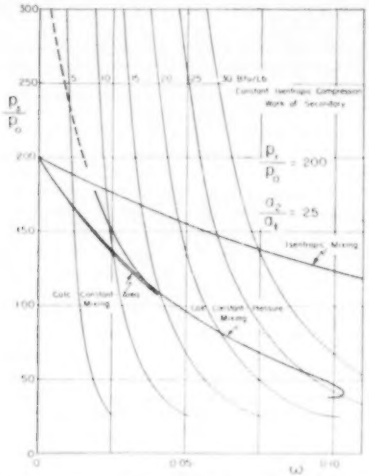


FIG. 7 ANALYTICAL RESULTS FOR REVERSIBLE DIFFUSION

The fact that the analysis predicts conditions at $G$ which are impossible can probably be ascribed to the assumption that the pressure is uniform in the plane of the primary-nozzle exit. Apparently this assumption is not always valid.

Sufficient decrease in area ratio $a_2/a_1$ or sufficient increase in pressure ratio $p_i/p_o$ will cause the curves to retract to the left. They vanish when the cross-sectional area of the primary stream at pressure $p_o$ is $a_1$.

Fig. 7 represents quantitatively the upper portion of Fig. 5. Curves of the stagnation pressure after mixing at constant pressure, constant area, and at constant total entropy are shown. Mixing at constant-total-entropy implies complete reversibility in the mixing process, a condition which could be attained only by the aid of reversible machinery. The machinery might consist, for example, of a reversible turbine for slowing down the primary stream and a reversible impeller for speeding up the secondary stream by means of the work from the turbine. The intersection of this curve with the curve of constant-area mixing corresponds to point $L$ in Fig. 5.

It should be noted that even with reversible diffusion following mixing, a secondary flow 10 per cent as great as the primary flow reduces the stagnation pressure by almost 80 per cent, as compared with the primary stagnation pressure. The reduction would be about one half as great if no irreversibility were to occur in the mixing process.

In Fig. 8 are shown the analytical values for an area ratio of 25 and for pressure ratios $p_i/p_o$, ranging from 8 to 200. In order to improve the distribution of the curves over the chart, the square roots of $p_2/p_o$ and $\omega$ rather than $p_2/p_o$ and $\omega$ themselves have been used as ordinate and abscissa, respectively. It can be seen that the envelope for constant-pressure mixing lies above that for constant-area mixing. Neither curve represents the computed performance of a single ejector since any point on either curve requires a particular primary nozzle, and in the case of constant-pressure mixing, a particular shape of the mixing tube as well. Fig. 9 shows the analytical values for a pressure ratio $p_i/p_o$ of 50 and for area ratios ranging from 6 to 100.

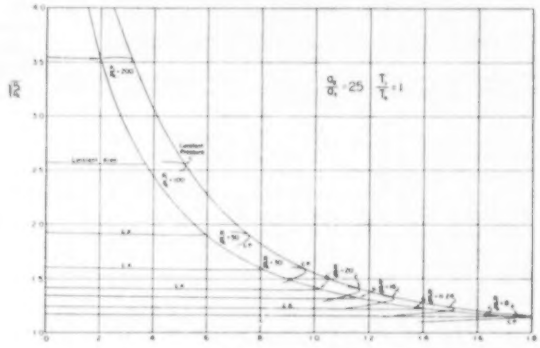


FIG. 8 ANALYTICAL RESULTS FOR CONSTANT-AREA AND CONSTANT-PRESSURE MIXING

(For these curves the diffuser was assumed to consist of a transverse shock at the section where mixing is complete followed by a reversible subsonic diffuser, i.e., the value of $p_i/p_o$ represents the stagnation pressure after a normal shock at the Mach number of the mixed stream.)

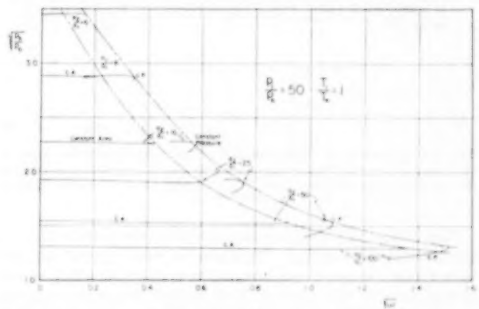


FIG. 9 ANALYTICAL RESULTS FOR CONSTANT-AREA AND CONSTANT-PRESSURE MIXING

(For these curves the diffuser was assumed to consist of a transverse shock at the section where mixing is complete followed by a reversible subsonic diffuser, i.e., the value of $p_i$ represents the stagnation pressure after a normal shock at the Mach number of the mixed stream.)

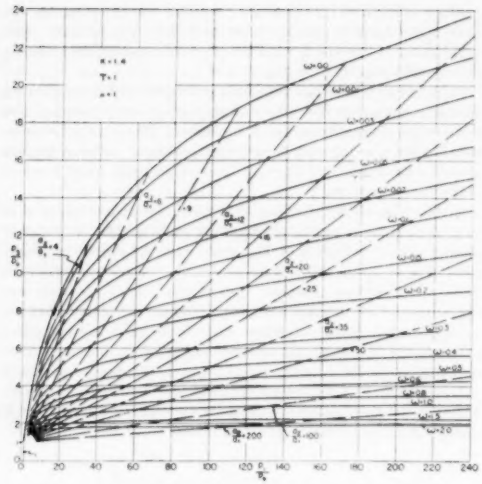

FIG. 10 ANALYTICAL RESULTS FOR CONSTANT-PRESSURE MIXING
(For these curves the diffuser was assumed to consist of a transverse shock at the section where mixing is complete, followed by a reversible subsonic diffuser.)

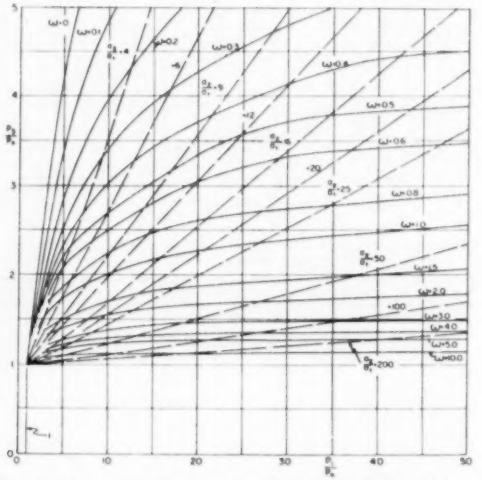

FIG. 11 ANALYTICAL RESULTS FOR CONSTANT-PRESSURE MIXING
(For these curves the diffuser was assumed to consist of a transverse shock at the section where mixing is complete followed by a reversible subsonic diffuser.)

Figs. 10 and 11 present a summary of the computed results for constant-pressure mixing. The data for these figures were obtained from a series of envelope curves, examples of which appear in Figs. 8 and 9. The ordinate $p_3/p_a$ in Figs. 10 and 11 is the ratio of the stagnation pressure after a shock following constant-pressure mixing to the initial stagnation pressure of the secondary stream. In each instance the performance represented here is the best value for the given conditions and for the assumption of shock after mixing.

## COMPARISON BETWEEN EXPERIMENT AND ANALYSIS

*Constant-Area Mixing.* Fig. 12 compares the measured and calculated results for constant-area mixing for values of area ratio $a_2/a_t$ ranging from 4 to 100, and of pressure ratio $p_t/p_a$ from 11.24 to 200. This comparison is made in terms of the ratio of measured to computed static pressure at the mixing-tube exit for a given value of the flow ratio $\omega$. In order to put all data on a comparative basis, the abscissa of Fig. 12 is presented as the ratio of this given value of $\omega$ to the maximum computed value. The data are shown in terms of the static pressure $p_2$ at the mixing-tube exit in order to simplify the experimental procedure by eliminating changes in the diffuser when the ejector geometry is varied. In general, the rise in pressure ratio from $p_2/p_a$ to $p_3/p_a$ in experiments would be slightly less than that indicated by analysis. It has been demonstrated by test data, part of which are presented here as Fig. 13, that the pressure rise across a subsonic diffuser attached to an ejector of sufficient length is approximately the same as for the same diffuser supplied separately with the same mass flow at the same mean pressure and velocity.

To obtain the experimental data on which Figs. 12 and 13 are based, the primary-nozzle exit was located at the entrance to the constant-area mixing tube, i.e., at $y/D = 0$, and the mixing-tube length was in general that value of $L/D$ which gave the highest value of $p_2$.

For the calculated values the exit area of the primary nozzle is always that corresponding to isentropic expansion to the point of

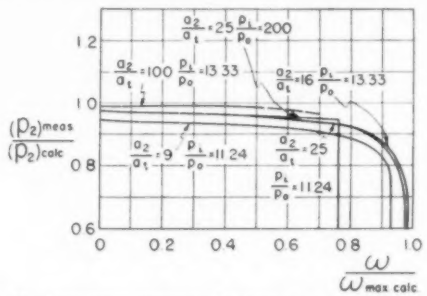

FIG. 12 COMPARISON BETWEEN MEASURED AND CALCULATED RESULTS FOR CONSTANT-AREA MIXING

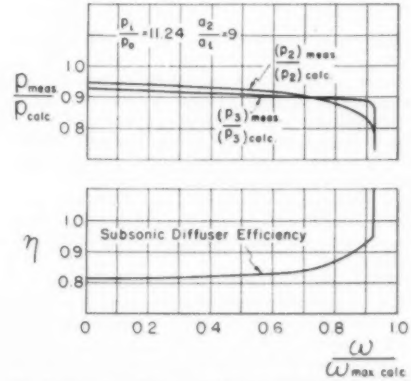


FIG. 13 COMPARISON BETWEEN MEASURED AND CALCULATED RESULTS FOR CONSTANT-AREA MIXING WITH SUBSONIC DIFFUSER

junction of the streams. For any one experimental curve, the exit area of the primary nozzle is fixed. It was usually fixed to correspond to expansion to $p_s$. For this reason, among others, the experimental curves should not be expected to correspond exactly to the analytical ones.

Fig. 12 shows that the measured value of the static pressure $p_2$ is between 93 and 99 per cent of the corresponding computed value for a broad range of conditions. When, however, the measured value of the flow ratio $\omega$ approaches the maximum computed value, the difference between measurement and computation becomes greater. This difference is most pronounced when the area $a_1''$ available to secondary flow is small compared to the area $a_1'$ occupied by the primary stream. Then irreversibilities in the primary nozzle become important. These irreversibilities result in a greater cross section of the primary stream at the nozzle exit than the area computed on the assumption of reversibility. If this increase in area is a large fraction of $a_1''$ the measured value of the maximum $\omega$ will be smaller than the corresponding computed value.

When the area occupied by the primary-nozzle wall, because of its finite thickness, is of the same order of magnitude as $a_1''$, that is, when the dimensions of the ejector are small, the measured secondary flow will be less than the computed secondary flow. In the analysis this wall is assumed to be of zero thickness.

For the curve labeled $a_2/a_1 = 25$ in Fig. 12, the dimensions of the ejector were small and the thickness of the primary-nozzle wall was correspondingly important. Moreover, for a pressure ratio $p_1/p_s$ of 200, the computed value of $a_1''$ was only 26 per cent of $a_1'$. Under these conditions irreversibility in the primary nozzle will reduce greatly the actual area available to the secondary stream. The maximum observed value of the abscissa in Fig. 12 for this condition is therefore only 0.76.

It would not be a difficult matter to correct the analysis for irreversibilities in the primary nozzle and for the finite wall thickness of a given design. In view of the many design variables which are not specified in the analysis, it seems best to omit all coefficients and factors for the sake of simplicity. Such coefficients of course may be introduced in any specific design.

The computed values used in the comparison in Fig. 12 correspond to the curve labeled "static pressure after a shock" in Fig. 5. One could, however, obtain a comparison on the basis of the static pressure before a shock if the pressure at the ejector exit were made low enough.

The schlieren photographs in Fig. 14 give qualitative information on the effect of changing the exhaust pressure. The primary nozzle in this instance was convergent and the pattern of two-dimensional shocks in view *A* is caused by the unguided expansion of the primary stream and the subsequent reflections of these disturbances. This pattern is steady and is fixed by the geometry of the ejector. The striations, visible in the left-hand portion of the illustration, represent streamlines. They were produced by allowing the air to flow over heated wires. In *B* the value of $p_2$ has been doubled, and a shock has appeared in the downstream end of the passage. This is a "transverse shock" of the kind found in the presence of a thick boundary layer. It consists of a mass of two-dimensional shocks extending between boundary layers. It is not anchored to the geometry of the ejector and therefore fluctuates in position so as to blur the image in the photograph. It should be noted that doubling the value of $p_2$ has not affected the value of $\omega$ which is in both instances 0.057. In Fig. 14 *C*, the value of $p_2$ has been raised until the shock has penetrated to the secondary inlet, and the value of $\omega$ has been decreased to 0.052. In Fig. 14 *D*, the shock has passed the secondary inlet and has vanished in the subsonic region. The pressure at the junction of the two streams has been raised to $p_s$ and the secondary flow has been reduced to zero.

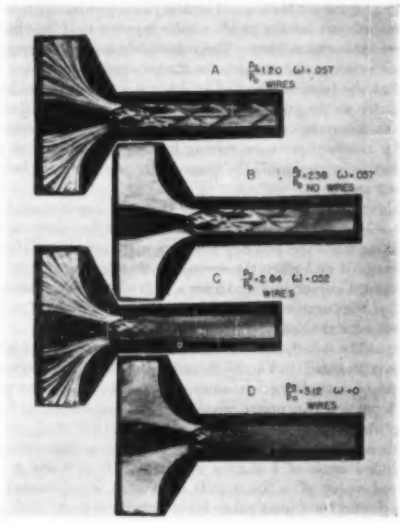


FIG. 14 SCHLIEREN PHOTOGRAPHS, $p_1/p_s = 11.24$, $a_2/a_1 = 4$
(Cross section of mixing tube is 0.504 in. high × 0.270 in. deep.)

When the shock ends at the exit of the constant-area passage, the experimental condition corresponds to the curve labeled static pressure after a shock in Fig. 5. When the shock is completely withdrawn from the constant-area passage by lowering the exhaust pressure, the experimental condition corresponds to the curve labeled "static pressure after mixing." The vertical portion of an experimental curve, such as may be found in Fig. 15, joins these two points with intermediate values which result from the finite length of the actual shock.

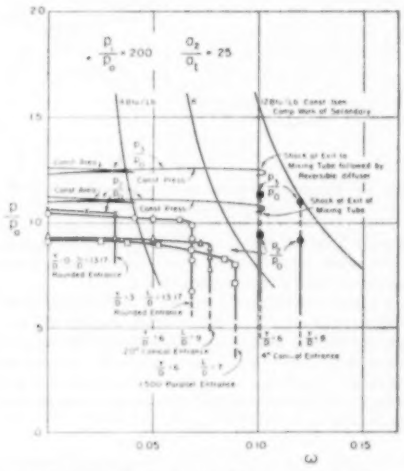


FIG. 15 COMPARISON BETWEEN MEASURED AND COMPUTED RESULTS

*Constant-Pressure Mixing.* The analytical results indicate that constant-pressure mixing yields results superior to those obtained with constant-area mixing. The reasonably good agreement between experiment and analysis for the constant-area mixing indicates that the basic method of analysis is adequate to represent reality. Up to the present time, however, it has been difficult to obtain an accurate comparison between analysis and measurement for constant-pressure mixing because of the lack of a rational means for designing the shape of the passage walls between sections $x$ and 1.

It might be expected, however, that the experimental conditions would approximate the assumptions for constant-pressure mixing when the primary nozzle is withdrawn some distance from section 1 and when the secondary flow is appreciable. The experimental curves in Fig. 15 for a $y/D$ of 6 show values at the "knee" of the curve which roughly approximate those of the constant-pressure analysis.

It should be noted, however, that the computed curves labeled "constant pressure" in Fig. 15, do not represent the computed performance of a single ejector, since each point on these curves requires a particular primary nozzle and a particular shape for the mixing tube.

Points are shown in Fig. 15 for a secondary entrance cone with an included angle of 4 deg for values of $y/D$ of 6 and 8. The measured value of $\omega$ for a $y/D$ of 6 is in close accord with the maximum computed value for constant-pressure mixing, the measured value of a $y/D$ of 8 exceeds the maximum computed value by almost 20 per cent.

Since it is possible to obtain experimental values which exceed the calculated values, the processes experienced by the stream must in some significant way differ from the assumed process. The difference may arise from inadequacy of either or both assumptions regarding, respectively, mixing and diffusion. To test for pressure variation in mixing, static-pressure measurements along the wall of the mixing region were taken. These measurements are shown in Fig. 16. For the cases in which $y/D$ is 6 and 8, the pressure does not depart appreciably from a constant value for the first six tube diameters after mixing starts. For both cases the mean velocity of the mixing streams is supersonic.

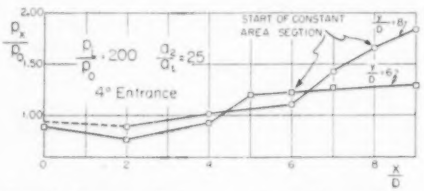


FIG. 16 PRESSURE DISTRIBUTION ALONG MIXING TUBE (4-deg convergent passage.)

Reference 3 indicates that a diffuser more efficient than the transverse shock can be made if a contraction in area occurs between sections 1 and 2, as indicated by Fig. 17.

For a supersonic diffuser involving a contraction, there is a value of the area ratio $a_d/a_c$ below which a shock will not pass through the diffuser for a given Mach number $\mathbf{M}_c$ at entrance. This value of the area ratio can be computed by one-dimensional analysis from energy and continuity considerations if it is assumed that the only irreversibilities present are those encountered in a shock, that is,

$$\left(\frac{a_c}{a_d}\right)_{min} = \frac{1}{\mathbf{M}^*_c}\left[\frac{2 + (k-1)(\mathbf{M}^*_c)^2}{k+1}\right]^{\frac{k+1}{2(k-1)}} \quad \ldots\ldots [11]$$

where $\mathbf{M}^*_c$, the Mach number following a shock at $\mathbf{M}_c$, is given by

$$\mathbf{M}^*_c = \sqrt{\frac{\mathbf{M}_c^2 + \frac{2}{k-1}}{\frac{2k}{k-1}\mathbf{M}_c^2 - 1}} \quad \ldots\ldots [12]$$

If it is assumed that processes $c$-$d$ and $e$-3 are reversible and adiabatic and that a transverse shock occurs between sections $d$ and $e$, the pressure rise from $c$ to 3 can be computed from Equation [8], and the conventional relations for reversible adiabatic flow.

The equation relating pressure rise and Mach number for the diffuser in Fig. 17 is obtained by assuming that a shock takes place at section $d$ and that all other processes are reversible and adiabatic.

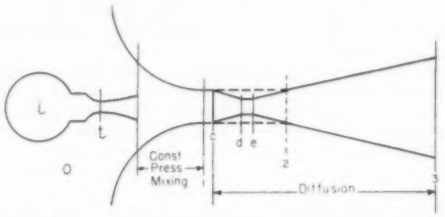


FIG. 17 DIAGRAM SHOWING CONTRACTION IN AREA BETWEEN SECTIONS 1 AND 2 OF NOZZLE DIFFUSER

If it is assumed that the streams are mixed 6 diameters downstream from the primary nozzle, then, for a $y/D$ of 6, mixing would be complete at area $a_2$, and the agreement between measurement and calculation should be good. This is consistent with the data in Fig. 15.

On the same assumption, for a $y/D$ of 8, Fig. 16 indicates convergence of the stream after mixing, with a consequent rise in pressure. If a shock occurs following this convergence, the efficiency of diffusion will be greater than for the assumed condition of a shock immediately after constant-pressure mixing The greater value of $\omega$ and the greater isentropic work of compression may be explained in this fashion.

The experimental curves for the 4-deg conical entrance appearing in Fig. 15, are reproduced as curves $A$ and $B$ in Fig. 18. Curve $D$ is the calculated curve for the same minimum area as in the experimental ejector. In the calculations for curve $D$, it is assumed that isentropic diffusion occurs through the maximum degree of contraction through which a shock will pass. The area corresponding to complete mixing varies along curve $D$.

Curve $B$ shows, as it should, a somewhat poorer performance than the best calculated value of the curve $D$. Curve $B$ represents the best performance obtained with this ejector with variation in $y/D$. It does not, presumably, correspond to the minimum value of $a_e/a_2$ (Fig. 4). Any attempt to reduce $a_e/a_2$ further by withdrawing the primary nozzle will result in placing the primary exit outside the convergent secondary inlet.

Curve $A$, on the other hand, corresponds approximately to the case where the shock exists at the end of the mixing section; that is, to the computed curve $E$. Conditions for curve $A$ are obtained from those of curve $B$ by decreasing the value of $y/D$, that is, the point of "complete" mixing is moved toward the section of minimum area.

For the 4-deg secondary-entrance cone with values of $y/D$ of 6 and 8, it is found that a discontinuity in performance occurs as the back pressure is raised. If the value of $P_3$ is raised sufficiently high, the flow in the secondary inlet reverses in direction

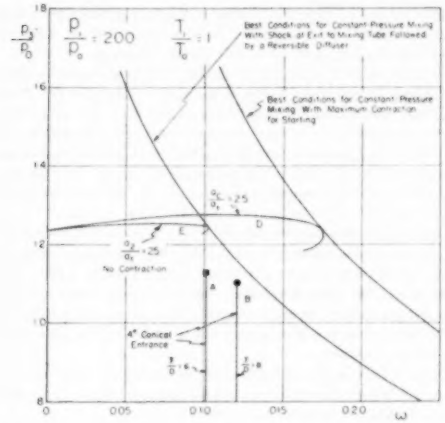


FIG. 18 EXPERIMENTAL RESULTS FOR 4-DEG CONICAL ENTRANCE

and cannot be restored to the original direction without lowering $p_2$ appreciably below the value corresponding to the reversal. This characteristic is consistent with the behavior of supersonic diffusers with convergence before the shock.

### CRITERION FOR BEST PERFORMANCE

If two experimental values having identical ordinates are compared, then the one with the greater value of abscissa may be considered the one of better performance. If two points on the same curve or points on different curves having different values of both co-ordinates are compared, it is not immediately apparent which point represents the better performance.

For fixed values of $p_i/p_o$ and $T_i/T_{oo}$ it may be assumed that the point representing the greater value of the isentropic work of compression of secondary fluid per pound of primary fluid is the better one. This is a comparison of the reversible adiabatic work quantities required to pump the amount of secondary fluid, corresponding to each pound of primary fluid, from state $o$ to $p_2$ or $p_3$. This method of comparison is inadequate for points corresponding to different values of $p_i/p_o$.

In Fig. 15 are shown curves of constant isentropic work of compression of secondary fluid per pound of primary fluid. For each point along any one of these curves the isentropic work of compressing $\omega$ (the value of the abscissa) pounds of secondary fluid from state $o$ through the pressure ratio corresponding to the value of the ordinate is the number of Btu indicated on the curve. In comparing two curves of constant isentropic work, the one for the greater isentropic work corresponds to the better performance. Thus, if the 4-deg entrance case is not considered, the 1.5-in. parallel entrance represents the best performance of Fig. 15.

### REQUIRED LENGTH BEFORE DIFFUSER

For purposes of analysis and also for control of the experimental variables, the ejector was considered to be composed of three parts or processes: namely, the entrance where the primary and secondary streams are accelerated before they meet, the mixing length where the primary stream accelerates the secondary stream, and the diffuser where the mixed stream is decelerated to increase its pressure. It is assumed in the analysis that mixing is complete at the entrance to the diffuser or decelerator; consequently it was necessary to determine experimentally the length required for "complete mixing." An effort was made to do this by holding constant all variables other than the length before the diffuser and measuring the over-all performance of the ejector.

Experimental observations indicate that the length required between the junction of the two streams and the entrance to the subsonic diffuser depends upon both the mixing process and the shock process. When the mixed flow is subsonic, the requirement of mixing dominates; when the mixed flow is supersonic, the requirement of the shock dominates.

The length required for the mixing process was indicated to be 7 to 8 "mixing-tube" diameters in reference (2), where the mixed stream was always subsonic. Some evidence was found of an increase in the required length with an increase in $p_i/p_o$.

The schlieren photographs in Fig. 14 and reference (6) suggest that a length is required for a shock. This is also evident in Fig. 19 which shows the variation in static pressure between sections 1 and 2. The lowest curve on this chart is for supersonic flow throughout. The other curves rise from this lowest curve and represent the pressure rise in the shock. The effect of a rise in back pressure is transmitted only to the upstream face of the shock. In this instance the tube seems to be of the proper length since, for maximum $p_2/p_o$ at maximum $\omega$, the pressure does not decline from frictional effects before section 2. When the secondary flow is zero, the tube is longer than necessary.

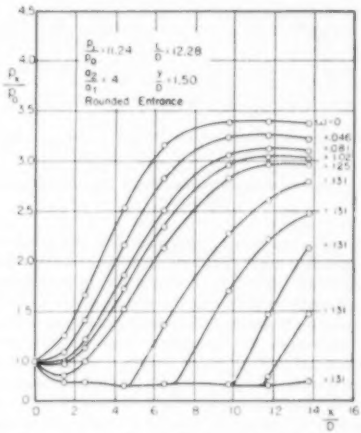


FIG. 19 VARIATION IN STATIC PRESSURE ALONG MIXING TUBE

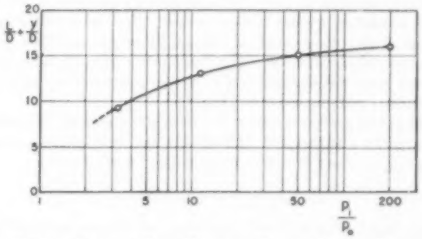


FIG. 20 BEST LENGTH FROM PRIMARY-NOZZLE EXIT TO DIFFUSER ENTRANCE, EXPRESSED AS A FUNCTION OF PRESSURE RATIO

It appears from many different observations, not all of which are presented here, that, regardless of the position of the primary nozzle relative to section 1, the total length from primary exit to

section 2 for best performance is nearly constant when the mixed stream is supersonic. The ratio of this total length to the minimum diameter is a weak function of $p_i/p_o$, as shown in Fig. 20. The nature of this function is much the same as that for a shock in a tube carrying a single stream. When the mixed flow is subsonic the functional relation is different.

*Position of Primary Nozzle.* Even with the best value of the total length the performance varies radically in some instances with $y/D$, that is, the position of the primary nozzle. Fig. 21

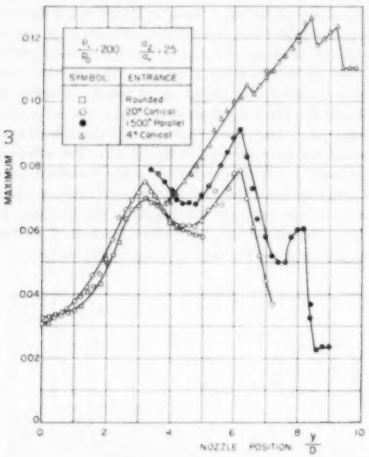


FIG. 21 VARIATION IN MAXIMUM-FLOW RATIO WITH NOZZLE POSITION

shows the variations in maximum $w$ with $y/D$ for four different types of secondary inlet. The four curves have certain characteristics in common. (*a*) They show that for the conditions stated the primary nozzle must be withdrawn some distance from section 1 to get good performance. This observation is consistent with the analytical results. (*b*) They show certain maxima and minima which correspond to given nozzle positions, regardless of the type of secondary inlet. These maxima and minima correspond to the pattern of the primary stream which, because of some unguided expansion beyond the primary exit, repeatedly diverges and converges as it approaches section 1. It appears that if the expanded part of the primary stream occurs at section 1, the secondary stream is obstructed; and if the contracted part occurs at section 1, the secondary stream has best access. The crests and troughs in Fig. 21 doubtless could be reduced by proper selection of the primary-nozzle exit area. The exact effect of such adjustment has not been determined, but it seems probable that little improvement over the crests will result.

The persistent rise of the curve for the 4-deg conical inlet doubtless indicates supersonic diffusion in the convergent passage. This feature was referred to in connection with Fig. 18.

## EXAMPLE OF EJECTOR DESIGN

An ejector using air for the working fluid is to be designed for a pressure ratio $p_i/p_o = 100$ and a stagnation temperature ratio $\tau = T_o/T_i = 1$. This ejector is to pump 0.27 lb of secondary fluid per lb of primary fluid, i.e., $\omega = 0.27$. It is desired to obtain the maximum pressure ratio $p_3/p_o$ across the ejector.

Assume that the pressure-recovery process consists of a transverse shock at the mixed Mach number $\mathbf{M}_1$, followed by a reversible subsonic diffuser. Mixing of the two streams is to take place at constant pressure. For these conditions there will be a best value of $p_x/p_o$ at which to mix the two streams.

The best value of $p_x/p_o$ can be determined by an iteration process. First, for a chosen value of $p_x/p_o$ the quantities $\mathbf{M'}_x{}^*$ and $\mathbf{M''}_x{}^*$ are calculated. Using these along with the prescribed values of $\omega$ and $\tau$, one may calculate $\mathbf{M}_1{}^*$ from Equation [7]. The value of $p_2/p_1$ can be found from $\mathbf{M}_1{}^*$, by conventional means for a normal shock, followed by isentropic diffusion. By repeating this procedure for various values of $p_x/p_o$, the conditions for maximum value of $p_3/p_o$ may be found.

Equation [7] can be solved for $\mathbf{M}_1{}^*$ for the given values of $\omega$ and $\tau$ and for a chosen value of $p_x/p_o$. After $\mathbf{M}_1{}^*$ has been found, the value of $r$ at 1 can be determined from the definition of $\mathbf{M}^*$. This value of $r$ or $\mathbf{M}_1{}^*$ then determines the pressure ratio $p_x/p_2$ for the assumed pressure-recovery process through the conventional ratio of the stagnation pressure after a shock at $\mathbf{M}_1$ to the static pressure before the shock.

Table 1 lists figures compiled to determine the best value of $p_x/p_o$ for the given conditions. A mixing pressure $p_x/p_o = 0.89$ yields the highest value of $p_3/p_o$ of 6.47.

The area ratios $a''_x/a'_x$, $a_t/a'_x$, $a_t/a_1$, corresponding to this value of $p_x/p_o$ can be computed from conventional isentropic relations; thus

$$\frac{a''_x}{a'_x} = \omega \frac{\frac{w'}{a'}}{\frac{w''}{a''}}$$

$$\frac{a''_x}{a'_x} = \left(\frac{p_i}{p_o}\right) \frac{\left(\frac{p_x}{p_i}\right)^{\frac{1}{k}} \sqrt{1 - \left(\frac{p_x}{p_i}\right)^{\frac{k-1}{k}}}}{\left(\frac{p_x}{p_o}\right)^{\frac{1}{k}} \sqrt{1 - \left(\frac{p_x}{p_o}\right)^{\frac{k-1}{k}}}} \omega\sqrt{\tau}$$

$$= \frac{0.0295}{0.001665} \times 0.27 = 4.78$$

$$\frac{a_t}{a'_x} = \frac{\left(\frac{w'}{a'_x}\right)}{\left(\frac{w'}{a_t}\right)} = \frac{\left(\frac{p_x}{p_i}\right)^{\frac{1}{k}} \sqrt{1 - \left(\frac{p_x}{p_i}\right)^{\frac{k-1}{k}}}}{\left(\frac{2}{k+1}\right)^{\frac{1}{k-1}} \sqrt{1 - \left(\frac{2}{k+1}\right)}}$$

$$= \frac{0.0295}{0.259} = 0.114$$

$$\frac{a_t}{a_2} = \frac{\left(\frac{w' + w''}{a_2}\right)\left(\frac{1}{1+\omega}\right)}{\frac{w'}{a_t}}$$

$$= \frac{\left(\frac{p_2}{p_o}\right)}{\left(\frac{p_i}{p_o}\right)} \sqrt{\frac{1}{(1+\omega)(1+\omega\tau)}} \frac{\left(\frac{p_2}{p_3}\right)^{\frac{1}{k}} \sqrt{1 - \left(\frac{p_2}{p_3}\right)^{\frac{k-1}{k}}}}{\left(\frac{2}{k+1}\right)^{\frac{1}{k-1}} \sqrt{1 - \left(\frac{2}{k+1}\right)}}$$

where $p_2/p_3$ is the ratio of the static pressure to the total pressure after a shock at $\mathbf{M}_1{}^*$,

$$\frac{a_t}{a_2} = \frac{6.47}{100} \sqrt{\frac{1}{(1.27)(1.27)}} \frac{0.202}{0.259} = 0.0398$$

TABLE 1 DETERMINING BEST VALUES OF $p_x/p_o$

| $\frac{p_x}{p_o}$ | $M''_x$ | $\frac{p_x}{p_i}$ | $M'_x$ | $M_i$ | $\frac{p_i}{p_x}$ | $\frac{p_i}{p_o}$ |
|---|---|---|---|---|---|---|
| | $\sqrt{\frac{k+1}{k-1}\left[1-\left(\frac{p_x}{p_o}\right)^{\frac{k-1}{k}}\right]}$ | $\frac{p_x}{p_o}/\frac{p_i}{p_o}$ | $\sqrt{\frac{k+1}{k-1}\left[1-\left(\frac{p_x}{p_i}\right)^{\frac{k-1}{k}}\right]}$ | $\frac{M'_x + \omega M''_x \sqrt{\tau}}{\sqrt{(1+w)(1+\omega\tau)}}$ | | $\left(\frac{p_i}{p_x}\right)\left(\frac{p_x}{p_o}\right)$ |
| 0.90 | 0.422 | 0.0090 | 2.107 | 1.748 | 7.18 | 6.46 |
| 0.89 | 0.444 | 0.0089 | 2.108 | 1.753 | 7.27 | 6.47 |
| 0.88 | 0.464 | 0.0088 | 2.109 | 1.759 | 7.34 | 6.46 |
| 0.85 | 0.521 | 0.0085 | 2.113 | 1.774 | 7.59 | 6.45 |

If $a''_x/a'_x$, $a_i/a'_x$, and $a_i/a_2$ are known, the design is determined from a one-dimensional standpoint. At this stage in the design it becomes necessary to make some approximation regarding the shape of the constant-pressure mixing region. No analytical means has been devised whereby the shape of this section can be predicted accurately. However, the results of a limited number of experiments indicate that a cone between $a_x$ and $a_i$ of length $(y + L)/(2D)$ yields results that are a fair approximation to the assumption of constant-pressure mixing. The best value of $(y + L)/D$ is approximated by means of Fig. 20. Then

$$\tan\frac{\theta}{2} = \frac{\sqrt{a_x/a_2} - 1}{\left(\frac{y+L}{D}\right)} = \frac{\sqrt{2.02} - 1}{15.5} = 0.028$$

The constant-area section of diameter $D$ between sections 1 and 2 is then made of length $(y + L)/(2D)$.

Coefficients to account for irreversibilities in the subsonic diffuser and the accelerating nozzles, and for friction along the mixing-tube walls could be added to the design procedure should a more precise prediction be desired. In the procedure adopted here, however, these effects are ignored in the course of the calculation. An over-all allowance can be made for them by empirical factors which may be applied to the computed values of $p_2/p_o$ and $\omega$. For example, an ejector designed according to the foregoing method for $d_i = 0.2$ in. yielded a measured value of $p_2/p_o$ equal to 86 per cent of the computed value at a measured flow of 85 per cent of its computed value.

ACKNOWLEDGMENT

A large portion of this investigation was originated and executed under the sponsorship of the Elliott Company. The investigation was later extended as part of a program at the Massachusetts Institute of Technology under the sponsorship of the Navy Department, Bureau of Ordnance Contract NOrd 9661.

BIBLIOGRAPHY

1 "Berechnung von Strahlapparaten," by G. Flügel, *VDI Forschungsheft*, no. 395, Berlin, Germany, 1939; also *Zeitschrift VDI*, vol. 83, 1939, pp. 1065–1069.

2 "A Simple Air Ejector," by J. H. Keenan and E. P. Neumann, JOURNAL OF APPLIED MECHANICS, Trans. ASME, vol. 64, 1942, pp. A-75–A-84.

3 "The Mechanics and Thermodynamics of Steady One-Dimensional Gas Flow," by A. H. Shapiro and W. R. Hawthorne, JOURNAL OF APPLIED MECHANICS, Trans. ASME, vol. 69, 1947, pp. A-317–A-336.

4 "Tables for Numerical Solution of Problems in the Mechanics and Thermodynamics of Steady One-Dimensional Gas Flow Without Discontinuities," by G. M. Edelman and A. H. Shapiro, JOURNAL OF APPLIED MECHANICS, Trans. ASME, vol. 69, 1947, pp. A-344–A-351.

5 "Gas Tables," by J. H. Keenan and J. Kaye, John Wiley & Sons, Inc., New York, N. Y., 1948.

6 "Supersonic Diffusers for Wind Tunnels," by E. P. Neumann and F. Lustwerk, JOURNAL OF APPLIED MECHANICS, Trans. ASME, vol. 71, 1949, pp. 195–202.

# A Mechanical Analyzer for Computing Transient Stresses in Airplane Structures

By R. L. BISPLINGHOFF,[1] T. H. H. PIAN,[1] AND L. I. LEVY[1]

**A mechanical-analogy-type analyzer is described which is used for computing the transient stresses in an undamped elastic structure. The two main functions of the analyzer are (*a*) to evaluate the stresses due to the deformations of an elastic structure in its various normal modes, and (*b*) to superpose the effects of the modes with proper regard taken of their phase relations. Function (*a*) is accomplished by the use of torsional-pendulum simulators, and function (*b*) by the proper design of the electronic pickup and recording circuit. The analyzer is particularly useful in the determination of dynamic landing stresses in airplane structures.**

## Introduction

THE response of an elastic structure subjected to external impact forces can be represented as a superposition of the responses of the natural modes. When the system is assumed to be undamped, the displacements of the natural modes are uncoupled, and the response of each mode is the same as that of an equivalent single-degree-of-freedom system excited by a generalized force. This general principle has been applied by Biot and Bisplinghoff (1)[2] to the determination of dynamic loads on airplane structures during landing. However, by the methods described in this paper (1), the transient stress is determined by adding, without regard for phase differences, the stresses corresponding to the maximum displacements in a few of the lower modes. The maximum displacements were evaluated by the use of a mechanical analyzer, which was originally designed and constructed by Biot, for computing transient stresses in elastic buildings due to earthquakes (2). The neglect of phase relations, which characterizes the method (1) has been found to lead to overly conservative results. It was considered desirable, therefore, to extend Biot's mechanical analyzer in such a way that it could superpose the stresses corresponding to the various modes with proper regard taken of their phase relations.

This development has been part of a research program on dynamic stresses in airplane structures, sponsored by the Bureau of Aeronautics, Navy Department.

## Transient Stresses in Airplane Structures During Landing

A method for determining transient stresses in undamped elastic structures has been described by Williams (3, 4). In this method the total stresses are considered as the sum of the stresses which would result if the system were restrained against vibrating and the additional stresses resulting from the vibratory motion. In the airplane-landing problem, the stresses computed in the first step, assuming no vibration, result from the rigid-body inertia forces due to translational and rotational accelerations and the external loads. The additional stresses result from the inertia forces corresponding to the acceleration responses of the vibration modes. The Williams method of approach has been followed by other investigators (5, 6), and the mechanical analyzer described in the present paper has been developed on this basis.

The theory of transient stresses in airplane structures during landing proceeds from consideration of an undamped elastic structure with $n$ degrees of freedom under the influence of prescribed external forces. Wind-tunnel tests and theoretical investigations have shown that the neglect of damping is justified when computing stresses resulting from the first shock of landing impact.

The equations of motion defining the deformation of the unrestrained elastic airplane in terms of displacements of the normal free-free modes of vibration are

$$M_r \ddot{q}_r + M_r \omega_r^2 q_r = Q_r(t) \quad r = 1 \ldots n \ldots\ldots [1]$$

where

$$Q_r(t) = \frac{\delta W_r}{\delta q_r} \ldots\ldots [2]$$

In these equations $q_r$ is the displacement of the $r$th normal mode $M_r$ is the $r$th generalized mass, $\omega_r$ is the circular frequency of the $r$th natural mode, and $Q_r$ is the generalized force corrresponding to the $r$th mode. The latter is determined from Equation [2] where $\delta W_r$ is the work done by the forces on the landing gear in a virtual displacement $\delta q_r$ of the $r$th normal mode. The deformation of the structure is assumed to be determined by superposition of the displacements of each of the normal modes. For an undamped system, the generalized forces $Q_r$, are known functions of time, and the equations of motion do not contain terms representing coupling between the co-ordinates. Therefore the equations may be solved independently. With initial conditions $q_r(0) = 0$, $\dot{q}_r(0) = 0$, the solution of Equation [1] may be written

$$q_r = \frac{1}{M_r \omega_r} \int_0^t Q_r(\tau) \sin \omega_r (t - \tau) d\tau \ldots\ldots [3]$$

The total stress pattern for any deformation of the structure may be considered to be a superposition of the stress patterns corresponding to displacements of each of the normal modes. The stress at a particular point $j$ may be expressed by

$$\sigma_j = \sum_{r=1}^{n} A_j^{(r)} q_r \ldots\ldots [4]$$

where the coefficients $A^r_j$, are constants which represent the stress at the $j$th point in the structure due to a unit displacement

---

[1] Department of Aeronautical Engineering, Massachusetts Institute of Technology, Cambridge, Mass.

[2] Numbers in parentheses refer to the Bibliography at the end of the paper.

Contributed by the Applied Mechanics Division and presented at the Annual Meeting, New York, N. Y., November 27–December 2, 1949, of The American Society of Mechanical Engineers.

Discussion of this paper should be addressed to the Secretary, ASME, 29 West 39th Street, New York, N. Y., and will be accepted until October 10, 1950, for publication at a later date. Discussion received after the closing date will be returned.

Note: Statements and opinions advanced in papers are to be understood as individual expressions of their authors and not those of the Society. Paper No. 49—A-8.

in the $r$th normal mode. This is equivalent to the stress produced by the inertia loading associated with a free vibration of unit amplitude in that mode.

If we assume that during the process of applying the external loads, the structure is restrained against vibrating, the displacements of the normal modes may be immediately determined by

$$q_{r(\text{static})} = \frac{Q_r(t)}{M_r \omega_r^2} \quad [5]$$

By substituting Equation [5] into Equation [4], we obtain the static stress at the $j$th point

$$\sigma_{j(\text{static})} = \sum_{r=1}^{n} A_j^{(r)} \frac{Q_r(t)}{M_r \omega_r^2} \quad [6]$$

It is important to observe that the stresses given by Equation [6] are the stresses commonly computed by the airplane designer when he assumes the structure to be rigid. The total displacement of the $r$th normal mode may be computed by rearranging Equation [1] as follows

$$q_r = \frac{Q_r(t)}{M_r \omega_r^2} - \frac{\ddot{q}_r}{\omega_r^2} \quad [7]$$

Upon substituting Equation [7] into Equation [4] and introducing Equation [6] we obtain

$$\sigma_j = \sigma_{j(\text{static})} - \sum_{r=1}^{n} \frac{A_j^{(r)}}{\omega_r^2} \ddot{q}_r \quad [8]$$

This equation shows that the stress in the structure at any instant is equal to the static stress at that instant plus an additional stress which is a linear function of the accelerations of the $n$ normal modes. Since the static stress is that stress usually obtained by the airplane designer when he assumes a rigid structure, it may be computed easily. The accelerations, $\ddot{q}_r$, may be computed by rearranging Equation [1] and substituting the integral expression, Equation [3], for $q_r$

$$\ddot{q}_r = \frac{Q_r(t)}{M_r} - \omega_r^2 q_r$$

$$\ddot{q}_r = \frac{Q_r(t)}{M_r} - \frac{\omega_r}{M_r} \int_0^t Q_r(\tau) \sin \omega_r(t-\tau)\, d\tau$$

and after integrating by parts, if $\dot{Q}_r(0) = 0$

$$\ddot{q}_r = \frac{1}{M_r} \int_0^t \cos \omega_r(t-\tau) \frac{d}{d\tau} Q_r(\tau)\, d\tau \quad [9]$$

Equations [4] and [8] apparently give equivalent results if enough terms of the series are considered. However, because of the labor in evaluating the characteristics of higher modes, only a small number of terms can be taken in a practical problem. Therefore it is desirable, whenever possible, to use the method giving the more rapid convergence of the series. The components corresponding to the static application of the loads are all contained in the first term in Equation [8], while in Equation [4] they are included in each term of the series. This suggests that a more rapid convergence of the series may be obtained by using Equation [8].

Since the generalized forces $Q_r$ are proportional to the external force $F(t)$, the static stress $\sigma_{j(\text{static})}$ is also proportional to $F(t)$. For convenience in computation we express $F(t)$ as

$$F(t) = F_{\max} f(t) \quad [10]$$

where $f(t)$ is a nondimensional function with a maximum amplitude of unity. We see that the stress at a particular point $j$ can be written in the form

$$\sigma_j = B_0 f(t) + \sum_{r=1}^{n} B_r K_r(t) \quad [11]$$

where

$$K_r(t) = \int_0^t \cos \omega_r(t-\tau) \frac{d}{d\tau} f(\tau)\, d\tau \quad [12]$$

The coefficients $B_0$ and $B_r$ are different for different types of stress, such as bending moment, torsional moment, or shear in the wing.

The solution of Equation [12] may be accomplished by numerical or analytical integration. However, both processes are tedious and are often impractical for the designer. Evaluation of the integral in Equation [12] and superposition of the terms in Equation [11] are the chief laborsaving features of the mechanical analyzer which is the subject of the present paper.

## Mechanical Analyzer for Computing Transient Stresses in Elastic Structures

*Fundamental Principles.* The present analyzer is an adaptation of the fundamental principles of the torsional pendulum simulator devised by Biot (2). Biot's machine is limited to problems involving a single vibration mode, whereas the present analyzer has been designed to solve problems in which several deformation modes are involved. Specifically, it was designed to evaluate the following form of Equation [11]

$$\sigma(t) = B_0 f(t) + B_1 K_1(t) + B_2 K_2(t) + B_3 K_3(t) \quad [13]$$

The analyzer has two basic functions, namely, (*a*) to evaluate the integrals $K_r(t)$ in Equation [12], and (*b*) to superpose the various terms of Equation [13]. It will be shown that function (*a*) is accomplished by the use of torsional-pendulum simulators, and function (*b*) by the proper design of the electronic pickup and recording circuits.

Consider the simple torsional-pendulum system shown in Fig. 1, consisting of a pendulum mass which is suspended at its

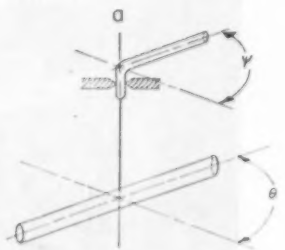


Fig. 1 Simple Torsional-Pendulum System

center by a vertical wire. When the point of suspension $a$ is given an arbitrary angular displacement $\psi(t)$, the angular displacement of the bar, $\theta(t)$, can be expressed by the following differential equation of motion

$$I\ddot{\theta} + K(\theta - \psi) = 0 \quad [14]$$

where

$K$ = torsional stiffness of wire
$I$ = mass moment of inertia of pendulum

This equation may be written as follows

$$\ddot{\theta} + \omega^2 \theta = \omega^2 \psi (t) \quad \ldots\ldots [15]$$

where $\omega^2 = K/I$, the natural frequency of the torsional pendulum when the upper support $a$ is held fixed. Equation [15] is of the same mathematical form as that of a single-degree-of-freedom elastic system subjected to a force of arbitrary time history, which is the form of Equation [1]. If the pendulum is initially at rest, the solution of Equation [15] can be written in terms of Duhamel's integral

$$\theta = \omega \int_0^t \psi(\tau) \sin \omega (t - \tau) \, d\tau \quad \ldots\ldots [16]$$

Solving for $\theta$ from Equation [15], we obtain

$$\ddot{\theta} = \omega^2 (\psi - \theta) = \omega^2 \Delta\theta \quad \ldots\ldots [17]$$

where $\Delta\theta$ is the angle of twist of the pendulum wire.

Another expression for the angular acceleration $\ddot{\theta}$, can be obtained by substituting Equation [16] into Equation [17] and integrating by parts, if $\psi (0) = 0$

$$\ddot{\theta} = \omega^2 \int_0^t \cos \omega(t - \tau) \frac{d}{d\tau} \psi (\tau) \, d\tau \quad \ldots\ldots [18]$$

From Equations [17] and [18] we conclude that

$$\Delta\theta(t) = \int_0^t \cos \omega(t - \tau) \frac{d}{d\tau} \psi (\tau) \, d\tau \quad \ldots\ldots [19]$$

Comparison of this expression with Equation [12] shows that if $\psi(t)$ is proportional to the nondimensional function $f(t)$, $[f(t) = c\,\psi(t)]$, and the pendulum is tuned so that its natural frequency is the same as that of the $r$th mode of the actual system, the relative angular displacement $\Delta\theta$, will be a measure of the function $K_r(t)$, $[K_r(t) = c\ \Delta\theta(t)]$. Actually, for practical applications, it is desirable to have the time scale of the pendulum slower than that of the actual system. When the time scale of the forcing function is multiplied by $n$, the periods of the vibration modes should also be adjusted properly, in order to fulfill the similarity condition. Thus if the pendulum support is displaced at a speed $1/n$ times that of the actual system, the frequency of the pendulum should be made $1/n$ times that of the actual system.

*Description.* The analyzer is illustrated in Fig. 2. It consists of three torsional pendulums ($A$, $B$, and $C$), each of which is made up of a magnesium T-bar ($D$) carrying two movable weights ($E$) and suspended by a steel wire ($F$) to the upper support ($G$). The frequencies of the pendulums may be adjusted by moving the weights along the bar, so that the ratios of their frequencies are comparable to those of the first few natural frequencies of the actual structure. The sizes and the frequency ranges of the different pendulums are listed in Table 1. The upper supports of the pendulums are vertical shafts mounted on ball bearings ($H$), which rest on a steel frame. These shafts are connected by means of a linkage system ($I$), and are linked to a fourth shaft through a pair of spur gears ($J$), having a gear ratio of 1 to 5. The fourth shaft is attached to another wire ($K$), the lower end of which is fixed rigidly to the frame. The fourth shaft is made to turn automatically according to a given displacement-time history by a horizontal cam ($L$), and a long follower arm ($M$). The follower is held against the edge of the cam by a heavy weight ($N$). The cam is driven at 2 rpm by a $^1/_{15}$-hp synchronous motor through reduction gears.

The forcing function $f(t)$, and the time integrals $K_1(t)$, $K_2(t)$ and $K_3(t)$, are proportional to the angles of twist of the fixed-end

TABLE 1 PHYSICAL PROPERTIES OF PENDULUM

| Mode | Wire length, in. | Wire diameter, in. | Bar length, in. | Weight, lb | Frequency range, cycles per sec |
|---|---|---|---|---|---|
| 1 | 28.0 | 0.1340 | 60.0 | 6.35 | 0.108–0.634 |
| 2 | 22.0 | 0.1340 | 48.0 | 6.35 | 0.150–0.914 |
| 3 | 16.0 | 0.1340 | 44.0 | 6.35 | 0.190–1.185 |

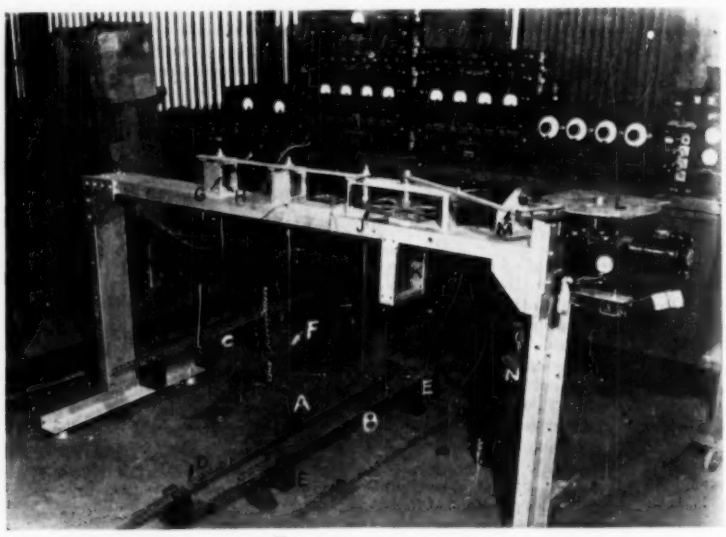


FIG. 2 VIEW OF TRANSIENT ANALYZER

wire and of the three pendulum wires, respectively. The angles of twist are picked up by means of a pair of wire-strain-gage elements (standard high-resistance nichrome wire, 0.001 in. diam) wrapped and cemented in opposite directions around the pendulum wire, at a 45-deg helix angle. These two strain gages are fed into a consolidated bridge-balance channel. The strain gages form two arms of a modified Wheatstone bridge. A center-tapped oscillator winding represents the other two arms, and the oscillator supplies 10 volts at 1000 cycles per sec across the gages. When the wire is twisted, one of the gages is elongated while the other is shortened. This sets the bridge out of balance. A signal proportional to the angle of twist may be taken from the common point of the two gages and the center tap of the oscillator output winding, and fed through an amplifier to the galvanometer of a recording oscillograph.

The magnitudes of all the signals can be attenuated according to the constants $B_r$, of Equation [13], and superposed by means of the transformer circuit shown in Fig. 3. Each strain-gage signal is fed from the bridge circuit into the primary winding of a transformer. A rheostat is connected across the secondary circuit of the transformer for adjusting the magnitude of the signal. With the leads from the four transformers connected as shown, the voltage output of all strain gages can be attenuated and added. This total signal is amplified and fed into one of the channels of the oscillograph. A double-throw switch has been introduced in each circuit to throw the voltage 180 deg out of phase, in order to account for negative values of the constants in Equation [13].

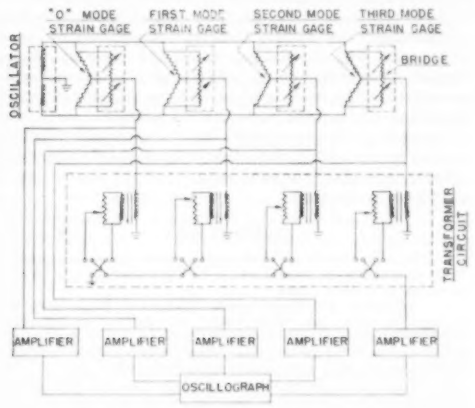


FIG. 3 WIRING DIAGRAM FOR TRANSIENT ANALYZER

## USE AND PROPERTIES OF THE ANALYZER

Prior to using the transient analyzer, it is necessary to determine the relations between the angular displacements of the pendulum wires and the deflections on the oscillograph record. Except for the amplifier and oscillograph, the system possesses perfect linearity. The property of nonlinear characteristics of the recording system at large oscillograph deflections is inherent. However, if the oscillograph deflection is restricted to $\pm 0.6$ in., the entire system is linear, and therefore its use in superposing the signals of the various modes is justified.

In calibrating the analyzer, it is desirable to use a unique displacement parameter which can be measured easily. The angular displacement $\psi$, of the pendulum support in radians can be expressed in terms of the linear displacement $y$, of the follower measured along its circular path, as follows

$$\psi = \frac{n}{r} y \qquad [20]$$

where

$n$ = gear ratio between pendulum shafts and fourth shaft
$r$ = length of follower arm, in.

The relative displacement, $\Delta\theta$, also can be expressed in terms of a reference displacement, $\bar{y}$, according to the following relation

$$\Delta\theta = \frac{n}{r} \bar{y} \qquad [21]$$

It can be seen that if the displacement of the follower varies according to $f(t)$, the displacement $\bar{y}$, corresponding to the $r$th mode pendulum will be $K_r(t)$.

The ratios between the oscillograph deflections and the new displacement parameter $y$, corresponding to the rigid-body mode and the three vibration modes, are denoted by $H_0$, $H_1$, $H_2$, and $H_3$, respectively, and they represent the over-all sensitivities of the system. These sensitivities can be varied by using different attenuation settings for the amplifier and different rheostat settings in the transformer circuit. The range of the rheostat setting has been divided evenly into 100 divisions. Fig. 4 is a typical graph indicating the variation of the sensitivities against the attenuations and rheostat settings.

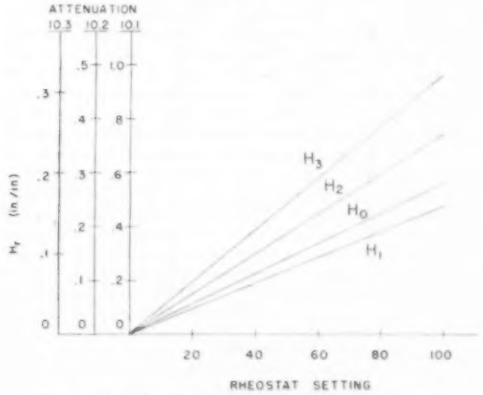


FIG. 4 OVER-ALL SENSITIVITY OF TRANSIENT ANALYZER

In operating the machine, the follower is made to displace according to a time history $y(t)$, which is proportional to $f(t)$, such that

$$[y(t) = y_{max} f(t)]$$

In this case the oscillograph deflection will be

$$x(t) = y_{max} [H_0 f(t) + H_1 K_1(t) + H_2 K_2(t) + H_3 K_3(t)] \qquad [22]$$

Comparing Equation [22] with Equation [13] indicates that the sensitivities of the analyzer should be set according to the following relations

$$H_0 : H_1 : H_2 : H_3 = B_0 : B_1 : B_2 : B_3$$

In addition, it can be seen that

$$\sigma(t) = \frac{B_0}{y_{max} H_0} x(t) \qquad [23]$$

### Example Illustrating Use and Precision of Analyzer

An example illustrating the determination of the transient stresses in an airplane structure during landing is given here to demonstrate the use and accuracy of the analyzer. It is desired to compute the bending moment at the root of the wing of a 23,000-lb seaplane during landing. The airplane weight is assumed to be supported fully by aerodynamic lift forces during the landing period. The stresses, corresponding to the transient motion of the structure due to the landing impact force, may be computed by the transient analyzer and must then be superposed upon those corresponding to the steady-state aerodynamic lift forces and 1 $g$ gravity forces.

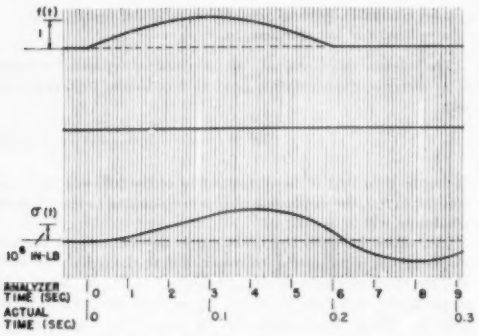


Fig. 5 Oscillograph Record for Computing Bending Moment at Wing Root

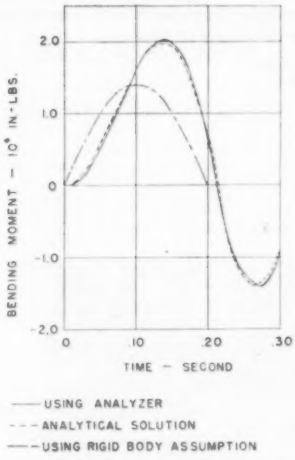


Fig. 6 Bending Moment at Wing Root Due to Landing Impact

The landing-impact force is assumed to act vertically on the hull and directly under the center of gravity of the airplane. The force-time curve of this vertical force is of the form of a half-sine wave, with a period of impact of 0.20 sec. The peak impact load corresponds to a load factor of 3.

In the analysis, the first three symmetrical modes are taken into consideration. Fig. 5 shows the oscillograph record obtained from the analyzer for computing the time-history of the bending moment at the wing root. There are two traces in this record. The upper one is from the signal of the bridge circuit corresponding to the fixed-end wire. This trace is of the same form as the applied impact force, i.e., a half-sine wave. The lower trace is from the summation circuit, and it is proportional to the bending moment at the wing root. It represents the sum of the contributions of the first three natural modes of the wing and the rigid-body mode. The result is replotted in Fig. 6, with the bending moment as ordinate, and the actual time as abscissa. The result from an analytical solution is plotted in the same figure. The stress obtained by using the usual rigid-body assumption also has been plotted for comparison.

Comparison of the curves in Fig. 6 indicates that the maximum bending moment obtained by the analyzer is less than 3 per cent different from the maximum bending moment obtained by an exact analytical method.

### BIBLIOGRAPHY

1 "Dynamic Loads on Airplane Structures During Landing," by M. A. Biot and R. L. Bisplinghoff, NACA Wartime Report No. W-92 (ARR 4410), October, 1944.

2 "Analytical and Experimental Methods in Engineering Seismology," by M. A. Biot, Trans. ASCE, vol. 108, 1943, pp. 365–408.

3 "Displacements of a Linear Elastic System Under a Given Transient Load," by D. Williams, presented at the Sixth Congress of Applied Mechanics, Paris, France, September, 1946.

4 "Dynamic Loads in Aeroplanes Under Given Impulsive Loads With Particular Reference to Landing and Gust Loads on a Large Flying Boat," by D. Williams, ARC Report and Memorandum no. 2221, 1948. (Submitted as RAE reports SME 3309 and 3316, 1945.)

5 "A Method for Predicting Dynamic Landing Loads," by L. S. Wasserman and E. H. Kramer, Engineering Division Memorandum Report, Serial No. MCREXA5-4595-8-2, Air Material Command, Feb. 20, 1948.

6 "Dynamic Loads on Airplane Structures," by E. S. Jenkins and C. D. P. Pancu, presented at the SAE National Aeronautic and Air Transport Meeting, April, 1948. (Abstract of paper published in *SAE Journal*, March, 1949, pp. 70, and 90–91.)

# Elastic-Plastic Analysis of Structures Subjected to Loads Varying Arbitrarily Between Prescribed Limits[1]

By P. S. SYMONDS[2] AND W. PRAGER,[3] PROVIDENCE, R. I.

**Very often in practice a structure is subjected to loads consisting of several components, whose respective maximum and minimum values are known, but whose order and instantaneous magnitudes cannot be specified in advance. For example, an airplane wing might be subjected to dead loads, maneuvering loads, gust loads, etc., whose maximum and minimum values can be estimated closely, but which are applied independently in a manner which is not predictable. Again, a machine part might be subjected to unspecified combinations of bending and torsional loads, whose respective greatest and least values only are known. The present paper deals with the analysis of structures of this kind, when plastic deformation in parts of the structure is permitted in order to obtain the most economical design consistent with safety. Emphasis is placed upon the use of a geometrical representation of the instantaneous state of stress in an appropriate "stress space." For simplicity the present discussion is based upon a pin-jointed plane truss as a typical structure. With appropriate changes of language the concepts developed here may be extended to more general structures and to problems of continua.**

## Introduction

THIS paper is concerned with the analysis of structures subjected to a "total load" which consists of one or more "component loads," whose individual maximum and minimum values only are specified. It is assumed that each one of the component loads may reach either of its extreme values indefinitely many times, and that all of the component loads may vary independently of each other. The primary problem considered here is that of determining whether a given structure will "fail" under a given load of this type. The term "load" here and throughout the paper is used in the sense of "total load," to mean the aggregate of maximum and minimum values of a set of "component loads."

It is first necessary to define what is meant by "failure" of a structure. This term has different meanings, depending upon whether or not wholly elastic behavior is assumed. If elastic behavior is assumed, the structure is said to "fail" if a combination of component loads is applied which causes a critical stress of the material to be exceeded at some point of the structure. If the maximum and minimum values of the component loads are such that the critical elastic stress can be just reached at some point, this would be regarded as a "critical failure load" of the structure. For example, if the component loads are such that the elastic limit is exceeded in parts of the structure the structure generally would be considered as unsafe, according to elastic-design theory. Actually, however, in many cases a structure may continue to perform its functions satisfactorily after plastic flow has occurred in certain of its parts. In these cases the elastic concept of failure is an unrealistic one.

The definition of "failure" which will be adopted here is one which applies in general to a structure subjected to loads which may cause permanent deformations in some of its parts. If the maximum and minimum values of the component loads are such that plastic deformation never ceases, but continues indefinitely in some parts of the structure as the load components take on all possible values within their prescribed ranges, this will be considered a load producing failure. By the phrase "plastic deformation never ceases" is meant that in some part of the structure plastic flow either continues indefinitely in one direction, or continues to alternate between positive and negative values as the loads take on various values.

In the first case, of unlimited flow in one direction, the structure is said to "collapse"; in the second case, even though the deformations are limited in magnitude, the continued alternation of the direction of plastic flow eventually leads to rupture of the material. In either case the structure would be considered "unsafe" on a more realistic basis than that of the elastic analysis.

A "critical failure load" will be defined as a set of extreme values of the component loads such that the structure is just safe, i.e., if these extreme values are all multiplied by a number greater than unity by an indefinitely small amount, failure may occur. The "factor of safety" is defined, as in the elastic case, as the factor by which all of the maximum and minimum values of the "working load" components must be multiplied, to just reach the values of a critical failure load.

The definition of failure just given means that in a safe structure there is eventually set up a system of permanent strains and a corresponding state of residual stresses, under vanishing external loads, such that for all further load applications no further plastic flow occurs in any part of the structure. The structure may then be said to have "shaken down" to a residual stress state on which only elastic stresses are superimposed. Such a state of residual stress will be called a "shakedown state of residual stress," or simply a "shakedown state."

In the present investigation it will be assumed that failure by collapse does not occur, i.e., the type of failure of particular interest here is that in which alternately positive and negative flow continues indefinitely in some part of the structure. Thus if shakedown occurs, any such reversals of plastic flow eventually cease. The critical failure load will mean particularly a set of extreme values of the component loads such that shakedown just

---

[1] The material for this paper was obtained in the course of research conducted under Contract N7onr-358 sponsored jointly by the Office of Naval Research and the Bureau of Ships.

[2] Assistant Professor of Engineering, Brown University.

[3] Professor of Applied Mechanics, Brown University. Mem. ASME.

Contributed by the Applied Mechanics Division and presented at the Annual Meeting, New York, N. Y., November 27–December 2, 1949, of THE AMERICAN SOCIETY OF MECHANICAL ENGINEERS.

Discussion of this paper should be addressed to the Secretary, ASME, 29 West 39th Street, New York, N. Y., and will be accepted until October 10, 1950, for publication at a later date. Discussion received after the closing date will be returned.

NOTE: Statements and opinions advanced in papers are to be understood as individual expressions of their authors and not those of the Society. Paper No. 49—A-3.

occurs; if these are increased by very small amounts shake-down becomes impossible. The condition that shakedown occurs is a necessary and sufficient condition that the structure does not collapse, but the reverse is obviously not true.

When elastic behavior is assumed, the analysis is straightforward, since the effects of the individual load components can be superimposed, and the most unfavorable combination of the component loads can be determined for any one member. In making use of the more realistic concepts of failure, involving plastic flow in parts of the structure, the analysis of shakedown is more difficult, primarily because superposition is no longer valid. The states of stress and strain depend to a great extent upon the previous history of loading, rather than upon the instantaneous load values, alone.

These concepts of failure, of critical failure load, and of factor of safety, for general loading beyond the elastic range are natural extensions of those which have been applied in a more restricted type of elastic-plastic analysis, i.e., that in which all the component loads are assumed to maintain fixed ratios to each other, so that the value of the load at any instant is specified by a single parameter. The problem of determining the value of the load parameter which corresponds to imminent collapse of the structure will be termed the "limit design" problem, to distinguish it from the shakedown problem in which no single load parameter exists.

Published work on this more general problem apparently dates from about 1931. F. Bleich's book (1),[4] published in 1932, contains clear statements of the two types of problems. This book gives several examples of analysis of continuous beams subjected to several independent loads, in which use is made of a theorem due to H. Bleich (2). The only earlier work on this problem, according to F. Bleich, is that of Kazinczy (3) in 1931. Subsequent investigations have been reported by E. Melan (4, 5). The term "shakedown" was apparently first used by Prager (6). The more restricted "limit design" problem has received considerably more attention. Papers by Kist (7), and by Grüning (8) may be cited as among the earliest published, with a notable series of papers published by German and Austrian authors in the early 1930's (see for example the bibliography given by Maier-Leibnitz, ref. 9). More recently an important series of investigations has been carried out by J. F. Baker and his coworkers in England (10, 11). The term limit design is due to Van den Broek (12, 13).

The purpose of the present paper is to introduce a new approach to the general problem of analyzing a structure to determine whether it can safely carry a set of external loads whose maximum and minimum values only are known. This new approach is used to point up the basic features of the problem and to present useful tools for analysis in what seems to be a particularly simple and direct manner.

The basic structure considered in this paper is a statically indeterminate plane truss, with loads applied at the joints. The latter are assumed to be smooth pins, so that each bar is in simple tension or compression. Three particularly simple trusses are discussed in detail, to exemplify the ideas of the paper, and to illustrate important characteristics of the problem. However, it will be evident that with appropriate changes in language other structures and even continuous media can be treated. Reference is made to a forthcoming paper by Neal (14) in which methods similar to those given here are applied to continuous beams and frames. In the latter part of the present paper methods for treating general plane trusses are indicated.

The discussion of the present paper is concerned primarily with the case of materials which exhibit "ideal plasticity," i.e., which flow under constant stress.[5] Thus each bar of the truss is supposed to have a force-extension diagram similar to that shown in Fig. 1(*a*). Each bar is characterized by an elastic coefficient ("spring constant") $c_i$, and by two yield forces, $Y_i$ in tension and $-Y_i'$ in compression. If the point $A$ in Fig. 1(*a*) represents a typical state of force $S_i$ and extension $\Delta_i$ in the $i$th bar, it is seen that the total extension $\Delta_i$ can be expressed as the sum of an elastic part $S_i/c_i$, and a permanent extension $\Lambda_i$, which is the part which remains when the bar force $S_i$ is reduced to zero. Thus, $\Delta_i$ can be written as

$$\Delta_i = S_i/c_i + \Lambda_i \quad [1]$$

However, it will be very convenient in the subsequent developments to use "reduced forces" $s_i$, and "reduced elongations" $\delta_i, \lambda_i$, defined as follows

$$s_i \equiv S_i/\sqrt{c_i}, \quad \delta_i \equiv \Delta_i\sqrt{c_i}, \quad \lambda_i \equiv \Lambda_i\sqrt{c_i} \quad [2]$$

In terms of these reduced forces and extensions, Equation [1] becomes

$$\delta_i = s_i + \lambda_i \quad [3]$$

and the force-elongation diagram takes the form shown in Fig.

[4] Numbers in parentheses refer to the Bibliography at the end of the paper.

[5] The case of materials exhibiting "linear strain-hardening" can be treated in the same framework of ideas, by means of a simple representational device which is discussed in the Appendix.

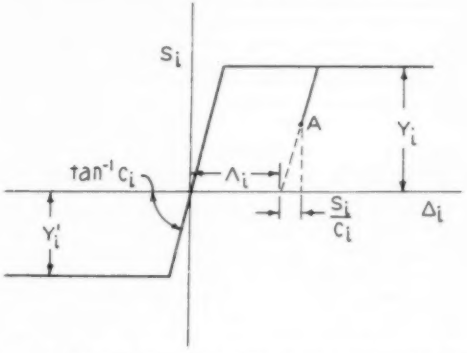


FIG. 1(*a*) ASSUMED FORCE-EXTENSION DIAGRAM OF TYPICAL BAR

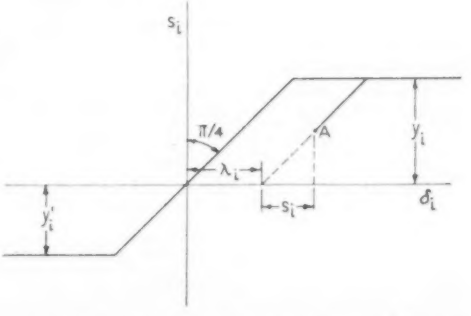


FIG. 1(*b*) "REDUCED FORCE"—"REDUCED EXTENSION" DIAGRAM

1(*b*). The "reduced yield forces," as shown, are $y_i = Y_i/\sqrt{c_i}$ and $y_i' = Y_i'/\sqrt{c_i}$.[6]

Typical trusses of the type under consideration are shown in Fig. 2. In case a support permits motion in one direction, this support may be replaced by a rigid bar perpendicular to the direction of motion, with one end fixed (see, for example, the right-hand support of the truss of Fig. 2). Counting any such bars as

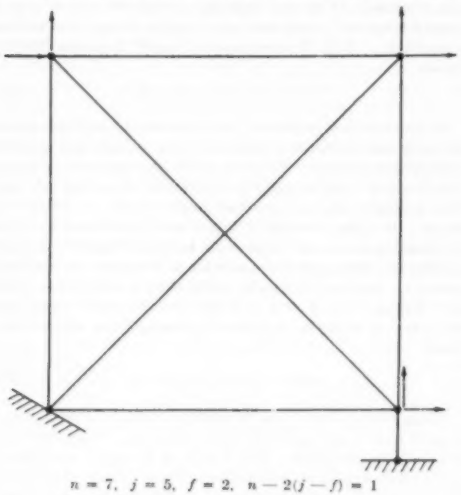

$n = 7,\ j = 5,\ f = 2,\ n - 2(j - f) = 1$

FIG. 2 TYPICAL TRUSS UNDER CONSIDERATION

these, let the total number of bars be $n$, let the total number of joints be $j$, and let the number of fixed joints be $f$. Now the state of stress in the truss is characterized, at any instant, by the $n$ values $(s_1, s_2 \ldots s_n)$. These $n$ quantities may be regarded as the rectangular Cartesian co-ordinates of a point in an $n$-dimensional Euclidean space, and thus the state of stress may be represented by a point in this "stress space" of $n$ dimensions. Moreover, the $n$ quantities $(s_1, s_2 \ldots s_n)$ may be thought of as the components of a vector in this stress space, and the state of stress may be represented by the vector joining the origin to the point with the co-ordinates $(s_1, s_2 \ldots s_n)$. Thus the stress state in the truss at given instant may be denoted conveniently by the vector $s$, using the customary notation for vectors in Euclidean space

$$\underset{\sim}{s} \equiv (s_1, s_2 \ldots s_n) \equiv (s_i) \ldots\ldots\ldots\ldots\ldots [4]$$

The usual rules of vector algebra apply. For example, the sum of two vectors $s'$ and $s''$ is defined as the vector whose components are $s_1' + s_1''$, $s_2' + s_2''$, etc., or more briefly, we may write

$$\underset{\sim}{s}' + \underset{\sim}{s}'' \equiv (s_i' + s_i''),\ i = 1, 2 \ldots n \ldots\ldots [5a]$$

The "scalar product" of two vectors $s'$, $s''$, is

$$\underset{\sim}{s}' \cdot \underset{\sim}{s}'' \equiv s_1's_1'' + s_2's_2'' + \ldots + s_n's_n'' = \sum_{i=1}^{n} s_i's_i'' \ldots [5b]$$

The "magnitude" $s$ of a stress-state vector $\underset{\sim}{s} = (s_i)$ is defined by the relation

$$s^2 = \underset{\sim}{s} \cdot \underset{\sim}{s} = \sum_{i=1}^{n} s_i^2 \ldots\ldots\ldots\ldots [5c]$$

[6] The important questions of rupture (in tension) and of stability (in compression) are discussed in the Appendix.

Two nonzero vectors $\underset{\sim}{s}'$, $\underset{\sim}{s}''$, are said to be "orthogonal" to each other if their scalar product is zero, i.e., if

$$\underset{\sim}{s}' \cdot \underset{\sim}{s}'' \equiv \sum_{i=1}^{n} s_i's_i'' = 0 \ldots\ldots\ldots\ldots [5d]$$

It may be noted at this point that the square of the magnitude of a stress-state vector is equal to twice the corresponding "elastic strain energy" $W$ of the truss, since

$$W = {}^1/_2 \sum_{i=1}^{n} \frac{1}{c_i} S_i^2 \equiv {}^1/_2 \sum_{i=1}^{n} s_i^2 \equiv {}^1/_2\, s^2 \ldots\ldots [6]$$

This relation, which is important in later developments, is the chief reason for introducing the "reduced" variables of force and extension. Another is that the reduced variables have the same dimensions, $\sqrt{\text{force} \times \text{length}}$, and thus a state of deformation may also be represented by a point in the stress space. In particular, the point with co-ordinates $(\lambda_1, \lambda_2 \ldots \lambda_n)$ represents the state of permanent extension. The vector $-\underset{\sim}{\lambda} = (-\lambda_i)$ will be called the "permanent set vector."

The dependence of the stress-state vector $s$ on the applied loads will now be considered. If there are $j - f$ nonfixed joints there are $2(j - f)$ load components which may be prescribed independently. At joint $p$, for example, there are two load components $H_p$, $V_p$. Corresponding to each of the applied load components, there is an equation of equilibrium which relates the given force component to the forces in the bars connected to the joint being considered. For example, corresponding to the load component $H_p$ there is an equation

$$a_{p1}s_1 + a_{p2}s_2 + \ldots + a_{pn}s_n = H_p \ldots\ldots\ldots [7]$$

The coefficients $a_{p1}$, $a_{p2} \ldots a_{pn}$ are numbers which depend only upon the geometry and materials of the truss, but have nothing to do with the state of loading. There are $2(j - f)$ equations of this type. Each of these equations has a simple geometrical interpretation in the $n$-dimensional stress space. Obviously, in a three-dimensional space, each equilibrium equation would define a plane, whose orientation would be fixed by the dimensions and materials of the truss, but whose distance from the origin would be proportional to the value of one load component. In the general case, each equilibrium equation defines a "hyperplane" in the stress space. Since the orientation of each hyperplane is fixed for a given truss, it is evident that, as each load component varies, the corresponding hyperplane simply "translates," remaining parallel to itself.

Now the stress-state point must be one common to all of the hyperplanes which correspond to a given state of loading. In other words, the locus of stress-state points for a given loading is the intersection of all of the $2(j - f)$ hyperplanes corresponding to the $2(j - f)$ given load components. If the truss were a statically determinate one, so that the number of bars $n$ is just equal to $2(j - f)$, then this intersection would be a point. If the truss were simply indeterminate the intersection would be a line, i.e., a subspace of one dimension.

In general, the locus of equilibrium states is a subspace of $n - 2(j - f)$ dimensions.[7] How the actual stress-state point is singled out from the possible equilibrium state points is determined by the requirements of geometrical compatibility of the bar extensions. In the elastic case, of course, the answer can be given at once by means of Castigliano's theorem of minimum strain energy, which says that of all the possible states the one closest to

[7] This implies that the bars meeting at a joint are not all parallel. There is only one equation of equilibrium at a joint connecting parallel bars. The term "truss" will be used also for these cases, for the sake of simplicity. The modifications in the present discussion are obvious.

the origin is the actual one. Thus, the perpendicular dropped from the origin onto the subspace of equilibrium states singles out the actual stress state, in this case. However, when plastic deformations in some of the bars are allowed to occur, this is no longer generally true. Then the actual stress depends very much upon the previous loading history, and not simply upon the instantaneous state of loading. Theorems for locating the stress-state point in the elastic-plastic case are considered in the next section.

Thus far the assumed yield conditions have not been taken into account. The assumption of ideal plasticity, as indicated by Fig. 1(*b*), means that each bar force $s_i$ must lie within the range $-y_i'$ to $y_i$, i.e., each $s_i$ is governed by an inequality

$$-y_i' \leqq s_i \leqq y_i \quad [8]$$

Interpreted geometrically, the force $s_i$ must not lie outside the two planes, $s_i = y_i$ and $s_i = -y_i'$, in the stress space. Since each bar force has its own pair of limiting planes, the stress-state point must lie within, or on the surface of, the parallelopiped in stress space which is defined by the $2n$ yield planes. This will be termed the "yield parallelopiped."

Some additional relations which are implied by the term "ideal plasticity" will now be given. If $s_i$ does not have the value $y_i$ or $-y_i'$ then there is no change in the (reduced) permanent deformation $\lambda_i$. In other words, then the time rate of change $\dot{\lambda}_i$ is zero. Furthermore $\dot{\lambda}_i$ is also zero if $s_i = y_i$, but if $s_i$ is decreasing; or if $s_i = -y_i'$, but if $s_i$ is increasing. These facts may be expressed concisely as follows

$$\text{when} \quad \left\{ \begin{array}{l} -y_i' < s_i < y_i \\ s_i = y_i,\ \dot{s}_i < 0 \\ s_i = -y_i',\ \dot{s}_i > 0 \end{array} \right\} \quad \text{then } \dot{\lambda}_i = 0 \quad [9a]$$

A further consequence of ideal plasticity is that the product $\dot{s}_i \dot{\lambda}_i$ is zero for each bar, since if $s_i$ is changing then $\dot{\lambda}_i$ must be zero, and contrarily if $\dot{\lambda}_i$ is changing then $\dot{s}_i = 0$ (and either $s_i = y_i$ or $s_i = -y_i'$). Finally, the rate of doing plastic work is positive, i.e., for any bar which is yielding the product $s_i \dot{\lambda}_i$ must be positive. For any bar which is not yielding it is, of course, zero. These last two facts can be expressed concisely as

$$\sum_{i=1}^{n} \dot{s}_i \dot{\lambda}_i \equiv \underline{\dot{s}} \cdot \underline{\dot{\lambda}} = 0 \quad [9b]$$

$$\sum_{i=1}^{n} s_i \dot{\lambda}_i \equiv \underline{s} \cdot \underline{\dot{\lambda}} \geqq 0 \quad [9c]$$

These relations will be used in the following section.

## Theorems for Elastic-Plastic Analysis of Structures

For future reference statements will next be given of several theorems which provide useful tools in the general analysis of elastic-plastic structures. Proofs of these can be made very simple and brief for the trusses under consideration, but will not be given here. It may be noted, however, that the reference to a plane truss as basic structure is primarily for the sake of simplifying the notation and the physical ideas as much as possible. Applications to beams and frames have already been given (14). Extensions to continuous media are planned for a later paper.

Certain forms of the principle of virtual displacements prove especially useful. Let $(s_i')$ and $(s_i'')$ be two sets of (reduced) bar forces which are in equilibrium with the same set of external forces. Further, let $(\delta_i^*)$ be any set of (small) bar extensions which satisfy the requirements of geometrical compatibility, i.e., which correspond to a set of displacements of the joints. Then from the principle of virtual displacements it follows that

$$\sum_{i=1}^{n} s_i''\delta_i^* = \sum_{i=1}^{n} s_i'\delta_i^* \quad [10a]$$

Using the vector notation of Equation [5*a*], this can be written

$$(\underline{s}'' - \underline{s}') \cdot \underline{\delta}^* = 0 \quad [10b]$$

It proves to be particularly convenient to take $\underline{s}'' = \underline{s}$, $\underline{s}$ being the actual stress-state vector; and also to take $\underline{\delta}^* = \underline{\delta} = \underline{s} + \underline{\lambda}$, $\underline{\delta}$ and $\underline{\lambda}$ being the actual total and permanent extension vectors, respectively. With these choices of $\underline{s}''$ and $\underline{\delta}^*$, Equation [10*b*] becomes

$$(\underline{s} - \underline{s}') \cdot (\underline{s} + \underline{\lambda}) = 0 \quad [11a]$$

In many cases it is necessary to deal with the small increments of forces and extensions which accompany small increments of the load components. For convenience the time rates of change $\dot{\underline{s}} = (\dot{s})$, $\dot{\underline{\lambda}} = (\dot{\lambda}_i)$, etc., may be introduced; in a sufficiently small time increment $dt$ the force increments are $ds_i = \dot{s}_i dt$, for example. In Equation [10*b*] $\underline{s}''$ and $\underline{s}'$ can be replaced by $\dot{\underline{s}}''$ and $\dot{\underline{s}}'$, these being rates of change of the bar forces which both satisfy equilibrium with a given set of rates of change of the load components. Similarly $\underline{\delta}^*$ can be replaced by a compatible system $\dot{\underline{\delta}}^*$. Taking $\dot{\delta}^* = \dot{\underline{\delta}} = \dot{\underline{s}} + \dot{\underline{\lambda}}$ (the actual rates of elongation) Equation [11*a*] can be put in the following form, which is used later.

$$(\underline{s} - \underline{s}') \cdot (\dot{\underline{s}} + \dot{\underline{\lambda}}) = 0 \quad [11b]$$

Using these forms of the principle of virtual displacements, it is quite easy to prove two minimum principles, whose statements only will be given here. One is that of Haar and von Kármán (16), which in a form appropriate to trusses states that "among all states of stress $\underline{s}'$ which are in equilibrium with given loads, and which do not violate the yield conditions of ideal plasticity, the actual stress state $\underline{s}$ renders the elastic strain energy $W(s')$ an absolute minimum." In the notation of the present paper, since $W(s') \equiv {}^1/_2 \sum_{i=1}^{n} (s_i')^2 = {}^1/_2 (s')^2$, the statement of the Haar-Kármán principle is

$$2W(s') - 2W(s) \equiv (s')^2 - s^2 \geqq 0 \quad [12]$$

It is important to note that this principle is valid, in general, only so long as those bars which have reached their yield forces do not cease yielding. This is a very restrictive condition, and the principle is obviously not valid for arbitrary loading sequences. Moreover, even when all load components maintain constant ratios to each other, and monotonically increase ("proportional loading"), the principle may not be valid. It is possible to give examples of quite commonplace trusses in which yielding is followed by unloading, in at least one bar (18).

A minimum principle which, unlike the Haar-Kármán principle, is valid for all arbitrary loading sequences has recently been proved by Greenberg (17) in a general form applicable to continuous media. This principle is concerned with the rates of change of the bar forces which correspond to given rates of change of the external load components. It should be remembered that rates rather than increments of forces and extensions are used for convenience only; no dynamic or viscous time effects are being considered.

Applied to trusses, Greenberg's principle states that "among all stress-rate states $\dot{\underline{s}}'$ which are in equilibrium with given rates of change of the external loads, and which do not cause the yield conditions of ideal plasticity to be violated, the actual stress-rate state $\dot{\underline{s}}$ renders the elastic "stress-rate energy" $V(\dot{s}')$ an absolute minimum." In vector notation

$$2V(\underline{s}') - 2V(\underline{s}) \equiv (\underline{s}')^2 - \underline{s}^2 \geq 0 \quad [13]$$

where

$$2V(\underline{s}) = \underline{s}^2 \equiv \sum_{i=1}^{n} s_i^2, \text{ etc.}$$

This principle shows, in the stress-space geometrical interpretation, that the stress-state point moves in such a way as to take the shortest route which is compatible with the requirements of equilibrium and of ideal plasticity.

The minimum principles which have been discussed in the preceding paragraphs apply to the general analysis of forces and displacements in elastic-plastic structures. Examples of their use will be given in the next section. A theorem will first be proved which is concerned specifically with the problem of shake-down, i.e., of determining whether a structure eventually will reach a state in which all further load changes within the prescribed limits produce only elastic increments of force and extension.

A state of residual stress is, by definition, a stress state in the subspace of equilibrium corresponding to zero values of all the external-load components. Corresponding to a typical state of stress $\underline{s} \equiv (s_i)$ there is an elastic stress state $\underline{e} \equiv (e_i)$, which is the stress state that would be calculated for a given state of load if all bars behaved completely elastically at all stress values. The state $\underline{e}$ may be used as a convenient means of specifying a particular state of loading.

Now if "unloading" means the removal of external loads in such a way that the stress-state point always moves inside the yield parallelopiped (as opposed to moving on its surface), then the state of residual stress obtained by unloading from a stress state $s$ is found by adding to this stress state the negative of the corresponding elastic stress state. Thus if $\underline{r} \equiv (r_i)$ denotes the residual stress state which is reached by unloading from a particular stress state $\underline{s}$, $\underline{r}$ is given by

$$r = \underline{s} - \underline{e}$$

or

$$r_i = s_i - e_i, \; i = 1, 2 \ldots n \quad [14]$$

Conversely, any state of stress $\underline{s}$ may be regarded as composed of a residual state of stress $\underline{r}$ plus an elastic stress state $\underline{e}$. (It is readily proved using Equation [11a] that the vectors $\underline{r}$ and $\underline{e}$ are orthogonal.) Now the term "shake-down state" as defined in the first section means a state of residual stress such that the application of any possible load combination (keeping the component loads within their prescribed limits) results only in elastic changes of force and extension. This is the case when no further permanent deformations occur. Thus if $\underline{r}^* \equiv (r_i^*)$ is a shake-down state, by definition it is one such that

$$-y_i' \leqq r_i^* + e_i \leqq y_i \quad [15]$$

where $(e_i)$ stands for the elastic stress state corresponding to any allowed state of loading.

The following theorem will now be proved: "If any state of residual stress $\underline{r}^*$ exists satisfying the conditions of a shakedown state, i.e., satisfying all of the inequalities of Equation [15], then the actual residual stress state $\underline{r}$ always approaches the state $\underline{r}^*$, in the sense that the length of the vector joining the point $(r_i^*)$ to the point $(r_i)$ always decreases if further yielding occurs." In other terms, if $\underline{D} \equiv \underline{r}^* - \underline{r}$, where $\underline{r}^* \equiv (r_i^*)$ satisfies Equation [15], then $D^2$ always decreases if further yielding takes place. The importance of the theorem lies in the fact that it means that if any residual-stress state can be found satisfying the shakedown conditions, then the structure eventually will shake down.

As will be seen from the examples in the next section, the shakedown state is not unique, in general, but depends upon the loading sequence followed. However, the theorem shows that the existence of any shake-down state, even if it could never be actually reached, insures that the structure will arrive eventually at some shakedown state. The theorem is due to H. Bleich (2), who proved it only for a structure with one or two indeterminate quantities. A more general proof for trusses was given later by E. Melan (4). The proof to be given is for a general truss, and is somewhat more direct than that of Melan. A similar proof for a beam on any number of supports has been given by Neal (14). The case of continuous media has been considered by Melan (5).

To prove Bleich's theorem, first define a quantity $E$ by

$$E \equiv D^2 = (\underline{r}^* - \underline{r}) \cdot (\underline{r}^* - \underline{r}) \quad [16]$$

where $\underline{r}^* \equiv (r_i^*)$ satisfies Equation [15], and $\underline{r}$ is the residual stress state obtained by unloading from any actual stress state $\underline{s}$; $\underline{r} = \underline{s} - \underline{e}$ as discussed previously. The time rate of change of $E$ is

$$\dot{E} = -2\dot{\underline{r}} \cdot (\underline{r}^* - \underline{r}) \quad [17a]$$

The principle of virtual displacements in the form of Equation [11b] shows that Equation [17a] is equivalent to

$$\dot{E} = 2\dot{\underline{\lambda}} \cdot (\underline{r}^* - \underline{r}) \equiv 2 \sum_{i=1}^{n} \dot{\lambda}_i (r_i^* - r_i) \quad [17b]$$

Now consider the bars in which $\dot{\lambda}_i \neq 0$. Suppose, as one possibility, that $r_i^* - r_i < 0$ in one of these bars. According to Equation [15]

$$r_i^* \geq -y_i' - e_i$$

Therefore, since $r_i > r_i^*$ by supposition

$$r_i > -y_i' - e_i$$

or

$$s_i = r_i + e_i > -y_i' \quad [18]$$

This means that the $i$th bar cannot be yielding in compression, and hence that $\lambda_i \geqq 0$. The product $(r_i^* - r_i)\dot{\lambda}_i$ cannot be positive, therefore. The other possibility is that $r_i^* - r_i > 0$. But by the same argument it is easily shown that if this is the case, the $i$th bar cannot be yielding in tension, and hence $\dot{\lambda}_i < 0$ in this case. Again the product $(r_i^* - r_i)\dot{\lambda}_i \leqq 0$. Thus, it has been shown that in all cases $\dot{E} \leqq 0$, which establishes the theorem.

It may be noted that, under certain conditions of loading and of yield values, the residual-stress state, as it has just been defined, may not be actually attainable. This would not affect the present argument. The statement that shake-down can occur in a given structure implies also that it will not "collapse" under any allowed combination of loads.

## Applications to Trusses of Two and Three Bars

In this section, three examples of simple trusses will be discussed, for which the appropriate stress space is either two- or three-dimensional. These examples, for which the shake-down problem can be completely depicted and solved graphically, serve to illustrate the concepts and theorems which have been discussed in the previous sections.

As the first example, a "truss" consisting of two concentric parallel bars is considered. The motions of the ends of the bars are made to be identical, and the load is a single force parallel to the bars, Fig. 3(*a*). This example will be discussed only briefly, since a similar structure has been discussed elsewhere (6). However, despite the simplicity of this case, it shows up so many features of the general problem that it merits careful study.

The stress space has two dimensions, there being two bar forces $s_1$, $s_2$, Fig. 3(*b*). There is one equation of equilibrium of the form

$$a_1 s_1 + a_2 s_2 = P$$

$a_1$ and $a_2$ being fixed constants for a given structure; $P$ is the applied force, which varies arbitrarily between two given limits. The "yield parallelopiped" is the rectangle whose sides are $s_1 = y_1, -y_1'$; $s_2 = y_2, -y_2'$. Typical equilibrium lines are indicated

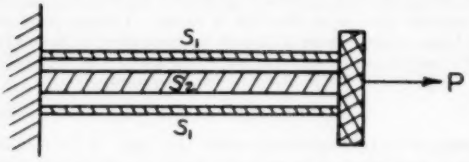


FIG. 3(*a*) STRUCTURE CONSISTING OF TWO PARALLEL (CONCENTRIC) BARS

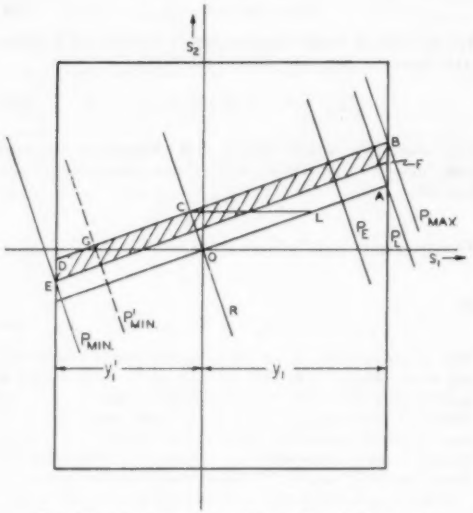


FIG. 3(*b*) CORRESPONDING "STRESS-SPACE" DIAGRAM

by $R$, $P_E$, $P_L$: the line $R$ which passes through the origin corresponds to no external load, and hence is the "subspace of residual-stress states." If the bars are unstressed initially, the stress-state point first moves along the "elastic line" $\overline{OA}$, as a tensile load is first applied.

Let us suppose that the extreme loads correspond to the equilibrium lines $P_{max}$, $P_{min}$. As the load increases beyond the value $P_L$ bar 1 yields in tension, and the stress point moves along the side $s_1 = y_1$ of the yield rectangle (this is the "shortest route" consistent with the yield conditions, which is required by Greenberg's principle). If $P$ is decreased from $P_{max}$ the stress point moves along the elastic line $\overline{BC}$ which passes through point $B$. With $P_{max}$ and $P_{min}$ as shown, any stress state in the shaded area can be reached, regardless of the previous loading history. With these values, therefore, the structure does not shake down; yielding (alternately positive and negative) may go on indefinitely. However, if the minimum load line is that indicated by $P'_{min}$, then shake-down will occur; once the value $P_{max}$ has been reached the stress point will move only in the line segment $\overline{GB}$. The residual-stress state at shake-down is represented by point $C$, and all stress states are elastic stresses, computed in the usual manner, superimposed on the residual stresses corresponding to point $C$.

In this case the permanent extensions are easily found graphically. Applying the yield Equations [9*b*], [9*c*], it is easily shown that the permanent extension in bar 1, when the load has reached the value $P_{max}$, for example, is represented by the line segment $\overline{CL}$.

Next will be considered two examples of trusses each having three bars, so that the stress space is a three-dimensional one. The first example is the truss shown in Fig. 4(*a*). There are two independent loads $V$ and $H$, each with extreme values specified, so that

$$V_{min} \leqq V \leqq V_{max}$$

$$H_{min} \leqq H \leqq H_{max}$$

The yield stresses in the three bars define 6 planes, each parallel to a co-ordinate plane, so that the stress states allowed by the plasticity conditions lie inside or on the surface of a rectangular parallelopiped, as shown in Fig. 4(*b*). The two equations of equilibrium can be written

$$a_1 s_1 + a_2 s_2 + a_3 s_3 = H$$

$$b_1 s_1 + b_2 s_2 + b_3 s_3 = V$$

Each of these is a plane whose orientation is fixed by the geometrical and material constants of the truss. Their intersection is a line having fixed orientation, but position determined by the values of $H$ and $V$. Thus the "subspace of equilibrium" for a given pair of values of $H$ and $V$ is a straight line. As the load components are first increased from zero, the truss behaves elastically, and the stress point moves in the plane through the origin which is normal to the equilibrium lines. The family of planes normal to the equilibrium lines may be termed the "elastic planes" since the stress point always moves in one of these planes so long as yielding is not taking place. In Fig. 4(*b*) the polygon *EFGHI* is the intersection of the elastic plane containing the origin with the yield parallelopiped.

The given extreme values of the loads determine the allowed locations of the equilibrium lines. These form a prism bounded by the four planes corresponding to $H_{max}$, $V_{max}$, $H_{min}$, and $V_{min}$. This will be termed the "load prism." Probably the most convenient way of specifying a particular state of load is by means of the corresponding elastic stress state $e$. In Fig. 4(*b*), the four-sided parallelogram *ABCD* is the intersection curve of the surface of the load prism and the elastic plane through the origin,

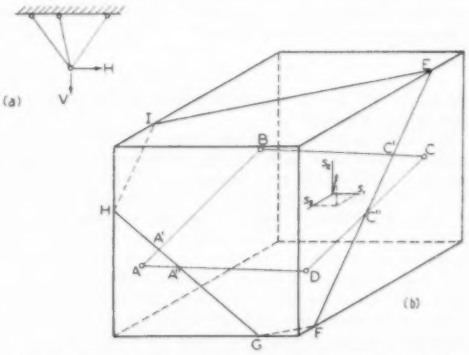


FIG. 4(*a*) THREE-BAR PLANE TRUSS. (*b*) "STRESS-SPACE" DIAGRAM FOR THREE-BAR PLANE TRUSS

i.e., points in this parallelogram represent elastic stress states corresponding to loads in the prescribed ranges. In general, this parallelogram is not entirely within the yield parallelopiped; in the example the corners $AA'A''$ and $CC'C''$ are outside the yield parallelopiped. This means simply that when the load is increased to a value such that the corresponding elastic stress state is a point in either area $AA'A''$ or $CC'C''$, then yielding occurs in one of the bars, and the stress-state point leaves the elastic plane containing the origin. The direction of motion of the stress point is determined by the Greenberg minimum principle as that which entails the smallest "stress-rate energy," without violating the yield conditions. Accordingly, the stress-state point is the intersection of the equilibrium line with the yield plane, when the load changes are such that the corresponding elastic-stress increments would move the stress point outside the yield parallelopiped. If both loads are reduced, after reaching a point such as $C$, the stress state moves in the elastic plane containing this point.

The possibility of shakedown in a given problem of this type is investigated most easily by drawing the projection of the yield parallelopiped onto a plane parallel to the elastic planes. This

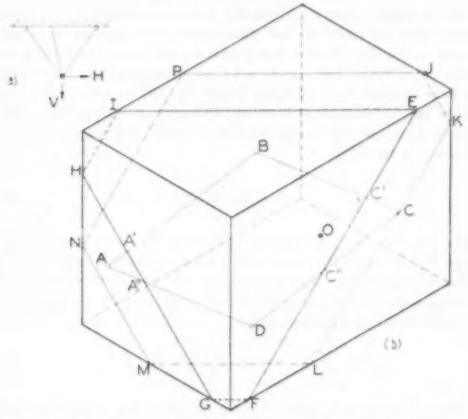


FIG. 5 PROJECTION VIEW OF "STRESS SPACE" FOR TRUSS SHOWN IN FIG. 4(a), LOOKING PARALLEL TO "EQUILIBRIUM LINES"

projection is shown in Fig. 5(b). The outline of the load prism is shown in its true shape by the parallelogram $ABCD$. The polygon $EFGHI$ is the intersection of the elastic plane through the origin with the yield parallelopiped, while the polygon $JKLMNP$ is the intersection with the yield parallelopiped of the elastic plane which passes through the corner $C$ of the load polygon $ABCD$. These polygons are shown in true shape in Fig. 5(b). It is clear that, with the load polygon and yield parallelopiped having the proportions shown in this example, once the load corresponding to point $C$ has been reached, no further plastic deformation takes place. Hence in this case the truss has a unique shakedown state of residual stress. This would be true of all three-bar trusses of the type shown in Fig. 4(a); if shakedown can occur at all, there is a unique state of residual stress to which the particular structure shakes down. It would be easy to construct an example of load ranges and truss geometry, for a truss of the type under consideration, for which no shakedown state exists.

The second example of a three-bar truss is shown in Fig. 6(a). This truss, like that in Fig. 4(a), has three bars, so the stress space is again a three-dimensional one. It differs essentially

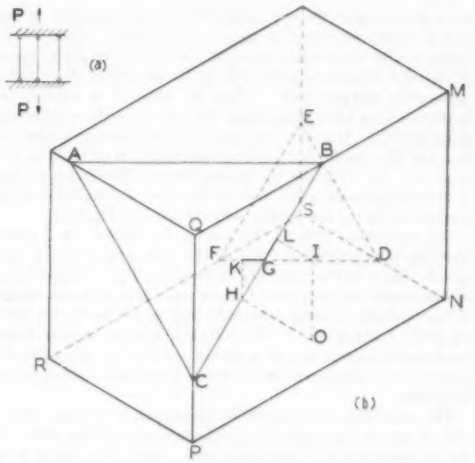


FIG. 6(a) SCHEMATIC REPRESENTATION OF STRUCTURE CONSISTING OF THREE PARALLEL (CONCENTRIC) BARS. (b) PROJECTION VIEW OF APPROPRIATE "STRESS SPACE," LOOKING PARALLEL TO "ELASTIC LINES"

from the truss in Fig. 4(a), in that there is only one load component to be specified. This means that there is only one equation of equilibrium instead of two, and hence the subspace of equilibrium is a plane instead of a line. The value of the load determines the perpendicular distance of this plane from the origin, but its orientation is fixed for a given truss. As the load is first increased from zero, the stress-state point moves on the line through the origin normal to the equilibrium planes. Thus there are now elastic lines as the counterpart to the elastic planes of the previous example.

In this case it is helpful, in studying the question of shakedown, to project the yield figure onto a plane parallel to the equilibrium planes. Such a projection is shown in Fig. 6(b). Each equilibrium plane intersects the yield parallelopiped in a certain polygon, which appears in its true shape in the projection drawing. Fig. 6(b) shows only two such polygons, the triangles $ABC$ and $DEF$. These are drawn as examples of the polygons representing the extreme load values, i.e., $ABC$ lies in the equilibrium plane corresponding to $P_{max}$, and $DEF$ in that corresponding to $P_{min}$.

Suppose the load is first increased monotonically toward $P_{max}$. The stress point moves first on the elastic line through the origin $O$; in Fig. 6(b) the trace of this line is the point $O$. Eventually, however, the load reaches a value which brings the stress in one of the bars to its yield stress. Then as the load is further monotonically increased, the stress point moves in the yield plane for that bar, e.g., plane $MNPQ$ in Fig. 6(b).

The Greenberg principle proves that the direction of motion of the stress point in a yield plane must be normal to the trace of the equilibrium plane in the yield plane. Since this trace is always parallel to the projection plane, in Fig. 6(b), the stress point moves along the line $OH$ which is perpendicular to $CB$. Once the stress point arrives at $H$, no further motion takes place in the "forward" direction, since $H$ is in the extreme equilibrium plane.

Now consider what happens when the load is monotonically decreased from $P_{max}$ toward $P_{min}$. First the stress point moves "backward" along the elastic line through $H$. Eventually, the

stress point reaches the yield plane *RSNP*, and thereafter, as the load is further decreased, it moves in this plane. Again in accordance with Greenberg's principle, the stress point moves along the line *HK* which is perpendicular to the side *FD* of the extreme equilibrium polygon *DEF*. When the point *K* is reached, no further yielding takes place, since this point is in the equilibrium plane for $P_{\min}$. It is seen now that, under the assumed values of $P_{\max}$ and $P_{\min}$, no further yielding takes place for all loads in this range, i.e., the structure has shaken down. The strain energy of the residual-stress state to which the truss has shaken down is represented by the line joining points *O* and *K* in Fig. 6(*b*).

The shakedown state in this case is not unique; it depends upon the path of loading. If, starting from zero, the load were first decreased to $P_{\min}$ and then increased to $P_{\max}$, the final elastic line would have the point *L* as its trace, and the strain energy of this residual-stress state would be represented by the line joining *O* and *L* in Fig. 6(*b*). It is easily seen that the residual-stress state at shakedown may be anywhere on the line segments *LG* and *GK*, depending upon the particular sequence of loading which is followed.

The possibility or otherwise of shakedown in a truss of this type is shown directly by the projection view in Fig. 6(*b*). If the two polygons, corresponding to the extreme load values, have any common area in this projection, then shakedown will take place; if there is no common area, then shakedown cannot occur. It may be noted that this criterion is precisely that of Bleich's theorem; this theorem will be applied directly, in the following section, to the analysis of trusses requiring a stress space of more than three dimensions.

### Tests for Shakedown in General Structures

The two and three-member trusses which have been considered in the foregoing section are special cases in that the appropriate stress space has either two or three dimensions. Hence, the yield parallelopiped, equilibrium planes, etc., can be drawn, and the behavior of the system may be studied with reference to one or another of the geometrical representations. In the general case of a truss with *n* bars analytical methods must be devised, in order to test for the possibility of shakedown.

In each of the two or three-dimensional cases the possibility of shakedown could be decided by calculating the stress states corresponding to each of the extreme load combinations. In each calculation any convenient path of loading may be followed; for example, the loads may be increased while maintaining the fixed proportion corresponding to each set of extreme values. In the truss in Fig. 4(*a*), for example, there are four extreme load values: ($H_{\max}$, $V_{\max}$), ($H_{\max}$, $V_{\min}$), ($H_{\min}$, $V_{\max}$), and ($H_{\min}$, $V_{\min}$). In the case of the three-bar truss in Fig. 4(*a*), if a shakedown residual-stress state exists, it is one of the residual-stress states corresponding to the extreme load combinations. In the case of the three-bar truss in Fig. 6(*a*), the possibility of shakedown can be decided by loading first to one extreme load, and then to the other extreme load; if the resulting residual-stress state is not a shakedown state, then none exists.

The ideas contained in these tests for shakedown of three-bar trusses can be expressed in a form applicable to a truss of any number of bars. However, it probably would be difficult to prove the general validity of a test which involves loading according to a prearranged program. Moreover, if there are many load components, the examination of all the extreme load combinations would be very laborious; in the case of *n* independent load components there are $2^n$ extreme load combinations. Thus, for only four independent load components, $2^4 = 64$ extreme load combinations exist, and a plastic-elastic analysis would have to be made for many of these, presumably.

A more fruitful line of attack seems to be one which goes back to the fundamental definition of a shakedown state as one such that the addition of all possible elastic stress states to the residual-stress state of shakedown results in a state which does not violate the yield conditions. Thus a shakedown state $r^*$ is one which satisfies a set of *n* inequalities, expressed by Equation [15], for a truss of *n* bars.

In each of these ($e_i$) is any elastic stress state allowed by the given load ranges. For each bar one can calculate the maximum and minimum elastic forces by standard methods. Denoting these by $e_i^{\max}$, $e_i^{\min}$, respectively, Equation [15] can be written as

$$-y_i' - e_i^{\min} \leqq r_i^* \leqq y_i - e_i^{\max}$$

or

$$-h_i' \leqq r_i^* \leqq h_i$$

where

$$h_i' \equiv y_i' + e_i^{\min} \qquad [19]$$

$$h_i = y_i - e_i^{\max}$$

Now Bleich's theorem shows that if any residual-stress state can be found satisfying Equation [15] or its equivalent Equation [19], then the structure will shake down, although the particular state to which it shakes down may depend upon the loading sequence. Hence the question of the possibility of shakedown can be decided by examining Equation [19] to see if there is at least one residual-stress state satisfying these inequalities. The examination of the inequalities is aided by writing the residual stresses in the form

$$r_i = \sum_{p=1}^{\nu} K_{ip} X_p \qquad [20]$$

Here $X_1, X_2 \ldots X_\nu$ are the stresses in the $\nu$ redundant bars, and $K_{ip}$ is the stress in bar *i* which results when a unit stress in the redundant bar *p* is applied, all the other redundant bars being considered as removed, and no external loads being applied. Equation [19] takes the form

$$-h_i' \leqq \sum_{p=1}^{\nu} K_{ip} X_p^* \leqq h_i, \quad (i = 1, 2 \ldots n) \qquad [21]$$

Interpreted geometrically, each of the foregoing relations defines a region between two hyperplanes in a space of $\nu$ dimensions, within which a point $X^* = (X_1^*, X_2^* \ldots X_\nu^*)$ must lie if it corresponds to a shakedown state. There are *n* such regions in the case of a truss with *n* bars. Of the *n* regions, those corresponding to the redundant bars, $p = 1, 2 \ldots \nu$, are of the type

$$-h_p' \leqq X_p^* \leqq h_p, \quad (p = 1, 2 \ldots \nu)$$

Thus these define a rectangular parallelopiped in the $\nu$-dimensional hyperspace.

The problem of determining whether or not shakedown can occur may be stated geometrically as that of determining whether the *n* regions defined by Equation [21] have at least one common point. Stated analytically, the problem is that of showing whether the inequalities of Equation [21] possess at least one "solution," i.e., a state $X_1^*, X_2^* \ldots X_\nu^*$ satisfying all of the inequalities.

It is clear that if $\nu$ is either 1 or 2, the answer can be given without difficulty, since all of the *n* regions defined by Equation [21] can then be drawn as one or two-dimensional figures. In the case of a continuous beam on any number of supports Neal (14) has shown how a series of two-dimensional diagrams can be utilized in the systematic investigation of the system of inequalities appropriate to this problem. For general rigid frames, and for trusses having more than two redundant members, these

graphical methods do not suffice. However, analytical methods are available for determining whether or not any system of linear inequalities possesses at least one solution[8] (19), (20). The application of these methods to the special systems of inequalities of trusses and frames is left to a later paper.

# Appendix

### Linear Strain-Hardening in Materials

A treatment of materials which exhibit linear strain-hardening might be based upon the following device: The actual bar, whose force-extension curve is indicated by $A$ in Fig. 7, is replaced by two parallel bars, which undergo the same end motions. One exhibits perfect elasticity at all stresses, the slope of the force-extension curve being that of the "post-yield" lines of the actual bar; this is indicated by curve $B$ in Fig. 7. The second bar has

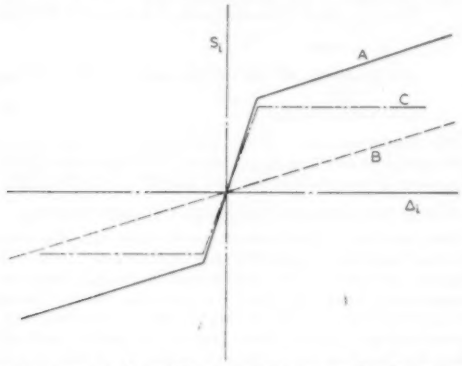


Fig. 7 Curve A: Force-Elongation Diagram of Bar Exhibiting "Linear Strain-Hardening;" Curves B and C: Force-Elongation Diagrams of Hypothetical Parallel Bars Which Replace the Actual Bar

the characteristic curve of ideal plasticity, curve $C$ in Fig. 7, which is obtained by subtracting curve $B$ from curve $A$. Both of these fictitious bars are of the type which has been considered in the present analysis.

### Permissible Elongations and Stability

The questions of permissible elongations and of stability must be considered in applying the present analysis to general trusses. In the case of bars which yield in tension, the amount of elongation is limited by the occurrence of rupture, or by other considerations which restrict the extension that may be permitted. A method for determining the permanent extension has been indicated, in connection with the two-dimensional example treated in Fig. 3. An attempt is now being made to develop means of estimating the magnitudes of the permanent elongations which may be produced by loading within given ranges, in the general problem.

Another, and probably more fundamental difficulty appears when one considers the stability of a strut loaded to the compression yield force. It is easy to see that, if a compression member actually could possess the flat yield curve which is characteristic of "ideal plasticity," it would be unstable once the yield force is reached. Moreover, the curve of force versus elongation would show a sharp drop from the yield force, as soon as buckling occurs. This fact may mean that no important member of a truss (the loss of which would throw excessive load onto other members) must be allowed to yield in compression, unless it is braced against lateral deflection. On the other hand, the existence of strain-hardening even in the materials with limited flat yield regions might mean that the compression characteristic, even with buckling, would not differ so greatly from the idealization in Fig. 1($a$), as to invalidate the present treatment. Experimental tests with actual materials whose properties approximate the ones assumed here will be helpful in deciding these questions.

[8] The authors are indebted to Prof. J. B. Diaz of Brown University for these references.

### BIBLIOGRAPHY

1 "Stahlhochbauten, ihre Theorie, Berechnung und bauliche Gestaltung," by Friedrich Bleich, Julius Springer, Berlin, Germany, vol. 1, 1932, pp. 397–410.

2 "Über die Bemessung statisch unbestimmter Stahltragwerke unter Berücksichtigung des elastisch-plastischen Verhaltens des Baustoffes," by Hans Bleich, *Der Bauingenieur*, no. 19/20, 1932, pp. 261–267.

3 "Die Weiterentwicklung der Elastizitätstheorie," by G. v. Kazinczy, Budapest, Technika, 1931.

4 "Theorie statisch unbestimmter Systeme aus idealplastischem Baustoff," by Ernst Melan, *Sitzungsberichte der Akademie der Wissenschaften in Wien*, vol. 145, 1936, part 2a, pp. 195–218.

5 "Der Spannungszustand eines 'Mises-Henckyschen' Kontinuums bei veränderlicher Belastung," by E. Melan, *Sitzungsberichte der Akademie der Wissenschaften in Wien*, vol. 147, 1938, part 2a, pp. 73–87.

6 "Problem Types in the Theory of Perfectly Plastic Materials," by W. Prager, *Journal of the Aeronautical Sciences*, vol. 15, 1948, pp. 337–341.

7 "Die Zähigkeit des Materials als Grundlage für die Berechnung von Brücken, Hochbauten, und ähnlichen Konstruktionen aus Flusseisen," by N. C. Kist, *Der Eisenbau*, vol. 11, 1920, p. 425.

8 "Die Tragfähigkeit statisch unbestimmter Tragwerke aus Stahl bei beliebig häufig widerholter Belastung," by M. Grüning, Julius Springer, Berlin, 1926.

9 "Die Bedeutung der Zähigkeit des Stahles für die Berechnung und Bemessung von Stahlhochbauwerken, insbesondere von statisch unbestimmten Konstruktionen: Versuche, Ausdeutung, und Anwendung der Ergebnisse," by H. Maier-Leibnitz, Preliminary Publication of the Second Congress of the International Association for Bridge and Structural Engineering, Berlin, 1936, pp. 103–137.

10 See a series of reports on "Investigation Into the Behavior of Welded Rigid Frame Structures," by J. F. Baker, J. W. Roderick, et al; for example "The Behavior of Stanchions Bent in Double Curvature," (Fifth Interim Report), Trans. Institute of Welding, "Welding Research," vol. 11, 1948, p. 2r.

11 "The Analysis of Engineering Structures," by A. J. S. Pippard, and J. F. Baker, Edward Arnold & Company, London, second edition, 1943. (See chapt. 24 on "The Behavior of Structures in the Elasto-Plastic Range.")

12 "Theory of Limit Design," by J. A. Van den Broek, Trans. ASCE, vol. 105, 1940, pp. 638–661. (A valuable series of discussions follows this paper).

13 "Theory of Limit Design," by J. A. Van den Broek, John Wiley & Sons, Inc., New York, N. Y., 1948.

14 "Shake-Down of Continuous Beams and Frames," by B. G. Neal, Technical Report A11-32 of Brown University to Office of Naval Research, March, 1949.

15 "De l'Équilibre des Systèmes Élastiques dans Lesquels se Produisent des Déformations Plastiques," by G. Colonnetti, *Journal de Mathématiques Pures et Appliquées*, ninth series, vol. 17, 1938, pp. 233–255.

16 "Zur Theorie der Spannungszustände in plastischen und sandartigen Medien," by A. Haar, and Th. von Kármán, Göttingen Nachrichten, mathematisch-physikalische klasse, 1909, pp. 204–218.

17 "Complementary Minimum Principles for an Elastic-Plastic Material," by H. J. Greenberg, *Quarterly of Applied Mathematics*, vol. 6, 1949, p. 85.

18 "The Plasticity of Metals—A Discussion of Mathematical Theory and Its Application to Civil Engineering Problems," by D. C. Drucker; paper presented at the Annual Meeting of the American Society of Civil Engineers in January, 1949; Technical Report A11-26 of Brown University to the Office of Naval Research, December, 1948.

19 "Systems of Linear Inequalities," by L. L. Dines, *Annals of Mathematics*, series 2, vol. 20, 1918–1919, p. 191.

20 "Associated Systems of Linear Equalities and Inequalities," by L. L. Dines, *Annals of Mathematics*, series 2, vol. 28, 1926, p. 41.

# Crushing of Aluminum Tubes Under Hydrostatic and Localized Pressure

By E. CREUTZ,[1] PITTSBURGH, PA.

**In the theory of elasticity equations have been derived by Sturm and Timoshenko for the crushing strength of long tubes subjected to external hydrostatic pressure. These equations have been found to fit experimental data on steel tubes, provided the length is several times the diameter, and the ratio of diameter to wall thickness exceeds about 30. No similar test data had been taken on aluminum tubes so an experimental study was carried out to determine whether the equations mentioned would apply. No satisfactory correlation was found to exist, but a simple equation was derived which is well within the reproducibility of the test results.**

IN the early days of the design of the uranium chain-reacting piles, several schemes were contemplated making use of aluminum tubing for cooling ducts.[2] In some of these, conditions were met where the pressure exterior to the tube exceeded that within it. Conditions were also expected in which two tubes would be tightly pressed against each other.

In the theory of elasticity, equations exist for the crushing strength of long tubes to which hydrostatic pressure is applied externally. In general, these fit the experimental data taken by various investigators on steel tubes, provided the length is several times the diameter, and the ratio of the diameter to the wall thickness is greater than about 30. Sturm's[3] equation and Timoshenko's[4] equation fit the data, for instance, of Jasper and Sullivan[5] rather well when the wall thickness is less than 2 to 3 per cent of the diameter. These equations follow:

Sturm's equation

$$P_S = \frac{2}{3} E \times \frac{W^2}{D^2} \frac{n^4 - n^2 + a^4K^2 + a^2K(2n^2 - m)}{n^2 (1 - m^2)} \quad [1]$$

Timoshenko's equation

$$P_T = \frac{EW^3}{4(1 - m^2)r^3} \quad [2]$$

where

$P_S, P_T$ = collapsing pressure, psi
$E$ = modulus of elasticity
$W$ = wall thickness of tube
$D$ = outside diameter of tube
$n$ = number of lobes in which tube collapses, taken as 2 for long tubes
$K = \frac{\pi^2 r^2}{L^2}$, where $r$ is outer radius of tube, and $L$ is length of tube
$a$ = parameter for end effects, taken as unity for long tubes
$m$ = Poisson's ratio

The simpler equation, that of Timoshenko, is found to give good agreement for "long tubes," that is, with the length greater than about 8 times the diameter, providing $W/r$ is small enough.

### Experimental Study to Determine Crushing Strengths

Since the data on steel tubes do not fit these equations when the wall thickness is appreciably greater than 2 per cent of the diameter, and since no data were located on aluminum tubes, an experimental study was made to determine these crushing strengths when hydrostatic pressure was applied uniformly to the exterior and also when a "linear" pressure was applied essentially along one line at the outer surface of the tube by pressing against it a parallel rod of approximately the same diameter. For these experiments a series of several sizes of tubes were prepared from 28 aluminum about $^1/_2$ hard. In cold-drawing each individual size, the drawing schedule was calculated to produce the same reduction in area from the initial annealed state so that the hardnesses of all the tubes were nearly identical.

The method of testing the tubes for hydrostatic pressure consisted, briefly, of mounting them in a special pressure vessel through the walls of which the ends of the specimen extended so that atmospheric pressure was always inside the tubes. The length used was $6^1/_2$ in., sufficient to make all but the 1-in-diam tubes fall into the class of "long tubes" as defined. The data obtained did not fit the equations nor the formulas for thick- and thin-walled brass and steel tubing given by Carman and Love.[6]

Since it may be of some use to estimate the crushing strength of arbitrary aluminum tubes in this range of $W/D$, an empirical formula was developed from these data as follows

$$P = 1.52 \times 10^7 \left( \log_{10} \frac{D^2}{W^2} - 2.95 \right) \frac{W^2}{D^2} \quad [3]$$

Table 1 lists the diameter of the tube in inches, the observed crushing strength in pounds per square inch, the crushing strength calculated from the empirical Equation [3], the crushing strength $P_T$ calculated from Equation [2], and the percentage difference between the observed crushing strength and that calculated by Equation [3]. It is seen that the formula fits the

[1] Carnegie Institute of Technology.

[2] "Atomic Energy for Military Purposes," by H. D. Smyth, Princeton University Press, 1945.

[3] Doctorate Thesis, by R. B. Sturm, submitted to the Department of Theoretical and Applied Mechanics, College of Engineering, University of Illinois, Urbana, Ill.

[4] "Applied Elasticity," by S. Timoshenko and J. M. Lessels, Westinghouse Technical Night School Press, East Pittsburgh, Pa., 1925, Equation [235], p. 248.

[5] "The Collapsing Strength of Steel Tubes," by T. McLean Jasper and J. W. W. Sullivan, Trans. ASME, vol. 53, paper no. APM-53-17b, 1931.

[6] Formulas by Carman and Love, Mechanical Engineers' Handbook, by L. S. Marks, fourth edition, 1941, p. 450.

Contributed by the Applied Mechanics Division and presented at the Annual Meeting, New York, N. Y., November 27–December 2, 1949, of The American Society of Mechanical Engineers.

Discussion of this paper should be addressed to the Secretary, ASME, 29 West 39th Street, New York, N. Y., and will be accepted until October 10, 1950, for publication at a later date. Discussion received after the closing date will be returned.

Note: Statements and opinions advanced in papers are to be understood as individual expressions of their authors and not those of the Society. Paper No. 49—A-23.

TABLE 1 DATA ON TUBES TESTED

| $D$, in. | $W$, in. | $P$ observed psi | $P$ calculated from empirical Formula [3], psi | $P_T$ calculated from Equation [2] psi | Difference (calculated by [3], observed), per cent |
|---|---|---|---|---|---|
| 1 | 0.020 | 290 | 260 | 179 | —10 |
| | 0.030 | 625 | 667 | 605 | + 7 |
| | 0.060 | 2450 | 2360 | 4770 | — 3 |
| | 0.080 | 2580 | 2660 | 11400 | + 3 |
| 0.750 | 0.020 | 520 | 504 | 425 | — 3 |
| | 0.025 | 840 | 831 | 828 | — 1 |
| | 0.030 | 1177 | 1200 | 1430 | + 2 |
| 0.500 | 0.020 | 1300 | 1200 | 1430 | — 8 |
| | 0.025 | 1754 | 1815 | 2800 | + 5 |
| | 0.030 | 2185 | 2360 | 4780 | + 8 |
| 0.202 | 0.015 | 2570 | 2690 | 9450 | + 5 |
| | 0.020 | 3115 | 700 | 22400 | |

data on tubes from 0.2 in. to 1 in. diam, with wall thicknesses from 2 to 8 per cent of the diameter, with a root-mean-square error of less than 6 per cent. The formula breaks down completely when the wall thickness exceeds 9 per cent of the diameter (e.g., 0.202-in. tube with 0.020-in. wall).

Using the value of $E$ for aluminum

$$1.00 \times 10^7 \text{ psi}$$

and the value of Poisson's ratio

$$m = 0.33$$

Timoshenko's equation may be written

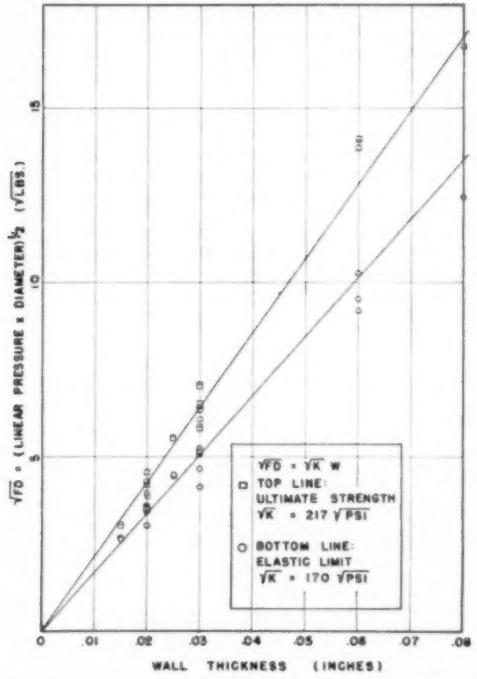


FIG. 1 EXPERIMENTAL DATA SHOWING ELASTIC LIMIT AND ULTIMATE STRENGTH OF ALUMINUM TUBES AGAINST WHICH A PARALLEL ROD HAS BEEN PRESSED WITH A FORCE PER LINEAR INCH = $F$

(The data are seen to follow roughly along a line whose equation is $\sqrt{FD} = \sqrt{K}\,W$, in which $D$ = tube diameter, in.; $W$ = wall thickness, in.; $F$ = lb per linear in.; $K$ = psi.)

$$P_T = 0.280\,E\,\frac{W^3}{r^3}$$

and the empirical relationship, Equation [3], becomes

$$P = 0.187\,E\,\frac{W^3}{r^3}\log\frac{r^3}{111\,w^3} = \frac{2}{3}\,P_T\log\frac{r^3}{111\,w^3} \quad \ldots\ldots [4]$$

It may be seen that $P_T = P$ when $W = 6.6$ per cent of $r$. However, for values of $W$ greater than 6.6 per cent of $r$, $P$ is less than $P_T$, and for values of $W$ less than 6.6 per cent of $r$, $P$ is greater than $P_T$. No simple relationship covering the full range of thin-walled tubes where Timoshenko's equation should be satisfied, as well as this range of intermediate walled tubes which obey the empirical relationship, was found.

## TEST RESULTS

The tests made with the application of pressure essentially to a linear element of the tube yielded the data given in Table 2.

TABLE 2 DATA FROM TESTS

| Outside diameter, in. | Wall, in. | Length, in. | Crushing strength: Yield (0.2 set), lb per in. | Crushing strength: Yield per cent lb per in. Average, lb per in. | Crushing strength: Ultimate, lb per in. | Crushing strength: Ultimate, Average, lb per in. |
|---|---|---|---|---|---|---|
| 0.202 | 0.015 | 1 | 36 | | 45 | |
| | | | 39 | 36 | 40 | 44 |
| | | | 34 | | 41 | |
| 0.202 | 0.015 | 2 | 34 | | 44 | |
| | | | 34.1 | 33.4 | 47.2 | 45.9 |
| | | | 33.2 | | 46.6 | |
| 0.202 | 0.020 | 1 | 60.8 | 63.0 | 88.5 | 88.2 |
| | | | 65.2 | | 88 | |
| 0.202 | 0.020 | 2 | 64.2 | | 91 | |
| | | | 58.5 | 61.1 | 82.2 | 85.9 |
| | | | 60.5 | | 84.7 | |
| 0.500 | 0.020 | 1 | 32 | | 42.5 | |
| | | | 30.2 | 30.6 | 39.5 | 41.1 |
| | | | 29.5 | | 41.2 | |
| 0.500 | 0.020 | 2 | 27.5 | | 40.0 | |
| | | | 30.5 | 29.3 | 40.4 | 41.3 |
| | | | 30.0 | | 43.5 | |
| 0.500 | 0.025 | 1 | 40.0 | | 65.5 | |
| | | | 38.5 | 39.5 | 59.0 | 61.9 |
| | | | 40.0 | | 61.2 | |
| 0.500 | 0.025 | 2 | 39.5 | | 61.0 | |
| | | | 38.2 | 38.9 | 61.9 | 61.3 |
| | | | 39.0 | | 61.0 | |
| 0.500 | 0.030 | 1 | 84.0 | 82.6 | 101.0 | 98.3 |
| | | | 81.2 | | 95.7 | |
| 0.500 | 0.030 | 2 | 84.5 | 81.0 | 108.0 | 100.3 |
| | | | 82.0 | | 96.5 | |
| | | | 76.5 | | 96.6 | |
| 0.500 | 0.030 | 4 | 70.3 | | 97.5 | |
| | | | 68.8 | 68.3 | 96.7 | 98.1 |
| | | | 65.8 | | 100.0 | |

In this case the crushing strength is given in pounds per linear inch, and the yield point, defined as the load causing a permanent deformation equal to 0.2 per cent of the diameter, was also determined. There is some indication of a slight decrease in strength with an increase in length of the tube. This may be due to difficulty in aligning the longer specimens or their deviation from straightness.

An inspection of the data shows that an equation of the form

$$F = KW^2/D \quad \ldots\ldots [5]$$

is well within the reproducibility of the results. Here $F$ is the force per linear inch, $W$ is the wall thickness in inches, and $D$ is the tube diameter in inches. If the square root of the product of the applied force per inch and the tube diameter is plotted against the wall thickness of the tube, the points follow quite well along a straight line whose slope is the square root of the constant $K$ (Fig. 1). The value of $K$ for the crushing strength is $4.7 \times 10^4$ psi. For the elastic limit, the constant has a value $2.9 \times 10^4$ psi. Table 2 lists the diameter of the tube, its wall thickness, the length of the specimen tested, the load in pounds per inch sufficient to reach the elastic limit, and the ultimate sustained load in pounds per inch. These observed values fit the

empirical equation given, with a root-mean-square error of less than 10 per cent.

## Acknowledgment

This work was carried out while the author was a member of the Metallurgical Laboratory, University of Chicago, under the Manhattan Project, and is described in Document MDDC 1448. The mechanical tests were performed by Armour Research Foundation. The aluminum tubes were prepared by Mr. James Schumar of the Wolverine Tube Division.

# Stability of Flow in a Rocket Motor[1]

By D. F. GUNDER[2] and D. R. FRIANT[3]

**This paper presents an analytical treatment leading to a criterion for the proper design of liquid rocket motors to insure freedom from the phenomenon of "chugging" without unnecessary increase in fuel-tank or fuel-pump pressures. The most successful of the several methods suggested here is that of Nyquist, which involves a simple conformal transformation. The analytical treatment presented in this paper has been applied successfully in practice to eliminate this type of instability.**

## Introduction

IN Fig. 1 is seen a simple monopropellant rocket system. It consists of a propellant tank containing liquid propellant fed by the constant pressure $p_1$ through a propellant line and, by way of an injection nozzle, into a combustion chamber where it burns and passes out the exhaust nozzle.

Consider the behavior of the system if for any reason the velocity of flow $v$ through the injection nozzle momentarily decreases by a small amount from its steady-state value. A short time after the decrease takes place, its effect is felt at the point of combustion (assuming point-combustion) in the form of a decrease in the rate of burning and therefore a decrease in pressure at the point. The pressure decrease spreads through the combustion chamber in a wave which ultimately reaches the injection nozzle and causes the rate of flow of propellant into the chamber to increase.

Shortly after the increase in flow occurs, the pressure at the point of combustion is increased, resulting finally in a decrease in the rate of flow from the injection nozzle. The cycle continues ad infinitum, with the propellant velocity pulsating. This pressure pulsation is known as "chugging."

It is clear that the amplitudes of the pulsations may become either larger or smaller with time, or they may remain the same. If they become larger, the system is unstable; otherwise it is stable. Continued chugging produces an undesirable irregularity of thrust and if too severe will result in rupture of the rocket combustion chamber.

## The System

The following nomenclature is used in connection with the system in Fig. 1:

$A$ = area of fluid column

$\alpha$ = delay time between reduction of flow from injection nozzle and resulting increase of flow from nozzle

$d$ = diameter of fluid column

$\Delta p$ = pressure drop from tank to combustion chamber $= p_1 - p_C$

$f$ = coefficient of fluid friction for propellant line

$g$ = gravitational acceleration

$k$ = pressure coefficient

$l$ = pipe length between tank and injection nozzle

$l'$ = equivalent pipe length between tank and injection nozzle

$p$ = pressure

$\rho$ = density of fluid, mass per unit volume (assumed constant along line)

$t$ = time

$v$ = velocity of fluid

$w$ = propellant flow rate, weight per unit time

Subscripts 1 and 2 refer to the tanks and lines, respectively. $A$, $v$, $d$, etc., with no number-subscripts, refer to properties of the injection jet. The chamber pressure near the nozzle is denoted by $p_C$. The subscript $S$ is a reference to a steady-state parameter. All other notations used will be defined as they are encountered.

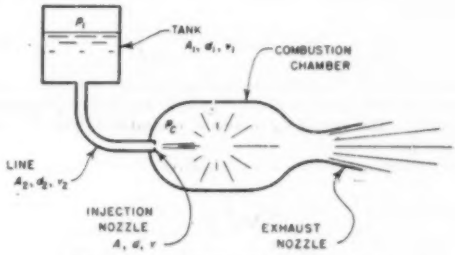


Fig. 1 Monopropellant Rocket System

($A$ and $d$ are dimensions of jets—not orifices. $l$ and $l'$ are actual and equivalent pipe lengths from tank to injection nozzle.)

We assume here that the rocket is not accelerating. Acceleration, in general, will assist the flow of propellant into the chamber; so that, rigorously, we shall be able to apply our results to rockets on test stands only. However, these results can be adapted for use with accelerating rockets. At any rate, an analysis similar to this one can be carried out in which acceleration is taken into account.

We neglect the effects of water hammer, compressibility of the liquid propellant, and pressure waves rebounding from the walls of the combustion chamber.

We assume point-combusion, that is, no propellant in the chamber burns until it has traveled a certain distance beyond the injection nozzle. It all burns at precisely that distance from the nozzle. In reality, the combustion of propellant is distributed throughout a sizable volume and is often not complete even at the exit of the exhaust nozzle. Assuming point-combustion will tend to make our results conservative, since distribution of combustion has the effect of smoothing out the pulsations of the system.



[1] Based on unpublished work by D. F. Gunder and an M.S. thesis by D. R. Friant under the direction of D. F. Gunder and R. J. Walker at Cornell University, 1948.

[2] Professor in charge Department of Mechanics of Engineering, Cornell University, Ithaca, N. Y., and Staff Consultant, Special Projects Department, M. W. Kellogg Company, Jersey City, N. J. Mem. ASME.

[3] Ordnance Engineer, Picatinny Arsenal, Dover, N. J. Jun. ASME.

Contributed by the Applied Mechanics Division and presented at the Annual Meeting, New York, N. Y., November 27–December 2, 1949, of The American Society of Mechanical Engineers.

Discussion of this paper should be addressed to the Secretary, ASME, 29 West 39th Street, New York, N. Y., and will be accepted until October 10, 1950, for publication at a later date. Discussion received after the closing date will be returned.

Note: Statements and opinions advanced in papers are to be understood as individual expressions of their authors and not those of the Society. Paper No. 49—A-15.

## Equations of Motion

Setting the external work done on the fluid in the tank and line during the infinitesimal time $dt$ equal to the change in kinetic energy plus losses gives

$$p_1 A_1 v_1 dt - p_C A v dt = {}^1/_2 \rho Q v_2^2 dt - {}^1/_2 \rho Q v_1^2 dt + \rho l A_2 v_2 dv_2 + {}^1/_2 \rho f \frac{l'}{d_2} A_2 v_2^2 dt$$

in which $Q$ is the rate of flow. For incompressible fluid

$$Q = Av = A_1 v_1 = A_2 v_2 \quad \text{and} \quad v = v_1 \left(\frac{d_1}{d_2}\right)^2 = v_2 \left(\frac{d_2}{d}\right)^2$$

Hence

$$p_1 - p_C = {}^1/_2 \rho v^2 - {}^1/_2 \rho \left(\frac{d}{d_1}\right)^4 v^2 + \rho l \left(\frac{d}{d_2}\right)^2 \frac{dv}{dt} + {}^1/_2 \rho f \frac{l'}{d_2} \left(\frac{d}{d_2}\right)^4 v^2$$

We let the velocity $v$ be made up of a steady-state velocity $v_s$ and a variation from steady-state velocity, $v'$, that is, $v = v_s + v'$. Neglecting terms containing $(d/d_1)^4$ and $v'^2$, we get

$$p_1 - p_C = \rho l \left(\frac{d}{d_2}\right)^2 \frac{dv'}{dt} + \rho v_s \left[1 + f \frac{l'}{d_2} \left(\frac{d}{d_2}\right)^4\right] v' + {}^1/_2 \rho v_s^2 \left[1 + f \frac{l'}{d_2} \left(\frac{d}{d_2}\right)^4\right] \quad \ldots\ldots [1]$$

For small oscillations, assume that the chamber pressure can be written

$$p_C = p_{CS} \left(1 + k \frac{v_a'}{v_s}\right) \quad \ldots\ldots [2]$$

where $p_{CS}$ is the steady-state chamber pressure and $k$ is a constant that tells how the chamber pressure varies with propellant velocity. The symbol $v_a'$ means $v'$ evaluated at time $t - \alpha$ rather than at time $t$.

Substituting Equation [2] into [1] gives

$$p_1 - p_{CS} = k \frac{p_{CS}}{v_s} v_a' + \rho l \left(\frac{d}{d_2}\right)^2 \frac{dv'}{dt} + \rho v_s \left[1 + f \frac{l}{d_2} \left(\frac{d}{d_2}\right)^4\right] v' + \rho v_s^2 \left[1 + f \frac{l'}{d_2} \left(\frac{d}{d_2}\right)^4\right] \quad \ldots\ldots [3]$$

But for steady flow

$$v' = 0, \quad v_a' = 0, \quad \frac{dv'}{dt} = 0$$

Hence from Equation [3] comes the equation

$$p_1 - p_{CS} = {}^1/_2 \rho v_s^2 \left[1 + \frac{fl'}{d_2} \left(\frac{d}{d_2}\right)^4\right] \quad \ldots\ldots [4]$$

which will be found useful in computations, and

$$\frac{dv'}{dt} + \frac{v_s}{l} \left(\frac{d_2}{d}\right)^2 \left[1 + \frac{fl'}{d_2} \left(\frac{d}{d_2}\right)^4\right] = -\frac{k}{\rho l} \left(\frac{d_2}{d}\right)^2 \frac{p_{CS}}{v_S} v_a'$$

or

$$\frac{dv'}{dt} + Ev' = -Gv_a' \quad \ldots\ldots [5]$$

$$E = \frac{v_S}{l} \left(\frac{d_2}{d}\right)^2 \left[1 + \frac{fl'}{d_2} \left(\frac{d}{d^2}\right)^4\right] > 0$$

$$G = \frac{K}{\rho l} \left(\frac{d_2}{d}\right)^2 \frac{p_{CS}}{v_S} > 0$$

## Solution

*Method 1.* Evaluation of $v'$ from the differential Equation [5] requires that some form of disturbance be assumed for $v'$. For instance, one can assume

$$\begin{cases} v' = 0 & t \leq -\alpha \\ v' = \text{arbitrary} & -\alpha < t < 0 \\ v' = 0 & t = 0 \end{cases}$$

For the interval in which $v'$ is arbitrary, the arbitrary function may be assumed expansible in the series

$$-Gv_a' \sum_1^\infty C_n e^{i\omega_n t} \qquad 0 < t < \alpha \qquad \omega_n = \frac{2n\pi}{\alpha}$$

Then values of $v'$ may be found by successive substitution and integration by intervals. However, these values, once determined, do not readily yield information regarding stability of the system.

*Method 2.* Equation [5] may be treated by Lap'ace transforms by assuming first that $v'(t)$ has a Laplace transforth $V(s)$, i.e.,

$$\mathfrak{L}[v'(t)] = V(s) = \int_0^\infty v(t) e^{-st}\, dt$$

Then note that

$$\mathfrak{L}\left[\frac{d}{dt} v'(t)\right] = sV(s) - v'(0+)$$

and

$$\mathfrak{L}[v_a'] = e^{-\alpha s} V(s) + \int_{-\alpha}^0 f(t) e^{-s(t+\alpha)}\, dt$$

where $f(t)$ is the disturbance $\approx v'(t)$ in the interval $-\alpha < t < 0$. Substituting these transformed terms into Equation [5] gives

$$sV(s) - v'(0+) + EV(s) = -Ge^{-\alpha s} V(s) - G \int_{-\alpha}^0 f(t) e^{-s(t+\alpha)}\, dt$$

or

$$V(s) = \frac{v'(0+) - G \int_{-\alpha}^0 f(t) e^{-s(t+\alpha)}\, dt}{Ge^{-\alpha s} + s + E} \quad \ldots\ldots [6]$$

The inverse transformation of this expression gives $v'(t)$. For example, let $f(t)$ be defined as follows

$$\begin{cases} f(t) = 1 & -\alpha < t < \beta < 0 \\ f(t) = 0 & \beta < t < \alpha \end{cases}$$

Then the inverse transformation, for which the authors are indebted to H. Pollard,[4] gives

$$v'(t) = \sum_0^{n=\left[\frac{t}{\alpha}\right]} \frac{(-1)^k}{k!} G^k \int_{k\alpha}^{\min[t(k+1)\alpha-\beta]} (t-u)^k e^{-E(t-u)}\, du$$

However, $v'(t)$ is not tractable for stability determinations in this form.

*Method 3.* The process to be considered now does give information on stability for the monopropellant case. Assume that $v'$ can be expended in the series

$$v' = \sum_0^\infty C_n e^{-\zeta_n \frac{t}{\alpha}} \quad \ldots\ldots [7]$$

Substitute one term of the expansion into Equation [5] to find

[4] Associate Professor of Mathematics, Cornell University.

the conditions the $\zeta$'s must satisfy in order for the series to solve the differential equation.

$$-\frac{\zeta}{\alpha}Ce^{-\zeta\frac{t}{\alpha}} + ECe^{-\zeta\frac{t}{\alpha}} = -GCe^{-\zeta\frac{t}{\alpha}+\zeta}$$

or

$$\zeta - B = He^{\zeta} \quad [8]$$

$$B = \alpha E,\ H = \alpha G$$

In general, $\zeta$ is complex and can be written

$$\zeta = \xi + i\eta$$

Equation [8] becomes

$$\xi + i\eta - B = He^{\xi}(\cos\eta + i\sin\eta)$$

or

$$\begin{cases} \xi = B + He^{\xi}\cos\eta & [9a] \\ \eta = He^{\xi}\sin\eta & [9b] \end{cases}$$

From Equations [9a] and [9b]

$$\xi = B + \frac{\eta}{\tan\eta} \equiv f_a \quad [10]$$

But from Equation [9b]

$$\xi = -\ln H + \ln\frac{\eta}{\sin\eta}$$

$$= H' + \ln\frac{\eta}{\sin\eta} \equiv f_b \quad [11]$$

The values of $\xi$ and $\eta$ for which $f_a = f_b$ give the possible values for $\zeta$ in Equation [7]. It is seen from Equations [10] and [11] that each possible real part $\xi$ of $\zeta$ can have associated with it both a positive $\eta$ and a negative $\eta$. The two resulting $\zeta$'s form a conjugate pair. If any pair of $\zeta$'s has its real parts negative, the corresponding pair of terms in the expansion of $v'$, Equation [7], will increase in amplitude with time; and the system therefore will be unstable.

The functions $f_a$ and $f_b$ are plotted in Fig. 2 for positive values of $\eta$. The ordinates at the intersections represent solutions of $\xi_n = f_a = f_b$. It is not difficult to show that if the first solution $\xi_0$, for which $0 \leq \eta < \pi$, is positive, then all the following $\xi_n$ are also positive and the system is stable.

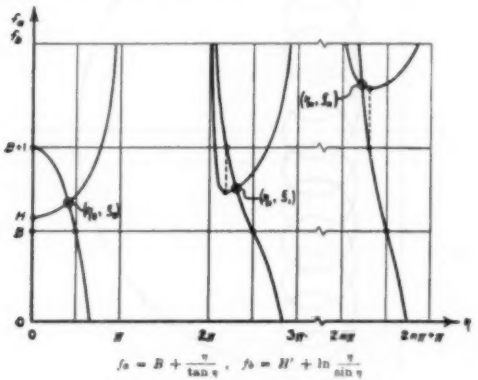


$f_a = B + \frac{\eta}{\tan\eta}$ , $f_b = H' + \ln\frac{\eta}{\sin\eta}$

FIG. 2 THE FUNCTIONS $f_a(\eta)$ AND $f_b(\eta)$

The critical condition is $\xi_0 = 0$ or

$$B + \frac{\eta_0}{\tan\eta_0} = 0 = \ln\frac{\eta_0}{H\sin\eta_0}$$

That is

$$B + \frac{\eta_0}{\tan\eta_0} = 0, \quad \frac{\eta_0}{H\sin\eta_0} = 1$$

From which

$$B + H\cos\eta_0 = 0 \quad \text{or} \quad \cos\eta_0 = -\frac{B}{H}$$

and

$$\eta_0 = H\sin\eta_0$$

Hence the critical condition becomes

$$\cos^{-1}\left(-\frac{B}{H}\right) = H\sqrt{1-\left(\frac{B}{H}\right)^2} = \sqrt{B^2 - H^2} \quad [12]$$

To a close approximation (1, 2),[b] Equation [2] can be written

$$p_C = k\frac{p_{CS}}{v_S}v_a$$

Then Equation [12] becomes

$$\pi - \cos^{-1}p^* = L\sqrt{\frac{1-p^{*2}}{p^*}} \quad [13]$$

where

$$p^* = \frac{2\Delta p}{p_{CS}}$$

$$L = \frac{\alpha}{l}\left(\frac{d_2}{d}\right)^2\sqrt{1+\frac{fl'}{d_2}\left(\frac{d}{d_2}\right)^4}\sqrt{\frac{p_{CS}}{\rho}}$$

or, by Equation [4]

$$L = 2\frac{\alpha}{l}AA_2\left(\frac{g}{w}\right)^2\sqrt{\rho p_{CS}}\ \Delta p$$

in which

$w$ = propellant flow rate, weight per unit time

$$\Delta p = p_i - p_C$$

Equation [13] is represented graphically in Fig. 3.

*Method 4.* This method is the easiest to use of any of the four; and in addition to yielding easily the solution for the monopropellant system, it is the only method of the four found to solve the bipropellant system to be considered next. Let us assume an expansion of $v'$ in the form

$$v' = \sum C_j e^{z_j t/\alpha}$$

Substituting in Equation [5] and canceling exponentials, we get for any $j$

$$f(z) \equiv B + z + He^{-z} = 0 \quad [14]$$

A theorem from complex variable theory becomes useful here: "If a function $f(z)$ is analytic, except for possible poles, on and within a given contour in the $z$-plane, then the number of times a plot of $f(z)$ in its own plane encircles the origin in a counterclockwise direction while $z$ travels clockwise once around the given contour is given by $P - N$, where $P$ and $N$ are, respectively,

[b] Numbers in parentheses refer to the Bibliography at the end of the paper.

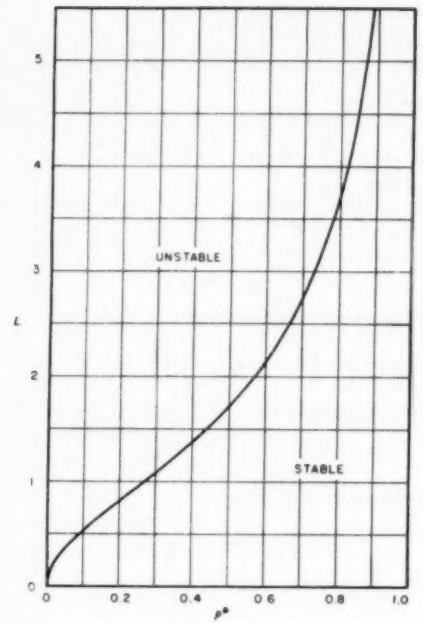


$$L = 2\,\frac{a}{l}\,AA_1\left(\frac{a}{w}\right)^2\sqrt{\rho\,Pcs}\;\Delta P, \quad P^* = \frac{2\,\Delta P}{Pcs}$$

FIG. 3 STABILITY DIAGRAM FOR MONOPROPELLANT SYSTEM

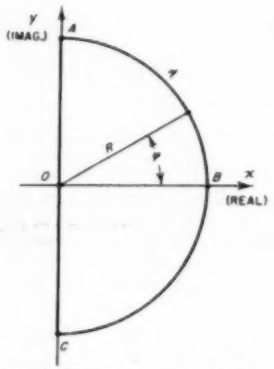


FIG. 4 THE CURVE γ IN THE $z$-PLANE

the number of poles and number of zeros of $f(z)$ within the contour, each pole and zero being counted according to its multiplicity." The theorem arises from the work of Cauchy. A derivation is given by Bode (3) in his book concerning the stability of electrical systems.

In accordance with the Nyquist method (3, 4, 5, 6) consider the values of $f(z)$ as $z$ varies around the path $\gamma$ in Fig. 4, made up of the imaginary axis and a semicircle which we can make larger and larger until, in the limit, it includes the whole right half-plane. Since our function $f(z)$ has no poles, we know from the foregoing theorem that if $f(z)$ be plotted in the $f(z)$-plane as $z$ travels once around the path $\gamma$, the number of times the plot encircles the origin will equal the number of zeros of $f(z)$ within the contour and hence in the entire right half-plane. It is clear that for stability the plot must not encircle the origin. Let us denote by $\lambda$ this plot in the $f(z)$-plane.

In general, $z$ is complex. Hence we may write

$$z = x + iy \qquad [15a]$$

$$= Re^{i\varphi} \qquad [15b]$$

We note that $x = R\cos\varphi$ and $y = R\sin\varphi$, where $\varphi$ is the phase angle of $z$. Values of $f(z)$ on the semicircle $ABC$ are found by substituting Equation [15b] into [14].

$$f(z) = B + R\cos\varphi + iR\sin\varphi + He^{-R\cos\varphi}\left[\cos(R\sin\varphi - i\sin(R\sin\varphi)\right] \qquad [16]$$

If $R$ is very large, then for all points on the semicircle, except in the neighborhood of $A$ and $C$, the factor $e^{-R\cos\varphi}$ is small, and Equation [16] can be written

$$f(z) = B + R\cos\varphi + iR\sin\varphi \qquad [17]$$

So the semicircular part of $\gamma$ transforms nearly into a semicircle in $\lambda$ with its center at $B + i0$.

To plot $\lambda$ for the vertical part of $\gamma$, substitute Equation [15a] into Equation [14] and set $x = 0$

$$f(z) = B + H\cos y + i(y - B\sin y) \qquad [18]$$

The complete plot is shown in Fig. 5. Notice that $\lambda$ is symmetrical about the real axis and that the curve $A'B'C'$ can have no effect on stability for sufficiently large $R$. So we need plot only the looping part of $\lambda$ for $y \geqslant 0$, as in Fig. 6. This plot actually can be drawn for each system analyzed. However, for the simple monopropellant system, we can use the plot merely as an aid to finding the analytical expression for the stability conditions.

It is easily shown that the loops do not open up until $B$ is far into impossible negative values. Then it is obvious from geometry that the critical condition exists when $B$ is small enough to

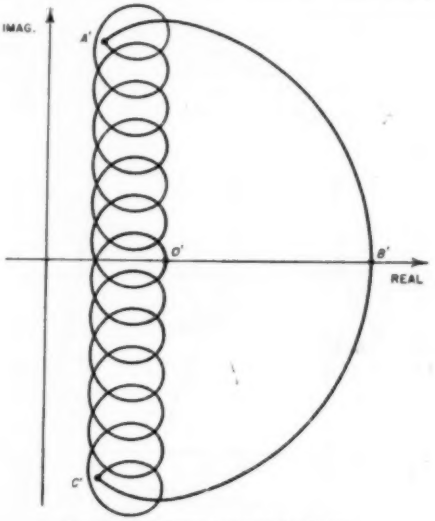


FIG. 5 THE CURVE λ IN THE $f(z)$-PLANE

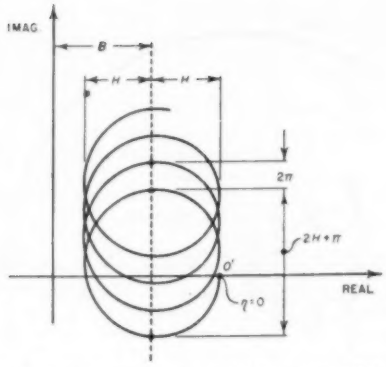


FIG. 6 ENLARGEMENT OF THE $f(z)$-PLANE FOR $y \geqslant 0$

allow the first loop to pass through the origin. When the curve passes through the origin

$$B + \frac{y}{\tan y} = 0 = \ln \frac{y}{H \sin y}$$

which is of course the result we obtained by the last method. It is obvious from geometry that the system is always stable if $B \geqslant H$, i.e., if $B/H \geqslant 1$.

## BIPROPELLANT SYSTEM

A simple bipropellant system is shown in Fig. 7. We use generally the same nomenclature as for the monopropellant system.

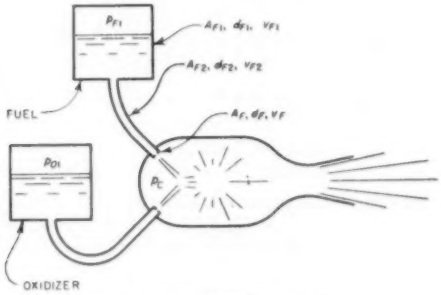


FIG. 7 BIPROPELLANT ROCKET SYSTEM

The subscript $F$ indicates properties of the fuel line, and the subscript $O$ indicates properties of the oxidizer system. We assume that $\alpha_O = \alpha_F = \alpha$.

From energy considerations, as before, we find

$$p_{F1} - P_{CS} = {}^1/_2 \rho_F v_{FS}^2 \left[1 + \frac{f_F l'_F}{d_{F2}} \left(\frac{d_F}{d_{F2}}\right)^4\right] \quad \ldots [18a]$$

and

$$p_{O1} - p_{CS} = {}^1/_2 \rho_O v_{OS}^2 \left[1 + \frac{f_O l'_O}{d_{O2}} \left(\frac{d_O}{d_{O2}}\right)^4\right] \quad \ldots [18b]$$

which correspond to Equation [4]; and assuming

$$p_C = p_{CS}\left(1 + k_F \frac{v'_{\alpha F}}{v_{FS}} + k_O \frac{v'_{\alpha O}}{v_{OS}}\right) \quad \ldots [19]$$

we get

$$\frac{dv'_F}{dt} + E_F v'_F = -G_F v'_{\alpha F} - L_F v'_{\alpha O} \quad \ldots [20a]$$

$$E_F = \frac{v_{FS}}{l_F}\left(\frac{d_{F2}}{d_F}\right)^2 \left[1 + \frac{f_F l'_F}{d_{F2}}\left(\frac{d_F}{d_{F2}}\right)^4\right]$$

$$G_F = \frac{k_F}{\rho_F l_F}\left(\frac{d_{F2}}{d_F}\right)^2 \frac{p_{CS}}{v_{FS}}$$

$$L_F = \frac{k_O}{\rho_F l_F}\left(\frac{d_{F2}}{d_F}\right)^2 \frac{p_{CS}}{v_{OS}}$$

By an interchange of subscripts

$$\frac{dv'_O}{dt} + E_O v'_O = -G_O v'_{\alpha O} - L_O v'_{\alpha F} \quad \ldots [20b]$$

$$E_O = \frac{v_{OS}}{l_O}\left(\frac{d_{O2}}{d_O}\right)^2 \left[1 + \frac{f_O l'_O}{d_{O2}}\left(\frac{d_O}{d_{O2}}\right)^4\right]$$

$$G_O = \frac{k_O}{\rho_O l_O}\left(\frac{d_{O2}}{d_O}\right)^2 \frac{p_{CS}}{v_{OS}}$$

$$L_O = \frac{k_F}{\rho_O l_O}\left(\frac{d_{O2}}{d_O}\right)^2 \frac{p_{CS}}{v_{FS}}$$

These equations correspond to Equation [5] of the monopropellant system. It is seen from Equation [19] that

$$k_F = \frac{v_{FS}}{p_{CS}} \frac{\partial p_C}{\partial v_F}$$

$$k_O = \frac{v_{OS}}{p_{CS}} \frac{\partial p_C}{\partial v_O}$$

Equations [20a] and [20b] may be reduced to one second-order equation by proceeding as follows:

Differentiate Equation [20a] with respect to $t$

$$\frac{d^2 v'_F}{dt^2} + E_F \frac{dv'_F}{dt} = -G_F \frac{d}{dt} v'_{\alpha F} - L_F \frac{d}{dt} v'_{\alpha O} \quad \ldots [21]$$

From Equations [20a] and [20b]

$$\frac{d}{dt} v'_{\alpha F} = -E_F v'_{\alpha F} - G_F v'_{2\alpha F} - L_F v'_{2\alpha O} \quad \ldots [22a]$$

$$\frac{d}{dt} v'_{\alpha O} = -E_O v'_{\alpha O} - G_O v'_{2\alpha O} - L_O v'_{2\alpha O} \quad \ldots [22b]$$

in which $v'_{2\alpha F}$ is $v'_F$ evaluated at time $t - 2\alpha$. From Equation [22a]

$$v'_{2\alpha O} = -\frac{1}{L_F}\left(\frac{d}{dt} v'_{\alpha F} + E_F v'_{\alpha F} + G_F v'_{2\alpha F}\right) \quad \ldots [23]$$

and from Equation [20a]

$$v'_{2\alpha O} = -\frac{1}{L_F}\left(\frac{dv'_F}{dt} + E_F v'_F + G_F v'_{\alpha F}\right) \quad \ldots [24]$$

Substitute Equations [23] and [24] into Equation [22b].

$$L_F \frac{d}{dt} v'_{\alpha O} = E_O\left(\frac{dv'_F}{dt} + E_F v'_F + G_F v'_{\alpha F}\right) + G_O\left(\frac{d}{dt} v'_{\alpha F} + E_F v'_{\alpha F} + G_F v'_{2\alpha F}\right) - L_F L_O v'_{2\alpha F} \quad \ldots [25]$$

Substitute Equation [25] into [21] and get

$$\frac{d^2v'_F}{dt^2} + E_F\frac{dv'_F}{dt} = -G_F\frac{d}{dt}v'_{aF} - E_O\left(\frac{dv'_F}{dt} + E_Fv'_F + G_Fv'_{aF}\right) - G_O\left(\frac{d}{dt}v'_{aF} + E_Fv'_{aF} + G_Fv'_{zaF}\right) + L_FL_Ov'_{zaF}$$

or

$$\frac{d^2v'_F}{dt^2} + (E_F + E_O)\frac{dv'_F}{dt} + E_FE_Ov'_F = -(G_F + G_O)$$

$$\frac{d}{dt}v'_{aF} - (E_FG_O + E_OG_F)v'_{aF} - (G_FG_O - L_FL_O)v'_{zaF} \ldots [26]$$

and since $G_FG_O - L_FL_O \equiv 0$

$$\frac{d^2v'_F}{dt^2} + \mu\frac{dv'_F}{dt} + \nu v'_F + \sigma\frac{d}{dt}v'_{aF} + \tau v'_{aF} = 0 \ldots [27]$$

$$\mu = E_F + E_O > 0 \quad \sigma = G_F + G_O$$
$$\nu = E_FE_O > 0 \quad \tau = E_FG_O + E_OG_F$$

Now assume a disturbance $v_F'$ in the interval $-\alpha < t < 0$ of such a form that it can be expanded in the series

$$v'_F = \sum C_je^{z_jt/\alpha}$$

Substituting this expression for $v_F'$ into Equation [27] for any $j$, we obtain

$$\frac{z^2}{\alpha^2} + \mu\frac{z}{\alpha} + \nu + \sigma\frac{z}{\alpha}e^{-z} + \tau e^{-z} = 0$$

or on multiplication by $\alpha^2$

$$z^2 + Mz + N + e^{-z}(Sz + T) \equiv f(z) = 0 \ldots [28]$$

$$M = \alpha\mu > 0 \qquad S = \alpha\sigma$$
$$N = \alpha^2\nu > 0 \qquad T = \alpha^2\tau$$

As before, if $f(z)$ has any zeros with positive real parts, our system is unstable. Again we let

$$z = x + iy \ldots [29a]$$
$$= Re^{i\varphi} \ldots [29b]$$

Values of $f(z)$ on the semicircle $ABC$ in Fig. 4 are found by substituting Equation [29b] into [28]

$$f(z) = R^2\cos 2\varphi + MR\cos\varphi + N + e^{-R\cos\varphi}[(RS\cos\varphi + T)\cos(R\sin\varphi) + RS\sin\varphi\sin(R\sin\varphi)] + i\{R^2\sin 2\varphi + MR\sin\varphi + e^{-R\cos\varphi}[RS\sin\varphi\cos(R\sin\varphi) - (RS\cos\varphi + T)\sin(R\sin\varphi)]\} \ldots [30]$$

To get $f(z)$ on $AOC$, substitute Equation [29a] into [28] and set $x = 0$

$$f(z) = (N - y^2 + Sy\sin y + T\cos y) + i(My + Sy\cos y - T\sin y) \ldots [31]$$

We can now plot in the $f(z)$-plane values of $f(z)$ for the complete path $\gamma$. We call this plot $\lambda$, as before. The curve thus plotted takes the form shown in Fig. 8. The loops correspond to the vertical part of $\gamma$, plotted from Equation [31]. The remainder corresponds to the semicircular part of $\gamma$ from Equation [20]. The curve is symmetrical about the real axis, and so we need plot only the part of $\lambda$ for which $y \geqslant 0$. Furthermore, we need not plot the semicircular part, for we can show that it always

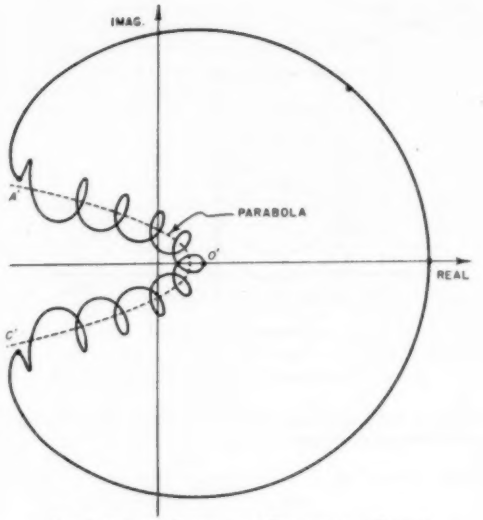


FIG. 8 THE $f(z)$-PLANE FOR A BIPROPELLANT SYSTEM

has the same general shape as in Fig. 8 for sufficiently large $R$. For this bipropellant system, we shall probably find it necessary to make the plot anew for each new set of numerical values of the system parameters. However, computation can be simplified by letting $B_F = \alpha E_F$, $B_O = \alpha E_O$, $H_F = \alpha G_F$, $H_O = \alpha G_O$, i.e.

$$\left.\begin{aligned} B_F &= v_{FS}\frac{\alpha}{i_F}\left(\frac{d_{F2}}{d_F}\right)^2\left[1 + \frac{f_Fl_F'}{d_{F2}}\left(\frac{d_F}{d_{F2}}\right)^4\right] \\ B_O &= v_{OS}\frac{\alpha}{l_O}\left(\frac{d_{O2}}{d_O}\right)^2\left[1 + \frac{f_Ol_O'}{d_{O2}}\left(\frac{d_O}{d_{O2}}\right)^4\right] \\ H_F &= \frac{k_F}{\rho_F}\frac{\alpha}{l_F}\left(\frac{d_{F2}}{d_F}\right)\frac{p_{CS}}{v_{FS}} \\ H_O &= \frac{k_O}{\rho_O}\frac{\alpha}{l_O}\left(\frac{d_{O2}}{d_O}\right)\frac{p_{CS}}{v_{OS}} \end{aligned}\right\} \ldots [32]$$

Or alternately, from Equations [32] and [18]

$$\left.\begin{aligned} B_F &= 2\frac{g\alpha A_{F2}}{w_{FS}l_F}\Delta p_F \\ B_O &= 2\frac{g\alpha A_{O2}}{w_{OS}l_O}\Delta p_O \\ H_F &= k_F\frac{g\alpha A_{F2}}{w_{FS}l_F}p_{CS} \\ H_O &= k_O\frac{g\alpha A_{O2}}{w_{OS}l_O} \end{aligned}\right\} \ldots [33]$$

where

$w_{FS}$ = fuel flow rate, weight per unit time

$w_{OS}$ = oxidizer flow rate, weight per unit time

$$k_F = \frac{w_{FS}}{p_{CS}}\frac{\partial p_C}{\partial w_F}$$

$$k_O = \frac{w_{OS}}{p_{CS}}\frac{\partial p_C}{\partial w_O}$$

Then

$$\left.\begin{aligned} M &= B_F + B_O & S &= H_F + H_O \\ N &= B_F B_O & T &= B_F H_O + B_O H_F \end{aligned}\right\} \quad \ldots [34]$$

A study of Equation [31] will yield the following information:

1 $(N - T)$ is the starting point of the curve (where $y = 0$).

2 $S$ and $T$ determine the size of the loops.

3 $M$ determines the parabola about which the curve loops, an increase in $M$ increasing the stability.

### Example

To apply the foregoing method to the idealized bipropellant system considered here, determine the four parameters $M$, $N$, $S$, and $T$, as defined by Equations [34], and plot in the complex plane, for $y \geqslant 0$, the function given by Equation [31]. If this plot encircles the origin, the system is unstable; otherwise it is stable. By applying the three observations at the end of the preceding paragraph, one can easily see from the plot how the parameters of an unstable system can be changed to make the system stable.

Consider the following example

| | |
|---|---|
| $\alpha = 8 \times 10^{-3}$ sec | $l_F = 2$ ft |
| $A_{F2} = 4.19 \times 10^{-4}$ sq ft | $l_O = 2$ ft |
| $A_{O2} = 7.10 \times 10^{-4}$ sq ft | $p_{CS} = 72{,}000$ psf |
| $\Delta p_F = 7200$ psf | $w_F = 0.365$ lb per sec |
| $\Delta p_O = 7200$ psf | $w_O = 0.635$ lb per sec |
| $k_F = 0.4$ | |
| $k_O = 0.6$ | |

From Equation [33]

| | |
|---|---|
| $B_F = 2.13$ | $H_F = 4.26$ |
| $B_O = 2.08$ | $H_O = 6.24$ |

Hence from Equations [34]

| | |
|---|---|
| $M = B_F + B_O = 4.21$ | $S = H_F + H_O = 10.50$ |
| $N = B_F B_O = 4.43$ | $T = B_F H_O + B_O H_F = 22.2$ |

Substituting these values in Equation [31] gives

$$f(z) = (N - y^2 + Sy \sin y + T \cos y) + i(My + Sy \cos y - T \sin y)$$

$$= (4.33 - y^2 + 10.50\, y \sin y + 22.2 \cos y) + i(4.21\, y + 10.50\, y \cos y - 22.2 \sin y)$$

This function is shown plotted in its own plane in Fig. 9. Since the plot encircles the origin, the system is unstable.

Let us change the system parameters as follows

| | |
|---|---|
| $A_{F2} = 1.74 \times 10^{-4}$ sq ft | $\Delta p_F = 44{,}600$ psf |
| $A_{O2} = 2.95 \times 10^{-4}$ sq ft | $\Delta p_O = 44{,}600$ psf |

We get

| | |
|---|---|
| $B_F = 5.48$ | $H_F = 1.768$ |
| $B_O = 5.35$ | $H_O = 2.59$ |

from which

| | |
|---|---|
| $M = 10.83$ | $S = 4.36$ |
| $N = 29.3$ | $T = 23.7$ |

The resulting function $f(z)$ is plotted in Fig. [10]. Since this plot does not encircle the origin, the modified system is stable.

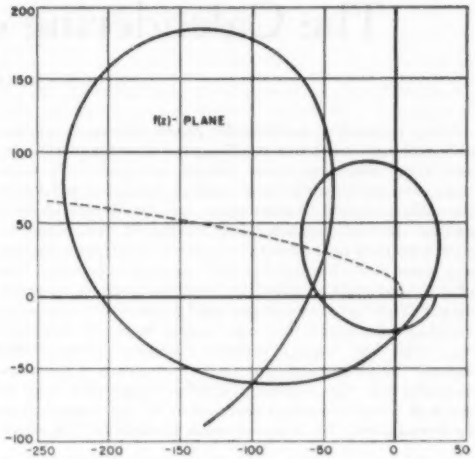


Fig. 9 Nyquist Diagram for a Rocket System (Unstable)

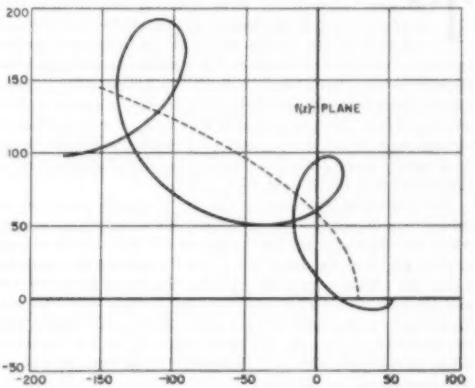


Fig. 10 Nyquist Diagram for a Rocket System (Stable)

### BIBLIOGRAPHY

1 "Evolution of Energy in Jet and Rocket Propulsion," by P. Bielkowicz, *Aircraft Engineering*, vol. 18, 1946, pp. 90, et seq.

2 "Mathematical Theory of Rocket Flight," by J. B. Rosser, R. R. Newton, and C. L. Gross, McGraw-Hill Book Company, Inc., New York, N. Y., 1947, pp. 237–248.

3 "Network Analysis and Feedback Amplifier Design," by H. W. Bode, D. Van Nostrand Company, Inc., New York, N. Y., 1945.

4 "The Dynamics of Automatic Controls," by R. C. Oldenbourg and H. Sartorius, translated from German and edited by H. L. Mason, ASME, New York, N. Y., 1948, 276 pp.

5 "Étude de la stabilité des systèmes accessibles a des mesures," by Yves Rocard, *La Revue Scientifique*, vol. 85, May 15, 1947, pp. 519–531.

6 "Regeneration Theory," by H. Nyquist, *Bell System Technical Journal*, vol. 11, January, 1932, pp. 126–147.

7 "Lehrbuch der Functionentheorie," by W. F. Osgood and B. G. Teubner, Leipzig, Germany, 1907.

# The Calendering of Plastic Materials

By R. E. GASKELL,[1] AMES, IOWA

**Many industries, notably the paper, linoleum, rubber, and steel industries, use a rolling process to form or otherwise treat sheets of these various materials. To most engineers, perhaps, the term "rolling" brings to mind only the rolling of steel or aluminum—solids with definite yield points. Several mathematical studies of the rolling of such materials have already been made.[2] In those studies, any shear stress beyond the yield stress is neglected. The plastic materials handled by other industries, however, do not often have the definite yield point of steel, or, after yielding takes place, they may behave more like liquids of very high and usually variable viscosity. Shear stress beyond the yield point, due to viscosity, cannot therefore be neglected. Consequently, a different approach must be made if a mathematical description of the process is to be formulated. Such an approach is made in this paper.**

## The Calendering or Rolling Process

THE term "calendering," which is usually used with reference to plastics such as linoleum mix, denotes the formation of a sheet by rolling a mass of material of indefinite shape between two cylinders. There are many variations of this process. Besides the mere formation of a sheet, a backing material may be passed through simultaneously. As in the steel industry, a sheet may be passed through several sets of rolls, or a sheet already formed may be calendered only to improve its surface finish. This paper, however, is concerned only with the formation of thin sheets by a two-roll calender.

This process is illustrated in Fig. 1. The rolls, which are assumed to be of great length, act upon a thin wedge of the material which is compressed, softened, and forced to flow through the nip of the rolls, where the distance between the rolls has the minimum value, $2t_0$. After passing through the nip, the material fills the gap between the rolls for some time, until, when some thickness $2t_E$ is reached, the material leaves the rolls as a solid sheet. This excess thickness over the thickness at the nip will be explained solely on the basis of flow characteristics of the material and not as a consequence of elasticity.

Materials that are calendered—linoleum mix, rubber, and other plastics—vary widely in their properties. None is a viscous liquid, for a true viscous liquid will not form a sheet. Hence, whatever mathematical procedure is used, it will be almost useless if it applies only to viscous liquids or even to materials which approximate a viscous liquid. A procedure which is valid for certain incompressible liquids of varying viscosity will be developed. For simplicity, it is developed first for viscous liquids, then extended in the section on "Structural Viscosity."

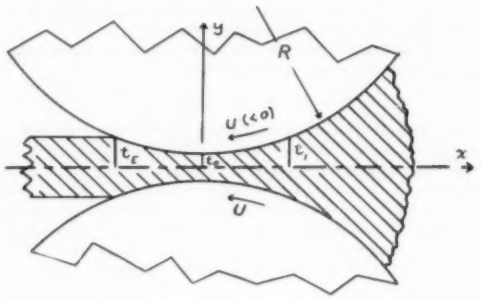


FIG. 1 CALENDERING PROCESS ILLUSTRATED

## Calendering of a Viscous Liquid

When a viscous liquid moves slowly between the parallel plates $y = \pm t$, so that the motion of any particle is always parallel to $Ox$, then the shear stress $\tau$, velocity $u$, and pressure $p$, satisfy the differential equations[3]

$$\tau = \mu\, du/dy \qquad [1]$$

$$dp/dx = d\tau/dy \qquad [2]$$

where $\mu$ is the viscosity. Combining Equations [1] and [2], we have

$$\mu d^2u/dy^2 = dp/dx \qquad [3]$$

and two integrations of Equation [3] together with the conditions $u(t) = u(-t) = U$, give

$$u = U + \frac{1}{2\mu}\frac{dp}{dx}(y^2 - t^2) \qquad [4]$$

Further, the total volume of flow, $Q$, is given by

$$Q = \int_{-t}^{t} u\, dy = 2t\left(U - \frac{t^2}{3\mu}\frac{dp}{dx}\right)$$

and so

$$\frac{dp}{dx} = \frac{3\mu U}{t^2}(1 - t_1/t) \qquad [5]$$

where $t_1 = Q/2U$. Having $dp/dx$, we can substitute in Equation [4] and get the velocity

$$u = \frac{U}{2}\left[\frac{3y^2}{t^2}(1 - t_1/t) - 1 + 3t_1/t\right] \qquad [6]$$

Now consider the flow between the two calender surfaces illustrated in Fig. 1

$$y = \pm t = \pm\,(t_0 + R - \sqrt{R^2 - x^2}) \qquad [7]$$

or, after expansion of the radical by the binomial theorem

$$y = \pm t = \pm[t_0 + x^2/(2R)] \qquad [8]$$

---

[1] Iowa State College.

[2] See, for example, "Beitrag zur Theorie des Walzvorganges," by Th. von Kármán, *Zeitschrift für angewandte Mathematik und Mechanik*, vol. 5, 1925, pp. 139–141.

Contributed by the Applied Mechanics Division and presented at the Annual Meeting, New York, N. Y., November 27–December 2, 1949, of THE AMERICAN SOCIETY OF MECHANICAL ENGINEERS.

Discussion of this paper should be addressed to the Secretary, ASME, 29 West 39th Street, New York, N. Y., and will be accepted until October 10, 1950, for publication at a later date. Discussion received after the closing date will be returned.

NOTE: Statements and opinions advanced in papers are to be understood as individual expressions of their authors and not those of the Society. Paper No. 49—A-34.

[3] "Hydrodynamics," by H. Lamb, Dover Publications, New York, N. Y., 1945, Equation [6], p. 574, and Equation [1], p. 582.

for small values of $x/R$. We have in Equation [5] an expression for $dp/dx$, when $t$ is constant. Let us assume that this still holds when $t$ is a function of $x$, as in Equation [8].[4] Further, let us use a dimensionless form of the variables $x$ and $y$

$$\xi = x/\sqrt{2Rt_0} = \pm\sqrt{t/t_0 - 1}$$

$$\eta = y/\sqrt{2Rt_0}$$

Then

$$\frac{dp}{d\xi} = \frac{6\mu U}{t_0\delta}\left[\frac{\xi^2 - \xi_1^2}{(1+\xi^2)^2}\right] \quad [9]$$

where

$$\xi_1 = x_1/\sqrt{2Rt_0} = \sqrt{t_1/t_0 - 1}$$

and

$$\delta = \sqrt{2t_0/R} \ll 1$$

Integration of Equation [9] gives

$$p = \frac{3\mu U}{4t_0\delta}\left\{\left[\frac{-1 + \xi^2 - 5\xi_1^2 - 3\xi^2\xi_1^2}{(1+\xi^2)^2}\right]\xi + (1 - 3\xi_1^2)\tan^{-1}\xi\right\} + C \quad [10]$$

We must now evaluate $\xi_1$ and the constant of integration in Equation [10] by finding or assigning two conditions from which to determine them. For one of these conditions we turn to the section at which the calendered material leaves the rolls, i.e., the exit, $\xi = \xi_E$. If we require that the velocity be uniform (independent of $y$) at the exit, then $\tau = 0$ there for every $y$; and by Equation [2]

$$dp/dx = dp/d\xi = 0$$

Hence from Equation [9]

$$\xi_E = -\xi_1$$

the negative sign being taken because the exit is to the left of the nip. Now evidently $p(\xi_E) = 0$, so

$$C = (1 - 3\xi_1^2)\tan^{-1}\xi_1 - (1 + 3\xi_1^2)\xi_1/(1 + \xi_1^2)$$

For any incompressible material $\xi_1$ can be determined by the relation $Q = 2Ut_1$, when the volume of calendered material and roll speed are known.

We observe that when a true viscous liquid is calendered, the pressure reaches a maximum at $\xi = \xi_1$, and falls to zero at $\xi = -\xi_1$. The shear stress is found by integrating Equation [2] and requiring that $\tau(0) = 0$

$$\tau = y\,dp/dx$$

Evidently $\tau = 0$ also when $\xi = \pm\xi_1$ (see Equation [9]). Streamlines can be constructed by integrating Equation [1] and finding $v$ so as to satisfy the continuity equation

$$\partial u/\partial x + \partial v/\partial y = 0$$

### Structural Viscosity

In the preceding section we dealt with an incompressible liquid with constant viscosity, a material which is called a "Newtonian liquid." Experiments show[5] that in many materials the viscosity, i.e., the ratio of shear stress to shear rate, is not constant at all. If, for a given material and under given conditions, the shear rate can be expressed as an odd function[6] of the shear stress alone, that is

$$du/dy = f(\tau) \quad [11]$$

that material is said to be a "Newtonian" or "non-Newtonian" liquid, according as $f(\tau)$ is "linear" or "nonlinear." Note that all materials cannot be classified thus; in particular, any material having some ability to recover its original shape is excluded.[7]

Let us use the method of the preceding section to find an expression for the pressure gradient during calendering of a non-Newtonian liquid. We shall use Equation [11] with Equation [2], but first let us substitute the dimensionless variables $\xi$, $\eta$, changing the equations to read[8]

$$du/d\eta = U\,F(\tau) \quad [12]$$

$$d\tau/d\eta = g(\xi) \quad [13]$$

where

$$F(\tau) = (2t_0/U\delta)f(\tau)$$

and

$$g = dp/d\xi$$

Since the problem is symmetric, $\tau(0) = 0$, so from Equation [13], $\tau = g\eta$, and Equation [12] can be written

$$du/d\eta = UF(g\eta) \quad [14]$$

Now if Equation [14] is integrated we have[9]

$$u/U = 1 - \frac{1}{g}\int_\tau^z F(\beta)d\beta$$

where $z = g\,\delta(1 + \xi^2)/2$. Note that when $y = t$, $\eta = \delta(1 + \xi^2)/2$, $\tau = z$, and $u/U = 1$. A second integration gives the rate of flow

$$Q = \frac{2U\delta R}{g}\int_0^z\left[1 - \frac{1}{g}\int_{\beta'}^z F(\beta)d\beta\right]d\beta' \quad [15]$$

But $t_1$ is defined so that

$$Q = 2Ut_1 = 2Ut_0(1 + \xi_1^2)$$

so Equation [15] may be reduced to

$$g^2\delta\,(\xi^2 - \xi_1^2)/2 = z\int_0^z F(\beta)d\beta - \int_0^z\int_0^{\beta'} F(\beta)d\beta d\beta' \quad [16]$$

Now the second integral in Equation [16] can be written as a single integral[10]

$$-\int_0^z F(\beta)(z - \beta)d\beta$$

so that Equation [16] becomes, after reduction

$$2(\xi^2 - \xi_1^2)/\delta(1 + \xi^2)^2 = z^{-2}\int_0^z \beta F(\beta)d\beta \quad [17]$$

Thus we have a relation between $z$ and $\xi$, and indirectly between $g$ and $\xi$. Given $\xi_1$, the pressure gradient $g(\xi)$ can be found.

---

[4] The same results will be found if the perturbation method is used.

[5] "A Survey of General and Applied Rheology," by G. W. Scott Blair, Pitman Publishing Corporation, New York, N. Y., 1944, pp. 32–34.

[6] A function $f(\tau)$ is odd if $f(-\tau) = -f(\tau)$.

[7] Experiments with linoleum mix indicate that it is very nearly incompressible, but no experimental results concerning its elastic behavior are available. However, it does not compare with some other materials such as vinylite in its elastic-recovery ability.

[8] The shear stress and pressure cannot be made dimensionless because in general there is no fixed quantity, connected with the problem, available as a standard.

[9] The variables $\beta$ occurring here and $\beta'$ in equation [15] are variables of integration. The integrals themselves are functions of the limits, $\tau$ and $z$.

[10] "The Mathematics of Physics and Chemistry," by H. Margenau and G. M. Murphy, D. Van Nostrand Company, Inc., New York, N. Y., 1943, pp. 507–508.

### Example—Calendering of Bingham Material

Let us assume that a given material possesses a shear stress-strain rate relation of the type

$$f(\tau) = \begin{cases} 0 & 0 < \tau < k \\ \nu(\tau - k) & k < \tau \end{cases}$$

with $f(\tau)$ odd. Such a material is called a "Bingham material," with the yield stress, $k$. To apply the results of the preceding section, we must write

$$F(\tau) = \begin{cases} 0 & 0 < \tau < k \\ 2l_0 \nu (\tau - k)/Uh & k < \tau \end{cases}$$

and then Equation [17] easily reduces to

$$\frac{\nu l_0}{6Uz^2}(2z^3 - 3kz^2 + 3k^3 \mp 2k^3) = (\xi^3 - \xi_1^3)/(1 + \xi^2)^2 \quad [18]$$

where the upper sign holds for $z \geqq k$, the lower sign for $z \leqq -k$.

Since $\tau = 0$ when $\eta = 0$, during calendering of Bingham material there will be a solid core of variable thickness within it. The thickness of this solid core depends upon the value of $\eta$, say, $\eta_0$, for which $\tau = \pm k$. Since $\tau = q\eta$, when $\tau = \pm k$, Equation [18] becomes

$$\nu k l_0 [3\rho^2 - 3 \mp 2(\rho^2 - 1/\rho)]/6U = (\xi^3 - \xi_1^3)/(1 + \xi^2)^2 \quad [19]$$

with $\rho = 2\eta_0/\delta(1 + \xi^2)$. Thus Equation [19] is a relation expressing $\eta_0$ in terms of $\xi$. We observe that for $0 < \rho \leqq 1$, the expression in brackets is zero when $\rho = 1$, positive when the upper sign is used ($z \geqq k$), and negative when the lower sign is used ($z \leqq -k$). The boundary of the solid core therefore touches the calender rolls at $\xi = \pm\xi_1$. For $\xi > \xi_1$, $\tau \geqq +k$ in the flowing material, while for $-\xi_1 < \xi < \xi_1$, $\tau \leqq -k$ there. A sketch of the core is given in Fig. 2.

We can give now a description of the behavior of Bingham material during calendering, derived entirely from the mathematical analysis. Entering on the right, the faces of the material are softened as the solid material moves into the rolls. The core speed increases, while the shear rate decreases, thus allowing some of the softened material to solidify again. When $\xi = \xi_1$, the speed of the core is that of the rolls, and the core extends from roll to roll.

After the material passes through the solid state at $\xi = \xi_1$, the core speed continues to increase, giving rise again to shear forces which soften the material near the rolls. This effect continues until at the nip ($\xi = 0$), the core velocity is a maximum, but its thickness is a minimum there. Beyond the nip, the reverse process takes place, and by the time the section $\xi = -\xi_1$ is reached, the solid core extends from roll to roll, and the calendered material leaves the rolls at that section. This is an interesting result, since in previous discussions of calendering it has been assumed that the sheet leaves the calender at the nip.[11] Unpublished experimental results of J. T. Bergen show that $t_1$ [$= (1 + \xi_1^2)t_0$] is actually from 20 per cent to 80 per cent greater than $t_0$.

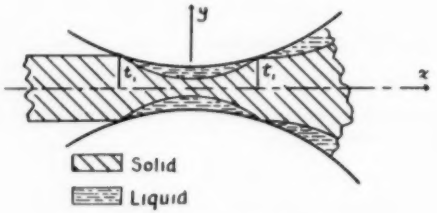


Fig. 2 Sketch of Core

### Some Generalizations of the Method

It is possible to reduce the problem of calendering with unequal roll diameters to the present symmetric problem by the substitution of

$$t = t_0 + x^2/2R_0$$

for Equation [8], where

$$\frac{1}{R_0} = \frac{1}{2}\left(\frac{1}{R_1} \pm \frac{1}{R_2}\right)$$

$R_1$ and $R_2$ being the two radii. The negative sign is used if the axis of the smaller roll lies inside the larger roll. The peripheral speeds of the two rolls must still be the same.

If the peripheral speeds are unequal, a more complex procedure, essentially a method of successive approximations, must be used to solve the relation that replaces Equation [17]. The same can be said of the problem of different roll temperatures, assuming that that temperature difference leads to a shear stress-strain rate relation of the form

$$du/d\eta = F(\tau)/(1 + \epsilon\eta/t)$$

### Acknowledgment

This paper contains some of the results of a project on the "Mathematics of Calendering," carried out for the Armstrong Cork Company, while the writer was at Brown University. The writer wishes to thank Prof. William Prager, who, as director of the project, contributed much to its success, Dr. G. W. Scott, and Mr. J. T. Bergen, for their patient guidance in the field of rheology, and officials of the Armstrong Cork Company who are making this publication possible.

[11] See for example, "Versuch der rationalen Bestimmung der Bombierung von Kalenderualsen," by V. Ardichvili, *Kautschuk*, vol. 14, 1938, pp. 23–25 and 41–45.

# Matrix Solution for the Vibration of Nonuniform Beams

By W. T. THOMSON,[1] MADISON, WIS.

**A matrix method for the determination of natural frequencies of any nonuniform beam is presented. It accomplishes the same task as that of Myklestad's tabular method with the added advantage of simplicity of formulation. Included is a procedure for the case where the nonuniform beam is represented by a series of uniform sections.**

## Nomenclature

The following nomenclature is used in the paper:

$S_i$ = shear at position just to the left of station $i$
$M_i$ = moment at $i$
$\theta_i$ = slope at $i$
$y_i$ = deflection at $i$
$\alpha_{S_i}$, $\alpha_{M_i}$ = angular displacement of $i$ with respect to a tangent at $i+1$, due to unit shear and unit moment at $i$
$d_{S_i}$, $d_{M_i}$ = linear displacement of $i$ with respect to a tangent at $i+1$, due to unit shear and unit moment at $i$
$m_i$ = mass at $i$
$\omega$ = frequency in radians/sec
$l_i$ = length of section $i$
$\beta_i = \dfrac{m_i\omega^2}{E_iI_i}$

## Introduction

Myklestad's tabular method[2] is probably the most successful method of determining the natural frequencies of nonuniform beams. The method is used successfully in the vibration analysis of airplane wings and fuselages, bridges, critical speeds of shafts, and so forth. The uniqueness of the method lies in the fact that the shape of the vibration curve need not be assumed and higher modes of vibration are obtained readily.

Myklestad's method assumes the mass distribution to be represented by concentrated masses at several stations along the beam. The stiffness coefficients for each section of the beam between stations are determined from the actual stiffness curve of the beam by the area-moment principle (see Computation Procedure). The geometric and equilibrium equations are then transformed to a tabular computational scheme by somewhat tedious algebraic substitutions which can be avoided by the matrix method.

## The Matrix Method

In problems of beam vibrations, the four quantities involved in the solution are the shear, moment, slope, and deflection at any point along the beam. In the matrix method, these quantities at any station $i+1$ must be expressed in terms of corresponding quantities at the adjacent station $i$.

From the diagram of Fig. 1 the quantities of interest can be expressed by the following equations.[2,3]

$$S_{i+1} = S_i + m_{i+1}\omega^2 y_{i+1} \quad [1]$$

$$M_{i+1} = l_iS_i + M_i \quad [2]$$

$$\theta_{i+1} = -\alpha_{S_i}S_i - \alpha_{M_i}M_i + \theta_i \quad [3]$$

$$y_{i+1} = -d_{S_i}S_i - d_{M_i}M_i - l_i\theta_{i+1} + y_i \quad [4]$$

$y_{i+1}$ and $\theta_{i+1}$ on the right side of Equations [1] and [4] are now replaced by quantities at $i$ by substituting Equation [3] in [4], and then Equation [4] in [1]. Arranged in matrix form, these equations become

$$\begin{bmatrix} S_{i+1} \\ M_{i+1} \\ \theta_{i+1} \\ y_{i+1} \end{bmatrix} = \begin{bmatrix} 1+m_{i+1}\omega^2(\alpha_{S_i}l_i - d_{S_i}) & m_{i+1}\omega^2(\alpha_{M_i}l_i - d_{M_i}) & -l_im_{i+1}\omega^2 & m_{i+1}\omega^2 \\ l_i & 1 & 0 & 0 \\ -\alpha_{S_i} & -\alpha_{M_i} & 1 & 0 \\ (\alpha_{S_i}l_i - d_{S_i}) & (\alpha_{M_i}l_i - d_{M_i}) & -l_i & 1 \end{bmatrix} \begin{bmatrix} S_i \\ M_i \\ \theta_i \\ y_i \end{bmatrix} \quad [5]$$

The shear, moment, slope, and deflection at $i+1$ are now in terms of corresponding quantities at $i$, and the quantities in the square matrix are all in terms of mass, length, and stiffness of the section for any chosen frequency $\omega$. Having determined the square matrix for each section, the quantities at $i$ may be replaced by quantities at $i-1$, etc., the final equation becoming

$$\begin{bmatrix} S_n \\ M_n \\ \theta_n \\ y_n \end{bmatrix} = \begin{bmatrix} A_{11} & A_{12} & A_{13} & A_{14} \\ A_{21} & A_{22} & A_{23} & A_{24} \\ A_{31} & A_{32} & A_{33} & A_{34} \\ A_{41} & A_{42} & A_{43} & A_{44} \end{bmatrix} \begin{bmatrix} S_0 \\ M_0 \\ \theta_0 \\ y_0 \end{bmatrix} \quad [6]$$

The square matrix of Equation [6] is obtained by multiplying all the square matrices of the form shown in Equation [5] where the $ij$-term is obtained by multiplying the $i$th row by the $j$th column.

Equation [6] holds for any boundary conditions, some of which are discussed in the section which follows.

*Cantilever Beam.* With the free and fixed ends at 0 and $n$, respectively, the boundary conditions become

$$S_0 = M_0 = \theta_n = y_n = 0$$

Substituting into Equation [6]

---

[1] Associate Professor of Mechanics, Department of Mechanics, College of Engineering, University of Wisconsin. Mem. ASME.

[2] "New Method of Calculating Natural Modes of Uncoupled Bending Vibrations," by N. O. Myklestad, *Journal of the Aeronautical Sciences*, vol. 11, 1944, pp. 153–162.

Contributed by the Applied Mechanics Division and presented at the Annual Meeting, New York, N. Y., November 27–December 2, 1949, of The American Society of Mechanical Engineers.

Discussion of this paper should be addressed to the Secretary, ASME, 29 West 39th Street, New York, N. Y., and will be accepted until October 10, 1950, for publication at a later date. Discussion received after the closing date will be returned.

Note: Statements and opinions advanced in papers are to be understood as individual expressions of their authors and not those of the Society. Paper No. 49—A-11.

[3] "Mechanical Vibrations," by W. T. Thomson, Prentice Hall, Inc. New York, N. Y., 1948, p. 172.

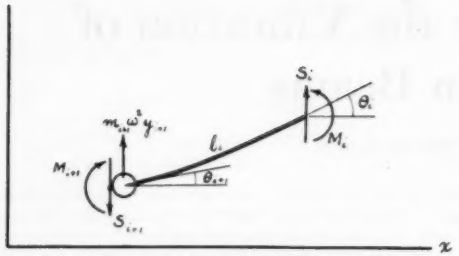


FIG. 1 FREE-BODY DIAGRAM OF SECTION $i$

$$A_{22}\theta_0 + A_{24}y_0 = 0$$
$$A_{42}\theta_0 + A_{44}y_0 = 0$$

Eliminating $\theta_0$ and $y_0$, the frequency equation becomes

$$-\frac{A_{42}A_{24}}{A_{22}} + A_{44} = 0 \quad \ldots\ldots\ldots\ldots\ldots [7]$$

*Beams With Hinged Ends.* The boundary conditions are

$$M_0 = M_n = y_1 = y_n = 0$$

Thus from Equation [6]

$$A_{21}S_0 + A_{23}\theta_0 = 0$$
$$A_{41}S_0 + A_{43}\theta_0 = 0$$

and the frequency equation becomes

$$-\frac{A_{41}A_{23}}{A_{21}} + A_{43} = 0 \quad \ldots\ldots\ldots\ldots\ldots [8]$$

*An Airplane Wing.* Placing station 0 at the wing tip and the fuselage at $n$, the boundary conditions for the symmetric and antisymmetric modes become

(*a*) Symmetric modes

$$S_0 = M_0 = S_n = \theta_n = 0$$

From Equation [6]

$$A_{13}\theta_0 + A_{14}y_0 = 0$$
$$A_{33}\theta_0 + A_{34}y_0 = 0$$

and the frequency equation is

$$-\frac{A_{13}A_{34}}{A_{33}} + A_{14} = 0 \quad \ldots\ldots\ldots\ldots\ldots [9]$$

(*b*) Antisymmetric modes

$$S_0 = M_0 = M_n = y_n = 0$$

Equation [6] then yields

$$A_{23}\theta_0 + A_{24}y_0 = 0$$
$$A_{43}\theta_0 + A_{44}y_0 = 0$$

leading to the frequency equation

$$-\frac{A_{23}A_{44}}{A_{43}} + A_{24} = 0 \quad \ldots\ldots\ldots\ldots\ldots [10]$$

Equations [9] and [10] correspond to $S_n = 0$ and $M_n = 0$, i.e., the shaking force and shaking moment necessary to maintain vibration at resonance is zero.

## COMPUTATION PROCEDURE

Numerical computations are carried out by first assuming a frequency $\omega$ and computing the elements of the square matrix, Equation [5], for each section of the beam. It should be noted that only the first row of Equation [5] depends on $\omega$. Multiplying out the square matrices from $n$ to 0, the matrix elements $A_{ij}$ of Equation [6] are obtained and substituted into the frequency equation. Repeating with other values of $\omega$, the natural frequencies are determined where the curve for the frequency equation passes through zero.

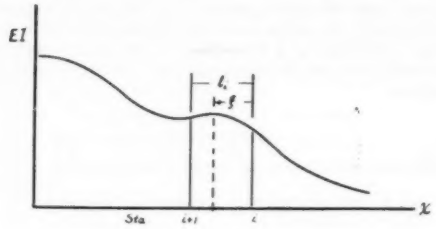


FIG. 2

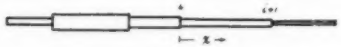


FIG. 3

*Stiffness.* The stiffness coefficients are determined by the area-moment principle. Referring to Fig. 2, they are

$$\alpha_{M_i} = \int_0^{l_i} \frac{d\xi}{EI}$$

$$\alpha_{S_i} = d_{M_i} = \int_0^{l_i} \frac{\xi d\xi}{EI}$$

$$d_{S_i} = \int_0^{l_i} \frac{\xi^2 d\xi}{EI}$$

If the $EI$-curve between stations is assumed to be a straight line these equations reduce to the expressions of Myklestad.[2]

*Nonuniform Beam Represented by a Series of Uniform Sections.* If the beam is represented by a series of uniform sections as in Fig. 3, the differential equation for the $i$th section becomes

$$\frac{d^4y}{dx^4} - \beta_i^4 y = 0$$

with the solution

$$y_{i+1} = \frac{1}{2}(\cosh \beta_i l_i + \cos \beta_i l_i)y_i + \frac{1}{2\beta_i}(\sinh \beta_i l_i + \sin \beta_i l_i)y_i'$$
$$+ \frac{1}{2\beta_i^2}(\cosh \beta_i l_i - \cos \beta_i l_i)y_i'' + \frac{1}{2\beta_i^3}(\sinh \beta_i l_i - \sin \beta_i l_i)y_i'''$$

Differentiating, the quantities at $i + 1$ can be expressed in terms of corresponding quantities at $i$ by the matrix equation

$$\begin{bmatrix} y_{i+1} \\ y'_{i+1} \\ y''_{i+1} \\ y'''_{i+1} \end{bmatrix} = \begin{bmatrix} a & b/\beta_i & c/\beta_i^2 & d/\beta_i^3 \\ \beta_i d & a & b/\beta_i & c/\beta_i^2 \\ \beta_i^2 c & \beta_i d & a & b/\beta_i \\ \beta_i^3 b & \beta_i^2 c & \beta_i d & a \end{bmatrix} \begin{bmatrix} y_i \\ y'_i \\ y''_i \\ y'''_i \end{bmatrix}$$

where

$$a = \frac{1}{2}(\cosh \beta_i l_i + \cos \beta_i l_i)$$

$$b = \frac{1}{2}(\sinh \beta_i l_i + \sin \beta_i l_i)$$

$$c = \frac{1}{2}(\cosh \beta_i l_i - \cos \beta_i l_i)$$

$$d = \frac{1}{2}(\sinh \beta_i l_i - \sin \beta_i l_i)$$

Thus the solution can be put in the form of Equation [6] with the corresponding frequency equations.

# Discussion

## Introduction to the Comprex[1]

G. M. Dusinberre.[2] There is an earlier paper by Kantrowitz[3] which appears to have escaped the author's attention. In that paper it was stated that the delivery pressure of the cold air will be greater than the inlet pressure of the hot gas. (Both pressures understood to be stagnation values.) The author shows the blower, $F$, in his Fig. 3, as in the Meyer paper,[4] and the pressure rise 3-7 in his Fig. 4. There is no combustion-chamber pressure drop shown in Fig. 4, so we are not to suppose that the blower is used for this reason.

Will the author comment on this disagreement?

T. C. Tsu.[5] The writer has always been fascinated by the comprex, an ingenious compression-expansion device, ever since its announcement in this country several years ago. Very few machines can match the uniqueness of the comprex, which is constructionally so simple, yet functionally so involved. The fact that the comprex has worked cannot be denied, and its potentialities in the field of gas-turbine applications should not be overlooked.

The writer, however, is puzzled by some of the author's results. For example, the author has shown that with a given scavenging velocity, $w_1/\sqrt{T_1}$, and a given pair of polytropic exponents, $n_c$ and $n_e$, all operating conditions of the comprex, namely, the pressure ratio $p_2/p_1$, the temperature ratio $T_6/T_1$, and the flow ratio $W_6/W_1$, are determined. One cannot help but wonder what would happen, if, without altering the scavenging velocity, the temperature ratio were raised arbitrarily by injecting more fuel into the combustor, or the flow ratio were varied by resetting the position of the by-pass valve.

Published performance data of the comprex are very meager. However, in a paper by Adolph Meyer,[4] and another by Hans Pfenninger,[6] both being connected with Brown Boveri which manufactured the first comprex, it is indicated that air enters the comprex at 4 atm and 400 F, leaves at 10 atm and 600 F; gas enters the comprex at 10 atm and 1800 F, and leaves at 4 atm and 1100 F. Based on these figures and using the author's notation, it is calculated that $n_c = 1.297$ and $n_e = 1.677$. This result contradicts the author's assumption of using values greater than 1.4 for $n_c$, and values less than 1.4 for $n_e$.

From a physical standpoint, it is difficult to visualize that a slight variation in the polytropic exponents, particularly that for expansion, should so tremendously affect the performance of the comprex, as indicated by the author's curves in Figs. 6, 7, 9, and 10. The author has concluded that if both the compression process and the expansion process are isentropic, the temperature ratio and the flow ratio become unity (see Figs. 9 and 10 of the paper.) This means that a perfect comprex is a useless comprex. This writer finds such a paradox hard to understand.

### Author's Closure

The paper by Kantrowitz, which the author has seen, deals with larger pressure ratios than does this paper. The losses in the high-pressure piping and the combustion chamber must be evaluated in the design of a particular unit; if they are small enough no blower is required.

If more fuel were injected the comprex would run at off-design conditions. The change in wave velocities would distort the assumed wave processes and the efficiencies of the compression and expansion processes would change. Off-design conditions are beyond the scope of this paper.

The author also has noticed that the figures for temperatures and pressures quoted by Brown Boveri disagree with his assumptions, but he has not been able to resolve the difference.

The paradox that a perfect comprex is a useless comprex has been hard for the author to understand also. However, he would like to point out that this paradox applies to another machine, the vortex refrigerator, which cannot operate unless viscous forces are present.

The author thanks the discussers and also Dr. Hussmann, who talked with the author about his report on the comprex.[7]

## Effect of Imperfections on Buckling of Thin Cylinders and Columns Under Axial Compression[1]

J. W. Clark[2] and Marshall Holt.[2] It was the authors' intention to apply their analysis to all known test data on the compressive strength of thin cylinders under axial compression. The purpose of this discussion is to make available some additional data obtained at the Aluminum Research Laboratories, some of which are quite new. The aluminum-alloy specimens are described in Tables 1, 2, and 3 of this discussion. Imperfections were reduced as much as possible by machining the outside surface of drawn tubing after the tubing had been shrunk onto an arbor, or completely machining the tubes from rolled rod. The ends were cut flat and perpendicular to the axis of the specimen.

The specimens of Group A were of uniform section, and, because they were so flimsy, they were fitted with snug-fitting rings to facilitate handling and to insure roundness at the ends. The ends of these specimens and those of Group B bore directly against the hardened platens of the testing machine. One platen was free to tip until a small load was placed on the specimen. It was then clamped in this position. The specimens of Group C had shouldered ends which held them round. The transition from the reduced central portion to the end was made with a fillet of quite generous proportions. In these tests the platens were aligned

[1] By F. W. Barry, published in the March, 1950, issue of the Journal of Applied Mechanics, Trans. ASME, vol. 72, pp. 47–53.

[2] Department of Mechanical Engineering, The Pennsylvania State College, State College, Pa. Mem. ASME.

[3] "Heat Engines Based on Wave Process," by Arthur Kantrowitz, paper No. 48—A-133, presented at the Annual Meeting, New York, N. Y., November 28–December 3, 1948, of The American Society of Mechanical Engineers.

[4] "Recent Developments in Gas Turbines," by Adolph Meyer, *Mechanical Engineering*, vol. 69, 1947, pp. 274–275.

[5] Associate Professor of Engineering Research, The Pennsylvania State College, State College, Pa. Mem. ASME.

[6] "Where Gas Turbine Will Fit in Future Power Fields," by Hans Pfenninger, *Power*, vol. 91, January, 1947, pp. 87(25)–88(26).

[7] "The Comprex, Description and Theoretical Discussion of a Special Type of Pressure Exchanger," by Albrecht Hussmann, USAF Technical Report No. F-TR-1189-ND, ATI No. 38398.

[1] By L. H. Donnell and C. C. Wan, published in the March, 1950, issue of the Journal of Applied Mechanics, Trans. ASME, vol. 72, pp. 73–83.

[2] Aluminum Research Laboratories, Aluminum Company of America, New Kensington, Pa.

TABLE 1 DESCRIPTION OF SPECIMENS OF GROUP A MACHINED FROM 178-T4 ALUMINUM-ALLOY DRAWN TUBING INITIALLY 4 IN. OD × 0.034 IN. WALL

| Specimen no. | Outside diameter, $D$, in. | Wall thickness, $t$, in. | Length, in. | Ratio, $R/t$ | Area, $A$, sq in. | Ultimate load, $P$, lb | Compressive strength $P/A$, psi |
|---|---|---|---|---|---|---|---|
| 33-1 | 3.944 | 0.0195 | 6.00 | 101 | 0.248 | 7160 | 28,870 |
| -2 | 3.945 | 0.0195 | 4.00 | 101 | 0.236 | 7950 | 33,690 |
| -3 | 3.945 | 0.0193 | 2.00 | 102 | 0.236 | 7980 | 33,810 |
| 34 | 3.930 | 0.0126 | 4.00 | 156 | 0.160 | 4200 | 26,250 |
| 35 | 3.928 | 0.0098 | 4.00 | 200 | 0.123 | 2548 | 20,720 |
| 36-1 | 3.920 | 0.0080 | 6.00 | 245 | 0.098 | 1828 | 18,650 |
| -2 | 3.924 | 0.0075 | 4.00 | 262 | 0.098 | 1820 | 18,570 |
| -3 | 3.920 | 0.0080 | 2.00 | 245 | 0.098 | 1875 | 19,130 |
| 37 | 3.903 | 0.0041 | 6.00 | 476 | 0.050 | 314 | 6,280 |
| 38 | 3.904 | 0.0033 | 3.50 | 591 | 0.041 | 136 | 3,320 |
| 39 | 3.904 | 0.0031 | 2.00 | 630 | 0.038 | 79.8 | 2,100 |

NOTE: Properties of material from which specimens were turned are as follows:
Tensile strength = 63,200 psi
Tensile yield strength (offset = 0.2 per cent) = 45,200 psi
Compressive yield strength (offset = 0.2 per cent) = 38,200 psi.

TABLE 2 DESCRIPTION OF SPECIMENS OF GROUP B MACHINED FROM 178-T4 ALUMINUM-ALLOY DRAWN TUBING INITIALLY 2 1/8 IN. OD × 0.203 IN. WALL

| Specimen no. | Outside diameter, $D$, in. | Wall thickness, $t$, in. | Length, in. | Ratio, $R/t$ | Area, $A$, sq in. | Ultimate load, $P$, lb | Compressive strength $P/A$, psi |
|---|---|---|---|---|---|---|---|
| 17-1 | 2.601 | 0.0655 | 1.90 | 19.4 | 0.522 | 25,200 | 48,300 |
| -2 | 2.601 | 0.0655 | 3.47 | 19.4 | 0.522 | 24,750 | 47,400 |
| -3 | 2.601 | 0.0655 | 5.70 | 19.4 | 0.522 | 24,800 | 47,500 |
| 19 | 2.572 | 0.0500 | 3.63 | 25.3 | 0.396 | 18,100 | 45,700 |
| 20 | 2.554 | 0.0415 | 2.09 | 30.3 | 0.328 | 15,000 | 45,730 |
| 24 | 2.524 | 0.0255 | 3.05 | 49.0 | 0.200 | 7,900 | 39,500 |
| 29 | 2.560 | 0.0430 | 2.88 | 29.3 | 0.340 | 15,500 | 45,600 |
| 31 | 2.537 | 0.0315 | 2.73 | 39.8 | 0.248 | 9,750 | 39,300 |

NOTE: Properties of material from which specimens were turned are as follows:
Tensile strength = 60 660 psi
Tensile yield strength (offset = 0.2 per cent) = 40 800 psi.

TABLE 3 DESCRIPTION OF SPECIMENS OF GROUP C MACHINED FROM 75S-T6 ALUMINUM-ALLOY 2-IN-DIAM ROLLED ROUND ROD

| Specimen no. | Outside diameter $D$, in. | Wall thickness, $t$, in. | Ratio, $R/t$ | Area $A$, sq in. | First test[a] Ultimate load, $P$, lb | First test[a] Compressive strength, $P/A$, psi | Second test[b] Ultimate load, $P$, lb | Second test[b] Compressive strength, $P/A$, psi |
|---|---|---|---|---|---|---|---|---|
| 1 | 1.719 | 0.1719 | 4.5 | 0.836 | 83,000 | 99,300 | | |
| 2 | 1.478 | 0.0515 | 13.8 | 0.231 | 19,000 | 82,300 | 19,350 | 83,850 |
| 3 | 1.433 | 0.0288 | 24.4 | 0.127 | 10,050 | 79,100 | 10,200 | 80,300 |
| 4 | 1.410 | 0.0176 | 39.6 | 0.0770 | 5,500 | 71,500 | 5,650 | 73,300 |
| 5 | 1.401 | 0.0121 | 57.4 | 0.0528 | 3,350 | 63,500 | 3,595 | 68,100 |
| 6 | 1.394 | 0.0093 | 74.5 | 0.0405 | 2,395 | 58,400 | 2,455 | 60,500 |

[a] 6-in-long reduced section between shouldered ends.
[b] 4.5-in-long uniform section cut from undamaged portion after first test.
NOTE: Properties of material from which specimens were turned are as follows:
Tensile strength = 85,700 psi
Tensile yield strength (offset = 0.2 per cent) = 76,100 psi
Compressive yeild strength (offset = 0.2 per cent) = 82,000 psi.

parallel within 0.0003 in. in 12 in. by means of a special leveling device and clamped in this position. In all cases the failure was quite sudden and the buckle pattern consisted of a number of small waves near one end. In the case of the specimens of Group C, the central portion of the specimen appeared undamaged so this was cut out and retested after the ends had been machined flat and perpendicular to the axis. The close agreement of these two sets of test results indicates that this detail of the method of testing was relatively unimportant.

The data are plotted in Fig. 1 herewith, together with the theoretical buckling curve for $U = 0.00015$ scaled from Fig. 9 of the paper. Some of these tubes developed higher ratios of critical stress to theoretical critical stress for perfect cylinders than were developed in any of the tests discussed by the authors.

The trend of the data points from specimens of Group A having $r/t$ ratios greater than about 200 crosses the theoretical curve, indicating increasing difficulties in making and testing specimens with high ratios of radius to wall thickness.

The specimens of Groups A and B with $r/t$ ratios less than 200, and four of the specimens in Group C failed at average stresses above the elastic stress range. The curves for $\sigma_y/(UE)$ equal to 20 and 50 have been transferred from Fig. 9, and appear to agree fairly closely with the test results in Fig. 1 herewith. The actual values of this parameter are 24.5 for Groups A and B, and 52.5 for Group C, when $\sigma_y$ is the compressive yield strength at 0.2 per cent offset. If, as the authors suggest, $\sigma_y$ were taken as a value

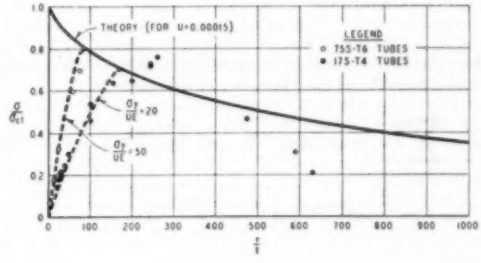


FIG. 1

near the proportional limit, the values of $\sigma_y/(UE)$ would be reduced, and the corresponding curves in Fig. 1 would probably be somewhat lower than those shown.

## AUTHORS' CLOSURE

The authors are much obliged to Messrs. Clark and Holt for the interesting new data which they add to the experiments which we were able to cite in our paper. We are somewhat amazed at the confirmation which this new data gives to our theoretical curves for plastically initiated buckling. We had only advanced

our results as rough approximations, even though we believed them to be the best which could be obtained at present.

In using our curves of Fig. 9 for design purposes, the following values of the unevenness factor $U$ should give reasonable results: 0.00015 to 0.0003 for machined cylinders (such as those of Clark and Holt or Robertson); 0.0003 to 0.0005 for cylinders carefully rolled from well-flattened sheet (such as those of Lundquist); 0.0005 to 0.0010 for cylinders rolled from unflattened sheet (such as those of Bridget or Donnell). The quantity $\sigma_y$ is defined in our paper and should be taken as the yield point of the material (not the proportional limit). This is an arbitrarily defined quantity for materials like the aluminum alloys, but the "yield point" as usually defined is probably as suitable as any simply defined quantity would be.

## Deflections and Moments Due to a Concentrated Load on a Cantilever Plate of Infinite Length[1]

H. D. Conway.[2] An approximate solution to the problem discussed by the author may be obtained quite simply by applying the well-known Levy method to a rectangular plate having two parallel edges simply supported, one edge clamped and one edge free. If the length-breadth ratio of the plate is then assumed to be fairly large (e.g., $a/b = 4$–$5$), the fact that the short sides of the plate are simply supported instead of free will not alter the magnitudes of the deflections and stresses in the central region to any appreciable extent. To illustrate this approximate method, the particular case where the concentrated load acts at equal distances from the clamped and free edges is considered. The labor involved in making the calculations can be considerably reduced by using the data given by Timoshenko[3] for another plate problem.

The differential equation for the loaded portion of the plate is

$$D\nabla^4\omega = q \qquad [1]$$

where $q$ is the intensity of loading. For the unloaded portions of the plate the corresponding equation is

$$\nabla^4\omega = 0 \qquad [2]$$

In the usual Levy manner, the deflection of the strip between the dotted lines $AB$ and $CD$, Fig. 1, may be written as

$$\omega = \sum_{m=1}^{\infty}\left(a_m + A_m\cosh\frac{m\pi y}{a} + B_m\sinh\frac{m\pi y}{a} + C_m\frac{m\pi y}{a}\sinh\frac{m\pi y}{a} + D_m\frac{m\pi y}{a}\cosh\frac{m\pi y}{a}\right)\sin\frac{m\pi x}{a} \qquad [3]$$

where

$$\omega_1 = \sum_{m=1}^{\infty} a_m \sin\frac{m\pi x}{a} \qquad [4]$$

represents the deflections due to cylindrical bending of the simply supported strip. By evaluating $a_m$ it may easily be shown that

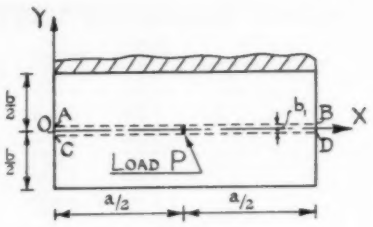


FIG. 1

$$\omega_1 = \frac{2Pa^3}{b_1 D\pi^4}\sum_{m=1,3,5}^{\infty}\frac{(-1)^{\frac{m-1}{2}}}{m^4}\sin\frac{m\pi x}{a} \qquad [5]$$

For the region above the line $AB$, we write

$$\omega' = \sum_{m=1}^{\infty}\left(A_m'\cosh\frac{m\pi y}{a} + B_m'\sinh\frac{m\pi y}{a} + C_m'\frac{m\pi y}{a}\sinh\frac{m\pi y}{a} + D_m'\frac{m\pi y}{a}\cosh\frac{m\pi y}{a}\right)\sin\frac{m\pi x}{a} \qquad [6]$$

and for the region below the line $CD$

$$\omega'' = \sum_{m=1}^{\infty}\left(A_m''\cosh\frac{m\pi y}{a} + B_m''\sinh\frac{m\pi y}{a} + C_m''\frac{m\pi y}{a}\sinh\frac{m\pi y}{a} + D_m''\frac{m\pi y}{a}\cosh\frac{m\pi y}{a}\right)\sin\frac{m\pi x}{a} \qquad [7]$$

Using the continuity conditions of deflection, slope, moment, and shearing force along the dotted line $AB$ and adopting the notation

$$\frac{m\pi b_1}{4a} = \beta_m$$

it is found that, if $\beta_m$ is assumed very small

$$\left.\begin{aligned} A_m - A_m' &= -a_m \\ B_m - B_m' &= a_m\beta_m \\ C_m - C_m' &= \frac{a_m}{2} \\ D_m - D_m' &= -a_m\beta_m \end{aligned}\right\} \qquad [8]$$

Four similar equations found for the line $CD$ give, when subtracted from the above equations

$$\left.\begin{aligned} A_m' &= A_m'' \\ B_m' &= B_m'' - 2a_m\beta_m \\ C_m' &= C_m'' \\ D_m' &= D_m'' + 2a_m\beta_m \end{aligned}\right\} \qquad [9]$$

Along the clamped edge $y = b/2$

$$\omega' = \frac{\partial\omega'}{\partial y} = 0 \qquad [10]$$

and along the free edge $y = -b/2$

$$\left.\begin{aligned} \frac{\partial^2\omega''}{\partial y^2} + \nu\frac{\partial^2\omega''}{\partial x^2} &= 0 \\ \frac{\partial^3\omega''}{\partial y^3} + (2-\nu)\frac{\partial^3\omega''}{\partial x^2\partial y} &= 0 \end{aligned}\right\} \qquad [11]$$

[1] By T. J. Jaramillo, published in the March, 1950, issue of the JOURNAL OF APPLIED MECHANICS, Trans. ASME, vol. 72, pp. 67–72.

[2] Professor of Mechanics, Cornell University, Ithaca, N. Y. Jun. ASME.

[3] "Theory of Plates and Shells," by S. Timoshenko, McGraw-Hill Book Company, Inc., New York, N. Y. 1940, pp. 146–149.

Assuming for convenience that $\nu = 0$, these four boundary conditions give, when taken with Equations [9]

$$A_m' = \frac{-\alpha_m\beta_m\{\alpha_m^2 + \sinh\alpha_m\cosh\alpha_m(\alpha_m^2 - 3\cosh^2\alpha_m + 1) + \alpha_m(1+\cosh^2\alpha_m)\}}{\alpha_m^2 + 3\sinh^2\alpha_m\cosh^2\alpha_m + 1}$$

$$B_m' = \frac{-\alpha_m\beta_m\{2\alpha_m\sinh\alpha_m\cosh\alpha_m + \sinh^2\alpha_m(2\alpha_m^2 - 2\sinh^2\alpha_m - \cosh^2\alpha_m)\}}{\alpha_m^2 + 3\sinh^2\alpha_m\cosh^2\alpha_m + 1}$$

$$C_m' = \frac{\alpha_m\beta_m\{\alpha_m\cosh^2\alpha_m + \sinh\alpha_m\cosh\alpha_m(2 - 3\cosh^2\alpha_m)\}}{\alpha_m^2 + 3\sinh^2\alpha_m\cosh^2\alpha_m + 1}$$

$$D_m' = \frac{\alpha_m\beta_m\{2\alpha_m\sinh\alpha_m\cosh\alpha_m - \alpha_m^2 - \sinh^2\alpha_m(3\cosh^2\alpha_m - 1)\}}{\alpha_m^2 + 3\sinh^2\alpha_m\cosh^2\alpha_m + 1} \quad \ldots\ldots [12]$$

where $\alpha_m = (m\pi b)/(2a)$. The remaining eight constants may be determined from Equations [8] and [9].

From Equation [3] the deflection under the load is

$$\omega = \frac{Pa^2}{2D\pi^3}\sum_{m=1,3,5}^{\infty}\frac{1}{m^3}\left\{\frac{\alpha_m^2 + \sinh\alpha_m\cosh\alpha_m(\alpha_m^2 - 3\cosh^2\alpha_m + 1) + \alpha_m(1+\cosh^2\alpha_m)}{\alpha_m^2 + 3\sinh^2\alpha_m\cosh^2\alpha_m + 1}\right\} \quad \ldots\ldots [13]$$

If this expression is evaluated for $a/b = 4$, the sum of the first four terms is found to be $-0.07213\ (Pb^2)/(\pi D)$ and the remaining terms simplify to become

$$\frac{-Pa^2}{2D\pi^3}\sum_{m=9,11}^{\infty}\frac{1}{m^3} \quad \ldots\ldots [14]$$

Since it may easily be shown that

$$\sum_{m=1,3,5}^{\infty}\frac{1}{m^3} = \frac{7}{8}\sum_{m=1,2,3}^{\infty}\frac{1}{m^3} = \frac{7}{8}\zeta(3) \quad \ldots\ldots [15]$$

where $\zeta(3)$ is a Riemann zeta function numerically equal to 1.202, the total sum of Equation [13] is found; its numerical value is $-0.0752\ (Pb^2)/(\pi D)$. If Equation [13] is summed for $a/b = 5$, an almost identical result is obtained, thus showing that the deflection is practically independent of the ratio $a/b$ for values greater than 4. The result given by the author for $\nu = 0.3$ is $-0.0794\ (Pb^2)/(\pi D)$ and it is considered that the discrepancy is due partly to the differences in the values of Poisson's ratio.

The bending moment $M_x$ at $x = a/2$, $y = b/2$ is found to be

$$M_x = \frac{P}{2\pi}\sum_{m=1,3,5}^{\infty}\frac{1}{m}\left\{\frac{4\alpha_m\cosh\alpha_m - 6\alpha_m\cosh^3\alpha_m - 2\alpha_m^2\sinh\alpha_m - 2\sinh\alpha_m}{\alpha_m^2 + 3\sinh^2\alpha_m\cosh^2\alpha_m + 1}\right\} \quad \ldots\ldots [16]$$

If this expression is evaluated for $a/b = 4$, the sum of the first five terms is $-0.3523\ P$ and the remaining terms simplify to become

$$\frac{-Pb}{a}\sum_{m=11,13}^{\infty}e^{-\alpha_m}$$

which is a geometrical series. The total sum of Equation [16] is then found to be $-0.3584\ P$ which compares favorably with the value $-0.370\ P$ given by the author. Again the discrepancy is partially due to differences in the values of Poisson's ratio.

### Author's Closure

The author greatly appreciates Professor Conway's interesting comments. The suggested approximate approach to the problem indeed seems to yield good results for the deflection at the centerline of the plate. It appears somewhat doubtful, however, whether the complete moment and deflection distribution throughout the significant central zone surrounding the load-point, can be obtained in the same manner with sufficient degree of accuracy.

## On Plastic Flow and Vibrations[1]

E. H. Lee.[2] The stress-strain curves of medium-carbon steel are used by the author as an example of the spring-dashpot model. However, apart from superficial appearance, they differ fundamentally in their main characteristics. For very slow rates of loading, the stress-strain curves for steel at room temperatures retain their form with comparatively little change.[3] The model would give extension at the work-hardening gradient from zero stress with no elastic region and no bend in the curve. In the case of mild steel, only small stress reduction occurs at constant strain, whereas the model would give relaxation down to the line given by the work-hardening gradient through the origin. On unloading, mild steel shows recovery of the elastic strain with a very small recovery of plastic strain. The model gives complete recovery to zero strain.

Thus in the main characteristics of plastic flow, the model gives fundamentally incorrect predictions. This is not surprising, for the linear equations of the model clearly cannot represent the nonlinear phenomenon of plastic flow, in which loading followed by unloading produces permanent strain. In fact, Prandtl's solid-friction model is in much closer agreement with plastic flow in metals than the viscous-friction model proposed in this paper.

In order to avoid repetition of the confusion which exists between plastic flow in metals and the time-dependent recoverable

[1] By C. J. Thorne, published in the March, 1950, issue of the Journal of Applied Mechanics, Trans. ASME, vol. 72, pp. 84–90.

[2] Associate Professor of Applied Mathematics, Brown University, Providence, R. I. Mem. ASME.

[3] "Time Effect in Testing Metals," by H. Quinney, *The Engineer*, vol. 157, 1934, pp. 332–334.

flow of such materials as textiles and organic plastics, the writer suggests that the latter phenomenon be termed time-dependent elasticity according to its long-time recovery, and that plasticity be restricted to the type of phenomena found in metals and associated with permanent strain.

### Author's Closure

The author made no attempt to justify the use of the spring-dashpot model in this paper. It was assumed that the paper by Fredrickson and Eyring was sufficient justification for the investigation. However, see also "Elasticity and Anelasticity of Metals" by Clarence Zener, University of Chicago Press, 1948, especially page 42. The theoretical basis of the model on the atomic or molecular level and the consequent expressions for the constants of the material in terms of structure properties of the fundamental units appeals to the author as basically correct.

It is well known that many materials including iron show the following types of deformation for loading or unloading. See "Elastic After-Effects in Iron Wires From 20 to 550 C," by W. A. West, Trans. AIME, vol. 167, 1946, pages 192–221:

1 Instantaneous deformation recoverable instantaneously in whole or in part.

2 Delayed deformation recoverable slowly in whole, in part, or not at all.

3 Permanent deformation.

West also found that the major part of strain is recoverable. The model as used in the paper implied recoverable deformations as indicated by primary creep. Secondary creep effects were not discussed.

A stress-strain curve composed of two straight-line segments is at least disturbing where it should have nonconstant continuous slope. Finally, it must be admitted that the model as used is not the final answer, but it is felt that many of its quantitative inadequacies will be traced to the fact that as used it represents an average of many similar units on a molecular scale.

# Book Reviews

## Numerical Analysis of Heat Flow

NUMERICAL ANALYSIS OF HEAT FLOW. By G. M. Dusinberre. McGraw-Hill Book Company, Inc., New York, N. Y., 1949. Cloth, 6 × 9 in., xiv and 227 pp., illustrations, $4.50.

REVIEWED BY VICTOR PASCHKIS[1]

THE author proposes to describe in this book the application of the "relaxation procedure" to heat-flow problems and thus provide practicing engineers with the "final numerical results" which they need (page 199). It includes sixteen sections which are all in juxtaposition without tying in such sections which are closely related under a common superior heading.

The first three sections (thermal properties, elementary computations, and analytical solutions) form a sort of introduction written in clear and elementary style. It is believed that even engineers who have been out of touch with mathematical texts for a considerable length of time will have no difficulty using this section. The next seven sections deal with steady-state problems, one- and two-dimensional. The following three sections deal with transient flow in one and two dimensions. The next two sections deal with refinements, namely, "cyclic transients and variable properties." In the last section the author deals with a number of engineering problems, partly solving them, partly only discussing them. In addition, this section includes some general speculation on engineering work, in general, and particularly connected with the relaxation method.

The text dealing exclusively with the one numerical method, the relaxation technique, is somewhat short in treating on page 68 the iteration method. In order to make the book more useful the author quotes applications from a large variety of fields. It is unavoidable that some errors in special applications occur: casehardening of steel, case page 139, is not done by induction heating. Casehardening is a technique which includes increasing the carbon content of steel near the surface in order to obtain greater surface hardness.

The book will be helpful to an engineer who wants to master the special technique of the relaxation method, sections dealing with this topic being written in the form of concise instructions. Only in a few instances are the instructions not clear. For example, pages 57–59 are not easy to follow; the additions in Figs. 8–12 are made for the right, not, as the text reads, from the left. Similarly on page 64, the technique of block relaxation is introduced which is not defined but is introduced only by inference.

Mathematical proofs, considerations of accuracy, and physical interpretations are held to a minimum. This is at the same time the main asset and the main disadvantage of the book. It would serve the purpose of an operator's instructions manual but will be insufficient for the reader who wants to evaluate accuracies and possible scope of the technique on a broad scale.

In almost all chapters a number of examples are given and ample problems for the use of students are presented.

The author takes great pains to place the numerical method in the right perspective in connection with the practice of heat-flow engineering.

Although the author discourages the use of charts and graphs as aids to the practicing engineer (pages 20 and 198) his case seems not too strong: he objects on the basis that charts and graphs have to be made on the basis of simplifying assumptions, for example, constant thermal properties; but most of the book is based on the same assumptions and only a few pages (section 15) give some indication how to handle temperature-dependent properties.

In weighing the advantages of the numerical method as against charts the author refers to the ability of the structural engineer to solve stress problems which usually are not presented in the form of graphs and tables. Against this, one might quote the steam tables—the author will not expect the thermodynamic engineer to calculate pressure heat content, etc., of steam for every problem, but will agree to the use of tables. The tool of numerical analysis will be very helpful to an engineer working daily with it. It is not a method that can be picked up in a few minutes by the practicing engineer usually not concerned with this kind of approach.

[1] Technical Director, Heat and Mass Flow Analyser Laboratory, Columbia University, New York, N. Y. Mem. ASME.

## Numerical Methods of Analysis in Engineering

NUMERICAL METHODS OF ANALYSIS IN ENGINEERING. A publication resulting from a symposium held at Illinois Institute of Technology. Arranged and edited by L. E. Grinter. The Macmillan Company, New York, N. Y., 1949. Cloth, 6¹/₄ × 9¹/₄ in., xvi and 207 pp., $5.80.

REVIEWED BY D. N. DE G. ALLEN[2]

WHEN a practical problem is confronted in engineering the solution required is usually a number (or numbers). The number is not necessarily required to be found exactly but only to within some specified degree of accuracy. These are two basic reasons why it is important that there should be a growing interest in and application of numerical methods: in the first place they often provide the only hope of obtaining even an approximate answer to many problems—and by sufficient labor their approximations can usually be improved as much as may be necessary; in the second place numerical methods often provide a sufficiently accurate result much more quickly than rigorous mathematical analysis, in cases when the latter can be used to find an exact solution. The book under review is one which will be of interest to many readers—both to those who are using and developing these methods and also to those engineers who may wish to find out what sort of problems can now be solved for them numerically. The book is composed of ten chapters by different authors and results from a symposium on numerical methods held at the Illinois Institute of Technology in honor of the twenty-fifth anniversary of the birth of the idea of moment distribution; the first chapter is a reprint of the original paper on moment distribution by Hardy Cross; today any further comment on that article would be superfluous.

Some of the chapters are descriptions of methods already established; some suggest new methods, or at least new modifications of known methods; and others are discussions of the background and fundamental hypotheses on which the methods are, in general, based. Thus F. S. Shaw contributes a brief description of the application of the relaxation method to solve boundary-value problems governed, in particular, by Laplace's equation.

[2] Lecturer, Imperial College of Science and Technology, South Kensington, London, England.

It is a little to be regretted that he finds it necessary to introduce variants of some of the hitherto accepted nomenclature and symbols. Dealing with the same (Laplace's) equation M. M. Frocht proposes a new idea for obtaining a good first approximation to the solution. R. V. Southwell has written a short but provocative chapter in which he discusses one of the underlying assumptions on which all finite-difference methods depend; this assumption is that of the validity of polynomial representation and his conclusion is, that in order to reduce the inherent error of a finite-difference replacement for a differential equation, a reduction in the size of the intervals is to be preferred to an introduction of more complicated finite-difference formulae.

Three chapters are, separately, surveys of certain topics or aspects of numerical methods: T. J. Higgins gives an account of the problem of the torsion of a cylinder, making particular reference to the application of variational methods and their use both contrasted with and complementary to the use of finite-difference methods. F. Baron is more concerned with the general approach to numerical solutions; he draws attention to the similarities that exist from the numerical point of view in solving a variety of problems, emphasizes the consequent importance of physical analogies as aids to solution, and discusses broadly the types of computational steps which are in common use and the orders in which they are applied. N. M. Newmark makes a rather more detailed comparison of some types (e.g., iterative step-by-step, relaxation, etc.) of numerical methods illustrated in application to stress and strain analysis.

Two chapters are devoted to numerical solutions of heat-transfer problems. G. M. Dusinberre solves one transient and one steady-state problem, both of which, in effect, are examples illustrating methods of solving sets of linear simultaneous algebraic equations. L. M. K. Boelter and M. Tribus employ finite differences to solve the heat-conduction equation and have devised a system of recording which is particularly effective when the temperature at one internal point only is under investigation.

The book is well produced and clearly printed with the exception that many of the diagrams, although carefully drawn, have been too much and unnecessarily reduced in size; it has been arranged and edited by L. E. Grinter who himself has written a chapter on grid analysis; emphasizing the statistical nature of stress, Dr. Grinter puts forward his belief that the stresses obtained using an analogous grid to replace a plate may be more useful than would be point stresses found by solving the equations of mathematical elasticity. He explains how the grid should be properly devised and also details the numerical procedure.

## Practical Analysis

PRACTICAL ANALYSIS—Graphical and Numerical Methods. By Friedrich A. Willers (Translated by Robert T. Beyer, Brown University). Dover Publications, Inc., New York, N. Y., 1948. Cloth, 6 × 9¼ in., x and 422 pp., 132 figs., tables, illustrations, $6.

REVIEWED BY V. L. SALERNO[3]

THE book describes graphical, numerical, and instrumental methods of practical analysis and consists of six chapters with the following headings: (1) Numerical calculation and its aids; (2) interpolation; (3) approximate integration and differentiation; (4) practical equation theory; (5) analysis of empirical function; (6) approximate integration of ordinary differential equations.

The first chapter is devoted to a discussion of errors, function scales, nomograms, and desk calculating machines such as the Marchant, Monroe, and the Friden.

The second chapter deals with the general interpolation formulas of Newton, Sterling, Bessel, and applications of these formulas.

The third chapter describes and gives the theory of the integrator and planimeter and discusses Euler's formula and mean-value methods used in approximating the values of integrals.

Chapter 4 is devoted to the approximate calculation of the roots of any equation by linear interpolation, Newton's method, iteration methods, and Graeffe's method. Some interesting methods for determining roots graphically are described. The chapter concludes with several analytical and graphical methods for solving simultaneous linear equations.

The fifth chapter is devoted to curve fitting by linear functions, power series, orthogonal functions, and by the method of least squares with several graphical methods for harmonic analysis.

The last chapter discusses the isoclinic, Runge-Kutta, and Adams methods for the approximate integration of ordinary differential equations.

The material is presented clearly with a large number of illustrative examples making the book quite useful for self-instruction.

It appears that the value of this book to present-day investigators would have been greatly enhanced by a discussion of computational machinery such as differential analyzers, digital and analog computers, and IBM machines.

## Theory of Wing Sections

THEORY OF WING SECTIONS: Including a Summary of Airfoil Data. By Ira H. Abbott and Albert E. von Doenhoff. McGraw-Hill Book Company, Inc., New York, N. Y.; Toronto, Can.; London, England, 1949. Cloth, 6 × 9 in., viii and 693 pp., illus., graphs, diagrams, figs., references, $15.

REVIEWED BY HUGH L. DRYDEN[4]

IN this book the authors present the results of ten years of experimental and theoretical research conducted by the National Advisory Committee for Aeronautics on the design of wing sections for use at subcritical speeds. Practical utility of the theoretical methods and experimental data to designers is the guiding principle of the treatment.

The step from wing-section characteristics to three-dimensional wing characteristics is sketchily described (30 pages, chapter 1), almost in cookbook-recipe fashion. Students would do better to begin with chapter 2, deferring chapter 1 until chapters 2 to 7 have been completed, with the expectation of additional reading of references on chapter 1.

Some 52 pages (chapter 9) are devoted to the effects of compressibility at subsonic speeds with such illustration and analysis as can be given from unclassified literature.

About half the book is devoted to description and experimental data on NACA families of wing sections of practical importance. The data were obtained in the 3 × 7½-ft two-dimensional low-turbulence pressure tunnel at Reynolds numbers from 3 to 9 million and Mach numbers less than 0.17.

Chapters 2, 3, and 4 give a systematic treatment of wing-section theory addressed to engineers with a limited background in theoretical aerodynamics and mathematics. Beginning with the equations of motion, the concepts of stream function, irrotational motion, vorticity, circulation, and potential are concisely developed in chapter 2 (14 pages) and examples are given of uniform flow, sources and sinks, doublets, vortex motion, and flow around a circular cylinder in a uniform stream with and without circulation.

Chapter 3 (17 pages) introduces complex variables and con-

[3] Associate Professor of Applied Mechanics, Polytechnic Institute of Brooklyn, Brooklyn, N. Y.

[4] Director, National Advisory Committee for Aeronautics, Washington, D. C. Fellow ASME.

formal transformations. The theory of wing sections of finite thickness is developed as the conformal transformation of the flow about a circular cylinder. Theodorsen's method for the flow about arbitrary wing sections is then presented in extended outline form. An empirical modification to account for the effect of the boundary layer as developed by Pinkerton is then described.

Chapter 4 (15 pages) describes the theory of thin wing sections following the treatment of Glauert. It is then explained how a combination of thin and thick-wing-section theory gives a simple method of quickly computing pressure distributions with engineering accuracy.

Chapter 5 (30 pages) is a brief treatise on the effects of viscosity, i.e., boundary-layer theory, including transition and separation of laminar and turbulent layers.

Chapter 6 (12 pages) describes the development of the NACA families of wing sections including the low-drag sections.

Chapter 7 (63 pages) gives a valuable systematic analysis of the extensive experimental data on these families set forth in the last half of the book. This includes such practical details as the effects of surface irregularities resulting both from current methods of manufacture of aircraft wings and from artificial roughness.

Chapter 8 (58 pages) is devoted to high-lift devices for improving the maximum lift coefficient, a subject of great importance to aircraft designers.

This is one of the indispensable books for any engineer concerned with aircraft or machinery design in which airfoil data are used.

## Introduction to the Laplace Transformation

AN INTRODUCTION TO THE LAPLACE TRANSFORMATION. By J. C. Jaeger. John Wiley and Sons, Inc., New York, N. Y., 1949. Cloth, $4^1/_4 \times 6^3/_4$ in., viii and 132 pp., $1.50.

REVIEWED BY JOHN A. HRONES[5]

THIS book, "An Introduction to The Laplace Transformation," by J. C. Jaeger, is a small book of some 130 pages divided into 4 chapters; the list of titles indicates the scope of the manuscript: (1) Fundamental Theory, (2) Electric Circuit Theory, (3) Further Theorems and Their Applications, and (4) Partial Differential Equations.

It is one of a series of books bearing the title Methuen's Monographs on Physical Subjects. The purpose of the series is to provide a compact and usable statement of the basic principles and their applications of each subject covered by the monograph. They are supposedly written at a level that can be read and understood by those whose educational background is of the level of a bachelor's degree in science or engineering and who are working in fields relating to those discussed in the series. This volume by Jaeger presents a very brief treatment of some fundamental applications of the Laplace transformation. It gives very concisely a few of the widely used theorems, in each case illustrating their use by actually carrying through the solution of several problems. The relatively large number of illustrative examples which are completely solved is one of the features of this book.

In the second chapter the Laplace transformation is applied to the solution of linear differential equations arising in the analysis of electric circuits. In the same chapter, applications to mechanical systems involving rotating shafts and disks are taken up. A brief discussion of applications to the analysis of servomechanisms is also included.

In the final chapter an introduction to the use of the Laplace transformation in the solution of partial differential equations is presented. The major application discussed in this respect is the electric transmission-line problem. A number of problems are included at the end of each chapter.

The book is well done and although limited in scope, would serve the needs of many engineers and scientists. A major criticism is the failure to include in the book a suitable table of functions and their corresponding Laplace transforms.

[5] Professor of Mechanical Engineering, Massachusetts Institute of Technology, Cambridge, Mass. Mem. ASME.

## Manual on Fatigue Testing

MANUAL ON FATIGUE TESTING. American Society for Testing Materials, Philadelphia, Pa., 1949, Special Technical Publication No. 91. 6 × 9 in., 88 pp. Heavy Paper Cover, $2.50; Cloth Cover, $3.15; to A.S.T.M. Members, Paper, $1.85; Cloth, $2.50.

REVIEWED BY G. S. CHERNIAK[6]

THIS manual has been compiled in recognition of the growing importance of the fatigue problem in modern machine design. The scope of the manual as stated by the personnel of the committee headed by R. E. Peterson is, "The formulation of methods for the determination of fatigue characteristics of simple and composite materials, components, and processed parts . . ."

The manual is divided into an introduction and seven sections presenting the consensus of the current viewpoint on the following topics: symbols and nomenclature for fatigue testing, fatigue-testing machines, specimens and their preparation, test procedure and technique, presentation of fatigue data, interpretation of fatigue data, and bibliography. While it is by no means a definitive text on the subject, and was not intended as such, it is undoubtedly an extremely valuable guide to workers in the field. As is inevitable in a first attempt at standardization of nomenclature, presentation of data, etc., in a highly specialized field, differences of opinion stemming from different professional viewpoints are apparent. However, what compromises were entailed in the presentation appear to be quite reasonable. There is some question in the reviewer's mind as to the justification for omitting any discussion of damage phenomena and the statistical interpretation of data in the manual.

This manual is highly recommended as a guide to workers in the field of fatigue.

## Solution of a Problem in Elasticity

RESOLOCION DE UN PROBLEMA DE ELASTICIDAD. Discussion, applications, and solution of G. B. Jeffrey's problem. By Federico Goded Echevarria. Instituto Technico de la Construccion y del Cemento No. 88, Madrid, Spain, 1949.

REVIEWED BY ERNESTO SALEME[7]

THE author claims to have solved Jeffery's problem—the eccentric ring under uniformly distributed internal and external normal loads, by applying the transformation of inversion to a concentric ring whose solution was given by Lamé. He works out the stress field and compares his results with those obtained by Jeffery[8] and finding them different qualifies Jeffery's solution as "approximate."

As anybody familiar with Jeffery's paper knows, his solution is given in a closed form and hence is exact within the usual restric-

[6] Chief Engineer, Lessells and Associates, Inc., Boston, Mass.

[7] Research Engineer, Armour Research Foundation of Illinois Institute of Technology, Chicago, Ill.

[8] "Plane Stress and Plane Strain in Bipolar Co-Ordinates," by G. B. Jeffery, Philosophical Transactions of the Royal Society of London, series A, vol. 221, 1920–1921, pp. 265–293.

tions of two-dimensional elasticity. The author was misled because the procedure he followed gives indeed the solution for the inverted problem if the region is simply connected but, as was pointed out by Mindlin[9] in multiply connected regions, as in the present case, a solution that is single-valued in the original domain, may originate multiple-valued solutions in the inverse domain.

It is unfortunate that the several technical applications studied by the author cannot be used because of the afore-mentioned fundamental error in the deduction of the formula. It should also be noticed that the author does not mention any bibliographic reference.

## Theoretical Hydrodynamics

THEORETICAL HYDRODYNAMICS. By L. M. Milne-Thomson. Second edition. College Department, The Macmillan Company, New York, N. Y., 1950. Cloth, 6 × 9¼ in., xxiv and 600 pp., illustrated, $8.50

REVIEWED BY R. C. BINDER[10]

THIS book is a reference work on the purely mathematical study of fluid motion. The book departs from the usual presentation in that vector methods and notation are used throughout. A large number of particular flow problems are analyzed in detail. The treatment is clear and methodical; the mathematics is reasonably self-contained.

Nineteen chapters deal with frictionless flow; the other chapter deals with laminar or viscous flow. All the chapters except the last assume an incompressible fluid. Exercises are listed at the end of each chapter.

Chapter 1 presents a number of introductory theorems. Chapter 2 covers properties of vectors useful in flow studies. Vectors are introduced without any reference to systems of co-ordinates. Chapter 3 presents the basic relations of continuity, energy, momentum, and vorticity in vector form. Chapter 4 is occupied with features of two-dimensional motion which can be treated without the complex variable. Chapter 5 presents the complex variable, defined as a vector operator, and conformal mapping. Chapters 6 through 14 form a unit in giving a detailed study of two-dimensional motion. These chapters make full use of the complex variable, conformal mapping, and Blasius' theorem. These chapters include kinematic studies, basic flows (as sources and sinks), Joukowski airfoils, the moving cylinder, the mapping theorem of Schwartz and Christoffel, and jets. Chapter 13 covers rectilinear vortexes, the Kármán vortex street, and the drag due to a vortex wake. Chapter 14 deals with two-dimensional wave motion.

[9] "Stress Systems in a Circular Disk Under Radial Forces," by R. D. Mindlin, JOURNAL OF APPLIED MECHANICS, Trans. ASME, vol. 59, 1937, p. A-115.

[10] Professor of Mechanical Engineering, Purdue University, W. Lafayette, Ind. Mem. ASME.

Chapter 15 introduces Stokes' stream function and the application of conformal mapping to three-dimensional problems with axial symmetry. The general motion of spheres and ellipsoids is treated in chapter 16. In chapter 17 partial differentiation with respect to a vector is applied to obtain Kirchhoff's equations in vector form, thus replacing six equations by two. Chapter 18 discusses vortex motion, in general, with application to the airfoil of finite span. Chapter 14 outlines the use of vector methods to viscous flow. Chapter 20 provides an introduction to subsonic and supersonic flow.

Apart from some rearrangements, this second edition differs from the first in that several new theorems have been introduced, and a chapter on compressible flow has been added.

Various types of books are necessary in engineering practice and engineering instruction. Some workers in applied mechanics may not favor vector analysis as the only approach to many flow problems. From the viewpoint of a purely mathematical treatment, however, the book by Professor Milne-Thomson is excellent.

## Nonlinear Problems in Mechanics of Continua

NON-LINEAR PROBLEMS IN MECHANICS OF CONTINUA. Proceedings of Symposia in Applied Mathematics. Volume I. American Mathematical Society, New York, N. Y., 1949. Cloth, 6¼ × 9¼ in., illustrated, viii and 219 pp., $5.25.

REVIEWED BY HUGH L. DRYDEN[11]

THIS volume is a collection of twenty-four papers, a few in abstract only, which were presented during the First Symposium on Applied Mathematics of the American Mathematical Society, which was held at Brown University in August, 1947. Sixteen of the papers deal with problems in fluid mechanics and eight with problems in elasticity and plasticity. The authors are A. Weinstein, S. Bergman, L. Bers, G. Birkhoff, S. R. Brinkley, Jr., and J. G. Kirkwood, N. Coburn and C. L. Dolph, H. W. Emmons, Y. H. Kuo, L. Lees, C. C. Lin, I. Opatowski, H. Poritsky, W. R. Sears, H. Polachek and R. J. Seeger, J. J. Stoker, A. H. Taub, F. D. Murnaghan, G. F. Carrier, D. C. Drucker, K. O. Friedrichs, W. Kaplan, S. Levy, W. Prager, and E. Reissner.

The collection gives a panoramic view of topics of special interest to mathematicians interested in applications. Ten of the papers are clearly summaries or short presentations of work published in greater detail elsewhere. Relatively few of the papers include the correlation of experimental and theoretical work. However, anyone interested in applied mechanics will find papers of interest in this collection.

[11] Director, National Advisory Committee for Aeronautics, Washington, D. C. Fellow ASME.